NAVIGATING CHAOS: RESONANT ORBITS FOR SUSTAINING CISLUNAR OPERATIONS

by

Maaninee Gupta

A Dissertation

Submitted to the Faculty of Purdue University

In Partial Fulfillment of the Requirements for the degree of

Doctor of Philosophy

School of Aeronautics and Astronautics

West Lafayette, Indiana

May 2024

THE PURDUE UNIVERSITY GRADUATE SCHOOL
STATEMENT OF COMMITTEE APPROVAL

Dr. Kathleen C. Howell, Chair

School of Aeronautics and Astronautics

Dr. Carolin E. Frueh

School of Aeronautics and Astronautics

Dr. David Arnas Martinez

School of Aeronautics and Astronautics

Dr. Thomas A. Pavlak

Jet Propulsion Laboratory, California Institute of Technology

Approved by:

Dr. Gregory A. Blaisdell

To my mom, my sister, my husband, and,

to the person who made it all possible, my dad:

Ajey Gupta

February 14, 1966 - April 25, 2021

ACKNOWLEDGMENTS

This work, everything that precedes it, and everything that will follow, is made possible by the support of my mom, Vandana, and my sister, Niveditaa. You have always had unwavering belief in me, from the day I left home to move to the US in 2014, till the day I defended this work in 2024. We did not know of the challenges that would come our way; I know, now, that together we can get through anything. Your strength has kept me going, and I am so proud to be related to you.

I would also like to thank my husband, Andrew, who has been a constant source of love and comfort since we embarked on this journey together. You have always been supportive of my goals and encouraged me to pursue the challenges that it entailed. Your support has pulled me out of the days when I did not believe in myself, and it has propelled me to see this work through. Despite the distance, you have been by my side every step of the way, and I am so lucky to have you in my life.

I would like to thank my advisor, Prof. Kathleen Howell, whose guidance and support have made this work possible. I am eternally grateful for all your feedback, suggestions, and edits through the years: you have made me a better student and a better researcher. You have always taken the time to provide mentorship and advice when I needed it, and for that I am grateful. Thank you for all the opportunities you gave me.

I would like to thank Prof. Carolin Frueh who, in addition to being on my committee, has gone out of the way to provide research help and advice that aided this work. You have always entertained my questions, no matter how small, and I am extremely thankful for your support. I am grateful to Dr. Thomas Pavlak for taking the time to be on my committee, and for reviewing this document. You have been extremely encouraging and supportive these past few years and I have learned so much from all your suggestions and insights. Thank you for agreeing to be on my committee! Finally, I would like to thank Prof. David Arnas for your feedback and questions. You encouraged me to challenge myself, and I appreciate the time you took to review this document.

In addition to my committee members, I would like to thank Professors Arthur Frazho, Martin Corless, James Longuski, Kenshiro Oguri, and Keith LeGrand for the knowledge and guidance shared through their courses at Purdue. It was an honor to learn from all of you.

My time at Purdue, especially in the years leading up to this work, was enriched by several people. I am indebted to Kenza Boudad, Nick LaFarge, Stephen Scheuerle, RJ Power, and Brian McCarthy for being great friends both at Purdue and beyond. I would also like to thank JP Almanza-Soto, Noah Sadaka, Jack Iannamorelli, Aneesh Khilnani, and Lacey Davis: I have had a great time navigating the final years of graduate school in your company. To all the current and previous members of the Multi-Body Dynamics Research Group, I am grateful for your friendship and camaraderie. I will miss doing trivia and playing pool at the Vault with you all! Finally, to all of my family in India and in the US, I am grateful for your support and encouragement these past few years.

I am thankful for financial support from the Air Force Office of Scientific Research as part of the Space University Research Initiative grant FA95502210092 through the University of Buffalo contract number R1304009. Financial support from the Purdue School of Aeronautics and Astronautics and the Purdue University Honors Engineering Program is appreciated as well. Thank you to Zonta International for financial support via the Amelia Earhart Fellowship.

Finally, to my dad, who dreamed this dream with me: thank you for believing in me, Papa. We did it.

TABLE OF CONTENTS

LIST OF TABLES

LIST OF FIGURES

ABSTRACT

The recent and upcoming increase in spaceflight missions to the lunar vicinity necessitates methodologies to enable operations beyond the Earth. In particular, there is a pressing need for a Space Domain Awareness (SDA) and Space Situational Awareness (SSA) architecture that encompasses the realm of space beyond the sub-geosynchronous region to sustain humanity's long-term presence in that region. Naturally, the large distances in the cislunar domain restrict access rapid and economical access from the Earth. In addition, due to the long ranges and inconsistent visibility, the volume contained within the orbit of the Moon is inadequately observed from Earth-based instruments. As such, space-based assets to supplement ground-based infrastructure are required. The need for space-based assets to support a sustained presence is further complicated by the challenging dynamics that manifest in cislunar space. Multi-body dynamical models are necessary to sufficiently model and predict the motion of any objects that operate in the space between the Earth and the Moon. The current work seeks to address these challenges in dynamical modeling and cislunar accessibility via the exploration of resonant orbits. These types of orbits, that are commensurate with the lunar sidereal period, are constructed in the Earth-Moon Circular Restricted Three-Body Problem (CR3BP) and validated in the Higher-Fidelity Ephemeris Model (HFEM). The expansive geometries and energy options supplied by the orbits are favorable for achieving recurring access between the Earth and the lunar vicinity. Sample orbits in prograde resonance are explored to accommodate circumlunar access from underlying cislunar orbit structures via Poincaré mapping techniques. Orbits in retrograde resonance, due to their operational stability, are employed in the design of space-based observer constellations that naturally maintain their relative configuration over successive revolutions. Sidereal resonant orbits that are additionally commensurate with the lunar synodic period are identified. Such orbits, along with possessing geometries inherent to sidereal resonant behavior, exhibit periodic alignments with respect to the Sun in the Earth-Moon rotating frame. This characteristic renders the orbits suitable for hosting space-based sensors that, in addition to naturally avoiding eclipses, maintain visual custody of targets in the cislunar domain. For orbits that are not eclipse-favorable, a penumbra-avoidance path constraint is implemented

to compute baseline trajectories that avoid Earth and Moon eclipse events. Constellations of observers in both sidereal and sidereal-synodic resonant orbits are designed for cislunar SSA applications. Sample trajectories are assessed for the visibility of various targets in the cislunar volume, and connectivity relative to zones of interest in Earth-Moon plane. The sample constellations and observer trajectories demonstrate the utility of resonant orbits for various applications to sustain operations in cislunar space.

1. INTRODUCTION

Over the past few decades, humanity has maintained a constant and sizable presence in the near-Earth orbital realm. Naturally, in pushing the technological and scientific boundaries, cislunar space is poised to become the next step for a sustained human presence in space. National Aeronautics and Space Administration (NASA), as well as space agencies across the globe, are eyeing a return specifically to the lunar vicinity. Recently completed missions include NASA's Artemis I mission that transited out to the vicinity of the Moon, into a Distant Retrograde Orbit (DRO), and back to the Earth, successfully testing the Orion spacecraft and the Space Launch System (SLS) rocket [1]. The Indian Space Research Organization (ISRO) successfully landed the Chandrayaan-3 mission on the lunar south pole, demonstrating roving capabilities as well as conducting in-situ experiments to further understand the composition of the Moon [2]. In January 2024, the JAXA Smart Lander for Investigating Moon (SLIM) demonstrated successful lunar landing as well, making Japan the fifth country to soft-land on the Moon [3]. Looking ahead, beginning September 2025, additional missions within NASA's Artemis program are expected to demonstrate crewed lunar flybys and lunar landings. In addition to lunar landers, missions are currently in development for operation in libration point orbits near the Moon. NASA's Lunar Gateway will operate in an L_2 Near Rectilinear Halo Orbit (NRHO) to enable access to the lunar surface, Mars, and beyond [4]. The Oracle spacecraft program, previously termed the Cislunar Highway Patrol System (CHPS), is currently in development by the Air Force Research Laboratory (AFRL) in collaboration with Advanced Space for launch in 2027 [5]. The aim of this program is to obtain and maintain custody of cislunar objects, along with assessing the capabilities of current navigation techniques and processing algorithms in this domain.

In addition to governmental endeavors, propelled by NASA's Commercial Lunar Payload Services (CLPS) program, several commercially-backed missions to the lunar surface are planned for launch within the next decade. The overarching goal of the program is to "advance capabilities for science, exploration or commercial development of the Moon" [6]. To that end, Astrobotic Technology was contracted to land its Peregrine lander, and to deliver the VIPER rover aboard its Griffin lunar lander in 2023 and 2024 respectively. While

the Peregrine Mission One suffered a propulsion anomaly that inhibited lunar landing, the Griffin lander is on track for the planned late-2024 launch [7]. Other contractors include Intuitive Machines, that recently became the first commercial-sector company to demonstrate soft-landing on the lunar surface with their Nova-C class lunar lander, Odysseus. Also a part of CLPS are Firefly Aerospace's Blue Ghost Missions 1 and 2, targeting landings in the northern lunar hemisphere and the lunar far-side, respectively [6].

This anticipated increase in the number of commercial and governmental assets beyond GEO necessitates regulation and constant monitoring of objects in space, similar to the Space Domain Awareness (SDA) and Space Situational Awareness (SSA) architectures currently in place in the sub-GEO regime. The United States Space Force (USSF) defines SDA as the "timely, relevant, and actionable understanding of the operational environment that allows military forces to plan, integrate, execute, and assess space operations" [8]. SSA is a subset of SDA and is defined as the foundational, current, and predictive knowledge and characterization of space objects and space domain [8]. The sources of knowledge in the space domain may be combinations of radar and/or optical sensors that are tasked with detecting, tracking, and identifying objects in space. To operate such sensors, two classes of trajectories that allow access in space are identified as being necessary [9]:

- **Lines of Communication (LOCs)**: trajectories along which assets traverse space, or that connect them with bases of operations. In the context of cislunar space, LOCs include spacecraft recovery trajectories, or transfer pathways from the geocentric regime to the cislunar realm.

- **Key Orbital Trajectories (KOTs)**: orbits from which a spacecraft can support users, collect information, or interface with other spacecraft. These may be inertial, i.e., defined relative to a celestial body, or orbital, i.e., defined relative to other trajectories.

However, a major challenge inherent to designing and operating spacecraft in these trajectories in cislunar space is the non-negligible gravitational influence of the Moon and the Sun as compared to the Earth. The resulting complex dynamical environment is not sufficiently modeled by Earth (or Moon) Keplerian dynamics. As such, a three-body dynamical model that better reflects the complex behavior of trajectories in cislunar space is necessary.

With the advent of technological improvements and computational capabilities, novel techniques in trajectory design are available to support human spaceflight goals. Within multi-body dynamical models, a class of trajectories that are recently being adopted for spaceflight include resonant orbits. Conceptually, resonant orbits and their invariant manifolds are familiar in the design of significantly low-cost and unusual trajectories in several planet-moon systems [10]. The inherent stability of some resonant orbits is understood for long-term mission design, while the intrinsically unstable trajectories are leveraged for application towards transfer trajectory design for low propellant usage. For applications in cislunar space, resonant orbits naturally remain phased with the lunar orbit while also traversing across various different areas within cislunar space. In addition, such orbits are also part of the network of trajectories that link the lunar vicinity with the near-Earth region. The availability of natural dynamical structures in the vicinity of these orbits broadens the solution space of trajectories and also yields local coverage. Tools from dynamical systems theory are also available to characterize the flow associated with the orbits to build an understanding of the complex cislunar dynamical regime.

1.1 Previous Contributions

1.1.1 Multi-Body Dynamics

The publication of *Astronomia Nova* by Johannes Kepler in 1609, in which he derived the three laws of planetary motion using empirical methods, cemented his legacy in celestial mechanics [11]. Since the laws were purely empirical, they did not offer a physical rationale to support the resulting behavior. Only in 1687, when Isaac Newton derived the inverse square force law, Kepler's laws were confirmed to be a consequence of the natural force of gravitation [12]. In his publication, Newton also formulated his three laws of motion, which have, coupled with the universal law of gravitation, shaped the current understanding of the mechanics of the universe. Unsuccessfully, Newton also attempted to solve the $\mathcal{N}$-body problem, later pursued by Leonhard Euler in 1772. Euler formulated the three-body problem, formulating the motion of three planetary bodies in a rotating coordinate frame [13]. Joseph-Louis Lagrange, in the same year, computed equilibrium solutions in the three-body

model, contributing additional insight into the problem. In 1836, Carl Gustav Jacob Jacobi demonstrated that combining the conservation of energy and angular momentum renders an integral of motion, termed the Jacobi integral [13]. In 1893, then, Henri Poincaré termed the three-body problem *restricted*, and offered a qualitative assessment of the problem. The work by Poincaré forms the basis of chaos theory and the theory of dynamical systems. In 1881, Poincaré introduced Poincaré mapping as a tool for the visualization of complex dynamical behaviour [13]. Due to the lack of technological capabilities until the 20^{th} century, the methods presented by Poincaré are only recently being adopted for solar system applications.

1.1.2 Resonant Orbits

The phenomenon of orbital resonance is well observed in the solar system and has long been used to explain trends in seemingly chaotic behavior [14], [15]. Specifically, the orbits of comets in resonance with Jupiter are validated via resonance and associated transitions [16], [17]. In 1997, Belbruno and Marsden discussed the motion of short-period comets under the effect of resonance, illustrating the temporary capture of the 3:2 and 2:3 resonant comets around Jupiter [18]. In 2000, Koon, et al. theoretically demonstrated the role of invariant manifolds in the low energy, planar resonant transfers and capture mechanisms for the Jupiter family of comets [19]. In 2001, Howell, Marchand, and Lo numerically confirmed those results and extended the analysis to spatial transfers [20]. In 2010, Vaquero employed Poincaré sections and dynamical systems techniques in understanding the relationships between the invariant manifolds of the $3:4$ and $5:6$ unstable resonant orbits in the Jupiter-Europa system [21]. Vaquero, in 2013, also demonstrated the role of resonant orbits in the design of planar and spatial transfer scenarios, along with cataloging resonant orbits in the Saturn-Titan system [22]. In 2018, Vutukuri employed resonances as transfer tools in the design of trajectories between non-resonant, stable periodic orbits [23]. Canales et al., in 2022, explore resonant orbits in the Mars-Deimos system as options for science orbits for the exploration of both the martian moons [24].

1.1.3 Cislunar Space Situational Awareness

The problem of cislunar Space Situational Awareness (SSA), and specifically, the design of trajectories in its support, is relatively new. Addressing the challenges associated with complex cislunar dynamics and the need for sensors that can traverse the expanse of cislunar space, several authors have investigated the applicability of libration point orbits for obtaining observations near the lunar vicinity. Vendl and Holzinger demonstrated the effectiveness of retrograde orbits in synodic resonance for cislunar object tracking [25]. Frueh et al. discuss the visibility of space objects in various CR3BP periodic orbits as observed from ground-based optical sensors [26]. Cislunar orbit determination leveraging space-based optical sensors is demonstrated by Thompson et al. for various observer-target orbit combinations [27]. In 2022, Dahlke et al. demonstrate the surveillance of targets in L_2 and L_3 Lyapunov orbits via sensors placed in various "touring orbits" in the CR3BP [28]. Leveraging the Bicircular Restricted Four-Body Problem (BCR4BP), Bhadauria et al. parameterize visibility conditions as a function of time to determine the general visibility conditions [29]. Fowler and Paley apply numerical observability techniques to compute sets of observer-target pairings for cislunar SSA [30]. More recently, LeGrand et al. and Iannamorelli et al. demonstrate cislunar tracking considering target visibility in various L_2 halo orbits and maneuvering trajectories, respectively [31], [32].

1.2 Scope of the Present Work

Building upon existing literature and recognizing the current needs, the primary goal of the present work is the exploration of resonant orbits to sustain cislunar operations. The challenging dynamics inherent to the cislunar regime are addressed by leveraging dynamical models that more realistically model the motion of bodies in this space. As such, the Circular Restricted Three-Body Problem (CR3BP) and the Higher-Fidelity Ephemeris Model (HFEM) are employed in the construction and validation of trajectories that aid in the long-term sustenance of cislunar operations. Specifically, this investigation seeks to meet the following research objectives:

1. **Construct and catalog Earth-Moon resonant orbits**

   Orbits with periods commensurate with the lunar sidereal period are constructed in the Earth-Moon CR3BP. Families of planar and spatial resonant orbits corresponding to various resonance ratios are introduced. From these families, options for orbits that provide periodically repeating geometries relative to the Earth, Moon, and the Sun are identified.

2. **Demonstrate the utility of resonant orbits for access within cislunar space**

   Resonant orbits are explored as options for recurring access between the Earth and the Moon. The applicability of proposed trajectories is demonstrated in both the CR3BP and the HFEM models. Poincaré mapping techniques from dynamical systems theory are employed to construct orbit chains that allow dictated excursions from the bounding periodic orbit geometry. The impact of eclipse events on the trajectories is assessed, and methods to construct eclipse-feasible baseline trajectories are implemented.

3. **Design and assess trajectories for cislunar surveillance applications via metrics for visibility and connectivity**

   The utility of sidereal resonant orbits is demonstrated for applications towards connectivity and coverage in cislunar space. Orbits exhibiting sidereal-synodic overlap demonstrate flexibility with regards to illumination and visibility conditions. Orbits for single observers as well as constellations of multiple space-based observers are designed and assessed in the CR3BP and HFEM.

The methodologies and analyses discussed in the current work facilitate in building an understanding of the complex dynamics that manifest within the volume of cislunar space. The work presented in this document is organized into the following chapters:

Chapter 2: Dynamical Models

In this chapter, the general $\mathcal{N}$-body model is introduced, followed by simplifications that reduce the model to the cases of two and three bodies. The Circular Restricted Three-Body Problem (CR3BP) is then introduced as the primary dynamical model for the current work. The relevant assumptions, equations of

motion, and the mathematical framework for the model are detailed. Equilibrium solutions and zero velocity curves in the CR3BP are then presented within the context of the Earth-Moon system. The Higher-Fidelity Ephemeris Model (HFEM) is introduced for validating trajectories constructed in the CR3BP in a higher-fidelity dynamical environment. Finally, coordinate transformations between the inertial and rotating CR3BP frames are derived.

Chapter 3: Trajectory Construction via Numerical Methods

This chapter introduces various approaches and techniques that are generally employed in the numerical construction of periodic orbits in the CR3BP. The state transition matrix is introduced, and the information offered by the matrix is utilized in the development of differential corrections schemes. The general formulation for single and multiple shooting algorithms is detailed and employed in the construction of periodic orbits in the CR3BP. Methodologies for generating families of periodic orbits are then discussed. The concept of stability of periodic orbits is detailed, followed by the different types of bifurcations in the CR3BP. Finally, invariant manifolds for periodic orbits are detailed, and Poincaré maps are introduced to aid the visualization of the complex dynamical motion associated with the orbits.

Chapter 4: Resonant Orbits

This chapter introduces the concept of resonance, with emphasis on orbital resonance. Resonant orbits in the two-body model are derived and visualized in both the inertial and the rotating frames. The concepts of interior and exterior resonances, as well as sidereal and synodic periods, are discussed. The methodology of translating the initial conditions corresponding to two-body resonant orbits into resonant orbits in the CR3BP is discussed. Families of sidereal resonant orbits corresponding to various resonance ratios and their associated geometries are presented. Spatial resonant orbit families emanating from planar resonant orbits in the Earth-Moon system are generated as well. Finally, sidereal resonant orbits

pertaining to different resonance ratios that are additionally commensurate with the lunar synodic period are identified.

Chapter 5: Computation of Resonant Trajectories for Repeating Earth-Moon Access

This chapter introduces methodologies for the construction of trajectories that yield repeating access between the neighborhoods of the Earth and the Moon. Families of retrograde and prograde $2:1$ sidereal resonant orbits are explored for applications towards cislunar connectivity, but the methodologies are expandable to other orbits as well. Access between the geosynchronous region and the Moon is demonstrated via these orbits in both the CR3BP and HFEM. Orbits from the prograde family are analyzed via Poincaré maps to expand access to the lunar far-side. Orbits from the retrograde family are employed in the construction of space-based sensor constellations to aid surveillance of the cislunar volume. Finally, techniques to detect and mitigate eclipse events are detailed to assess and improve the operational feasibility of the proposed trajectories.

Chapter 6: Constellations for Visibility and Connectivity in Cislunar Space

Metrics for assessing the utility of cislunar trajectories for visibility and connectivity in this regime are introduced. Visibility criteria that are introduced include line-of-sight availability, observed visual magnitude, and orientation relative to solar, Earth, and lunar exclusion zones. Fixed target locations near the Moon, as well as targets dispersed across the cislunar volume, are introduced and evaluated as viewed from candidate observer orbits. Additionally, leveraging known periodic solutions in the Earth-Moon CR3BP, targets operating in cislunar orbits are evaluated. Constellations that comprise of observers operating in sidereal and synodic resonant orbits are constructed and evaluated for cislunar applications in the Earth-Moon CR3BP and the Earth-Moon-Sun-Jupiter HFEM.

Chapter 7: Concluding Remarks

This chapter offers some concluding remarks based on the current work. The

efficacy of resonant orbits for cislunar trajectory design is summarized, along with their utility for SSA applications. Finally, recommendations for future work in the investigation of resonant orbits and cislunar SSA are suggested.

2. DYNAMICAL MODELS

The general scenario for an $\mathcal{N}$-body problem is introduced, serving as the basis for the derivation of subsequent dynamical models. The dynamical models that are relevant to this investigation begin with the two-body dynamical model. Next, increasing the order of fidelity, is the Circular Restricted Three-Body Problem (CR3BP) that incorporates the gravitational influence of two bodies on a spacecraft, capturing the dynamical behavior that is not adequately represented by standard Keplerian motion. Finally, the Higher-Fidelity Ephemeris Model (HFEM) increases the fidelity of dynamical modeling by incorporating the gravity of additional celestial bodies and their true ephemerides at any given epoch.

2.1 The $\mathcal{N}$-Body Problem

The $\mathcal{N}$-body problem is the most general model employed in celestial mechanics to illustrate the interaction of bodies under their mutual gravitational attraction. Due to their generally spherical shapes and the large relative distances, the bodies are modeled as point-mass particles. Each body, denoted P_i, is assumed to be under the gravitational influence of the remaining $\mathcal{N}-1$ bodies that together comprise the $\mathcal{N}$-body system. Let the non-negligible mass of each body be represented as M_i. An inertial frame is defined by the dextral orthonormal triad $\{\hat{\boldsymbol{X}}, \hat{\boldsymbol{Y}}, \hat{\boldsymbol{Z}}\}$ and centered on an inertially-fixed point, denoted $\mathcal{O}$, that locates each celestial body in space. Figure 2.1 illustrates the inertial frame, where the quantity $\boldsymbol{R}_i$ represents the 3-dimensional position vector from point $\mathcal{O}$ to the respective body P_i. Applying Newton's second law and incorporating the universal gravity as the force model, the vector equation describing the motion of body P_i under the gravitational influence of the other bodies in the system is,

$$M_i \boldsymbol{R}_i'' = -\tilde{G} \sum_{\substack{j=1 \\ j \neq i}}^{\mathcal{N}} \frac{M_i M_j}{R_{ji}^3} \boldsymbol{R}_{ji} \tag{2.1}$$

where the relative position vector for P_i with respect to P_j is $\boldsymbol{R}_{ji} = \boldsymbol{R}_i - \boldsymbol{R}_j$, and $\tilde{G} \approx 6.674 \times 10^{-20}$ km^3 kg^{-1} s^{-2} is the universal gravitational constant. Note that bold characters

denote vector quantities, and primes indicate the derivative with respect to dimensional time, represented as T. The $\mathcal{N}$-body problem is reformulated to produce a representation of the motion for each P_i relative to a body, e.g., a central body P_q, under the gravitational influence of the $\mathcal{N}-1$ bodies in the system. The resulting vector equation of motion is,

$$\boldsymbol{R}_{qi}'' + \underbrace{\tilde{G}\frac{(M_i + M_q)}{R_{qi}^3}\boldsymbol{R}_{qi}}_{\text{dominant}} = \tilde{G}\sum_{\substack{j=1 \\ j\neq i,q}}^{\mathcal{N}} M_j\left(\underbrace{\frac{\boldsymbol{R}_{ij}}{R_{ij}^3}}_{\text{direct}} - \underbrace{\frac{\boldsymbol{R}_{qj}}{R_{qj}^3}}_{\text{indirect}}\right) \tag{2.2}$$

The second term on the left side of Equation (2.2), denoted the 'dominant' term, reflects the gravitational acceleration of P_i due solely to the central body P_q. While it is termed *dominant* as a consequence of the formulation of the relative equations of motion, the term is, by no means, always the term with the largest magnitude or gravitational impact on the motion of P_i. The term denoted 'direct' on the right side of Equation (2.2) encompasses the gravitational influence of the other $\mathcal{N}-2$ bodies on P_i, from which the gravitational forces of those bodies on P_q are subtracted via the term denoted 'indirect'. Together, the direct and indirect terms signify the perturbing accelerations on P_i due to the bodies that comprise the $\mathcal{N}$-body system.

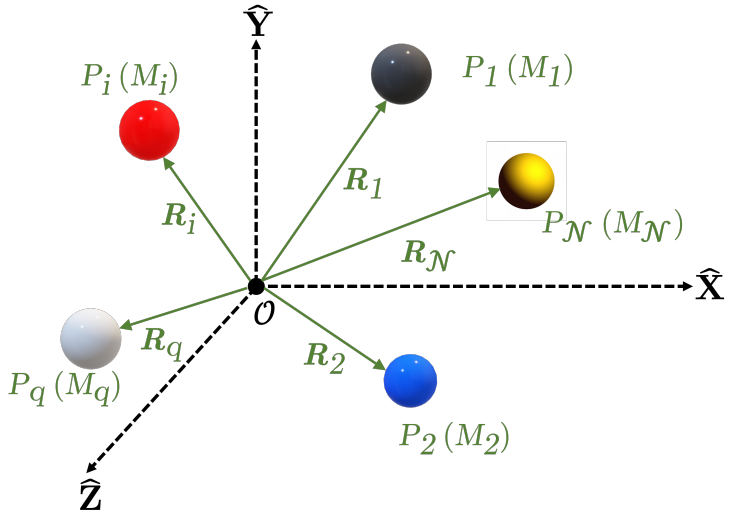

Figure 2.1. Inertial frame representation of the $\mathcal{N}$-body system.

For each particle in the $\mathcal{N}$-body system, the vector second-order differential equation in Equation (2.1) is easily rewritten as six scalar first-order differential equations. In total, then, there are $6\mathcal{N}$ coupled scalar nonlinear differential equations that govern the translational dynamics of the system. Thus, an analytical solution requires $6\mathcal{N}$ integrals of motion. Only ten scalar constants are currently known: six that arise from conservation of linear momentum, three from conservation of angular momentum, and one from the conservation of energy. As such, the general $\mathcal{N}$-body problem does not possess a closed-form analytical solution. Nonetheless, leveraging the reformulation of Equation (2.1) into Equation (2.2), some specific cases of spacecraft motion arise that lay the groundwork for trajectory design.

2.2 The Two-Body Problem

The reformulation of the general $\mathcal{N}$-body equations of motion in Equation (2.1) into the relative motion case in Equation (2.2) leads to the convenient modeling of spacecraft dynamics under the well-studied Keplerian motion. By setting the value of $\mathcal{N} = 2$ in Equation (2.2), all the perturbing accelerations (direct and indirect terms) are zero, reducing the problem to a single second-order vector differential equation, that is,

$$\boldsymbol{R}''_{qi} + \tilde{G}\frac{(M_i + M_q)}{R_{qi}^3}\boldsymbol{R}_{qi} = \boldsymbol{0} \tag{2.3}$$

Furthermore, for modeling the motion of a spacecraft relative to a celestial body (e.g., the Earth), it is rightfully assumed that the mass of the spacecraft, M_i, is infinitesimal relative to the mass of the celestial central body, M_q. As such, for this two-body case, the standard gravitational parameter, $\tilde{\mu}$, is approximated as $\tilde{\mu} = \tilde{G}(M_i + M_q) \approx \tilde{G}M_q$. The resulting equation of relative motion for the two-body case is then,

$$\boldsymbol{R}''_{qi} + \frac{\tilde{\mu}}{R_{qi}^3}\boldsymbol{R}_{qi} = \boldsymbol{0} \tag{2.4}$$

The relative formulation of the vector equation of motion conveniently reduces the problem to six first-order scalar differential equations that require six integrals of the motion for a solution. As such, there exists a closed-form analytical solution that governs the relative

motion of two bodies, a result that has led to decades of applications in trajectory design. For systems of more than two bodies ($\mathcal{N} > 2$), however, the relative equation does not possess a closed-form analytical solution. This fundamental limitation is a significant aspect behind the current research focus in multi-body dynamics.

2.3 The Circular Restricted Three-Body Problem

To increase the fidelity of the dynamical modeling, the natural next step is the examination of a scenario where $\mathcal{N} = 3$. Such a dynamical system is employed to model the motion of a spacecraft under the gravitational influence of a planet-moon or a Sun-planet pair. However, the increase in the fidelity of dynamical modeling is accompanied by an increase in the complexity of the problem. The general three-body problem is formulated by considering the motion of three bodies, P_i, of mass M_i for $i = 1, 2, 3$. Equation (2.1) is then rewritten for only three bodies as,

$$M_3 \boldsymbol{R}_3'' = -\tilde{G}\frac{M_3 M_1}{R_{13}^3}\boldsymbol{R}_{13} - \tilde{G}\frac{M_3 M_2}{R_{23}^3}\boldsymbol{R}_{23} \tag{2.5}$$

The solution for Equation (2.5) requires knowledge of the relative position vectors $\boldsymbol{R}_{13}$ and $\boldsymbol{R}_{23}$. These position vectors are not available since P_1 and P_2 are influenced by the motion of P_3 and its instantaneous position. Solving for all three position vectors simultaneously requires 18 integrals of motion; only 10 constants of the motion are available. However, recall from the two-body problem that reformulation of the differential equation into relative motion affords additional insight and yields an analytical solution. Repeating the process for the case of three bodies, the relative motion of P_3 with respect to both P_1 and P_2 is given as,

$$\boldsymbol{R}_{13}'' + \tilde{G}\frac{M_1 + M_3}{R_{13}^3}\boldsymbol{R}_{13} = \tilde{G}M_2\left(\frac{\boldsymbol{R}_{32}}{R_{32}^3} - \frac{\boldsymbol{R}_{12}}{R_{12}^3}\right) \tag{2.6}$$

$$\boldsymbol{R}_{23}'' + \tilde{G}\frac{M_2 + M_3}{R_{23}^3}\boldsymbol{R}_{23} = \tilde{G}M_1\left(\frac{\boldsymbol{R}_{31}}{R_{31}^3} - \frac{\boldsymbol{R}_{21}}{R_{21}^3}\right) \tag{2.7}$$

This formulation results in two second-order vector differential equations, that, together, serve as the dynamical model for the time history governing $\boldsymbol{R}_{13}$ and $\boldsymbol{R}_{23}$. However, the analytical solution is unavailable since this formulation still requires 12 integrals of the motion. Although the problem does not possess a closed-form analytical solution, insight is gained by introducing some simplifying assumptions to render the problem more tractable. The following simplifications and assumptions originate with a general three-body problem and yield a formulation of the three-body model that is termed the Circular Restricted Three-Body Problem (CR3BP).

2.3.1 Simplifying Assumptions

The CR3BP is a stepping stone in orbital mechanics that builds upon insights from the two-body model while incorporating some of the complexities of the $\mathcal{N}$-body model. The three bodies that comprise the system are P_1 and P_2, labeled the primaries, and the third body, denoted P_3, that may represent a spacecraft or a smaller celestial body. Assuming that the motion of P_3 under the gravitational influence of the other two bodies is of interest, the following assumptions are introduced into the general three-body problem:

- The mass of P_3 is infinitesimal relative to the masses of P_1 and P_2, such that $M_3 << M_2 \leq M_1$. This relationship is a reasonable assumption when modeling the motion of a spacecraft under the influence of a set of larger primaries, for instance, a planet and a moon. This assumption implies that P_3 does not influence the motion of the two primaries. Additionally, as remains true, the internal mass distributions of all bodies are such that they are modeled as point masses.

- Being independent of P_3, the motion of the primaries is modeled as an isolated two-body system. The solution of the system is known to be a conic. In the systems of interest, the behavior of the primary system is a closed planar conic orbit.

- The primaries P_1 and P_2 move on circular orbits about their mutual barycenter. The mutual plane of motion of the two primaries is fixed. However, P_3 is free to move in any spatial dimension.

The simplified model resulting from these assumptions is illustrated in Figure 2.2. The model is formulated in a reference frame that rotates with the motion of the primaries and is centered on their mutual barycenter, denoted $\mathcal{B}$. This rotating frame is denoted $\mathcal{R}$ and is represented by the dextral orthonormal triad $\{\hat{\boldsymbol{x}}, \hat{\boldsymbol{y}}, \hat{\boldsymbol{z}}\}$, where the two primaries lie along the $\hat{\boldsymbol{x}}$-axis. This rotating frame is oriented relative to an arbitrary inertial frame, denoted $\mathcal{I}$ and represented by $\{\hat{\boldsymbol{X}}, \hat{\boldsymbol{Y}}, \hat{\boldsymbol{Z}}\}$ such that the angle θ is measured in the plane of motion of the primaries, as indicated in Figure 2.2. The rate of change of θ, i.e., θ', represents the angular velocity of the primary system, that is constant for the circular orbits of the primaries. This rate is also equal to the mean motion for the orbits of the primaries.

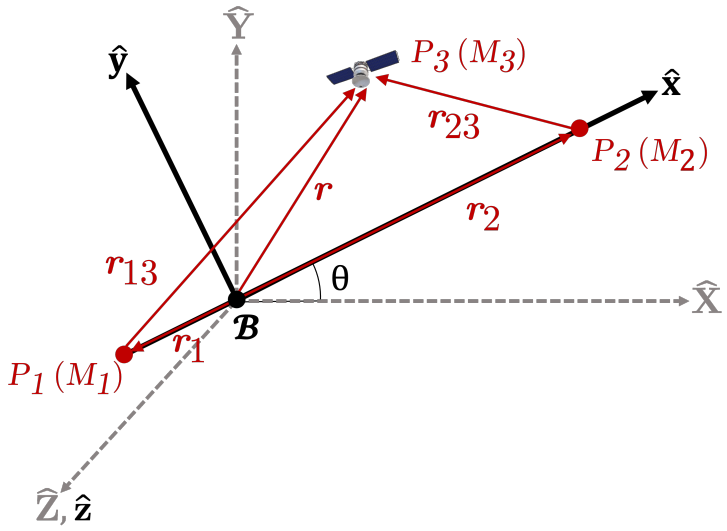

Figure 2.2. Representation of the rotating, $\{\hat{\boldsymbol{x}}, \hat{\boldsymbol{y}}, \hat{\boldsymbol{z}}\}$, and inertial frames $\{\hat{\boldsymbol{X}}, \hat{\boldsymbol{Y}}, \hat{\boldsymbol{Z}}\}$ in the CR3BP model.

2.3.2 Derivation of the Equations of Motion

To construct a generalized formulation that is agnostic to the bodies in the system, and to minimize truncation and round-off errors resulting from numerical integration, it is convenient to nondimensionalize the equations of motion associated with the CR3BP. To nondimensionalize, the following characteristic quantities are first identified: l^*, m^*, t^*, that are termed the characteristic length, characteristic mass, and characteristic time,

respectively. The characteristic length is simply the mean distance between the two primaries and is given as,

$$l^* = R_1 + R_2 \tag{2.8}$$

which is equal to the dimensional value of the distance between the primaries. Similarly, the characteristic mass is the sum of the masses of the primaries, i.e.,

$$m^* = M_1 + M_2 \tag{2.9}$$

Finally, the characteristic time is selected such that the nondimensional mean motion of the system is equal to unity. The dimensional mean motion of the system is,

$$\mathbb{N} = \sqrt{\frac{\tilde{G}m^*}{l^{*3}}} \tag{2.10}$$

where $\tilde{G}$ represents the dimensional value of the universal gravitational constant. By defining the characteristic time quantity as,

$$t^* = \sqrt{\frac{l^{*3}}{\tilde{G}m^*}} \tag{2.11}$$

the nondimensional mean motion is evaluated as,

$$\underline{n} = \mathbb{N} \cdot t^* = \sqrt{\frac{\tilde{G}m^*}{l^{*3}}} \cdot \sqrt{\frac{l^{*3}}{\tilde{G}m^*}} = 1 \tag{2.12}$$

In general, the dimensional values associated position, velocity, and time may be nondimensionalized such that,

$$\boldsymbol{r}_i = \frac{\boldsymbol{R}_i}{l^*} \tag{2.13}$$

$$\boldsymbol{v}_i = \frac{\boldsymbol{V}_i \cdot t^*}{l^*} \tag{2.14}$$

$$t = \frac{T}{t^*} \tag{2.15}$$

It is also useful to introduce the CR3BP mass parameter, denoted μ, that is defined as a function of the masses of the primaries,

$$\mu = \frac{M_2}{M_1 + M_2} = \frac{M_2}{m^*} \tag{2.16}$$

For the Earth-Moon CR3BP system in this investigation, the value of this parameter is equal to $\mu = 0.0121505842699404$. Together with the characteristic quantities, the mass ratio provides insight into the physical scale of the CR3BP system. Given the definition of the mass ratio, the nondimensional masses of the primaries, denoted $\breve{m}_i$, are expressed as,

$$\breve{m}_1 = \frac{M_1}{m^*} = 1 - \mu \tag{2.17}$$

$$\breve{m}_2 = \frac{M_2}{m^*} = \mu \tag{2.18}$$

Using the standard definition for locating the center of mass of a system, it is straightforward to locate the system barycenter, $\mathcal{B}$, as well as the primaries, along the $\hat{\boldsymbol{x}}$-axis in the CR3BP rotating frame. In general,

$$\boldsymbol{R}_{\mathcal{B}} = \frac{\sum_{i=1}^{i=\mathcal{N}} M_i \boldsymbol{R}_i}{\sum_{i=1}^{i=\mathcal{N}} M_i} \tag{2.19}$$

For the CR3BP primary system, the location of the center of mass as viewed from P_1 is,

$$R_{\mathcal{B}} = \frac{M_1 \cdot R_1 + M_2 \cdot R_2}{M_1 + M_2} \tag{2.20}$$

$$\Rightarrow R_1 = \frac{M_1 \cdot 0 + M_2 \cdot l^*}{m^*} \tag{2.21}$$

$$\Rightarrow r_1 l^* = \frac{\mu \cdot m^* \cdot l^*}{m^*} \tag{2.22}$$

$$\Rightarrow r_1 = \mu \tag{2.23}$$

Since the nondimensional distance between the primaries is equal to unity, the location of P_2 from the barycenter is, thus, equal to $r_2 = 1 - \mu$. Since the primaries lie along the $\hat{\boldsymbol{x}}$-axis,

the nondimensional position vectors for the two primaries, expressed in the rotating frame, are defined,

$$\boldsymbol{r}_{P_1} = [-\mu, \quad 0, \quad 0]^T \tag{2.24}$$

$$\boldsymbol{r}_{P_2} = [1-\mu, \quad 0, \quad 0]^T \tag{2.25}$$

Let the nondimensional position vector, $\boldsymbol{r}$, locate the spacecraft, denoted P_3 in Figure 2.2, where the subscript is removed for brevity. In the rotating frame, this vector is defined as,

$$\boldsymbol{r} = x\hat{\boldsymbol{x}} + y\hat{\boldsymbol{y}} + z\hat{\boldsymbol{z}} \tag{2.26}$$

Relative to the primaries, the position of the spacecraft is then expressed in rotating coordinates as,

$$\boldsymbol{r}_{13} = (x+\mu)\hat{\boldsymbol{x}} + y\hat{\boldsymbol{y}} + z\hat{\boldsymbol{z}} \tag{2.27}$$

$$\boldsymbol{r}_{23} = (x-1+\mu)\hat{\boldsymbol{x}} + y\hat{\boldsymbol{y}} + z\hat{\boldsymbol{z}} \tag{2.28}$$

Recall that Equation (2.5) yields a dimensional expression for the general motion of P_3 in terms of the masses of the primaries and the relative position vectors. Given the first assumption in the CR3BP, that is, $M_3 << M_1, M_2$, Equation (2.5) reduces to,

$$\boldsymbol{R}'' = -\tilde{G}\frac{M_1}{R_{13}^3}\boldsymbol{R}_{13} - \tilde{G}\frac{M_2}{R_{23}^3}\boldsymbol{R}_{23} \tag{2.29}$$

where, again, $\boldsymbol{R}$ represents the position vector of P_3 relative to the barycenter. To nondimensionalize this equation, use the characteristic quantities to yield,

$$^{\mathcal{I}}\frac{\mathrm{d}^2\boldsymbol{r}}{\mathrm{d}t^2}\left(\frac{l^*}{t^{*2}}\right) = -\tilde{G}\frac{(1-\mu)m^*}{r_{13}^3\cdot {l^*}^3}\boldsymbol{r}_{13}l^* - \tilde{G}\frac{\mu m^*}{r_{23}^3\cdot {l^*}^3}\boldsymbol{r}_{23}l^* \tag{2.30}$$

Canceling the l^* terms and substituting the value of t^{*2} from Equation (2.11),

$$ {}^{\mathcal{I}}\ddot{\boldsymbol{r}} = -\tilde{G}\frac{(1-\mu)m^*\boldsymbol{r}_{13}}{r_{13}^3 \cdot l^{*3}}\left(\frac{l^{*3}}{\tilde{G}m^*}\right) - \tilde{G}\frac{\mu m^*\boldsymbol{r}_{23}}{r_{23}^3 \cdot l^{*3}}\left(\frac{l^{*3}}{\tilde{G}m^*}\right) \tag{2.31} $$

$$ {}^{\mathcal{I}}\ddot{\boldsymbol{r}} = -\frac{1-\mu}{r_{13}}\boldsymbol{r}_{13} - \frac{\mu}{r_{23}}\boldsymbol{r}_{23} \tag{2.32} $$

where the dots indicate the derivative with respect to nondimensional time, t. It is noted that Equation (2.32) includes the derivatives of the position of P_3 with respect to an inertial observer; for a set of differential equations in the rotating frame, further transformations are required. The Basic Kinematic Equation (BKE) is leveraged to rewrite the derivatives in rotating coordinates. Recall that the angular velocity of the CR3BP rotating frame, $\mathcal{R}$, relative to an inertial frame, $\mathcal{I}$, is simply equal to the nondimensional mean motion of the system and is expressed as,

$$ {}^{\mathcal{I}}\boldsymbol{\omega}^{\mathcal{R}} = \underline{\underline{n}}\hat{\boldsymbol{z}} \tag{2.33} $$

Leveraging this quantity, the position vector of the spacecraft, expressed in rotating coordinates as given in Equation (2.26), is differentiated with respect to nondimensional time to produce,

$$ {}^{\mathcal{I}}\frac{\mathrm{d}\boldsymbol{r}}{\mathrm{d}t} = {}^{\mathcal{R}}\frac{\mathrm{d}\boldsymbol{r}}{\mathrm{d}t} + \left({}^{\mathcal{I}}\boldsymbol{\omega}^{\mathcal{R}} \times \boldsymbol{r}\right) \tag{2.34} $$

$$ {}^{\mathcal{I}}\dot{\boldsymbol{r}} = \dot{x}\hat{\boldsymbol{x}} + \dot{y}\hat{\boldsymbol{y}} + \dot{z}\hat{\boldsymbol{z}} + \left[\underline{\underline{n}}\hat{\boldsymbol{z}} \times (x\hat{\boldsymbol{x}} + y\hat{\boldsymbol{y}} + z\hat{\boldsymbol{z}})\right] \tag{2.35} $$

$$ {}^{\mathcal{I}}\dot{\boldsymbol{r}} = \left(\dot{x} - \underline{\underline{n}}y\right)\hat{\boldsymbol{x}} + \left(\dot{y} + \underline{\underline{n}}x\right)\hat{\boldsymbol{y}} + \dot{z}\hat{\boldsymbol{z}} \tag{2.36} $$

Similarly, the second derivative yields,

$$ {}^{\mathcal{I}}\frac{\mathrm{d}\dot{\boldsymbol{r}}}{\mathrm{d}t} = {}^{\mathcal{R}}\frac{\mathrm{d}\dot{\boldsymbol{r}}}{\mathrm{d}t} + \left({}^{\mathcal{I}}\boldsymbol{\omega}^{\mathcal{R}} \times \dot{\boldsymbol{r}}\right) \tag{2.37} $$

$$ {}^{\mathcal{I}}\ddot{\boldsymbol{r}} = \left(\ddot{x} - \underline{\underline{n}}\dot{y}\right)\hat{\boldsymbol{x}} + \left(\ddot{y} + \underline{\underline{n}}\dot{x}\right)\hat{\boldsymbol{y}} + \ddot{z}\hat{\boldsymbol{z}} + \left\{\underline{\underline{n}}\hat{\boldsymbol{z}} \times \left[\left(\dot{x} - \underline{\underline{n}}y\right)\hat{\boldsymbol{x}} + \left(\dot{y} + \underline{\underline{n}}x\right)\hat{\boldsymbol{y}} + \dot{z}\hat{\boldsymbol{z}}\right]\right\} \tag{2.38} $$

$$ {}^{\mathcal{I}}\ddot{\boldsymbol{r}} = \left(\ddot{x} - 2\underline{\underline{n}}\dot{y} - \underline{\underline{n}}^2 x\right)\hat{\boldsymbol{x}} + \left(\ddot{y} + 2\underline{\underline{n}}\dot{x} - \underline{\underline{n}}^2 y\right)\hat{\boldsymbol{y}} + \ddot{z}\hat{\boldsymbol{z}} \tag{2.39} $$

Combining the results of Equation (2.39) with the form produced previously in Equation (2.32) yields the nondimensional scalar equations of motion for the CR3BP as,

$$\ddot{x} - 2\dot{y} - x = -\frac{(1-\mu)(x+\mu)}{r_{13}^3} - \frac{\mu(x-1+\mu)}{r_{23}^3} \tag{2.40}$$

$$\ddot{y} + 2\dot{x} - y = -\frac{(1-\mu)y}{r_{13}^3} - \frac{\mu y}{r_{23}^3} \tag{2.41}$$

$$\ddot{z} = -\frac{(1-\mu)z}{r_{13}^3} - \frac{\mu z}{r_{23}^3} \tag{2.42}$$

where, recall from Equation (2.12) that the value of the nondimensional mean motion, $\underline{n}$, is equal to unity. Additionally, the values for $\boldsymbol{r}_{13}$ and $\boldsymbol{r}_{23}$ are obtained from Equations (2.27) and (2.28). Together, then, the three scalar second-order nondimensional differential equations in Equations (2.40) – (2.42) describe the motion of a spacecraft under the gravitational influence of the two primaries in the CR3BP dynamical model and expressed in rotating coordinates. Since time does not appear explicitly in these equations, the system is autonomous.

As the formulation in Equations (2.40) – (2.42) is developed in rotating coordinates, the integral of the differential equations yields one *pseudo-potential function*, denoted U^*, that is essentially an augmented potential function. The inertial potential function for the CR3BP is expressed as,

$$U = \frac{(1-\mu)}{r_{13}} + \frac{\mu}{r_{23}} \tag{2.43}$$

The pseudo-potential function for the CR3BP, then, simply augments Equation (2.43) as,

$$U^* = \frac{(1-\mu)}{r_{13}} + \frac{\mu}{r_{23}} + \frac{x^2+y^2}{2} \tag{2.44}$$

The differential equations of motion are also expressible as a function of the partial derivative in Equation (2.44). The resulting form of the equations of motion is,

$$\ddot{x} - 2\dot{y} = \frac{\partial U^*}{\partial x} \tag{2.45}$$

$$\ddot{y} + 2\dot{x} = \frac{\partial U^*}{\partial y} \tag{2.46}$$

$$\ddot{z} = \frac{\partial U^*}{\partial z} \tag{2.47}$$

Note that the equations of motion are coupled and nonlinear, and no general closed-form solution is available. Analysis of the properties of these differential equations yields useful particular solutions.

2.3.3 The Jacobi Constant

Since the potential function that yields the equations of motion for the CR3BP is autonomous, the system is conservative. As such, there exists an energy-like quantity that is constant for the problem formulation in the rotating frame. To compute this energy-like integral, consider the nondimensional velocity vector in rotating coordinates,

$$^{\mathcal{R}}\boldsymbol{v} = {}^{\mathcal{R}}\dot{\boldsymbol{r}} = \dot{x}\hat{\boldsymbol{x}} + \dot{y}\hat{\boldsymbol{y}} + \dot{z}\hat{\boldsymbol{z}} \tag{2.48}$$

Then, the dot product between the velocity vector in Equation (2.48) and the form of the acceleration of the particle in Equations (2.45) – (2.47) yields,

$$\dot{x}\ddot{x} - 2\dot{x}\dot{y} = \frac{\partial U^*}{\partial x}\dot{x} \tag{2.49}$$

$$\dot{y}\ddot{y} + 2\dot{y}\dot{x} = \frac{\partial U^*}{\partial y}\dot{y} \tag{2.50}$$

$$\dot{z}\ddot{z} = \frac{\partial U^*}{\partial z}\dot{z} \tag{2.51}$$

Adding the three scalar equations,

$$\dot{x}\ddot{x} + \dot{y}\ddot{y} + \dot{z}\ddot{z} = \frac{\partial U^*}{\partial x}\dot{x} + \frac{\partial U^*}{\partial y}\dot{y} + \frac{\partial U^*}{\partial z}\dot{z} \tag{2.52}$$

Since U^* is only a function of position and not time, the right side of Equation (2.52) is equal to the total derivative, $\frac{\mathrm{d}U^*}{\mathrm{d}t}$. Thus, integrating both sides of Equation (2.52) with respect to nondimensional time yields the integration constant of interest, denoted C,

$$\frac{1}{2}\left(\dot{x}^2 + \dot{y}^2 + \dot{z}^2\right) = U^* - \frac{C}{2} \tag{2.53}$$

Rearranging the terms in Equation (2.53) supplies the following definition of the integration constant C, hereby termed the Jacobi constant:

$$C = 2U^* - v^2 \tag{2.54}$$

where v is the speed of the body P_3 in the rotating frame. The Jacobi constant is inversely proportional to the energy of the system and remains constant for ballistic propagation in the CR3BP. While the existence of one integral of motion is not sufficient for a clear, closed-form solution, it does aid numerical analysis. Specifically, the accuracy of a solution propagated via numerical integration is assessed via the error in the instantaneous Jacobi constant value along the trajectory. Additionally, for any given CR3BP system, the knowledge of the Jacobi constant along any trajectory provides bounds on the natural dynamical motion of the infinitesimal third body. Finally, the Jacobi constant is also leveraged to reduce the dimension of the phase space, that furthers the understanding of the dynamics in the CR3BP and aids trajectory design.

2.3.4 Equilibrium Solutions

Any equilibrium solutions that exist are a fundamental property of a dynamical system that offer practical insight into its behavior over time. The equilibrium solutions in the CR3BP are locations in the CR3BP rotating frame where all components of the velocity and

acceleration vectors are zero. Thus, the time derivatives of all state components are equal to zero, i.e., $\dot{x} = \dot{y} = \dot{z} = 0$, and $\ddot{x} = \ddot{y} = \ddot{z} = 0$ at these locations. Substituting these values into the equations of motion yields,

$$\frac{\partial U^*}{\partial x} = x - \frac{(1-\mu)(x+\mu)}{r_{13}^3} - \frac{\mu(x-1+\mu)}{r_{23}^3} = 0 \tag{2.55}$$

$$\frac{\partial U^*}{\partial y} = y - \frac{(1-\mu)y}{r_{13}^3} - \frac{\mu y}{r_{23}^3} = 0 \tag{2.56}$$

$$\frac{\partial U^*}{\partial z} = -\frac{(1-\mu)z}{r_{13}^3} - \frac{\mu z}{r_{23}^3} = 0 \tag{2.57}$$

If a particle is placed at any of the equilibrium solutions with zero velocity, the gravitational and centrifugal forces cancel, and the particle remains stationary in the rotating frame indefinitely. As such, these points are frequently termed the stationary points. In the CR3BP, these solutions are labeled the libration points, or Lagrange points after the work of Joseph-Louis Lagrange towards constructing the locations of two of the five points [13]. In this investigation, the solutions are denoted the libration points and are represented as L_i. To compute the locations of these points, rearrange Equation (2.57) such that,

$$-z\left(\frac{1-\mu}{r_{13}^3} + \frac{\mu}{r_{23}^3}\right) = 0 \tag{2.58}$$

which is only true for values of $z = 0$. Thus, all libration points lie in the plane of motion of the primaries, i.e., in the $\hat{\boldsymbol{x}} - \hat{\boldsymbol{y}}$ plane in the CR3BP rotating frame. Let the values x_{eq} and y_{eq} represent the locations of the libration points along the $\hat{\boldsymbol{x}}$ and $\hat{\boldsymbol{y}}$ axes. Consider, then, the solution to Equation (2.56), i.e., the case when $y_{eq} = 0$ and the libration points lie along the $\hat{\boldsymbol{x}}$-axis connecting the two primaries. Substituting this value into Equation (2.55),

$$x_{eq} - \frac{(1-\mu)(x_{eq}+\mu)}{|x_{eq}+\mu|^3} - \frac{\mu(x_{eq}-1+\mu)}{|x_{eq}-1+\mu|^3} = 0 \tag{2.59}$$

Define the terms $\mathbb{A} = \text{sgn}(x_{eq}+\mu)$ and $\mathbb{B} = \text{sgn}(x_{eq}-1+\mu)$ that arise from the removal of the absolute value function. The following three cases then occur:

- **Case 1**: $\mathbb{A} > 0, \mathbb{B} < 0 \Rightarrow -\mu < x_{eq} \leq 1-\mu$

- **Case 2**: $\mathbb{A}, \mathbb{B} > 0 \Rightarrow 1 - \mu < x_{eq} \leq \infty$
- **Case 3**: $\mathbb{A}, \mathbb{B} < 0 \Rightarrow -\infty < x_{eq} \leq -\mu$

With initial guesses that lie within the specified intervals for the CR3BP system of interest, a Newton-Raphson root solving scheme is leveraged to compute the locations of the first three libration points. Since the points lie on the $\hat{\boldsymbol{x}}$-axis, they are termed the collinear libration points. Conventionally, these points are numbered as L_1, L_2, and L_3, consistent with their numbering in the three cases above. The point located between the primaries is, thus, denoted L_1, the point to the right of P_2 is L_2, and the point to the left of P_1 is L_3, as represented in Figure 2.3.

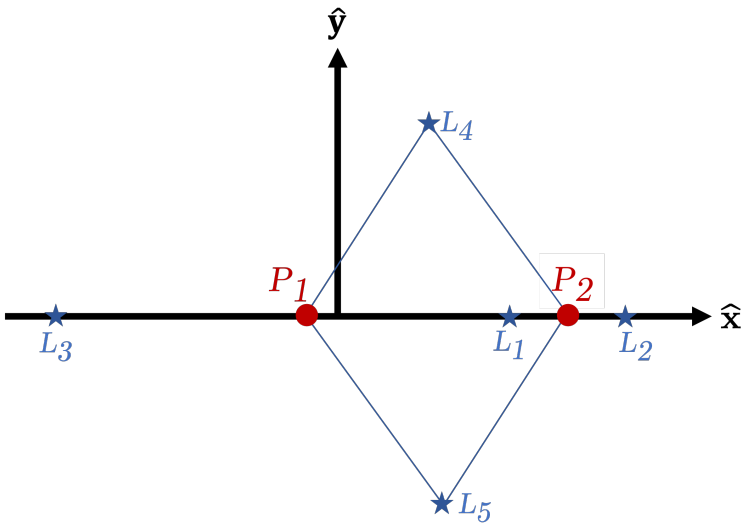

Figure 2.3. The libration points visualized in the CR3BP rotating frame.

In addition to the collinear libration points, there exist two additional equilibrium solutions that lie off the $\hat{\boldsymbol{x}}$-axis. To determine their location, consider when $y_{eq} \neq 0$. Use Equation (2.56) and rearrange the equation,

$$y_{eq}\left(1 - \frac{1-\mu}{r_{13}^3} - \frac{\mu}{r_{23}^3}\right) = 0 \tag{2.60}$$

Since $y_{eq} \neq 0$, the term in the parentheses must equal zero. Rearranging the terms,

$$\frac{1-\mu}{r_{13}^3} = 1 - \frac{\mu}{r_{23}^3} \tag{2.61}$$

Substituting Equation (2.61) into Equation (2.55),

$$x - \frac{(1-\mu)(x+\mu)}{r_{13}^3} - \frac{\mu(x-1+\mu)}{r_{23}^3} = 0 \tag{2.62}$$

$$-x + \left(1 - \frac{\mu}{r_{23}^3}\right)(x+\mu) + \frac{\mu x + \mu^2 - \mu}{r_{23}^3} = 0 \tag{2.63}$$

$$-x + x + \mu - \frac{\mu x}{r_{23}^3} - \frac{\mu^2}{r_{23}^3} + \frac{\mu x + \mu^2 - \mu}{r_{23}^3} = 0 \tag{2.64}$$

$$\mu\left(1 - \frac{1}{r_{23}^3}\right) = 0 \tag{2.65}$$

$$\Rightarrow r_{23} = 1 \tag{2.66}$$

Given this result, Equation (2.61) yields $r_{13} = 1$. Thus, the remaining two libration points lie at the points where unit circles about the two primaries intersect. From the equation of a circle,

$$(x_{eq} + \mu)^2 + y_{eq}^2 = (x_{eq} - 1 + \mu)^2 + y_{eq}^2 \tag{2.67}$$

which is satisfied when $x_{eq} = \frac{1}{2} - \mu$. Substituting this value into the equation of a circle about either of the primaries yields,

$$(x_{eq} + \mu)^2 + y_{eq}^2 = 1 \tag{2.68}$$

$$\frac{1}{4} + y_{eq}^2 = 1 \tag{2.69}$$

$$y_{eq} = \pm\frac{\sqrt{3}}{2} \tag{2.70}$$

Thus, the locations of the two remaining libration points, denoted L_4 and L_5, are given as,

$$x_{L_{4,5}} = \frac{1}{2} - \mu \tag{2.71}$$

$$y_{L_{4,5}} = \pm\frac{\sqrt{3}}{2} \tag{2.72}$$

where L_4 is conventionally selected to possess a positive y_{eq}-value. These points form equilateral triangles with the two primaries and are, thus, termed the triangular or the equilateral points. With the known locations of the libration points, the dynamics of the system relative to these solutions are insightful.

2.3.5 Zero Velocity Surfaces

The existence of an integral of the motion for the CR3BP, i.e., the Jacobi constant, provides bounds on the motion of the third body, P_3, under natural propagation. For a known Jacobi constant value, the magnitude of the rotating velocity of P_3 is evaluated as,

$$v^2 = 2U^* - C \tag{2.73}$$

It is immediately apparent that the right side of this equation must be positive. As such, the following constraint arises,

$$C \leq 2U^* \tag{2.74}$$

where the boundary $C = 2U^*$ delineates the regions of possible physical motion with regions that are dynamically *forbidden*. Substituting the condition for this boundary into Equation (2.73) yields

$$v^2 = 2U^* - C = 0 \tag{2.75}$$

Equation (2.75) implies that the boundaries identify locations with zero relative velocity magnitude in terms of rotating coordinates and confine the regions of possible motion for

P_3 in the CR3BP. Expanding the equation for the Jacobi constant for the cases when Equation (2.75) holds,

$$C = (x^2 + y^2) + \frac{2(1-\mu)}{r_{13}} + \frac{2\mu}{r_{23}} \tag{2.76}$$

Since an infinite number of sets of x, y, and z values satisfy Equation (2.76), all solutions together represent a surface in 3D space. These solutions are termed the Zero Velocity Surfaces (ZVS); for planar motion, these surfaces reduce to Zero Velocity Curves (ZVC) that reflect a slice of the ZVS through $z = 0$. Regions outside the bounds of allowable motion are, aptly, denoted the *forbidden regions*, and for a given value of the Jacobi constant, P_3 cannot cross into these regions. Traversing through forbidden regions requires a change in the Jacobi constant value, that may be achieved via a change in the velocity magnitude of the particle. Further analysis of these surfaces and curves at various energy levels offers great insight into the underlying dynamical environment.

The libration points corresponding to a specific CR3BP system must always lie on the ZVS since, by definition, these equilibrium solutions require the relative velocity and acceleration magnitudes to be zero. For reference, the values of the Jacobi constant associated with the libration points in the Earth-Moon systems are summarized in Table 2.1. It is noted that the values of the Jacobi constant decrease for successive libration points. The zero velocity curves for various energy levels in the Earth-Moon CR3BP system appear in Figures 2.4 and 2.5. In each figure, the Earth and Moon are indicated by solid black markers; all the libration points are located via black stars. The blue curves identify regions that are naturally accessible to the spacecraft at a given level of Jacobi constant (energy). For instance, Figure 2.4(a) illustrates the bounds on possible motion when the Jacobi constant value is equal to $C = 3.3$, which is greater than the Jacobi constant of the L_1 libration point, denoted C_{L_1}. Two distinct regions about either primary emerge in this case; a spacecraft at this energy value remains bounded within either of these regions and does not cross through them naturally. In addition to these interior bounds, the larger blue curve illustrates an exterior boundary on the range of possible motions, encompassing L_3 and the triangular libration points. As the Jacobi constant value decreases below this value, however, more

regions in space become accessible, associated with an increase in the energy of the spacecraft. For a Jacobi constant value equal to that of L_1, as illustrated in Figure 2.4(b), the bounding regions about the Earth and the Moon expand and converge to the location of L_1. Decreasing the Jacobi constant value further, for instance, the case when $C = 3.18025$ as illustrated in Figure 2.4(c), causes the interior bounds on the accessible regions to merge, opening a *gateway* that links the regions in the proximity of the primaries. At this energy level and lower, the spacecraft is able to naturally traverse through the interior neighborhood of P_1 and P_2 without restrictions. Decreasing the Jacobi value to equal that of L_2 results in an expansion of the interior region and contraction of the exterior region, as apparent in Figure 2.4(d), converging at the location of L_2.

Table 2.1. Jacobi constant values for the libration points in the Earth-Moon CR3BP system ($\mu = 0.0121505842699404$).

L_1	L_2	L_3	L_4	L_5
3.18834	3.17216	3.01215	2.98799	2.98799

The next critical evolution in the ZVC is illustrated in Figure 2.5(a), which occurs at a Jacobi constant value greater than C_{L_2}. At this energy level, the interior and exterior bounds merge, allowing the L_2 gateway to open and enabling access to the exterior of the Earth-Moon system. Continuing to decrease the value of the Jacobi constant, as evident in Figures 2.5(b) and 2.5(c), the forbidden region shrinks rapidly, making it possible for the spacecraft to travel extensively within the Earth-Moon domain and eventually opening up the L_3 gateway as well. When the Jacobi value is equal to or below $C_{L_{4,5}}$, the zero velocity curves disappear in the $\hat{\boldsymbol{x}}$-$\hat{\boldsymbol{y}}$ plane. Thus, the spacecraft is free to move around the primaries or exit the system, as illustrated in Figure 2.5(d). However, inaccessible regions may remain beyond the plane [33].

2.4 The Higher-Fidelity Ephemeris Model

The Circular Restricted Three-Body Problem establishes a baseline that guides preliminary orbit selection and analysis. However, to simulate real-world scenarios and achieve a

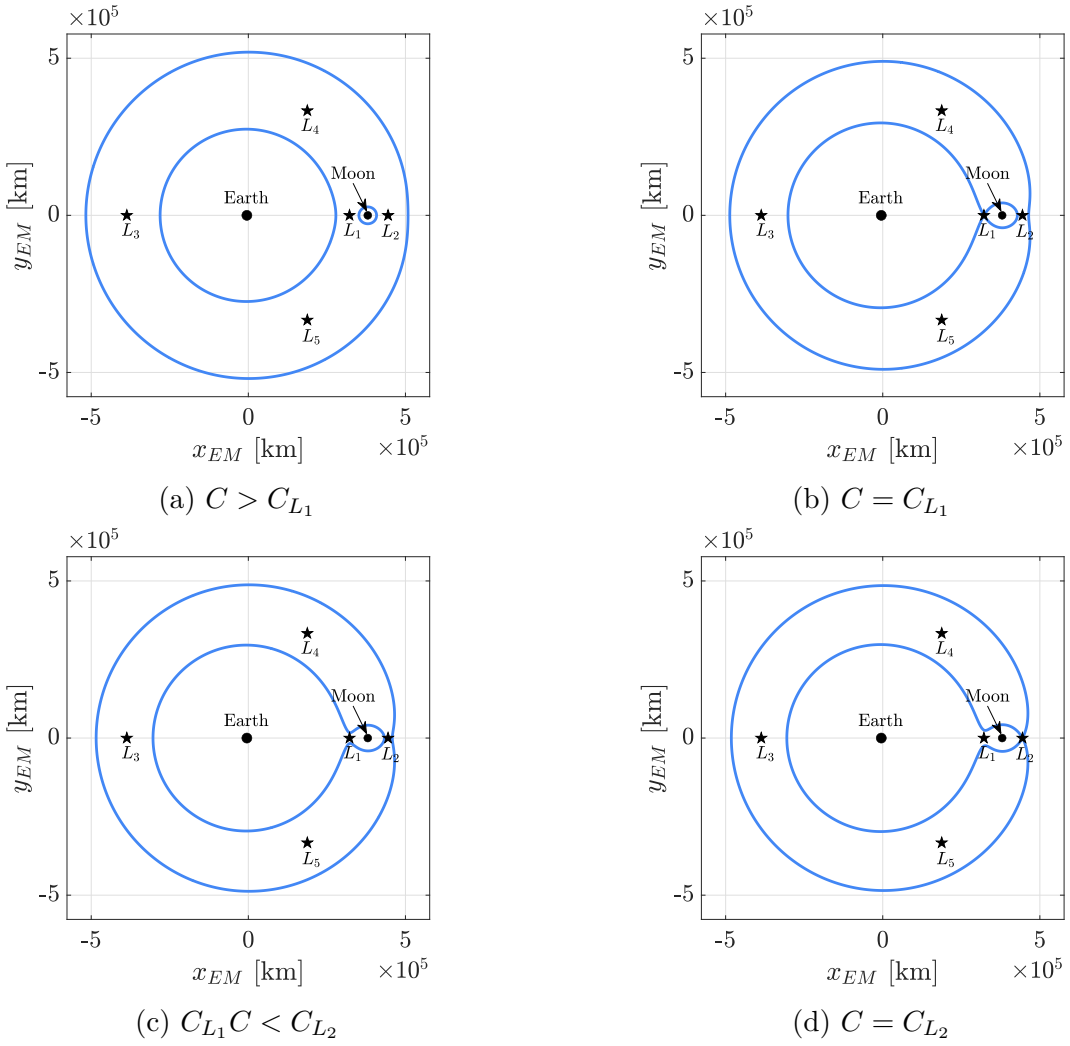

(a) $C > C_{L_1}$ (b) $C = C_{L_1}$

(c) $C_{L_1} C < C_{L_2}$ (d) $C = C_{L_2}$

Figure 2.4. Evolution of the Zero Velocity Curves (ZVC) in the Earth-Moon CR3BP system.

higher fidelity of dynamical modeling, it is necessary to incorporate additional forces that influence the motion of spacecraft. Among these forces are the gravitational influences of other celestial bodies that, in addition to affecting the motion of the spacecraft itself, impact the orbits of other celestial bodies in the dynamical system. Doing so supplies higher fidelity in modeling the orbits of the primaries themselves. Thus, the Higher-Fidelity Ephemeris Model (HFEM) is leveraged to incorporate these additional gravitational forces and assess the utility of any trajectories constructed in the CR3BP. In addition to incorporating gravitational forces, this model utilizes the true positions and velocities of the celestial bodies

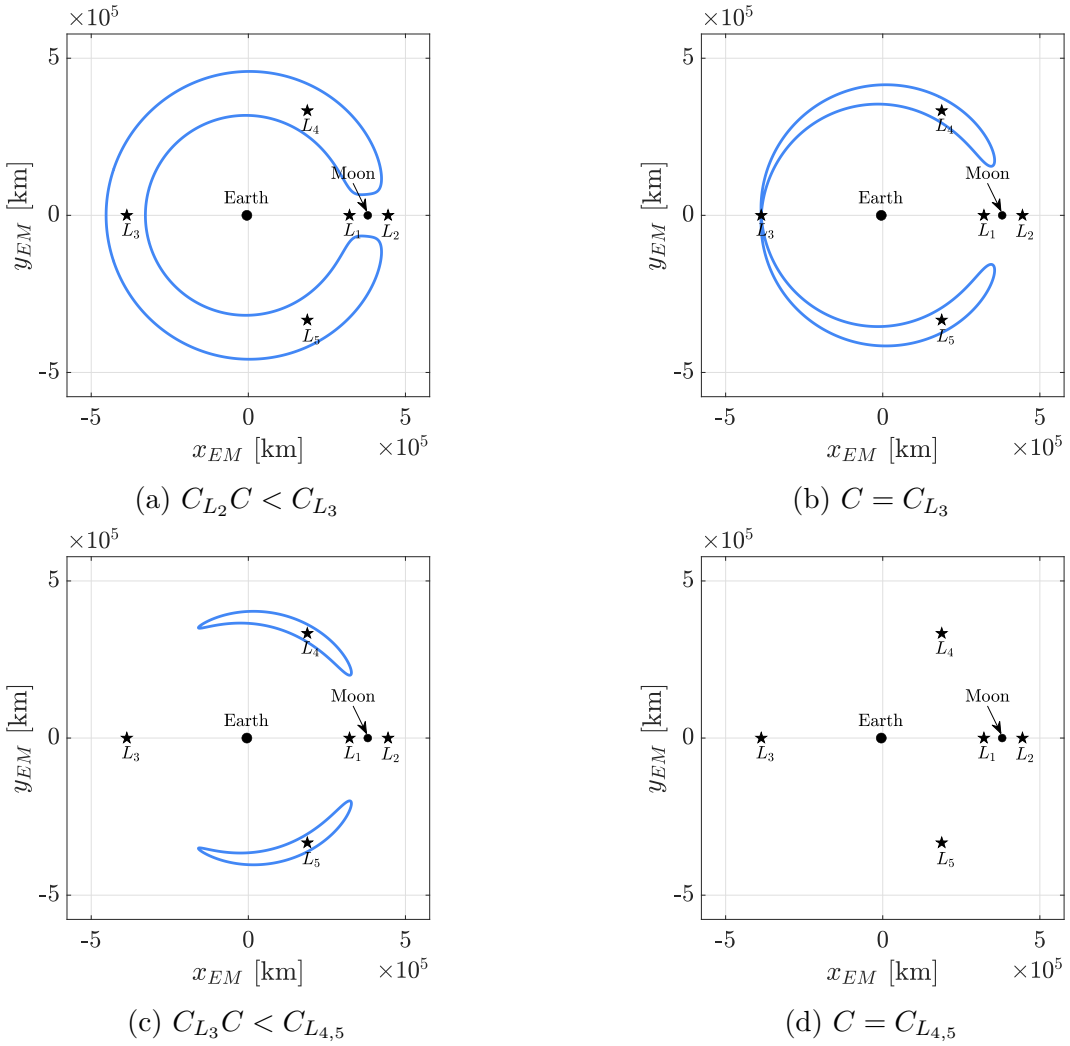

(a) $C_{L_2}C < C_{L_3}$ (b) $C = C_{L_3}$

(c) $C_{L_3}C < C_{L_{4,5}}$ (d) $C = C_{L_{4,5}}$

Figure 2.5. Evolution of the Zero Velocity Curves (ZVC) in the Earth-Moon CR3BP system for additional energy levels.

that comprise the model. These planetary ephemerides are obtained via the DE440 SPICE kernel from the Jet Propulsion Laboratory's Navigation and Ancillary Information Facility (NAIF) database [34].

While the gravitational forces exerted by the Earth and the Moon dominate the motion of a spacecraft operating in their respective vicinity, it is also useful to evaluate the impact of other gravitational forces throughout the Earth-Moon system in general. This analysis guides the selection of celestial bodies that comprise the HFEM utilized in this investigation. As an example, Figure 2.6 illustrates the acceleration magnitudes due to various celestial

bodies. Figure 2.6(a) illustrates the acceleration levels for various spacecraft locations along the $\hat{\boldsymbol{x}}$-axis in the Earth-Moon CR3BP rotating frame. Similarly, the acceleration levels for various locations along the $\hat{\boldsymbol{y}}$- and the $\hat{\boldsymbol{z}}$-axes appear in Figures 2.6(b) and 2.6(c) respectively. Intuitively, the acceleration levels that appear in Figure 2.6(a) peak at the locations of the Earth and the Moon. The Sun's gravitational impact is typically an order of magnitude lower than that of the Earth. At this epoch, the Sun's influence is, surprisingly, comparable to that of the Moon farther from its vicinity and near L_3. While Jupiter's gravity is the next significant force in the three cases considered in Figure 2.6, it is approximately four orders of magnitude smaller than that of the Earth and the Moon. The remaining bodies plotted in Equation (2.1), Venus, Saturn, and Mars, perturb the spacecraft to an even lesser extent. For this example, the epoch January 01, 2025 at 00:00:00 UTC is utilized to obtain the positions of the celestial bodies relative to the spacecraft and the Earth-Moon system. The results here are relatively consistent for other epochs, with the exception that the magnitudes of acceleration imparted by Jupiter and Venus interchange at certain epochs. It is also possible to compute the acceleration levels over a range of times and assess the average acceleration magnitude due to each celestial body at various locations [35].

Consistent with the insights from Figure 2.6, this work is based on the Earth-Moon-Sun-Jupiter ephemeris model for trajectory validation in a higher-fidelity dynamical environment. The equations of motion in Equation (2.2) are propagated where, depending upon the trajectory, the Earth or the Moon is selected as the central body. Similar to the scheme employed in the CR3BP, the relevant quantities for propagation in the HFEM are also nondimensionalized for preserving numerical accuracy and scaling the spacecraft state components consistently.

2.5 Coordinate Frame Transformations

By virtue of the model definition, most analyses in the CR3BP leverage the rotating frame introduced in Figure 2.2. However, visualization in inertial frames allows further critical insight into the geometry and evolution of various trajectories [17]. As such, frame transformations between the CR3BP rotating frame and the inertial frame are necessary.

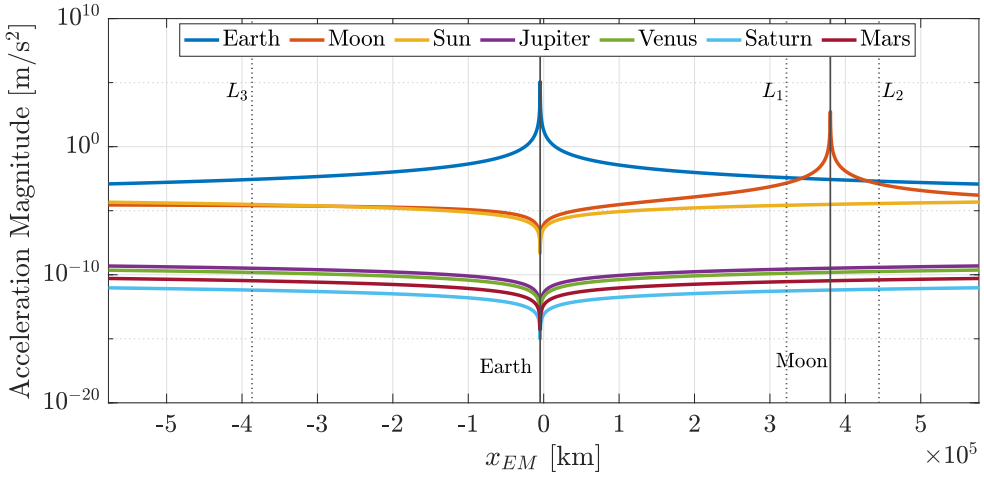

(a) Variation in $x-$location.

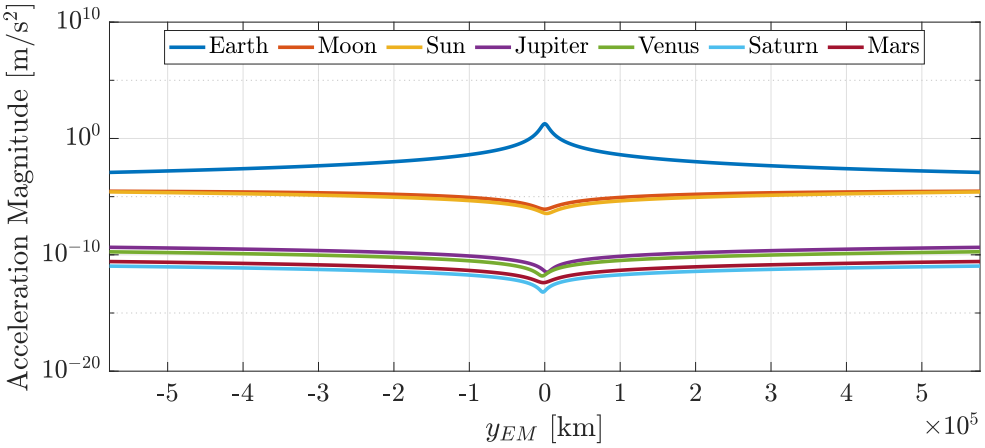

(b) Variation in $y-$location.

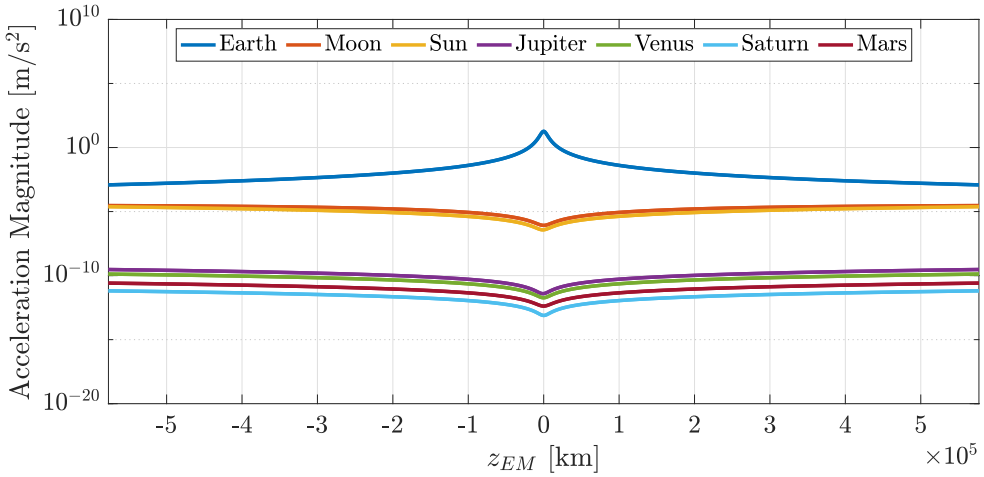

(c) Variation in $z-$location.

Figure 2.6. Acceleration magnitudes in the Earth-Moon vicinity due to various celestial bodies. Epoch: January 1, 2025.

2.5.1 Transforming between the CR3BP Rotating and an Arbitrary Inertial Frame

Recall the inertial frame, denoted $\mathcal{I}$, that orients the CR3BP rotating frame, denoted $\mathcal{R}$, as described in Figure 2.2. Equation (2.26) defines the nondimensional position vector that locates the spacecraft (P_3) relative to the system barycenter, $\mathcal{B}$, as,

$$^{\mathcal{R}}\boldsymbol{r} = x\hat{\boldsymbol{x}} + y\hat{\boldsymbol{y}} + z\hat{\boldsymbol{z}} \tag{2.77}$$

where the pre-superscript indicates that the vector is expressed in terms of the rotating frame coordinates. Similarly, the nondimensional position vector is expressed in inertial coordinates as,

$$^{\mathcal{I}}\boldsymbol{r} = X\hat{\boldsymbol{X}} + Y\hat{\boldsymbol{Y}} + Z\hat{\boldsymbol{Z}} \tag{2.78}$$

Note that the angle θ orients the rotating frame relative to the inertial frame and is defined as,

$$\theta = \underline{\underline{n}} \cdot (t + t_0) \tag{2.79}$$

where $\underline{\underline{n}}$ represents the nondimensional mean motion of the CR3BP primaries and is equal to unity. If the two frames are aligned at initial time, then $\theta = t$. Otherwise, the initial angular offset in the orientation of the two frames is incorporated into the value of θ with the addition of t_0. In general, for a given θ value, the axes that constitute the rotating frame are related to the inertial frame as follows,

$$\hat{\boldsymbol{x}} = \cos\theta\hat{\boldsymbol{X}} + \sin\theta\hat{\boldsymbol{Y}} \tag{2.80}$$

$$\hat{\boldsymbol{y}} = -\sin\theta\hat{\boldsymbol{X}} + \cos\theta\hat{\boldsymbol{Y}} \tag{2.81}$$

$$\hat{\boldsymbol{z}} = \hat{\boldsymbol{Z}} \tag{2.82}$$

These relationships yield the following direction cosine matrix (DCM) that relates the rotating and inertial coordinates,

$$
{}^{\mathcal{R}}\mathbf{C}^{\mathcal{I}} = \begin{bmatrix} \cos\theta & \sin\theta & 0 \\ -\sin\theta & \cos\theta & 0 \\ 0 & 0 & 1 \end{bmatrix} \tag{2.83}
$$

Leveraging this DCM, an inertial position vector may be transformed into the rotating frame as,

$$
{}^{\mathcal{R}}\boldsymbol{r} = {}^{\mathcal{R}}\mathbf{C}^{\mathcal{I}} \cdot {}^{\mathcal{I}}\boldsymbol{r} \tag{2.84}
$$

where the vectors before and after the transformation are assumed to be column vectors. It is also straightforward to produce the inverse transformation, i.e., transforming the position vector from the rotating coordinates to the inertial frame as,

$$
{}^{\mathcal{I}}\boldsymbol{r} = {}^{\mathcal{I}}\mathbf{C}^{\mathcal{R}} \cdot {}^{\mathcal{R}}\boldsymbol{r} \tag{2.85}
$$

where the DCM is now,

$$
{}^{\mathcal{I}}\mathbf{C}^{\mathcal{R}} = \begin{bmatrix} \cos\theta & -\sin\theta & 0 \\ \sin\theta & \cos\theta & 0 \\ 0 & 0 & 1 \end{bmatrix} \tag{2.86}
$$

This process allows the transformation of a position vector between the rotating frame and any arbitrary inertial frame. Recall from Equation (2.34) that the inertial velocity, ${}^{\mathcal{I}}\dot{\boldsymbol{r}}$, is determined from the rotating velocity, ${}^{\mathcal{R}}\dot{\boldsymbol{r}}$, via the application of the BKE:

$$
{}^{\mathcal{I}}\dot{\boldsymbol{r}} = {}^{\mathcal{R}}\dot{\boldsymbol{r}} + \left({}^{\mathcal{I}}\boldsymbol{\omega}^{\mathcal{R}} \times {}^{\mathcal{R}}\boldsymbol{r}\right) \tag{2.87}
$$

where ${}^{\mathcal{I}}\dot{\boldsymbol{r}}$ is expressed in terms of the rotating frame coordinates as,

$$ {}^{\mathcal{I}}\dot{\boldsymbol{r}} = \left(\dot{x} - \underline{\underline{n}}y\right)\hat{\boldsymbol{x}} + \left(\dot{y} + \underline{\underline{n}}x\right)\hat{\boldsymbol{y}} + \dot{z}\hat{\boldsymbol{z}} \tag{2.88} $$

Leveraging Equation (2.85), ${}^{\mathcal{I}}\dot{\boldsymbol{r}}$ is also easily expressed in the inertial coordinate frame. In general, it is possible to transform the full nondimensional state vector from the rotating to the inertial frame. To do so, the sub-matrix ${}^{\mathcal{I}}\dot{\mathbf{C}}^{\mathcal{R}}$ is first constructed as,

$$ \frac{\mathrm{d}\,{}^{\mathcal{I}}\mathbf{C}^{\mathcal{R}}}{\mathrm{d}t} = \frac{\mathrm{d}\,{}^{\mathcal{I}}\mathbf{C}^{\mathcal{R}}}{\mathrm{d}\theta}\frac{\mathrm{d}\theta}{\mathrm{d}t} \tag{2.89} $$

$$ = \begin{bmatrix} -\sin\theta & -\cos\theta & 0 \\ \cos\theta & -\sin\theta & 0 \\ 0 & 0 & 0 \end{bmatrix}\dot{\theta} \tag{2.90} $$

where $\dot{\theta}$ is equal to the nondimensional mean motion, i.e., unity for the CR3BP. Together, Equations (2.86) and (2.90) yield the following convenient full-state transformation from the rotating to inertial coordinates,

$$ \boldsymbol{X} = \underbrace{\begin{bmatrix} {}^{\mathcal{I}}\mathbf{C}^{\mathcal{R}} & 0_{3\times3} \\ {}^{\mathcal{I}}\dot{\mathbf{C}}^{\mathcal{R}} & {}^{\mathcal{I}}\mathbf{C}^{\mathcal{R}} \end{bmatrix}}_{{}^{\mathcal{I}}\underline{\underline{\mathbf{C}}}^{\mathcal{R}}}\boldsymbol{x} \tag{2.91} $$

where ${}^{\mathcal{I}}\underline{\underline{\mathbf{C}}}^{\mathcal{R}}$ is the 6×6 transformation matrix. The column vector $\boldsymbol{x} = [x\ y\ z\ \dot{x}\ \dot{y}\ \dot{z}]^T$ represents the state with respect to an observer in the rotating frame and expressed in

rotating coordinates, while $\boldsymbol{X} = [X\ Y\ Z\ \dot{X}\ \dot{Y}\ \dot{Z}]^T$ is the inertial state expressed in inertial coordinates. More explicitly, the full state transformation is given as,

$$\begin{bmatrix} X \\ Y \\ Z \\ \dot{X} \\ \dot{Y} \\ \dot{Z} \end{bmatrix} = \begin{bmatrix} \cos\theta & -\sin\theta & 0 & 0 & 0 & 0 \\ \sin\theta & \cos\theta & 0 & 0 & 0 & 0 \\ 0 & 0 & 1 & 0 & 0 & 0 \\ -\sin\theta & -\cos\theta & 0 & \cos\theta & -\sin\theta & 0 \\ \cos\theta & -\sin\theta & 0 & \sin\theta & \cos\theta & 0 \\ 0 & 0 & 0 & 0 & 0 & 1 \end{bmatrix} \begin{bmatrix} x \\ y \\ z \\ \dot{x} \\ \dot{y} \\ \dot{z} \end{bmatrix} \tag{2.92}$$

Conveniently, the inverse of the full DCM supplies the transformation from inertial to rotating coordinates,

$$\boldsymbol{x} = \left({}^{\mathcal{I}}\underline{\underline{\mathbf{C}}}^{\mathcal{R}}\right)^{-1} \boldsymbol{X} \tag{2.93}$$

Note that, by definition of the rotating position and velocity vectors, Equations (2.91) and (2.93) yield transformations between the rotating frame and an inertial frame centered on the system barycenter, $\mathcal{B}$. When osculating Keplerian orbital elements are of interest, it is also insightful to consider transformations to an inertial frame centered on either primary. For transforming a barycentric rotating frame state to a P_1-centered inertial frame, the base point of the initial rotating frame state vector is shifted such that,

$$\boldsymbol{x} = \begin{bmatrix} x + \mu \\ y \\ z \\ \dot{x} \\ \dot{y} \\ \dot{z} \end{bmatrix} \tag{2.94}$$

Then, Equation (2.91) is employed to produce the equivalent state vector in the P_1-centered inertial frame. Similarly, to evaluate the state vector in a P_2-centered inertial frame, prior to the transformation, the rotating frame vector is translated as,

$$\boldsymbol{x} = \begin{bmatrix} x - 1 + \mu \\ y \\ z \\ \dot{x} \\ \dot{y} \\ \dot{z} \end{bmatrix} \tag{2.95}$$

Following the translation, Equation (2.91) yields the analogous state vector in the P_2-centered inertial frame. Finally, in case a P_1- or P_2-centered inertial state vector is required to be transformed into the CR3BP rotating frame, Equation (2.93) is first directly applied to obtain the equivalent primary-centered rotating state. A simple translation to the barycenter of the primary system then supplies the desired state vector in the rotating frame.

3. TRAJECTORY CONSTRUCTION VIA NUMERICAL METHODS

In the absence of a closed-form solution, other approaches for investigating the long-term dynamics to support desirable behavior are necessary. Dynamical Systems Theory (DST) offers tools that allow the assessment of particular solutions within the CR3BP and HFEM for trajectory design. First, the State Transition Matrix (STM) is introduced to quantify state sensitivities within both models. Differential corrections techniques are then described to modify initial guesses to achieve favorable dynamical behavior. Periodic orbits in the CR3BP are introduced, followed by methods of computing families of periodic orbits that exhibit similar characteristics. Linear stability analysis and bifurcation theory provide insight into the qualitative nature of any constructed solutions. Finally, the invariant manifold theory and Poincaré maps are valuable tools to incorporate other dynamical structures in the trajectory design process. The approaches discussed in this chapter are detailed in the context of general periodic orbits and trajectory generation in the CR3BP.

3.1 State Transition Matrix

Numerical integration of the equations of motion for the CR3BP and HFEM yields a phase space portrait of the desired trajectory. It is also, then, useful to assess the behavior in its vicinity and to produce information about other nearby dynamical structures. To accomplish this task, the equations of motion are linearized relative to a nearby reference path, yielding the State Transition Matrix (STM) [36]. The STM supplies a direct mapping of a state at time t_0 to a downstream time t_i [37], and is employed to approximate the behavior of a particle in a nonlinear system with respect to a reference solution. In trajectory design, the STM aids in adjusting initial conditions in the CR3BP to yield desired behavior, and to assess the stability characteristics of periodic solutions.

To derive the STM, first examine the variational equations. Under natural dynamics, the nonlinear system of differential equations is represented as,

$$\dot{\boldsymbol{x}} = \boldsymbol{f}\left(\boldsymbol{x}, t\right) \tag{3.1}$$

where $\boldsymbol{x}$ is a nondimensional state vector with six elements, and t is the nondimensional time. Let a particular reference path, or reference trajectory, be represented as $\boldsymbol{x}^*(t)$. Then, a nearby trajectory evaluated at the same time is defined as,

$$\boldsymbol{x}(t) = \boldsymbol{x}^*(t) + \delta\boldsymbol{x}(t) \tag{3.2}$$

where $\delta\boldsymbol{x}(t)$ is the variation relative to the reference trajectory, as illustrated in Figure 3.1. Substituting Equation (3.2) into Equation (3.1) yields,

$$\dot{\boldsymbol{x}} = \boldsymbol{f}\left(\boldsymbol{x}^* + \delta\boldsymbol{x}, t\right) = \dot{\boldsymbol{x}^*} + \delta\dot{\boldsymbol{x}} \tag{3.3}$$

The Taylor series expansion for Equation (3.3) about the reference solution, $\boldsymbol{x}^*(t)$, is straightforward as,

$$\dot{\boldsymbol{x}} = \boldsymbol{f}(\boldsymbol{x}^*, t) + \left.\frac{\partial \boldsymbol{f}}{\partial \boldsymbol{x}}\right|_{\boldsymbol{x}^*} (\boldsymbol{x} - \boldsymbol{x}^*) + \text{H.O.T.s} \tag{3.4}$$

Substituting in Equation (3.3) on the left side of the equation yields,

$$\dot{\boldsymbol{x}}^* + \delta\dot{\boldsymbol{x}} = \dot{\boldsymbol{x}}^* + \left.\frac{\partial \boldsymbol{f}}{\partial \boldsymbol{x}}\right|_{\boldsymbol{x}^*} \delta\boldsymbol{x} + \text{H.O.T.s} \tag{3.5}$$

that further reduces to,

$$\delta\dot{\boldsymbol{x}} = \left.\frac{\partial \boldsymbol{f}}{\partial \boldsymbol{x}}\right|_{\boldsymbol{x}^*} \delta\boldsymbol{x} + \text{H.O.T.s} \tag{3.6}$$

Neglecting the higher-order terms, the Taylor series reduces to the linear approximation,

$$\delta\dot{\boldsymbol{x}} = \left.\frac{\partial \boldsymbol{f}}{\partial \boldsymbol{x}}\right|_{\boldsymbol{x}^*} \delta\boldsymbol{x} = A(t)\delta\boldsymbol{x} \tag{3.7}$$

Equation (3.7) represents the linear, time-varying variational equations, where the Jacobian matrix, $A(t)$, is evaluated along the reference solution, $\boldsymbol{x}^*$. A solution to the Equation (3.7) is,

$$\delta\boldsymbol{x}(t) = \Phi(t, t_0)\delta\boldsymbol{x}(t_0) \tag{3.8}$$

where $\Phi(t, t_0)$ is the STM evaluated from time t_0 to t, and is defined as,

$$\Phi(t, t_0) = e^{A(t-t_0)} \tag{3.9}$$

The STM reflects the variations in the state at a time t, represented as $\boldsymbol{x}_f = \boldsymbol{x}(t)$, as a result of any perturbations in the initial state, $\boldsymbol{x}_0 = \boldsymbol{x}(t_0)$. Mathematically, this relationship is expanded as the following matrix of partial derivatives,

$$\begin{bmatrix} \delta x_f \\ \delta y_f \\ \delta z_f \\ \delta \dot{x}_f \\ \delta \dot{y}_f \\ \delta \dot{z}_f \end{bmatrix} = \begin{bmatrix} \frac{\partial x}{\partial x_o} & \frac{\partial x}{\partial y_o} & \frac{\partial x}{\partial z_o} & \frac{\partial x}{\partial \dot{x}_o} & \frac{\partial x}{\partial \dot{y}_o} & \frac{\partial x}{\partial \dot{z}_o} \\ \frac{\partial y}{\partial x_o} & \frac{\partial y}{\partial y_o} & \frac{\partial y}{\partial z_o} & \frac{\partial y}{\partial \dot{x}_o} & \frac{\partial y}{\partial \dot{y}_o} & \frac{\partial y}{\partial \dot{z}_o} \\ \frac{\partial z}{\partial x_o} & \frac{\partial z}{\partial y_o} & \frac{\partial z}{\partial z_o} & \frac{\partial z}{\partial \dot{x}_o} & \frac{\partial z}{\partial \dot{y}_o} & \frac{\partial z}{\partial \dot{z}_o} \\ \frac{\partial \dot{x}}{\partial x_o} & \frac{\partial \dot{x}}{\partial y_o} & \frac{\partial \dot{x}}{\partial z_o} & \frac{\partial \dot{x}}{\partial \dot{x}_o} & \frac{\partial \dot{x}}{\partial \dot{y}_o} & \frac{\partial \dot{x}}{\partial \dot{z}_o} \\ \frac{\partial \dot{y}}{\partial x_o} & \frac{\partial \dot{y}}{\partial y_o} & \frac{\partial \dot{y}}{\partial z_o} & \frac{\partial \dot{y}}{\partial \dot{x}_o} & \frac{\partial \dot{y}}{\partial \dot{y}_o} & \frac{\partial \dot{y}}{\partial \dot{z}_o} \\ \frac{\partial \dot{z}}{\partial x_o} & \frac{\partial \dot{z}}{\partial y_o} & \frac{\partial \dot{z}}{\partial z_o} & \frac{\partial \dot{z}}{\partial \dot{x}_o} & \frac{\partial \dot{z}}{\partial \dot{y}_o} & \frac{\partial \dot{z}}{\partial \dot{z}_o} \end{bmatrix} \begin{bmatrix} \delta x_0 \\ \delta y_0 \\ \delta z_0 \\ \delta \dot{x}_0 \\ \delta \dot{y}_0 \\ \delta \dot{z}_0 \end{bmatrix} \tag{3.10}$$

Some important properties of the STM include [38],

$$\Phi(t, t) = \Phi(0) = I \tag{3.11}$$

$$\Phi(t_2, t_0) = \Phi(t_2, t_1)\Phi(t_1, t_0) \tag{3.12}$$

$$\Phi(t_0, t_1) = \Phi^{-1}(t_1, t_0) \tag{3.13}$$

Additionally, the STM satisfies the following first-order matrix differential equation,

$$\dot{\Phi}(t, t_0) = A(t)\Phi(t, t_0) \tag{3.14}$$

Due to the lack of an analytical solution, to produce the elements of the STM at a time t, Equation (3.14) is numerically integrated, with the initial value at t_0 supplied by Equation (3.11). For the CR3BP and HFEM, the associated 36 first-order scalar differential equations, corresponding to each element of the STM, are numerically integrated simultaneously with the respective six first-order scalar equations of motion.

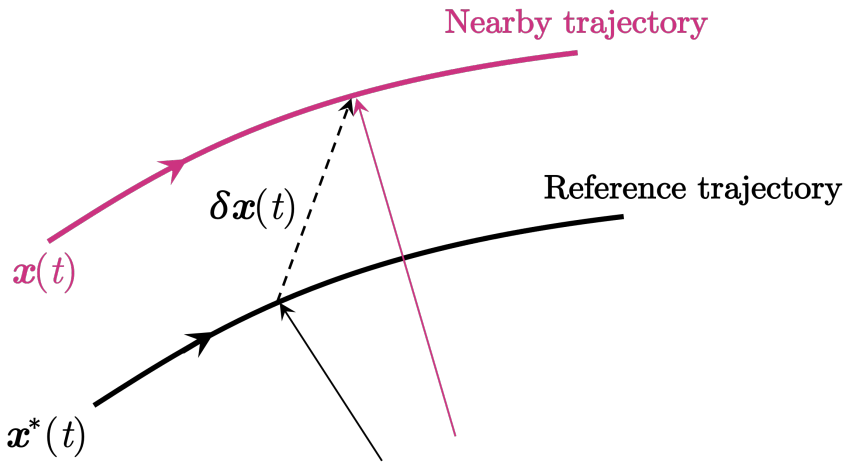

Figure 3.1. Representation of a reference trajectory and a trajectory in its neighborhood.

3.1.1 CR3BP Linear Variational Equations

To compute the STM in the CR3BP, the first-order variational matrix, $A(t)$ from Equation (3.7) is leveraged. The numerical integration of Equation (3.14) provides each element

of the STM, since no analytical solution exists for this model. For the CR3BP, the $A(t)$ matrix is a 6×6 matrix of the form,

$$A(t) = \begin{bmatrix} 0 & 0 & 0 & 1 & 0 & 0 \\ 0 & 0 & 0 & 0 & 1 & 0 \\ 0 & 0 & 0 & 0 & 0 & 1 \\ U^*_{xx} & U^*_{xy} & U^*_{xz} & 0 & 2 & 0 \\ U^*_{yx} & U^*_{yy} & U^*_{yz} & -2 & 0 & 0 \\ U^*_{zx} & U^*_{zy} & U^*_{zz} & 0 & 0 & 0 \end{bmatrix} \tag{3.15}$$

where the elements U^*_{ij} represent the partial derivative of the CR3BP pseudo-potential function, $\dfrac{\partial^2 U^*}{\partial i \partial j}$. Using the definition of the CR3BP pseudo-potential function, these partial derivatives are derived as,

$$U^*_{xx} = 1 - \frac{1-\mu}{r_{13}^3} + \frac{3(1-\mu)(x+\mu)^2}{r_{13}^5} - \frac{\mu}{r_{23}^3} + \frac{3\mu(x-1+\mu)^2}{r_{23}^5} \tag{3.16}$$

$$U^*_{yy} = 1 - \frac{1-\mu}{r_{13}^3} + \frac{3(1-\mu)y^2}{r_{13}^5} - \frac{\mu}{r_{23}^3} + \frac{3\mu y^2}{r_{23}^5} \tag{3.17}$$

$$U^*_{zz} = -\frac{1-\mu}{r_{13}^3} + \frac{3(1-\mu)z^2}{r_{13}^5} - \frac{\mu}{r_{23}^3} + \frac{3\mu z^2}{r_{23}^5} \tag{3.18}$$

$$U^*_{xy} = \frac{3(1-\mu)(x+\mu)y}{r_{13}^5} + \frac{3\mu(x-1+\mu)y}{r_{23}^5} = U^*_{yx} \tag{3.19}$$

$$U^*_{xz} = \frac{3(1-\mu)(x+\mu)z}{r_{13}^5} + \frac{3\mu(x-1+\mu)z}{r_{23}^5} = U^*_{zx} \tag{3.20}$$

$$U^*_{yz} = \frac{3(1-\mu)yz}{r_{13}^5} + \frac{3\mu yz}{r_{23}^5} = U^*_{zy} \tag{3.21}$$

These partial derivatives are evaluated along the reference trajectory or arc and, together with Equation (3.7), supply the elements of the STM.

3.1.2 HFEM Linear Variational Equations

Similar to the CR3BP, the Jacobian matrix $A(t)$ is also defined in the HFEM to allow the numerical computation of the associated STM. Assume the mass of the spacecraft, M_i is negligible relative to the masses of the celestial bodies in the HFEM. For the general HFEM, the $A(t)$ matrix is also a 6×6 matrix that takes the form,

$$A(t) = \begin{bmatrix} 0 & 0 & 0 & 1 & 0 & 0 \\ 0 & 0 & 0 & 0 & 1 & 0 \\ 0 & 0 & 0 & 0 & 0 & 1 \\ U_{xx} & U_{xy} & U_{xz} & 0 & 0 & 0 \\ U_{yx} & U_{yy} & U_{yz} & 0 & 0 & 0 \\ U_{zx} & U_{zy} & U_{zz} & 0 & 0 & 0 \end{bmatrix} \tag{3.22}$$

where the elements U_{ij} represent the partial derivative of the ephemeris potential function, $\dfrac{\partial^2 U}{\partial i \partial j}$. These partial derivatives are derived from Equation (2.2) and are evaluated along the reference trajectory or arc. In terms of the position components of the spacecraft (denoted

via the subscript i) relative to the HFEM central body (denoted via the subscript q), these partials are derived as,

$$U_{xx} = \tilde{G}M_i\left(\frac{3x_{qi}^2}{R_{qi}^5} - \frac{1}{R_{qi}^3}\right) + \tilde{G}\sum_{\substack{j=1\\ j\neq i,q}}^{\mathcal{N}} M_j\left(\frac{3\left(x_{qj}-x_{qi}\right)^2}{|\boldsymbol{R}_{qj}-\boldsymbol{R}_{qi}|^5} - \frac{1}{|\boldsymbol{R}_{qj}-\boldsymbol{R}_{qi}|^3}\right) \tag{3.23}$$

$$U_{yy} = \tilde{G}M_i\left(\frac{3y_{qi}^2}{R_{qi}^5} - \frac{1}{R_{qi}^3}\right) + \tilde{G}\sum_{\substack{j=1\\ j\neq i,q}}^{\mathcal{N}} M_j\left(\frac{3\left(y_{qj}-y_{qi}\right)^2}{|\boldsymbol{R}_{qj}-\boldsymbol{R}_{qi}|^5} - \frac{1}{|\boldsymbol{R}_{qj}-\boldsymbol{R}_{qi}|^3}\right) \tag{3.24}$$

$$U_{zz} = \tilde{G}M_i\left(\frac{3z_{qi}^2}{R_{qi}^5} - \frac{1}{R_{qi}^3}\right) + \tilde{G}\sum_{\substack{j=1\\ j\neq i,q}}^{\mathcal{N}} M_j\left(\frac{3\left(z_{qj}-z_{qi}\right)^2}{|\boldsymbol{R}_{qj}-\boldsymbol{R}_{qi}|^5} - \frac{1}{|\boldsymbol{R}_{qj}-\boldsymbol{R}_{qi}|^3}\right) \tag{3.25}$$

$$U_{xy} = \tilde{G}M_q\left(\frac{3x_{qi}y_{qi}}{\boldsymbol{R}_{qi}^5}\right) + \tilde{G}\sum_{\substack{j=1\\ j\neq i,q}}^{\mathcal{N}} M_j\left(\frac{3(x_{qj}-x_{qi})(y_{qj}-y_{qi})}{|\boldsymbol{R}_{qj}-\boldsymbol{R}_{qi}|^5}\right) = U_{yx} \tag{3.26}$$

$$U_{xz} = \tilde{G}M_q\left(\frac{3x_{qi}z_{qi}}{\boldsymbol{R}_{qi}^5}\right) + \tilde{G}\sum_{\substack{j=1\\ j\neq i,q}}^{\mathcal{N}} M_j\left(\frac{3(x_{qj}-x_{qi})(z_{qj}-z_{qi})}{|\boldsymbol{R}_{qj}-\boldsymbol{R}_{qi}|^5}\right) = U_{zx} \tag{3.27}$$

$$U_{yz} = \tilde{G}M_q\left(\frac{3y_{qi}z_{qi}}{\boldsymbol{R}_{qi}^5}\right) + \tilde{G}\sum_{\substack{j=1\\ j\neq i,q}}^{\mathcal{N}} M_j\left(\frac{3(y_{qj}-y_{qi})(z_{qj}-z_{qi})}{|\boldsymbol{R}_{qj}-\boldsymbol{R}_{qi}|^5}\right) = U_{zy} \tag{3.28}$$

Note that the expressions here are, for consistency with Equation (2.2), derived in terms of dimensional quantities. For numerical integration, the CR3BP characteristic quantities are leveraged to produce these expressions in terms of nondimensional values. Substituting these U_{ij} into Equation (3.22) yields the STM for the HFEM model.

3.2 Differential Corrections

A trajectory constructed in the baseline dynamical model does not always meet the desired criteria; differential corrections are then employed until the desired or specified characteristics are achieved. Relevant to this investigation is the application of a differential corrections strategy towards constructing periodic orbits in the CR3BP and for transition-

ing solutions from the CR3BP to the HFEM. This process is also termed a *targeting* problem, since the algorithm aims to *target* a desired solution.

In theory, the shooting method is simply a multi-dimensional version of a Newton-Raphson root solver. Many approaches exist for formulating a differential corrections algorithm; various types of implementation methods are also possible. The strategy detailed ahead is employed in this investigation. The initial step in formulating the differential corrections algorithm is the selection of the design variable and constraint vectors. These vectors are specific to the problem and the desired final state. In general, however, the design variable vector is represented by a vector $\boldsymbol{X}$ and takes the form,

$$\boldsymbol{X} = \begin{bmatrix} X_1 \\ X_2 \\ X_3 \\ \vdots \\ X_n \end{bmatrix} \tag{3.29}$$

where n is the number of free variables in the problem, and $\boldsymbol{X} \in \mathbb{R}^n$. These free variables are possibly position or velocity components, time along the trajectory, or in the case of HFEM, the epoch at points along the trajectory. The problem is subject to m constraints that together comprise the constraint vector, represented as $\boldsymbol{F}(\boldsymbol{X})$ and of the form,

$$\boldsymbol{F}(\boldsymbol{X}) = \begin{bmatrix} F_1(\boldsymbol{X}) \\ F_2(\boldsymbol{X}) \\ F_3(\boldsymbol{X}) \\ \vdots \\ F_m(\boldsymbol{X}) \end{bmatrix} \tag{3.30}$$

The goal of the differential corrections problem is to determine a design vector $\boldsymbol{X}^*$ such that,

$$\boldsymbol{F}(\boldsymbol{X}^*) = \boldsymbol{0}_{m\times 1} \tag{3.31}$$

An initial guess for the design variable vector, $\boldsymbol{X}_0$, is iterated until the desired $\boldsymbol{X}^*$ is achieved to some acceptable tolerance. In general, for any $\boldsymbol{X}^j$ representing the design variable vector at the j^{th} iteration of the corrections process, $\boldsymbol{F}(\boldsymbol{X}^{j+1})$ is approximated using a first-order Taylor series expansion as,

$$\boldsymbol{F}(\boldsymbol{X}^{j+1}) \approx \boldsymbol{F}(\boldsymbol{X}^j) + D\boldsymbol{F}(\boldsymbol{X}^j)(\boldsymbol{X}^{j+1} - \boldsymbol{X}^j) = \boldsymbol{0} \tag{3.32}$$

Here, $D\boldsymbol{F}(\boldsymbol{X}^j)$ is an $m \times n$ matrix of the partial derivatives of the constraints with respect to the free variables, and is evaluated at $\boldsymbol{X}^j$ as,

$$D\boldsymbol{F}(\boldsymbol{X}^j) = \frac{\partial \boldsymbol{F}}{\partial \boldsymbol{X}^j} = \begin{bmatrix} \frac{\partial F_1}{\partial X_1} & \frac{\partial F_1}{\partial X_2} & \cdots & \frac{\partial F_1}{\partial X_n} \\ \frac{\partial F_2}{\partial X_1} & \frac{\partial F_2}{\partial X_2} & \cdots & \frac{\partial F_2}{\partial X_n} \\ \vdots & \vdots & \ddots & \\ \frac{\partial F_m}{\partial X_1} & \frac{\partial F_m}{\partial X_2} & \cdots & \frac{\partial F_m}{\partial X_n} \end{bmatrix} \tag{3.33}$$

From Equations (3.31) and (3.32), an update equation to iteratively solve for $\boldsymbol{X}^j$ is formulated as,

$$\boldsymbol{F}(\boldsymbol{X}^j) + D\boldsymbol{F}(\boldsymbol{X}^j)(\boldsymbol{X}^{j+1} - \boldsymbol{X}^j) = \boldsymbol{0} \tag{3.34}$$

where, in general, $||\boldsymbol{F}(\boldsymbol{X}^{j+1})|| < ||\boldsymbol{F}(\boldsymbol{X}^j)||$. Equation (3.34) is iteratively solved for $\boldsymbol{X}^{j+1}$ until a certain tolerance ε is met, i.e.,

$$||\boldsymbol{F}(\boldsymbol{X}^{j+1})|| < \varepsilon \tag{3.35}$$

For this investigation, $\varepsilon = 1 \times 10^{-12}$ for most targeting problems. The update equation represented in Equation (3.34) takes different forms depending on the number of design variables, n, and the number of constraint equations in the problem, m [39]. Specifically, the following three cases arise:

1. $n = m$

   The number of free variables is equal to the number of constraints. Consequently, the matrix $D\boldsymbol{F}(\boldsymbol{X}^j)$ is a square matrix and is invertible. In general, only one solution exists that is produced by solving for $\boldsymbol{X}^{j+1}$ such that,

$$\boldsymbol{X}^{j+1} = \boldsymbol{X}^j - D\boldsymbol{F}(\boldsymbol{X}^j)^{-1}\boldsymbol{F}(\boldsymbol{X}^j) \tag{3.36}$$

2. $n > m$

   The number of free variables is greater than the number of constraints. As such, infinitely many solutions exist. One approach for producing a solution is the minimum norm approach, resulting in the following form of the update equation,

$$\boldsymbol{X}^{j+1} = \boldsymbol{X}^j - D\boldsymbol{F}(\boldsymbol{X}^j)^T \left[D\boldsymbol{F}(\boldsymbol{X}^j) \cdot D\boldsymbol{F}(\boldsymbol{X}^j)^T\right]^{-1} \boldsymbol{F}(\boldsymbol{X}^j) \tag{3.37}$$

3. $n < m$

   The number of free variables is less than the number of constraints. The system is, thus, overdetermined and no exact solutions exist. However, with the application of least squares, an approximate solution is produced,

$$\boldsymbol{X}^{j+1} = \boldsymbol{X}^j - \left[D\boldsymbol{F}(\boldsymbol{X}^j)^T \cdot D\boldsymbol{F}(\boldsymbol{X}^j)\right]^{-1} D\boldsymbol{F}(\boldsymbol{X}^j)^T \boldsymbol{F}(\boldsymbol{X}^j) \tag{3.38}$$

In solving these equations iteratively, issues of importance include the radius of convergence, the speed of convergence, and the efficiency of the process; the number of iterations for the solution to converge impacts the result significantly.

3.2.1 Single Shooting

One implementation of a targeting algorithm is the single shooting method, that involves correcting a single trajectory arc to reach a desired state. Single shooting algorithms are frequently employed to target any state or combination of states. To demonstrate the construction of solutions to targeting problems, an illustrative example is discussed that seeks

to propagate a spacecraft from a fixed initial position state to a final desired position over a fixed propagation time, allowing the initial velocity to vary. Figure 3.2 illustrates a schematic of the procedure, where a representative initial guess vector for the actual path appears in red, and the path that arrives at the targeted position, or the desired path, appears in black. This example assumes propagation in the Earth-Moon CR3BP dynamical model.

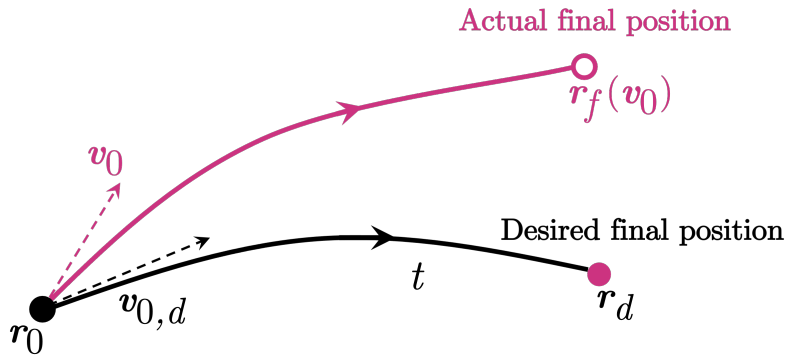

Figure 3.2. Representation of a single shooting scheme targeting a desired position.

As an example, the initial position is not allowed to vary. The initial state vector is then represented as $\boldsymbol{x} = [\boldsymbol{r}_0 \ \boldsymbol{v}_0]^T$, where $\boldsymbol{r}_0$ and $\boldsymbol{v}_0$ denote the initial position and the initial velocity vectors. Since the initial position is fixed, the design vector is of the form,

$$\boldsymbol{X} = \boldsymbol{v}_0 = \begin{bmatrix} \dot{x}_0 \\ \dot{y}_0 \\ \dot{z}_0 \end{bmatrix} \tag{3.39}$$

The goal of the problem, then, is to determine the $\boldsymbol{v}_0^d$, or the desired initial velocity that is necessary to achieve the desired position at the end of the propagation, $\boldsymbol{r}_d$. The constraint vector for this problem is constructed as,

$$\boldsymbol{F}(\boldsymbol{X}) = \boldsymbol{r}_d - \boldsymbol{r}_f(\boldsymbol{v}_0) = \begin{bmatrix} x_d - x_f(\boldsymbol{v}_0) \\ y_d - y_f(\boldsymbol{v}_0) \\ z_d - z_f(\boldsymbol{v}_0) \end{bmatrix} \tag{3.40}$$

where the subscript f represents the position at the end of the propagation, and the subscript d indicates the components of the desired final position. In this formulation, the Jacobian matrix $D\boldsymbol{F}(\boldsymbol{X})$ is a 3×3 matrix,

$$D\boldsymbol{F}(\boldsymbol{X}) = \frac{\partial \boldsymbol{F}}{\partial \boldsymbol{r}_f} \frac{\partial \boldsymbol{r}_f}{\partial \boldsymbol{v}_0} \tag{3.41}$$

$$= \begin{bmatrix} \frac{\partial(x_d - x_f(\boldsymbol{v}_0))}{\partial x_f} & \frac{\partial(x_d - x_f(\boldsymbol{v}_0))}{\partial y_f} & \frac{\partial(x_d - x_f(\boldsymbol{v}_0))}{\partial z_f} \\ \frac{\partial(y_d - y_f(\boldsymbol{v}_0))}{\partial x_f} & \frac{\partial(y_d - y_f(\boldsymbol{v}_0))}{\partial y_f} & \frac{\partial(y_d - y_f(\boldsymbol{v}_0))}{\partial z_f} \\ \frac{\partial(z_d - z_f(\boldsymbol{v}_0))}{\partial x_f} & \frac{\partial(z_d - z_f(\boldsymbol{v}_0))}{\partial y_f} & \frac{\partial(z_d - z_f(\boldsymbol{v}_0))}{\partial z_f} \end{bmatrix} \cdot \begin{bmatrix} \frac{\partial x_f}{\partial \dot{x}_0} & \frac{\partial x_f}{\partial \dot{y}_0} & \frac{\partial x_f}{\partial \dot{z}_0} \\ \frac{\partial y_f}{\partial \dot{x}_0} & \frac{\partial y_f}{\partial \dot{y}_0} & \frac{\partial y_f}{\partial \dot{z}_0} \\ \frac{\partial z_f}{\partial \dot{x}_0} & \frac{\partial z_f}{\partial \dot{y}_0} & \frac{\partial z_f}{\partial \dot{z}_0} \end{bmatrix} \tag{3.42}$$

Note that the first matrix in Equation (3.42) is simply $-I_{3\times3}$. In terms of the elements of the STM, the Jacobian matrix for this problem is, thus, rewritten as,

$$D\boldsymbol{F}(\boldsymbol{X}) = -\begin{bmatrix} \Phi_{14} & \Phi_{15} & \Phi_{16} \\ \Phi_{24} & \Phi_{25} & \Phi_{26} \\ \Phi_{34} & \Phi_{35} & \Phi_{36} \end{bmatrix} \tag{3.43}$$

Since the number of design variables is equal to the number of constraints in this problem, the update equation in Equation (3.36) is employed until $\boldsymbol{F}(\boldsymbol{X}^*) = \boldsymbol{0}$. The resulting $\boldsymbol{X}^*$ supplies the initial velocity that, at the end of the propagation, converges to the desired final position.

3.2.2 Multiple Shooting

While the single shooting process is relatively straightforward to implement, there are inherent limitations that render it unsuitable for various applications. For instance, when the problem entails long times of flight and passage through numerically sensitive dynamical regions, it is advantageous to utilize multiple short arcs that distribute the sensitivities among various points along the targeted solution [40]. Figure 3.3 illustrates a general multiple shooting problem formulation. In contrast to the single shooting formulation, multiple nodes,

or patch points, comprise the approximate solution prior to the corrections process. This approximate solution is typically described by a set of n discrete points, $\boldsymbol{x}_i$, for $i = 1, 2, ..., n$, where the propagation time between each point is denoted as t_i. Together, these points constitute $n - 1$ arcs that represent the approximate solution. In general, regardless of the dynamical model, numerical propagation from each $\boldsymbol{x}_i$ for its respective t_i does not coincide with the subsequent patch point, as illustrated in Figure 3.3. In terms of the states themselves, this fact is represented as,

$$\boldsymbol{x}_i^f \neq \boldsymbol{x}_{i+1} \quad \text{for} \quad i = 1, 2, ..., n-1 \tag{3.44}$$

As such, the goal of the multiple shooting scheme is to determine the new set of discrete points that, when propagated, together form a continuous trajectory, i.e., $\boldsymbol{x}_i^f = \boldsymbol{x}_{i+1}$. While this general scheme represented in Figure 3.3 only reflects continuity in the state components, continuity in other parameters (such as epoch in the HFEM) is also likely to be desired as well.

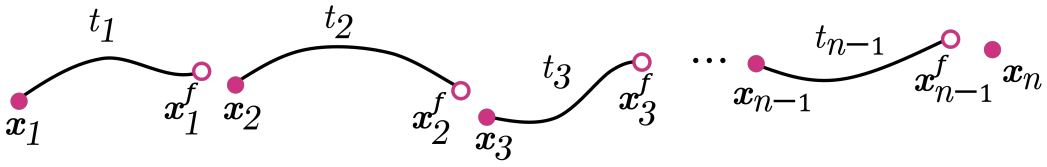

Figure 3.3. Representation of a general multiple shooting scheme prior to corrections.

As an illustrative example, consider the case where $t_1 = t_2 = ... = t_{n-1} = t$. For this fixed time multiple shooting scenario, the design vector is sized as $6n \times 1$, such that,

$$\boldsymbol{X} = \begin{bmatrix} \boldsymbol{x}_1 \\ \boldsymbol{x}_2 \\ \vdots \\ \boldsymbol{x}_n \end{bmatrix} \tag{3.45}$$

This general formulation assumes that the position and velocity components of all patch points are allowed to vary. For this problem, the constraint vector is constructed to ensure full state continuity between the internal patch points. As such, the vector size is $6(n-1)\times 1$ and appears as,

$$\boldsymbol{F}(\boldsymbol{X}) = \begin{bmatrix} \boldsymbol{x}_1^f - \boldsymbol{x}_2 \\ \boldsymbol{x}_2^f - \boldsymbol{x}_3 \\ \vdots \\ \boldsymbol{x}_{n-1}^f - \boldsymbol{x}_n \end{bmatrix} \tag{3.46}$$

The general goal for the problem is consistent with the single shooting scheme, i.e., to determine the $\boldsymbol{X}^*$ such that $\boldsymbol{F}(\boldsymbol{X}^*) = \boldsymbol{0}$ to the desired tolerance. The Jacobian matrix for this problem is now sized $6(n-1)\times 6n$ and is constructed as,

$$D\boldsymbol{F}(\boldsymbol{X}) = \begin{bmatrix} \dfrac{\partial(\boldsymbol{x}_1^f - \boldsymbol{x}_2)}{\partial \boldsymbol{x}_1} & \dfrac{\partial(\boldsymbol{x}_1^f - \boldsymbol{x}_2)}{\partial \boldsymbol{x}_2} & \cdots & \dfrac{\partial(\boldsymbol{x}_1^f - \boldsymbol{x}_2)}{\partial \boldsymbol{x}_n} \\ \dfrac{\partial(\boldsymbol{x}_2^f - \boldsymbol{x}_3)}{\partial \boldsymbol{x}_1} & \dfrac{\partial(\boldsymbol{x}_2^f - \boldsymbol{x}_3)}{\partial \boldsymbol{x}_2} & \cdots & \dfrac{\partial(\boldsymbol{x}_2^f - \boldsymbol{x}_3)}{\partial \boldsymbol{x}_n} \\ \vdots & \vdots & \ddots & \vdots \\ \dfrac{\partial(\boldsymbol{x}_{n-1}^f - \boldsymbol{x}_n)}{\partial \boldsymbol{x}_1} & \dfrac{\partial(\boldsymbol{x}_{n-1}^f - \boldsymbol{x}_n)}{\partial \boldsymbol{x}_2} & \cdots & \dfrac{\partial(\boldsymbol{x}_{n-1}^f - \boldsymbol{x}_n)}{\partial \boldsymbol{x}_n} \end{bmatrix} \tag{3.47}$$

Note that $\dfrac{\partial(-\boldsymbol{x}_i)}{\partial \boldsymbol{x}_i} = -I_{6\times 6}$. Additionally, $\dfrac{\partial \boldsymbol{x}_i^f}{\partial \boldsymbol{x}_i}$ is simply the STM at the end of the propagation of each arc. The remaining elements of the Jacobian matrix are all zero. Thus, Equation (3.47) reduces to,

$$D\boldsymbol{F}(\boldsymbol{X}) = \begin{bmatrix} \dfrac{\partial \boldsymbol{x}_1^f}{\partial \boldsymbol{x}_1} & -I_{6\times 6} & \mathbf{0}_{6\times 6} & \cdots & \mathbf{0}_{6\times 6} & \mathbf{0}_{6\times 6} \\ \mathbf{0}_{6\times 6} & \dfrac{\partial \boldsymbol{x}_2^f}{\partial \boldsymbol{x}_2} & -I_{6\times 6} & \cdots & \mathbf{0}_{6\times 6} & \mathbf{0}_{6\times 6} \\ \vdots & \vdots & \vdots & \ddots & \vdots & \vdots \\ \mathbf{0}_{6\times 6} & \mathbf{0}_{6\times 6} & \mathbf{0}_{6\times 6} & \cdots & \dfrac{\partial \boldsymbol{x}_{n-1}^f}{\partial \boldsymbol{x}_{n-1}} & -I_{6\times 6} \end{bmatrix} \tag{3.48}$$

Then, since the number of free variables is more than the number of constraints, Equation (3.37) is used here to iteratively compute the minimum norm solution. Multiple shooting schemes are employed in the construction of various trajectories in the CR3BP. In this investigation, multiple shooting algorithms are leveraged to transition solutions from the CR3BP to the HFEM.

3.3 Periodic Orbits

In addition to the equilibrium solutions (i.e., the libration points), another fundamental type of behavior that arises in the CR3BP is an infinite variety of periodic motion. Specifically, there exist periodic orbits that traverse the vicinity of all the libration points, as well as orbits in the neighborhoods of the two primaries in the rotating frame. However, simple numerical integration of initial conditions may not yield solutions that are perfectly periodic. Given an initial guess for a solution that is reasonably close to the desired solution, targeting algorithms are employed to modify the initial conditions to achieve periodic solutions in the CR3BP. An initial guess for a periodic orbit in the CR3BP is typically constructed from i) a linear approximation of periodic behavior near the libration points, ii) primary-centered two-body orbits, or iii) existing periodic solutions in the CR3BP.

As a representative example, the construction of a planar periodic solution about the L_1 libration point is introduced. These planar solutions, that exist in the vicinity of the collinear libration points (i.e., L_1, L_2, and L_3), are termed Lyapunov orbits, and are symmetric across the $\hat{\boldsymbol{x}}$-axis in the Earth-Moon rotating frame. Leveraging this symmetry, let the initial state vector for this orbit lie along the $\hat{\boldsymbol{x}}$-axis and be defined as,

$$\boldsymbol{x}_0 = [x_0 \;\; 0 \;\; 0 \;\; 0 \;\; \dot{y}_0 \;\; 0]^T \tag{3.49}$$

where the $\hat{\boldsymbol{z}}$-components of position and velocity are zero in this planar case. Given that the velocity along the $\hat{\boldsymbol{x}}$-direction is zero (i.e., $\dot{x}_0 = 0$), and that the point lies along the $\hat{\boldsymbol{x}}$-axis (i.e., $y_0 = 0$), Equation (3.49) indicates a perpendicular crossing of the $\hat{\boldsymbol{x}}$-axis. Then, the application of the Mirror theorem permits corrections that yield a symmetric periodic orbit. This theorem, proposed and proved by Roy and Ovenden in 1955, states that if $\mathcal{N}$-point masses are moving under their mutual gravitational forces, their orbits are periodic if, at two separate epochs, a mirror configuration occurs [41]. Thus, with the initial point along the orbit restricted to lie at one of the perpendicular crossings, the initial guess in Equation (3.49) need only be integrated for half the orbit period, i.e., until the next perpendicular crossing of the $\hat{\boldsymbol{x}}$-axis. In one implementation of this symmetric periodic orbit targeting scheme, the design and constraint vectors are formulated as,

$$\boldsymbol{X} = \begin{bmatrix} \dot{y}_0 \\ t \end{bmatrix} \tag{3.50}$$

$$\boldsymbol{F}(\boldsymbol{X}) = \begin{bmatrix} \dot{x}_f \\ y_f \end{bmatrix} \tag{3.51}$$

where t is the nondimensional propagation time. Equation (3.51) represents targeting a perpendicular crossing, i.e., for the final, converged $\boldsymbol{X}^*$, $\boldsymbol{F}(\boldsymbol{X}^*) = \boldsymbol{0}$. The Jacobian matrix for this problem is,

$$D\boldsymbol{F}(\boldsymbol{X}) = \begin{bmatrix} \dfrac{\partial \dot{x}_f}{\partial \dot{y}_0} & \dfrac{\partial \dot{x}_f}{\partial t} \\ \dfrac{\partial y_f}{\partial \dot{y}_0} & \dfrac{\partial y_f}{\partial t} \end{bmatrix} = \begin{bmatrix} \Phi_{45} & \ddot{x}_f \\ \Phi_{25} & \dot{y}_f \end{bmatrix} \tag{3.52}$$

where Φ_{ij} represents the $(i,j)^{th}$ element of the STM at the end of the propagation, and $\ddot{x}_f$ and $\dot{y}_f$ are the time derivatives at the final time. Equation (3.36) is then employed to iteratively solve for the design variables, since the number of constraints and design variables is equal. Figure 3.4 illustrates the corrected L_1 Lyapunov orbit in red, along with the initial guess arc plotted in black. Note the two perpendicular crossings of the $\hat{\boldsymbol{x}}$-axis for the corrected solution, whereas the initial guess does not intersect the $\hat{\boldsymbol{x}}$-axis perpendicularly at the end of the propagation. While only half of the corrected orbit appears in Figure 3.4, reflection of the states across the $\hat{\boldsymbol{x}}$-axis yields the complete planar periodic solution. It is noted that the targeting scheme implemented here is representative of a general methodology for the computation of periodic solutions. Typically, the construction of Lyapunov orbits is achieved by simpler implementations that directly leverage the perpendicular crossings. In such cases, recognizing the functional dependencies of the state components at the location of the perpendicular crossing reduces the number of free variables and constraints in the problem to one each. As a result, only the necessary free variables and constraint equations are included, alleviating any numerical issues that may arise under more complex implementations.

3.4 Continuation Schemes

The existence of a single periodic orbit as an isolated trajectory is not as insightful or useful towards trajectory design as a group of orbits with similar characteristics or geometries. Poincaré states that, in the CR3BP, the computation of a single periodic orbit potentially leads to the determination of a set of periodic orbits, typically denoted a *family* [42]. The

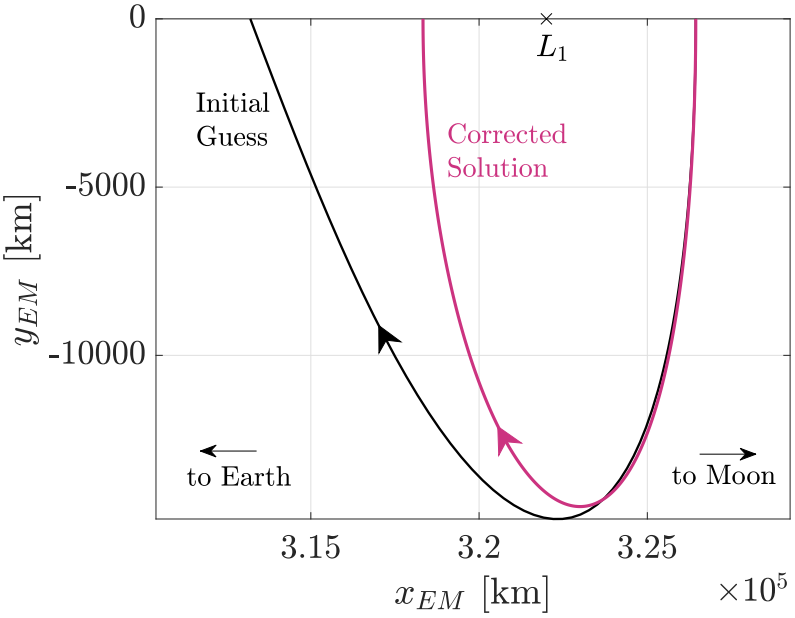

Figure 3.4. Computation of an L_1 Lyapunov orbit through a perpendicular crossing targeter in the Earth-Moon system.

process of continuation to produce a family of orbits offers valuable insight into the evolution of stability and energy characteristics across the orbits. Two continuation schemes that are utilized to compute orbit families in the CR3BP are introduced here. It is important to note that the continuation schemes represent numerical processes that support dynamical investigations. To avoid introducing numerical challenges that hinder dynamical insights, the simplest numerical approach available is always employed. While each continuation strategy offers advantages and disadvantages, no one scheme is superior, and the ability to discern the best approach for a given scenario is key.

3.4.1 Natural Parameter Continuation

Natural parameter continuation leverages the knowledge of physical parameters associated with previously converged solutions to produce a family of similar solutions. These physical parameters may be components of position or velocity, the Jacobi constant value, or the time of flight (period) of a solution. In general, a sufficiently small perturbation ap-

plied to the initial state of a converged solution along one parameter yields the initial guess for differential corrections of subsequent solutions. The initial conditions corresponding to each member of a family of periodic orbits seed the initial guess for each subsequent orbit. Iterative application of this process, thus, yields a family of topologically-related solutions.

For instance, examine the L_1 Lyapunov orbit represented in Figure 3.4. Selecting the initial x position as the natural parameter of interest, a sufficiently small perturbation in x_0 is applied to determine the next member in the family of L_1 Lyapunov orbits. Representative members of the L_1 Lyapunov family are illustrated in Figure 3.5, with the color scheme corresponding to the value of Jacobi constant for each orbit. The collinear libration points are indicated by the black x-markers along the $\hat{\boldsymbol{x}}$-axis. Natural parameter continuation is generally effective in the computation of families, given that the continuation parameter evolves monotonically along the family. For more complex scenarios, it may be necessary to continue along a different physical parameter to avoid missing orbits within a family due to lack of convergence.

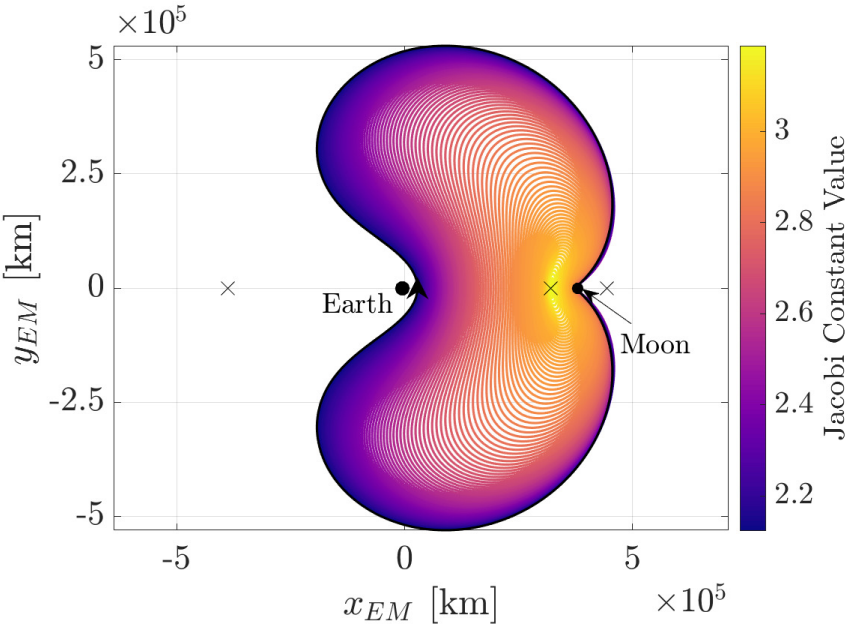

Figure 3.5. Family of L_1 Lyapunov orbits constructed in the Earth-Moon CR3BP via natural parameter continuation.

3.4.2 Pseudo-Arclength Continuation

Pseudo-arclength continuation is an alternative continuation scheme that is particularly useful when the physical parameters along an orbit family do not evolve monotonically, or in cases when the shape of the family is unknown. While still employing prior converged solutions to seed subsequent initial guesses, the fundamental difference in this approach arises in the step direction: rather than stepping along a physical parameter, psuedo-arclength schemes step along the direction tangent to the family [43]. Let $\boldsymbol{X}^*_{j-1}$ represent the $n \times 1$ design vector for a previously converged solution, where, for an $m \times 1$ constraint vector, $\boldsymbol{F}(\boldsymbol{X}^*_{j-1}) = \boldsymbol{0}$. The $m \times n$ Jacobian matrix, $D\boldsymbol{F}(\boldsymbol{X}^*_{j-1})$, possesses a one-dimensional null space when $n - m = 1$, that is,

$$\Delta \boldsymbol{X}^*_{j-1} = \text{null}(D\boldsymbol{F}(\boldsymbol{X}^*_{j-1})) \tag{3.53}$$

This vector dictates the direction of continuation to construct the subsequent solution. The design or free variable vector for the next (j^{th}) orbit is, thus, computed as,

$$\boldsymbol{X}_j = \boldsymbol{X}^*_{j-1} + s\Delta \boldsymbol{X}^*_{j-1} \tag{3.54}$$

where s denotes the step size along the family tangent vector. The implementation of this continuation scheme adds the following scalar constraint to the targeting problem,

$$F_{\text{PAC}}(\boldsymbol{X}_j) = (\boldsymbol{X}_j - \boldsymbol{X}^*_{j-1})^T \cdot \Delta \boldsymbol{X}^*_{j-1} - s \tag{3.55}$$

Equation (3.55) is appended to the original constraint vector, $\boldsymbol{F}(\boldsymbol{X}_j)$ to yield the new, augmented constraint vector,

$$\boldsymbol{G}(\boldsymbol{X}_j) = \begin{bmatrix} \boldsymbol{F}(\boldsymbol{X}_j) \\ F_{\text{PAC}}(\boldsymbol{X}_j) \end{bmatrix} \tag{3.56}$$

To accommodate the additional constraint, the Jacobian matrix for this scheme is also appended with the partial derivative $\frac{\partial F_{\text{PAC}}}{\partial \boldsymbol{X}_j}$. The resulting augmented Jacobian matrix is of the form,

$$D\boldsymbol{G}(\boldsymbol{X}_j) = \frac{\partial \boldsymbol{G}(\boldsymbol{X}_j)}{\partial \boldsymbol{X}_j} = \begin{bmatrix} D\boldsymbol{F}(\boldsymbol{X}_j) \\ \Delta \boldsymbol{X}_{j-1}^{*T} \end{bmatrix} \tag{3.57}$$

This augmented Jacobian is an $n \times n$ square matrix. A simple, iterative update equation yields the desired $\boldsymbol{X}_j^*$ such that $\boldsymbol{G}(\boldsymbol{X}_j^*) = \boldsymbol{0}$. As an example, members from the family of the L_2 Lyapunov orbits are obtained using pseudo-arclength continuation and appear in Figure 3.6. The orbits are colored by their Jacobi constant value. While natural parameter continuation suffices for most orbits considered in this investigation, the merits of pseudo-arclength continuation are recognized for complex geometries or non-monotonic evolution of physical parameters along an orbit family.

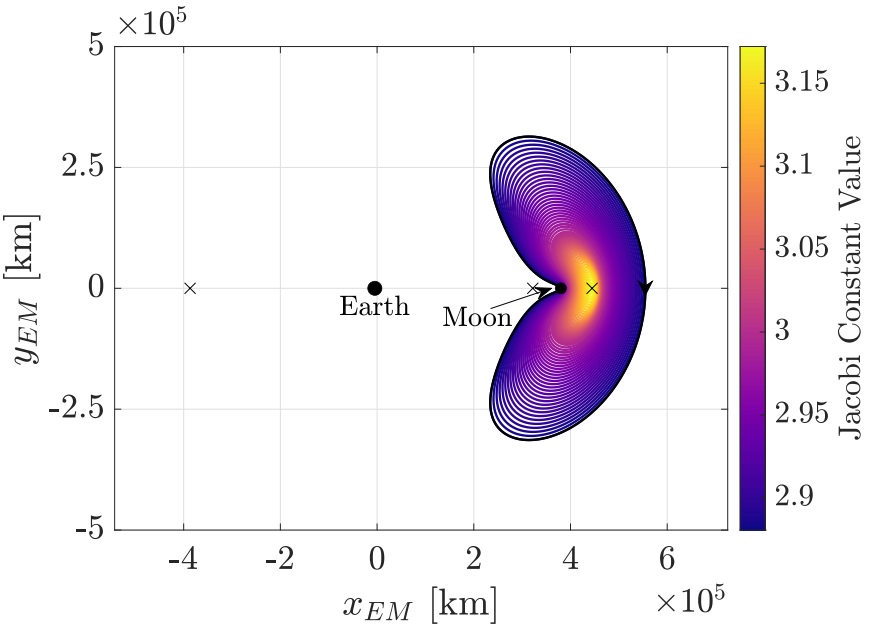

Figure 3.6. Family of L_2 Lyapunov orbits constructed in the Earth-Moon CR3BP via pseudo-arclength continuation.

3.5 Stability of Periodic Orbits

With the availability of periodic orbits in the CR3BP, the next step is an understanding of the behavior of these orbits to leverage their characteristics towards spacecraft trajectory design. One variable that offers useful insight is the linear stability of a periodic orbit and its evolution across a family. The linear stability for a periodic orbit is associated with its Φ, and the assessment of the elements that change along an orbit. Thus, it is necessary to investigate the properties of the full cycle STM, that is, the STM at precisely one full period along an orbit, also termed the *monodromy matrix*. For an orbit of precise period $\mathbb{T}$, the monodromy matrix is represented as $\Phi(\mathbb{T}, 0)$ or $\Phi(\mathbb{T} + t_0, t_0)$. The matrix is constructed originating from any point along an orbit. The six eigenvalues from the monodromy matrix, λ_j, possess a constant value along the orbit. Additionally, since the CR3BP is a time-invariant system, Lyapunov's theorem applies [44]. Thus, for any periodic orbit, if λ_j is an eigenvalue of the monodromy matrix, λ_j^{-1} is also an eigenvalue. Owing to the periodic nature of the orbit, at least one eigenvalue from the monodromy matrix is equal to one. Because of their existence in reciprocal pairs, it is apparent that at least two eigenvalues of a periodic orbit are equal to unity. This pair of eigenvalues is also identified as the trivial pair. Since the monodromy matrix is real, if any of the four remaining eigenvalues are complex, they occur in complex conjugate pairs, represented as $\lambda_j = a \pm bi$. If the magnitude of the real part of such eigenvalues is greater than one, the resulting solution is linearly unstable; if the magnitude of the real part is less than or equal to one, the resulting solution is linearly stable. Solely imaginary eigenvalues of the form $\lambda_j = \pm bi$ correspond to oscillatory motion, and the solution neither grows or decays over time [45]. In summary, the following three cases occur that determine the linear stability of a periodic orbit in the CR3BP:

- **Unstable Eigenvalues**: If $|\lambda_j| > 1$, then the eigenvalue is linearly unstable, and the periodic orbit is defined as unstable. These eigenvalues lie beyond the unit circle, and any perturbation along the orbit grows with time.
- **Stable Eigenvalues**: If $|\lambda_j| < 1$, then the eigenvalue is linearly stable. These eigenvalues lie within the unit circle.

- **Marginally Stable Eigenvalues**: If $|\lambda_j| = 1$, then the eigenvalue is marginally stable. These eigenvalues lie on the unit circle.

Note that the existence of even one unstable eigenvalue renders the orbit unstable. For stability, however, all eigenvalues of the monodromy matrix are required to be stable. Nonetheless, due to the reciprocal nature of eigenvalues in the CR3BP, the existence of a stable eigenvalue guarantees the existence of a corresponding unstable eigenvalue. Therefore, only unstable and marginally stable orbits – those with all eigenvalues equal to one – exist in the CR3BP.

3.5.1 Stability Index

One useful measure for the stability of an orbit is the *stability index*, ν_j, that is a function of the eigenvalues of the monodromy matrix, λ_j [46], [47]. For any periodic orbit, the value of ν_j is evaluated as,

$$\nu_j = \frac{1}{2}\left(||\lambda_j|| + \frac{1}{||\lambda_j||}\right) \tag{3.58}$$

Due to the reciprocal pairs of eigenvalues in the CR3BP, each periodic orbit is characterized by three unique stability indices. Owing to the unity pair of eigenvalues, at least one stability index for all periodic orbits in the CR3BP equals unity. If any of the remaining two stability indices are greater than unity, the orbit is unstable in a linear sense. Conversely, if the values of all three stability indices are less than or equal to unity, the orbit is linearly stable. The magnitude of the stability index itself informs the evolution of the stability properties for an orbit, where larger magnitudes indicate faster departure from the vicinity of the baseline orbit.

3.6 Periodic Orbit Bifurcations

Analyzing the stability for a family of periodic orbits leads to the concept of *bifurcations* and *bifurcating orbits*. By definition, a bifurcation occurs when there is a change in the form or character of the stability across a family [45], [48]. For instance, such changes occur when the stable or marginally stable eigenvalues of a periodic orbit cross the unit circle, causing the

corresponding eigenvalues of orbits further along the family to become unstable. Qualitative changes such as these result in the formation of bifurcating orbits, possibly signaling new families of periodic solutions or, in some cases, delivering the end of a family of solutions. When a new family arises as a consequence of a bifurcation, the bifurcating orbit is common to both families. There are three ways in which a change in the stability properties of a family of periodic orbits signals the occurrence of a bifurcation [49]:

- **Tangent Bifurcation:** A pair of eigenvalues moves along the unit circle and collides at the value +1 on the real axis, and then continues to the real axis, as illustrated in Figure 3.7(a). When a tangent bifurcation occurs at an extremum of the Jacobi constant value along a family, it does not result in the formation of a new family of periodic solutions. Such bifurcations are denoted *cyclic folds*.
- **Period Doubling Bifurcation:** A pair of eigenvalues moves along the unit circle and collides at the value -1 on the real axis; then the eigenvalues shift to the real axis, as illustrated in Figure 3.7(b).
- **Secondary Hopf Bifurcation:** Two pairs of eigenvalues collide on the unit circle, but off the real axis, and split into the complex plane, as illustrated in Figure 3.7(c).

By investigating the eigenvalues from the monodromy matrix for various orbits along a family, bifurcations are frequently identified. In this investigation, tangent and period doubling bifurcations are explored to yield additional families of periodic orbits in the Earth-Moon CR3BP.

3.7 Invariant Manifold Theory

Much insight emerges when solutions to differential equations are explored via both classical analysis techniques and a global geometric approach. The former involves analyzing individual trajectories and their properties, while the latter approach is based in the phase space of a dynamical system and involves understanding the global behavior of the flow. The structure and geometry of the phase space is investigated by exploring periodic solutions as well as the local flow associated with these particular solutions [50]. The knowledge of the

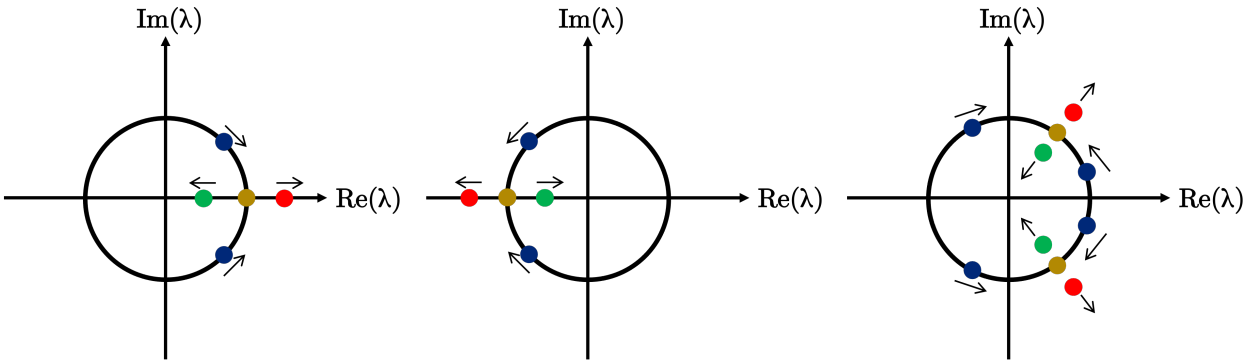

(a) Tangent bifurcation (b) Period-doubling bifurcation (c) Secondary Hopf bifurcation

Figure 3.7. Change in eigenvalue structure associated with each type of bifurcation [48].

flow structure is frequently leveraged towards trajectory design, especially involving transfers between unstable orbits [51], [52]. The following section introduces the methodology to compute stable and unstable manifolds for periodic orbits.

3.7.1 Manifolds for Periodic Orbits

Invariant manifolds corresponding to an unstable periodic orbit are constructed by discretizing the orbit into a specified number of *fixed points*, represented by $\boldsymbol{x}^*$. Recall from Section 3.5 that the eigenvalues of the monodromy matrix, as computed at any fixed point along a periodic orbit, remain precisely the same along the orbit. The eigenvectors, however, corresponding to each point on the orbit reflect the natural flow near that specific fixed point and, thus, vary along the orbit. Therefore, the eigenvectors are determined along various fixed points on the orbit to accurately compute the associated manifolds. Let λ_S and $\lambda_U = \frac{1}{\lambda_S}$ denote one pair of the stable and unstable eigenvalues of the periodic orbit. The components of their corresponding eigenvectors, $\boldsymbol{v}_S$ and $\boldsymbol{v}_U$, are decomposed as,

$$\boldsymbol{v}_S = [x_S \quad y_S \quad z_S \quad \dot{x}_S \quad \dot{y}_S \quad \dot{z}_S]^T \tag{3.59}$$

$$\boldsymbol{v}_U = [x_U \quad y_U \quad z_U \quad \dot{x}_U \quad \dot{y}_U \quad \dot{z}_U]^T \tag{3.60}$$

The eigenvectors are normalized in terms of three position components, three velocity components, or the full six element state. Normalization along the position components allows

the physical characterization of the states, and is the selected strategy for normalization in this investigation. Then, the normalized states of the stable and unstable eigenvectors are evaluated as,

$$\boldsymbol{v}^{W^S} = \frac{\boldsymbol{v}_S}{\sqrt{x_S^2 + y_S^2 + z_S^2}} \tag{3.61}$$

$$\boldsymbol{v}^{W^U} = \frac{\boldsymbol{v}_U}{\sqrt{x_U^2 + y_U^2 + z_U^2}} \tag{3.62}$$

A point on a half-manifold is located by stepping off a fixed point along the direction of the stable and unstable eigenvectors. The positive half branch of the stable manifold, W^{S+}, departs the fixed point along the positive direction of the stable eigenvector, $\boldsymbol{v}_S$, while the negative half branch, W^{S-}, departs along the negative direction of the stable eigenvector, $-\boldsymbol{v}_S$. Similarly, the positive half branch of the unstable manifold, W^{U+}, departs along the positive direction of the unstable eigenvector, $\boldsymbol{v}_U$, while the negative half branch, W^{U-}, departs along the negative direction of the unstable eigenvector, $-\boldsymbol{v}_U$. A nondimensional perturbation, denoted by d, is introduced relative to the fixed point in the direction of the eigenvectors. The selection for the value of d is crucial: if the value of d is too large, the resulting point might not lie on the manifold itself; if the value is too small, the trajectory remains in the vicinity of the fixed point for a longer time, leading to little progress along the manifold trajectory and the accumulation of numerical integration error. Once an appropriate value of d is selected, the point on the local stable and unstable half-manifolds is evaluated as,

$$\boldsymbol{x}_{S_\pm} = \boldsymbol{x}^* \pm d \cdot \boldsymbol{v}^{W^S} \tag{3.63}$$

$$\boldsymbol{x}_{U_\pm} = \boldsymbol{x}^* \pm d \cdot \boldsymbol{v}^{W^U} \tag{3.64}$$

where $\pm$ corresponds to the positive and negative directions along each manifold. This process is repeated for each fixed point along the periodic orbit to produce trajectories that lie on its stable and unstable manifolds. Trajectories that lie on the true stable manifold

asymptotically approach the orbit in time, while trajectories on the actual unstable manifold asymptotically depart the orbit when propagated forwards in time.

The construction of periodic orbit manifolds is illustrated within the context of an L_2 Lyapunov orbit in the Earth-Moon system represented in Figure 3.8. The orbit, plotted in black, is discretized into 50 fixed points spaced evenly in time, and a step-off distance of $d = 40\ km$ is selected. Trajectories that lie on the negative stable/unstable half-manifolds appear in light blue/red, while those on the positive stable/unstable half-manifolds appear in dark blue/red. Together, the stable manifold trajectories comprise the stable manifold surface, while the set of unstable manifold trajectories comprise the unstable manifold surface of the periodic orbit. Visualizing the projection of the manifolds onto the configuration space aids in the identification of trajectories that naturally approach and depart the orbit in time. While the trajectories in Figure 3.8 appear to remain in the vicinity of the orbit for the selected propagation time, longer propagation intervals reflect more complex geometries that are difficult to assess solely by their projection in configuration space. As such, other tools for analyzing flow behavior to identify useful characteristics are explored.

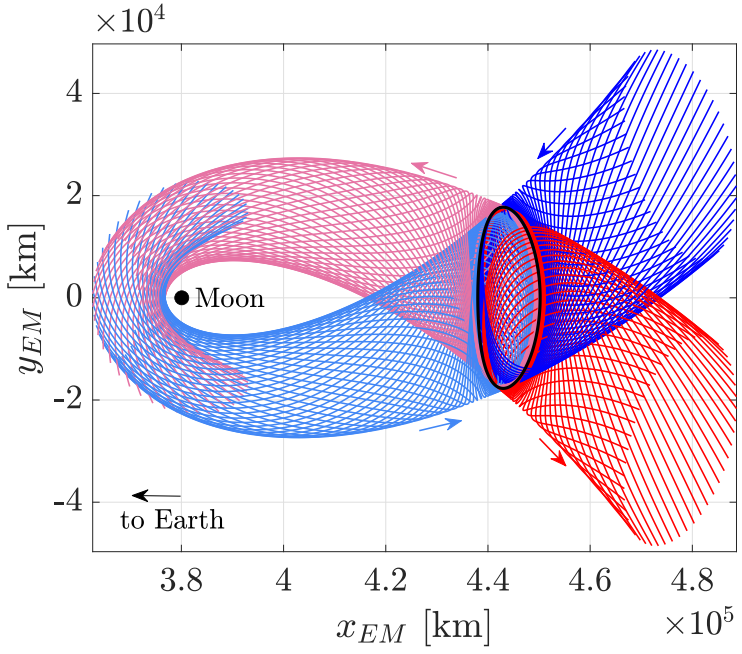

Figure 3.8. Trajectories on the stable (blue) and unstable (red) manifold for an L_2 Lyapunov orbit in the Earth-Moon CR3BP.

3.8 Poincaré Maps

Poincaré sections or maps are a valuable tool to represent systems of differential equations as maps, a concept first utilized by Henri Poincaré in his analysis of the CR3BP [42]. Exploiting maps to understand chaos is quite effective with extensive development in the last few decades. This type of formulation allows a continuous time system (flow) to be reduced to the examination of an associated discrete time system (map). The advantages of the technique include:

- **Reduction of dimension**: The construction of a Poincaré map eliminates at least one variable in the problem, reducing the study to a lower dimensional system.
- **Understanding of global dynamics**: In a lower dimensional analysis, Poincaré maps offer insight into the global dynamics of a system, often highlighting trends that might not otherwise be apparent.
- **Conceptual clarity**: Concepts that are otherwise too complex to interpret in terms of ordinary differential equations are concisely stated for the corresponding Poincaré map.

Within the context of the CR3BP, Poincaré mapping techniques are leveraged in the investigation to exploit other dynamical structures within the vicinity of various periodic orbits. To construct a Poincaré map for a trajectory in the CR3BP, an $(n-1)$ dimensional hyperplane, denoted Σ, is defined such that the flow is transverse to the hyperplane, i.e., the trajectory possesses some component normal to the plane. The hyperplane Σ is defined after specific time intervals, or after specific geometries.

Consider a periodic orbit Γ, and let $\boldsymbol{x}^*$ be a state along the orbit. The hyperplane Σ is transverse to Γ at $\boldsymbol{x}^*$. A trajectory through $\boldsymbol{x}^*$ crosses Σ at $\boldsymbol{x}^*$ in time $\mathbb{T}$, where $\mathbb{T}$ is the period of the orbit. Trajectories that originate on Σ in a sufficiently small neighborhood of $\boldsymbol{x}^*$ intersect Σ in the vicinity of $\boldsymbol{x}^*$ in approximately the time $\mathbb{T}$. In general, a state $\boldsymbol{x}$ is evolved through the flow until it crosses the hyperplane and returns to the map at $P(\boldsymbol{x})$, where $P(\cdot)$ represents the Poincaré map for the system. Figure 3.9 illustrates a Poincaré map, where the hyperplane appears in pink and is denoted Σ. The periodic orbit, Γ, originates at $\boldsymbol{x}^*$ on

the map and returns to the exact same point after precisely one period; as such, periodic orbits are aptly denoted as fixed points within the context of a Poincaré map. In contrast, when a second point $\boldsymbol{x}$ that lies near the fixed point is propagated for precisely one period, the return to the map is recorded at a different location, denoted $P(\boldsymbol{x})$ in Figure 3.9.

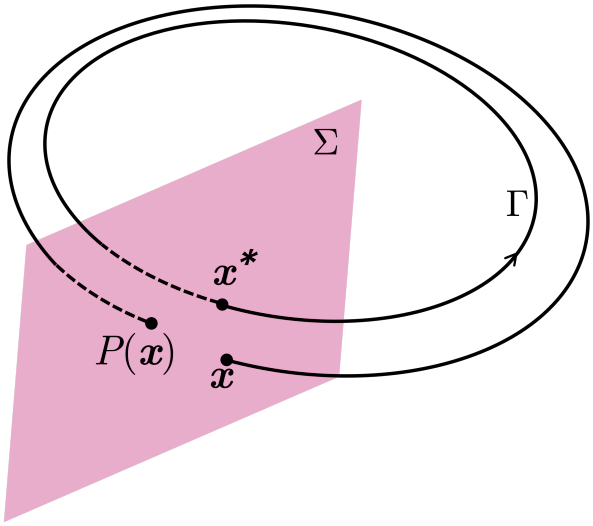

Figure 3.9. Representation of a Poincaré map with the representative hyperplane Σ.

Poincaré maps are particularly useful for understanding the stability of periodic solutions in the CR3BP. The stability properties associated with a fixed point on a Poincaré map are correlated with the stability of the periodic orbit. For a fixed point $\boldsymbol{x}^*$ on a hyperplane Σ, consider an initial state $\boldsymbol{x}_0$ in the vicinity of the fixed point. The initial state is propagated numerically for a given time interval, and its intersections with the hyperplane are recorded as $P_1(\boldsymbol{x}_0)$, $P_2(\boldsymbol{x}_0)$, and so on, until the last return $P_n(\boldsymbol{x}_0)$. If subsequent returns to the map approach the fixed point $\boldsymbol{x}^*$ on the hyperplane, the orbit is considered 'stable'. If the returns appear to diverge from the fixed point, the periodic orbit is unstable. If the returns to the map are disordered, the orbit is considered to be chaotic. The first case corresponds to stable manifolds associated with the fixed point, while the second case is representative of unstable manifold returns.

Recall the invariant manifolds for the L_2 Lyapunov orbit illustrated in Figure 3.8. To visualize dynamical behavior near the orbit for longer propagation times, a Poincaré map is

constructed. For this planar orbit in $\mathbb{R}^4$, a geometric hyperplane Σ is defined by fixing one of the four coordinates, reducing the problem to a surface in $\mathbb{R}^3$. In this case, Σ is defined to be $y = 0$, or intersections with the $\hat{\boldsymbol{x}}$-axis. The local stable and unstable manifolds constructed from fixed points along the periodic orbit are propagated numerically for approximately 10.15 nd (45 $days$), or 3 periods of the orbit. Any intersections with the hyperplane of the global stable and unstable manifolds are recorded. As an example, the values of x and $\dot{x}$ at each intersection are used to visualize the returns to the map, but other variables may also be employed. Note that the Jacobi constant value for this map is fixed. As such, the remaining unknown state component, $\dot{y}$, for each trajectory represented on the map may be recovered to obtain the full state vector. Figure 3.10 illustrates the resulting Poincaré map, zoomed-in near the location of the orbit, where each point on the map corresponds to a return. The blue points are associated to returns of the stable manifold trajectories, while the red points correspond to returns of unstable manifold trajectories. To obtain more returns to the map, the manifold trajectories are propagated for longer times; for denser curves within the map, more fixed points along the underlying periodic orbit are considered. Some of the regions of interest on the map include locations where the stable and unstable manifolds intersect, which correspond to homoclinic connections [33]. Additionally, black curves bound the regions of possible returns to the map at this value of the Jacobi constant. Maps are frequently employed in the computation of low-cost and even natural transfers between orbits in the CR3BP.

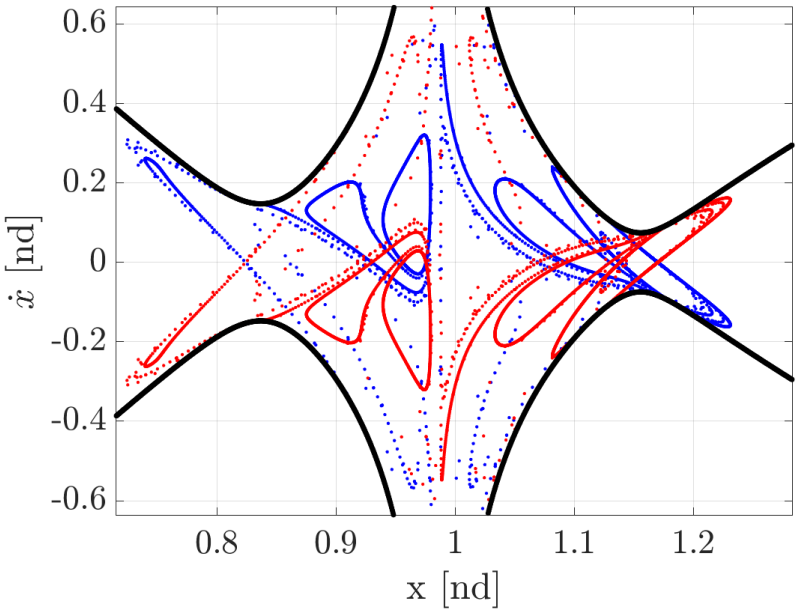

Figure 3.10. Poincaré map for an L_2 Lyapunov orbit with the hyperplane $\Sigma : y = 0$.

4. RESONANT ORBITS

This investigation is focused on an in-depth analysis of resonant orbits and their characteristics in the CR3BP. The concept of mean motion resonance is introduced in this chapter, followed by the construction of sidereal resonant orbits in the two-body model and their transition to the Earth-Moon CR3BP. Planar orbit families corresponding to different resonances are evaluated. Spatial analogs for various planar orbits families are obtained and their stability is evaluated. Finally, various sidereal resonant orbits that exhibit synodic resonance as well are introduced.

4.1 Orbital Resonance

The phenomenon of resonance is a direct consequence of subtle gravitational effects that determine the dynamical structure of the solar system [11]. In general, the type of resonance in a system that is most relevant here occurs when there exists a simple numerical relationship between frequencies or periods (both orbital and rotating) of two or multiple bodies. Within the scope of orbital mechanics, it is useful to analyze this relationship between planetary bodies and leverage it towards identifying favorable orbital characteristics.

4.1.1 Occurrences in the Solar System

The basic theory behind observed orbital resonances in the solar system is discussed. Planetary systems have been observed to demonstrate two types of resonant behaviors [53]:

- **Mean Motion Resonance**:
  Mean motion resonance occurs when the orbital periods (inversely, the mean motions) for two celestial bodies orbiting the same central body exist as a ratio of small integers. The impact of mean motion resonance is observed over shorter time scales.

- **Secular Resonance**:
  Secular resonance arises when the slow frequencies of orbital precession are commensurable, resulting in synchronized orbital precession that changes the eccentricity and

inclination of the smaller resonant body. The impact of secular resonance is observed over longer time scales, such as thousands over years.

The focus of this investigation is mean motion resonance, also termed orbit-orbit resonance. Resonances are typically described via simple integer ratios of periods, denoted generally as $p:q$. For two bodies A and B in mean motion resonance, this ratio is equal to $\mathbb{P}_B:\mathbb{P}_A$, where $\mathbb{P}_A$ and $\mathbb{P}_B$ are the periods for the orbits of bodies A and B, respectively. Notably, the orbits of Pluto and Neptune are in a $2:3$ mean motion resonance, i.e., for approximately every two revolutions of Pluto around the Sun, Neptune orbits the Sun three times. A special case of orbit-orbit resonance is observed in the Jovian system, where the periods of Ganymede, Europa, and Io are in two consecutive mean motion resonances. Specifically, Io is in a $2:1$ resonance with Europa, which is in a $2:1$ resonance with Ganymede. The geometry of the resonance, however, is such that triple conjunctions of the moons never occur: whenever a conjunction between any pair occurs, the third moon is always at least 60° away [54], [55]. This phenomenon was first observed by Pierre-Simon Laplace, and has since been noted to occur in extrasolar systems as well [56].

The occurrence of resonance in a system potentially leads to the long term stabilization of the orbits involved, as in the case of Neptune and Pluto; in other scenarios, resonance destabilizes the orbits. Another example of stabilization due to resonance is observed in the Hilda group of asteroids that exist in a $3:2$ resonance with the orbit of Jupiter [57]. However, in the same region, resonance destabilization is associated with the Kirkwood gaps in the asteroid belt between Mars and Jupiter, at the locations corresponding to $3:1$, $2:1$, $5:2$, and $7:3$ mean-motion resonances with Jupiter [58]. Similar destabilization is also observed in the Cassini Division in the rings of Saturn that are cleared out due to a $2:1$ resonance with Saturn's moon Mimas [59].

4.2 Resonant Orbits in the Two-Body Model

Resonance in the two-body model serves as a foundation for later transition to the higher-fidelity CR3BP. Of the possible closed-form solutions in the two-body model, elliptical orbits, that is, closed orbits in the inertial frame, are the focus of this investigation. Consider a

spacecraft, denoted with the subscript s, on an elliptical orbit around the Earth. Then, the spacecraft is said to be in orbital resonance with the Moon around the Earth if the spacecraft completes p orbits around the Earth in the same time that the Moon completes q revolutions around the Earth, where p and q are positive integers. Mathematically, this relationship is expressed as,

$$\frac{p}{q} = \frac{\mathbb{N}_s}{\mathbb{N}_{\leftmoon}} = \frac{\mathbb{P}_{\leftmoon}}{\mathbb{P}_s} \tag{4.1}$$

where $\mathbb{P}_{\leftmoon}$ is the period of the Moon and $\mathbb{P}_s$ is the period of the spacecraft. The quantities $\mathbb{N}_{\leftmoon}$ and $\mathbb{N}_s$ are the mean motions of the Moon and the spacecraft, respectively, evaluated as,

$$\mathbb{N}_i = \sqrt{\frac{\tilde{G}M_i}{a_i^3}} \tag{4.2}$$

Here, $\tilde{G}M_i = \tilde{\mu}_i$ is the gravitational parameter associated with the central body (Earth, in this case), and a_i is the semi-major axis in the Moon or the spacecraft orbit. Together, Equations (4.1) and (4.2) yield the following relationship between the resonance ratio and the semi-major axes for the two bodies in resonance,

$$\frac{p}{q} = \frac{\mathbb{N}_s}{\mathbb{N}_{\leftmoon}} = \sqrt{\frac{a_{\leftmoon}^3}{a_s^3}} \tag{4.3}$$

For a spacecraft in resonance with the Moon orbiting the Earth, the knowledge of the semi-major axis of the Moon, $a_{\leftmoon}$, aids in the computation of the semi-major axis of the spacecraft orbit, a_s, for any given resonance ratio $p\,{:}\,q$. The value of a_s is then determined as,

$$a_s = \left(\frac{q^2 a_{\leftmoon}^3}{p^2}\right)^{\frac{1}{3}} \tag{4.4}$$

Equation (4.4) is employed to construct orbits in the two-body model for the required resonance ratio. To simplify the analysis and to aid their eventual transition into the Earth-Moon CR3BP, the resonant orbits are constructed assuming a circular lunar orbit.

As an illustrative example, consider a spacecraft orbiting the Earth in a planar 3:4 mean motion resonance with the Moon. Since the focus is the two-body model, recall that the Moon is modeled as massless and does not influence the motion of the Earth. Assume that the gravitational parameter value of the central body, Earth, is equal to 398600.44 km^3/s^2. Then, the semi-major axis of the spacecraft orbit, a_s, is determined using Equation (4.4) with the ratio $p:q = 3:4$, and is equal to 466088.99 km. Next, the initial state vector for the resonant orbit in the two-body inertial frame is defined as ${}^{\mathcal{I}}\boldsymbol{X}_{0,2B} = [X_0 \;\; Y_0 \;\; Z_0 \;\; X_0' \;\; Y_0' \;\; Z_0']^T$. Here, the superscript $\mathcal{I}$ represents the inertial frame, and the primes denote derivatives with respect to dimensional time. Since the resonant orbit is planar, the initial values of position and velocity along the $\hat{\boldsymbol{Z}}$ direction, i.e., Z_0 and Z_0', are equal to 0. Assume that at initial time, denoted $T = 0$, the spacecraft is located at an apse. The initial position in the $\hat{\boldsymbol{Y}}$ direction and the initial velocity in the $\hat{\boldsymbol{X}}$ direction are equal to 0, i.e., $Y_0 = 0$ and $X_0' = 0$. The eccentricity of the orbit of the spacecraft is selected such that at the initial time, the spacecraft lies beyond the orbit of the Moon, i.e., at apogee relative to the Earth. In this case, the eccentricity is selected as $e_s = 0.8$, a value that corresponds to an apogee distance of $r_a = 838960.19$ km. Thus, the initial position along the $\hat{\boldsymbol{X}}$ direction is $X_0 = -r_a$. The magnitude of the initial velocity is then determined as,

$$V_0 = \sqrt{2\tilde{\mu}\left(\frac{1}{R_0} - \frac{1}{2a_s}\right)} \tag{4.5}$$

where R_0 is the magnitude of initial position. Recall that the components of velocity in the $\hat{\boldsymbol{X}}$ and $\hat{\boldsymbol{Z}}$ directions are zero. Thus, based on Equation (4.5), the final component of the initial state vector, Y_0', is determined to be equal to 0.30825 km/s, acting along the negative-$\hat{\boldsymbol{Y}}$ direction since the spacecraft is at apogee. The initial state vector is, thus, given as,

$${}^{\mathcal{I}}\boldsymbol{X}_{0,2B} = [-838960.199\ km \;\; 0 \;\; 0 \;\; 0 \;\; 0.30825\ km/s \;\; 0]^T \tag{4.6}$$

The resonant orbit that results from these initial states in the inertial frame is illustrated in black in Figure 4.1(a). The orbit of the Moon, assumed to be circular, appears in grey as well.

When the orbit is propagated for multiple revolutions in the two-body model and visualized in the rotating frame, specifically for $p = 3$ orbital periods (also equal to $q = 4$ orbits of the Moon), additional characteristics emerge. Equation (2.93) provides the transformation from the inertial to an Earth-centered Earth-Moon rotating frame. The resulting orbit appears in Figure 4.1(b) in black, with the Earth and the Moon denoted by black markers.

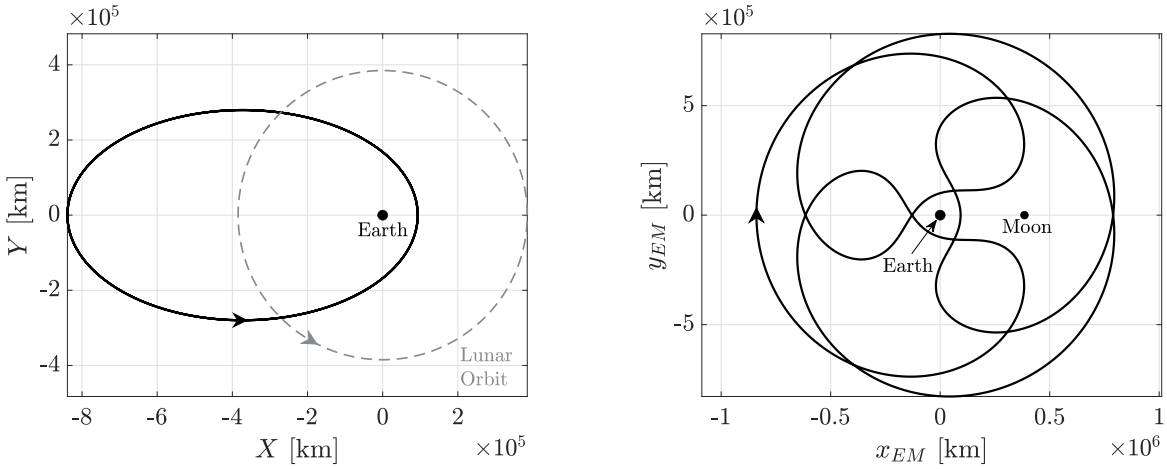

(a) Earth-centered inertial frame

(b) Earth-Moon rotating frame

Figure 4.1. Orbit in 3 : 4 resonance with the Moon constructed in the Earth two-body model and plotted in an Earth-centered inertial and Earth-centered rotating frames.

For the 3 : 4 resonance ratio, the spacecraft orbits the Earth three times in the same time interval required for the Moon to orbit the Earth four times. A stark difference between the inertial and rotating frame views of the resonant orbit is the formation of *loops* that appear in Figure 4.1(b). The number of loops that appear in this frame correspond to the value of p in the $p : q$ resonance ratio for any resonant orbit. For this resonance ratio, the loops represent the periapse passes along the orbit: at periapses, the velocity of the spacecraft around the Earth is faster than the velocity of the Moon in its orbit, a fact that renders the spacecraft to seemingly reverse its direction of motion in orbit. In addition to highlighting their unique geometry, the transformation into the rotating frame also precedes the construction of resonant orbits in the CR3BP. When the two-body orbit is propagated for multiple revolutions, specifically for $p = 3$ periods in this example, it repeats 3 times in the inertial frame view in Figure 4.1(a). However, in the rotating frame view in Figure 4.1(b),

the orbit is closed and appears to complete one full revolution in that time, without repeating over itself. As such, the apparent period of the resonant orbit in the rotating frame view is equal to $p \cdot \mathbb{P}_s$, where $\mathbb{P}_s$ is period of the spacecraft in the conventional two-body model, and is evaluated as,

$$\mathbb{P}_s = 2\pi\sqrt{\frac{a_s}{\tilde{\mu}}} \tag{4.7}$$

Here a_s is the semi-major axis of the orbit, and $\tilde{\mu}$ is the gravitational parameter of the central body. For this example, the period of the spacecraft is equal to $\mathbb{P}_s = 36.65$ *days*; in the rotating frame, the orbit appears closed over $3 \cdot \mathbb{P}_s = 109.96$ *days*.

4.2.1 A Note on Nomenclature: Sidereal vs. Synodic Resonant Orbits

In trajectory design, resonant orbits are frequently described by both sidereal and synodic periods. These periods, specifically within the context of the Earth-Moon dynamical system, are described [60]:

- **Sidereal Period**: the time required for the Moon to complete a 360° revolution and return to the same orientation relative to the "fixed" stars as viewed from the Earth. The lunar sidereal period is equal to its orbital period of 27.3217 *days*.
- **Synodic Period**: the time required for the Moon to appear in the same location relative to both the Earth and the Sun as viewed from the Earth. The lunar synodic period is approximately equal to 29.53 *days*, and is also the period of the lunar phases.

For the orbits in this investigation, specifically, orbits of spacecraft in mean motion resonance with the Moon, the relevant quantity is the sidereal period of the Moon. Recall from Equation (4.1), mean motion resonance entails the period of revolution, or the orbital period of the bodies involved. As such, the sidereal period of the Moon is employed in the determination of the resonance ratio and the construction of resonant orbits. These orbits are, thus, more appropriately termed "sidereal resonant orbits"; for brevity, they are simply denoted "resonant orbits" in this investigation. Where the lunar synodic period is employed, the term "synodic resonant orbits" is explicitly used to avoid confusion.

4.3 Resonant Orbits in the CR3BP

The determination of resonant orbits in the CR3BP builds upon resonant orbits as first constructed in the two-body model. However, one major distinction that arises between resonant orbits in the two models is the difference in resonance ratios. For resonant orbits in the two-body model with perfect integer resonance ratios, the equivalent orbits in the CR3BP no longer possess precise integer ratios, but approximate rational fractions. Thus, for $3:4$ resonant orbits in the CR3BP, the spacecraft completes p orbits around the Earth in *approximately* the time required for the Moon to complete q orbits around the Earth. Nonetheless, such orbits in the CR3BP are precisely periodic in the rotating frame and, as demonstrated in the following sections, exhibit the same rotating frame geometries as their two-body counterparts.

One approach for constructing resonant orbits in the Earth-Moon CR3BP, the initial guess is generated from the analogous resonant orbit in the two-body model. Return to the $3:4$ resonant orbit in the two-body problem as seen in Section 4.2. The two-body model assumes the Moon to be massless, clearly no longer true in the CR3BP. Consequently, the additional gravitational effect of the Moon perturbs the orbit in the CR3BP and initially results in an orbit that is not periodic. Therefore, the initial conditions corresponding to the periodic orbit in the two-body model require adjustments via a differential corrections scheme for the construction of its analog in the CR3BP. To illustrate this process, recall the six-element dimensional initial state vector for the $3:4$ resonant orbit in the two-body inertial frame, i.e.,

$$^{\mathcal{I}}\boldsymbol{X}_{0,2B} = [-838960.199\ km \quad 0 \quad 0 \quad 0 \quad 0.30825\ km/s \quad 0]^T \tag{4.8}$$

Using Equation (2.93), the following vector is produced that represents the initial state for the spacecraft in the Earth-Moon rotating frame centered on the Earth,

$$^{\mathcal{R}}\boldsymbol{X}_{0,2B} = [-838960.199\ km \quad 0 \quad 0 \quad 0 \quad 1.92480\ km/s \quad 0]^T \tag{4.9}$$

The initial state vector in Equation (4.9) is then converted into rotating CR3BP nondimensional coordinates, along with a coordinate shift to the Earth-Moon barycenter at the origin. The resulting nondimensional CR3BP state in the rotating frame is,

$$^{\mathcal{R}}\boldsymbol{x}_0 = [-2.19269 \;\; 0 \;\; 0 \;\; 0 \;\; 1.87954 \;\; 0\;]^T \tag{4.10}$$

Propagating the initial state in Equation (4.10) for one period in the rotating frame (approximately 110 *days*, or for $p = 3$ revolutions in the inertial frame) using the CR3BP nonlinear equations of motion results in a trajectory that is neither closed nor periodic in the rotating frame. As such, a corrections scheme is necessary to adjust the initial conditions and produce a periodic resonant orbit in this model. The single shooting scheme employed to construct the L_1 Lyapunov orbit in Section 3.3 is adopted to produce the periodic trajectory. The initial state from Equation (4.10) seeds the initial guess for the perpendicular crossing targeter. Adjusting the six-element nondimensional initial state in the CR3BP rotating frame yields,

$$^{\mathcal{R}}\boldsymbol{x}_{0,corr} = [-2.19269 \;\; 0 \;\; 0 \;\; 0 \;\; 1.89204 \;\; 0\;]^T \tag{4.11}$$

In dimensional units, this initial state vector is rewritten as,

$$^{\mathcal{R}}\boldsymbol{x}_{0,corr} = [-843635.11\ km \;\; 0 \;\; 0 \;\; 0 \;\; 1.93761\ km/s \;\; 0\;]^T \tag{4.12}$$

The corrected resonant orbit appears in red in Figures 4.2(a) and 4.2(b) in the Earth-centered inertial and Earth-Moon rotating frames, respectively. Notably, in the inertial frame, the three revolutions of the spacecraft are not perfectly overlaid as in the case of the two-body orbit in Figure 4.1(a). Instead, the gravitational perturbations applied by the Moon cause oscillations about the line of apsides. In the rotating view in Figure 4.2(b), the initial guess from the two-body model appears in black. For this particular orbit, the two-body solution supplies an appropriate initial guess in the CR3BP, and minimal departures in geometry are observed. The corrected orbit possesses a period of 109.57 days and a Jacobi constant value equal to 2.14178. While this corrections strategy directly supplies the resonant orbit in the CR3BP from the two-body initial guess, other strategies, such as continuation in the

CR3BP mass ratio value, μ, are sometimes leveraged to deliver CR3BP resonant orbits as well [61].

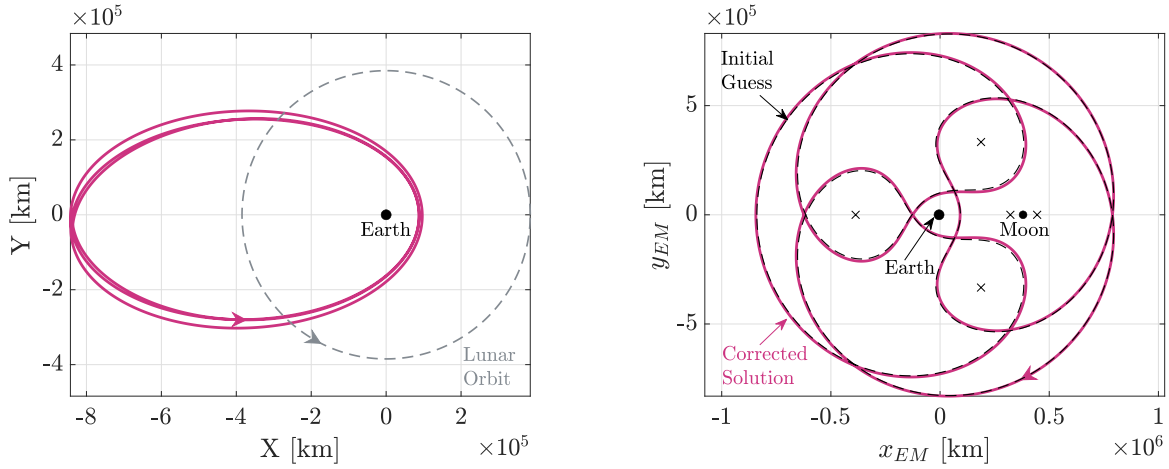

(a) Earth-centered inertial frame

(b) Earth-Moon rotating frame

Figure 4.2. Orbit in 3 : 4 resonance with the Moon constructed in the Earth-Moon CR3BP and plotted in the inertial and rotating frames.

4.3.1 Osculating Orbital Elements: CR3BP Resonant Orbits

Visualizing resonant orbits in the inertial and rotating frames allows insight into their varying geometries. The orbits exhibit notable features in the rotating frame that are unique to sidereal resonant orbits. Given that the definition of resonant orbits originates in two-body Keplerian orbits, it is also useful to assess the orbital elements for orbits in dynamical models of higher fidelity. While the orbital elements are defined only in the context of the two-body model, *osculating* orbital elements provide insight into the orbital analogs in other models as well.

To produce the osculating orbital elements in the CR3BP, the osculating conic section is constructed at each point in time. This osculating conic orbit, one that exists about the central body in the absence of perturbations, is tangent to the actual orbit at every point with the same velocity as the actual orbit at that precise point [62]. In the Earth-Moon CR3BP, the third-body perturbations from the Moon significantly vary the orbital elements in comparison to the Keplerian analogs. To produce these osculating orbital elements, the

Earth-centered inertial states that appear in Figure 4.2(a) are employed to evaluate the osculating orbital elements at each point in time. Let $\boldsymbol{R}_k$ and $\boldsymbol{V}_k$ denote the dimensional position and velocity vectors in inertial coordinates at each time step, t_k. The first step in delivering the orbital elements is the availability of the osculating orbital angular momentum vector and its magnitude, i.e.,

$$\boldsymbol{h}_k = \boldsymbol{R}_k \times \boldsymbol{V}_k \tag{4.13}$$

$$h_k = ||\boldsymbol{h}_k|| \tag{4.14}$$

Next, the eccentricity vector evaluation yields the osculating eccentricity for the orbit,

$$\boldsymbol{e}_k = \frac{\boldsymbol{V}_k \times \boldsymbol{h}_k}{\tilde{\mu}} - \frac{\boldsymbol{R}_k}{R_k} \tag{4.15}$$

$$e_k = ||\boldsymbol{e}_k|| \tag{4.16}$$

where $\tilde{\mu}$ is the dimensional gravitational parameter for the central body. Next, the osculating inclination appears as,

$$i_k = \arccos\left(\frac{h_{k,\hat{\boldsymbol{Z}}}}{\boldsymbol{h}_k}\right) \tag{4.17}$$

where $h_{k,\hat{\boldsymbol{Z}}}$ is the component of the angular momentum along the $\hat{\boldsymbol{Z}}$ direction. For the osculating right ascension of the ascending node (RAAN), denoted Ω_k, the osculating angular velocity vector is first determined as,

$$\tilde{\boldsymbol{\omega}}_k = [0 \quad 0 \quad 1]^T \times \boldsymbol{h}_k \tag{4.18}$$

Then, the following two cases arise that are considered in the computation of the osculating RAAN,

$$\Omega_k = \begin{cases} \arccos\left(\dfrac{\tilde{\omega}_{k,\hat{\boldsymbol{X}}}}{\tilde{\boldsymbol{\omega}}_k}\right) & \tilde{\omega}_{k,\hat{\boldsymbol{Y}}} \geq 0 \\ 2\pi - \arccos\left(\dfrac{\tilde{\omega}_{k,\hat{\boldsymbol{X}}}}{\tilde{\boldsymbol{\omega}}_k}\right) & \tilde{\omega}_{k,\hat{\boldsymbol{Y}}} < 0 \end{cases} \tag{4.19}$$

Next, the osculating argument of periapsis is determined for the following two options for the osculating eccentricity vector,

$$\omega_k = \begin{cases} \arccos\left(\dfrac{\boldsymbol{e}_k \cdot \tilde{\boldsymbol{\omega}}_k}{e_k \tilde{\omega}_k}\right) & \boldsymbol{e}_{k,\hat{\boldsymbol{z}}} \geq 0 \\ 2\pi - \arccos\left(\dfrac{\boldsymbol{e}_k \cdot \tilde{\boldsymbol{\omega}}_k}{e_k \tilde{\omega}_k}\right) & \boldsymbol{e}_{k,\hat{\boldsymbol{z}}} < 0 \end{cases} \tag{4.20}$$

For completeness, the relationships for producing the osculating true anomaly are,

$$\theta_k^* = \begin{cases} \arccos\left(\dfrac{\boldsymbol{e}_k \cdot \boldsymbol{R}_k}{e_k R_k}\right) & \boldsymbol{e}_k \cdot \boldsymbol{R}_k \geq 0 \\ 2\pi - \arccos\left(\dfrac{\boldsymbol{e}_k \cdot \boldsymbol{R}_k}{e_k R_k}\right) & \boldsymbol{e}_k \cdot \boldsymbol{R}_k < 0 \end{cases} \tag{4.21}$$

Finally, the osculating semi-major axis value is a function of the inertial position,

$$a_k = \frac{1}{\dfrac{2}{R_k} - \dfrac{V_k^2}{\tilde{\mu}}} \tag{4.22}$$

Using the osculating semi-major axis, the osculating orbital period is available as well, allowing a direct comparison of the two-body and the CR3BP resonance ratios. The osculating orbital period is,

$$\mathbb{P}_k = 2\pi \sqrt{\frac{a_k^3}{\tilde{\mu}}} \tag{4.23}$$

As an example, Figure 4.3(a) illustrates the relevant osculating orbital elements for the $3:4$ CR3BP resonant orbit in Figure 4.2. The osculating semi-major axis appears in Figure 4.3(a), where the black line indicates the "ideal" semi-major axis, i.e., the value associated with the $3:4$ resonant orbit in the two-body model, determined via Equation (4.4). Notably, the osculating value oscillates about the ideal value, with "spikes" corresponding to perigee and perilune passes. Figure 4.3(b) illustrates the osculating resonance ratio for this particular orbit, where the black line indicates the precise value of the ratio, i.e., $\frac{3}{4} = 0.75$. Visualizing the osculating resonant ratio illustrates the difference between the two-body resonant ratio

and the *approximate* resonant ratio that manifests in higher-fidelity models. Figure 4.3(c) illustrates the osculating eccentricity for the three-body orbit, where the black line denotes the eccentricity of the underlying two-body resonant orbit from Figure 4.1 that seeded the initial guess for the CR3BP construction. Here, the perturbations to the two-body conic that manifest in the CR3BP become apparent at the locations of close encounters with both the primaries as well. While not illustrated here, the osculating inclination and RAAN values for this orbit are also available. Since the orbit is planar and prograde, the inclination and RAAN remain constant and equal to zero for each time step. For spatial resonant orbits, close lunar passes may perturb these orbital elements significantly as well.

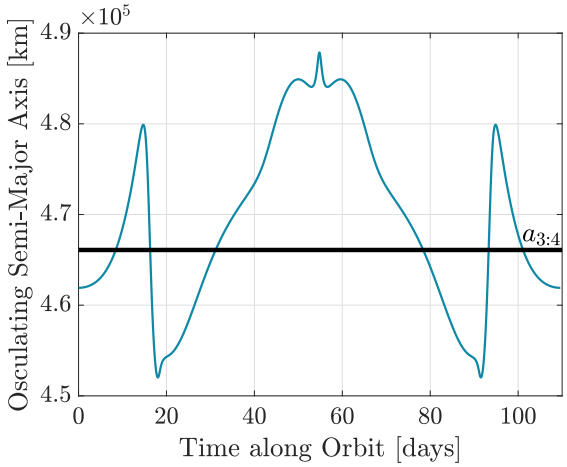

(a) Osculating semi-major axis

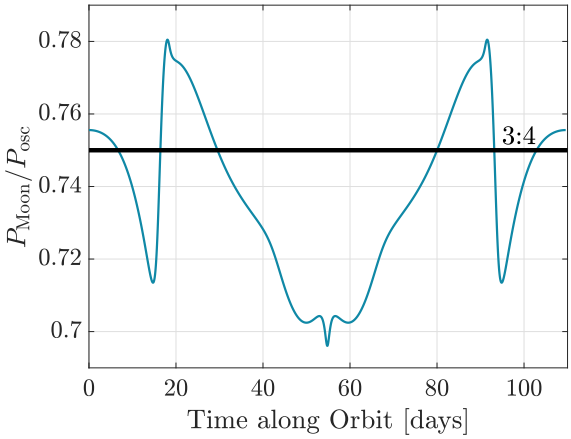

(b) Osculating orbital period

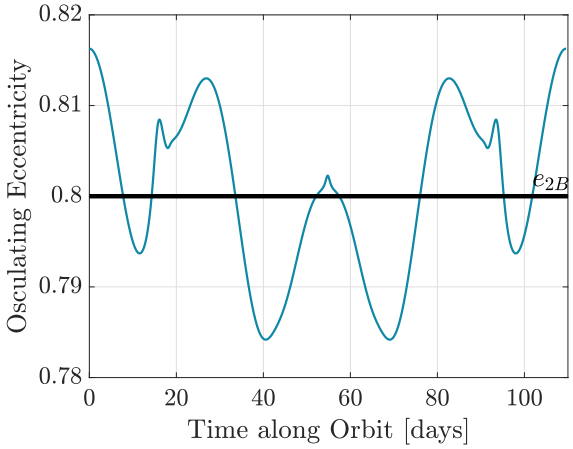

(c) Osculating eccentricity

Figure 4.3. Osculating semi-major axis, orbital period (resonance ratio), and eccentricity for the 3 : 4 resonant orbit in the CR3BP.

4.3.2 Interior and Exterior Resonant Orbits

Depending on the resonance ratio, resonant orbits are classified as *interior* or *exterior* resonances. For an integer resonance ratio of $p:q$, orbits with $p > q$ are denoted interior resonant orbits. The periods of these orbits, as viewed in the inertial frame, are shorter than the period of the Moon. In general, these orbits remain interior to the Earth-Moon system. Alternatively, when $p < q$, the orbits are termed exterior resonant orbits. The orbital periods in this case are longer than the period of the Moon. The geometries of these orbits exhibit excursions beyond the Earth-Moon system, with potential opportunities for closer passes of the two primaries. The $3:4$ orbit in Figure 4.2 is an exterior resonant orbit, characterized by its long period and excursions beyond the lunar orbit, as apparent in Figure 4.2(a).

4.4 Families of Planar Earth-Moon Resonant Orbits

The existence of a periodic resonant orbit in the CR3BP guarantees the existence of a family of resonant orbits. In contrast to resonant orbits in the two-body model that exist as isolated solutions for a given resonance ratio and eccentricity, families of resonant orbits in the CR3BP cover a range of suitable options. Although the orbits in a family of solutions exist over a range of periods and, as a result, are *nearly resonant*, they exhibit resonant behavior and characteristics that retain the utility of the underlying sidereal resonant orbits. These additional orbits are typically constructed by varying a physical parameter, such as a position or velocity coordinate via natural parameter continuation (Section 3.4.1), or by continuing along the direction tangent to the family via pseudo-arclength continuation (Section 3.4.2). In this investigation, natural parameter continuation and perpendicular crossing targeting algorithms are employed to evolve families of resonant orbits. The first orbit in the family is produced via an initial guess from the two-body model. This process is repeated for various resonance ratios within the Earth-centered two-body model.

Families of planar sidereal resonant orbits corresponding to various resonance ratios are constructed in the Earth-Moon CR3BP and appear in Figures 4.4 – 4.7. In each figure, the left column illustrates representative members of the orbit families colored by their Jacobi constant values. For each family, the orbits highlighted in black represent the direction of

motion along the orbit. The columns on the right reflect the evolution of the stability index, obtained via Equation (3.58), plotted in blue on the left vertical axis as a function of the Jacobi constant along the orbit family. Also plotted in the right column is the evolution of the period in the CR3BP (i.e., the period in the rotating frame), appearing in red along the right vertical axis for each family. Overall, the orbit families illustrate vastly differing geometries and stability properties spanning various energy levels. This characteristic of resonant orbits renders them particularly useful for trajectory design in the cislunar domain, since access to various regions within this space is available via their expansive geometries and energy levels. The corrected nondimensional initial states, values of Jacobi constant, and nondimensional period for selected orbit members from each resonant family are summarized in Table 4.1. Since the orbits are planar and symmetric about the $\hat{\boldsymbol{x}}$-axis, the initial state vector is of the form $\boldsymbol{x}_0 = [x_0 \ 0 \ 0 \ 0 \ \dot{y}_0 \ 0]^T$. The values provided in Table 4.1 correspond to orbits from each family that are closest in period to their respective "ideal" resonant ratio.

4.5 Families of Spatial Earth-Moon Resonant Orbits

The availability of planar resonant orbit families and the evaluation of their stability properties enables the search for three-dimensional resonant orbit families [63]. The availability of such solutions opens additional dynamically viable regions for spacecraft pathways over various values of the Jacobi constant. To construct spatial families of resonant orbits, the eigenvalue structure along their planar analogs is investigated in search of bifurcating orbits. Specifically, certain tangent bifurcations from planar resonant families bifurcate into spatial resonant families [22].

Once the bifurcating orbit is identified, a slight perturbation in the initial state corresponding to the orbit is introduced in the $\hat{\boldsymbol{z}}$-direction. Then, the initial state to construct the first spatial orbit is of the form $\boldsymbol{x}_0 = [x_0 \ \ 0 \ \ \Delta z \ \ 0 \ \ \dot{y}_0 \ \ 0]^T$, where Δz is the perturbation along the $\hat{\boldsymbol{z}}$-direction. This perturbed state is adjusted for periodicity using a three-dimensional targeting scheme focused on perpendicular crossings, during which the value of the initial position in the $\hat{\boldsymbol{z}}$-direction is held fixed. Following a strategy for natural parameter continuation, as employed in the construction of planar families of resonant orbits, families of spatial

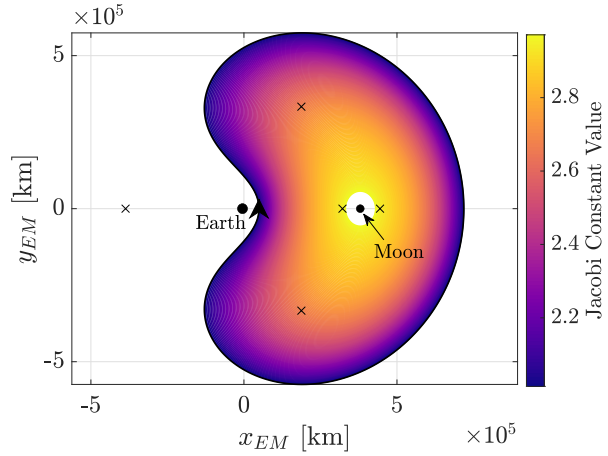

(a) 1 : 1 resonant orbit family

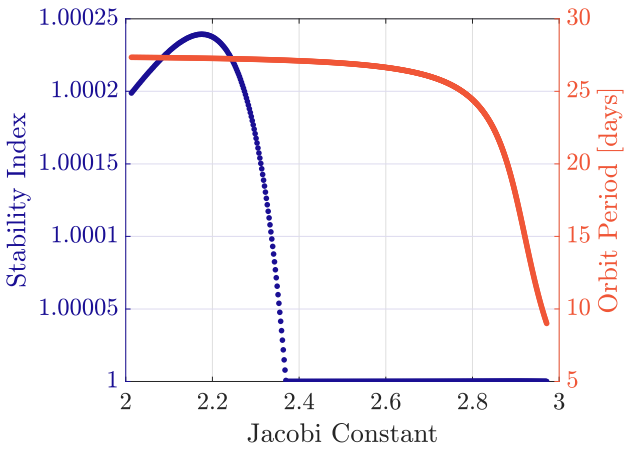

(b) 1 : 1 stability and period evolution

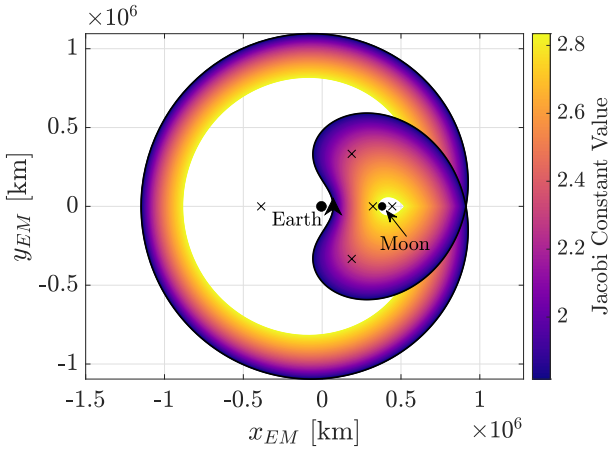

(c) 1 : 2 resonant orbit family

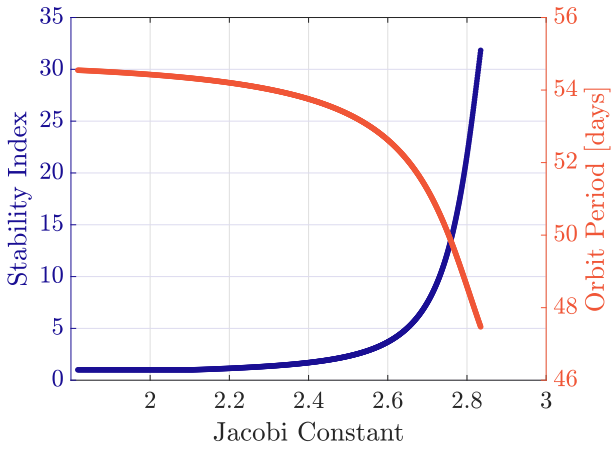

(d) 1 : 2 stability and period evolution

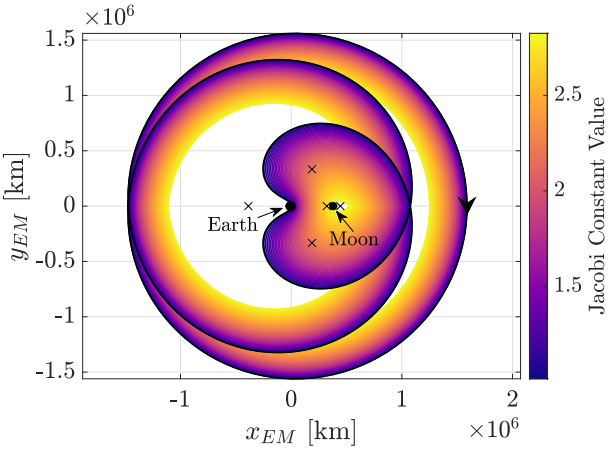

(e) 1 : 3 resonant orbit family

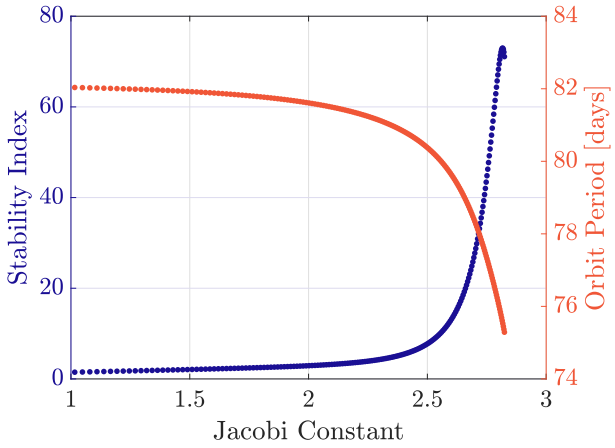

(f) 1 : 3 stability and period evolution

Figure 4.4. Families of planar resonant orbits corresponding to various $1:q$ resonant ratios obtained in the Earth-Moon CR3BP.

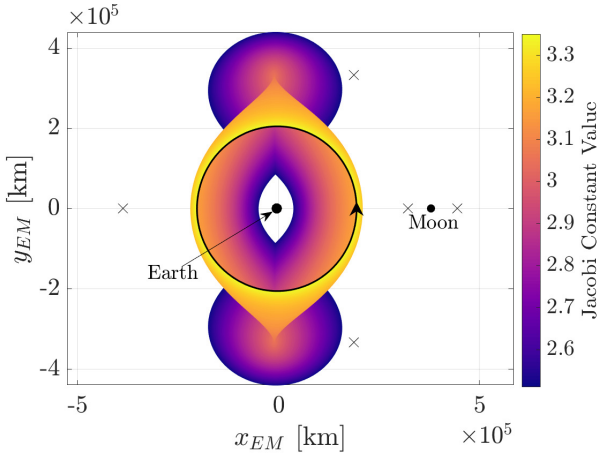

(a) 2 : 1 resonant orbit family

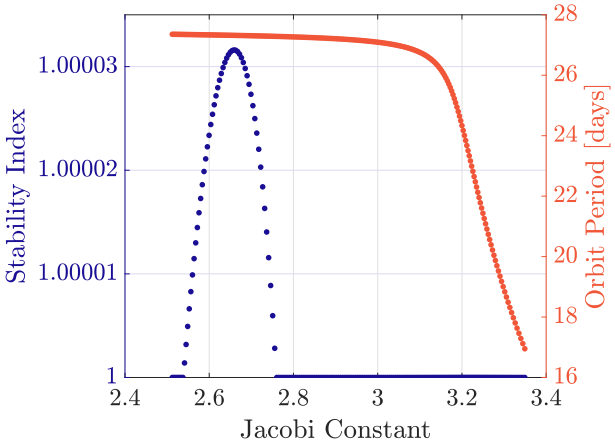

(b) 2 : 1 stability and period evolution

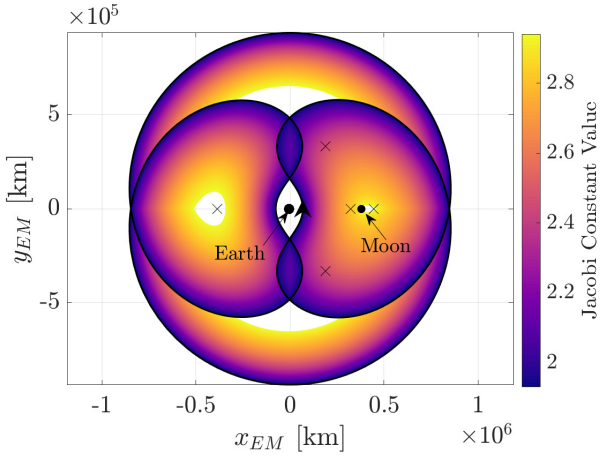

(c) 2 : 3 resonant orbit family

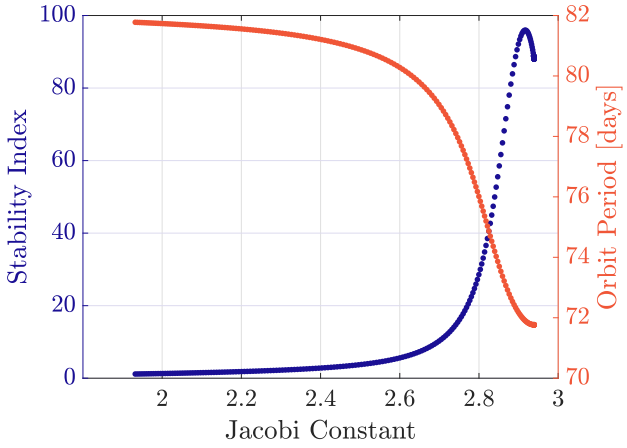

(d) 2 : 3 stability and period evolution

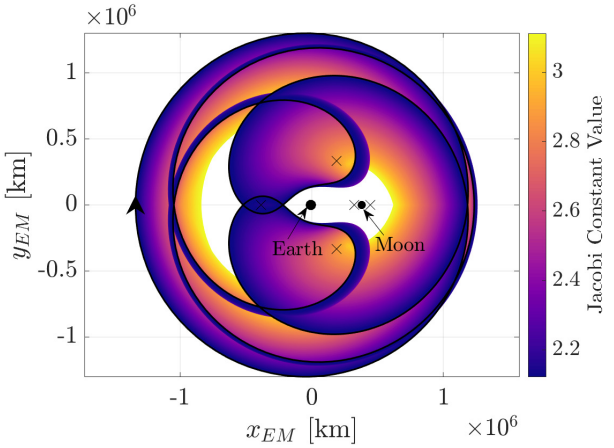

(e) 2 : 5 resonant orbit family

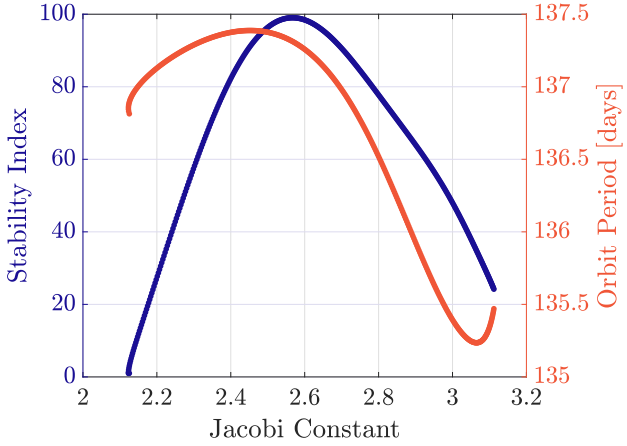

(f) 2 : 5 stability and period evolution

Figure 4.5. Families of planar resonant orbits corresponding to various $2:q$ resonant ratios obtained in the Earth-Moon CR3BP.

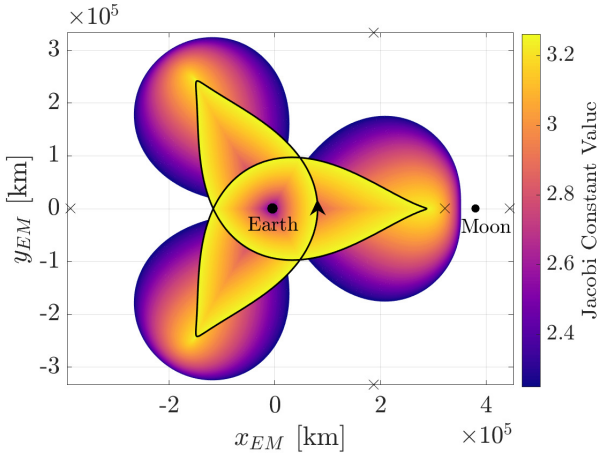

(a) 3 : 1 resonant orbit family

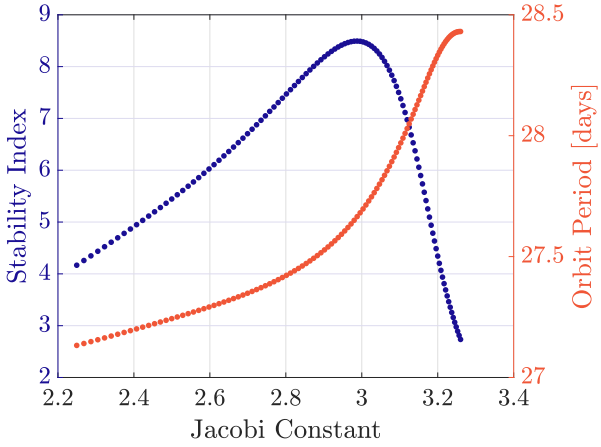

(b) 3 : 1 stability and period evolution

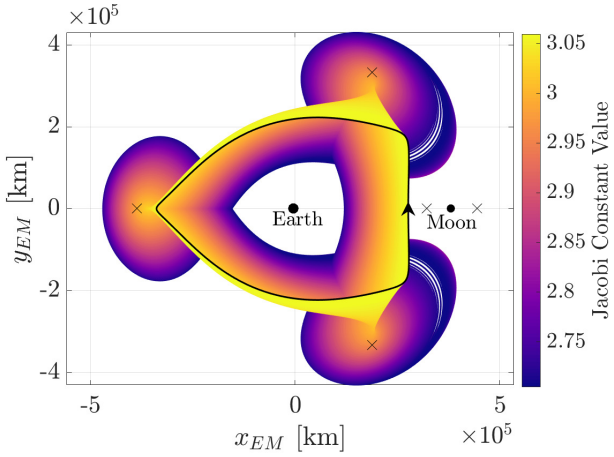

(c) 3 : 2 resonant orbit family

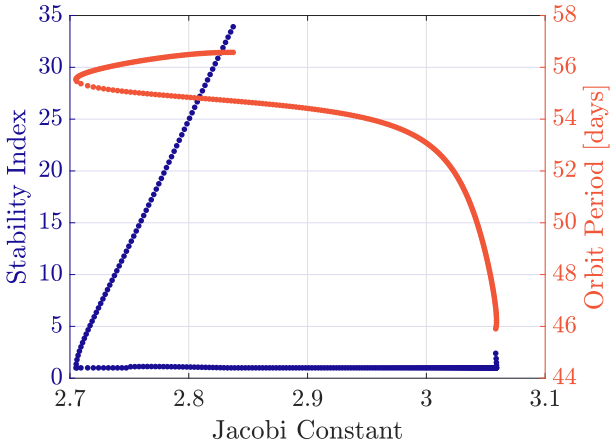

(d) 3 : 2 stability and period evolution

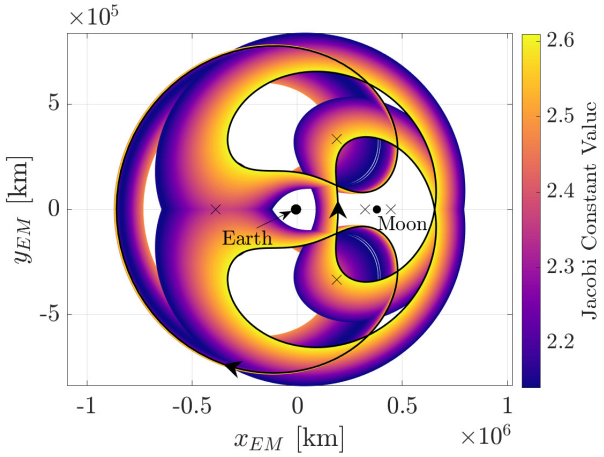

(e) 3 : 4 resonant orbit family

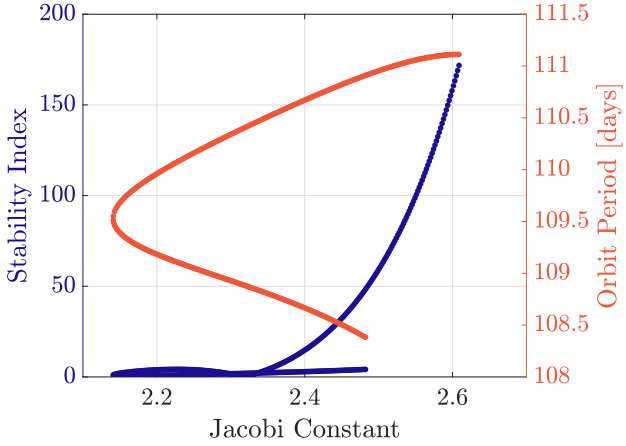

(f) 3 : 4 stability and period evolution

Figure 4.6. Families of planar resonant orbits corresponding to various $3 : q$ resonant ratios obtained in the Earth-Moon CR3BP.

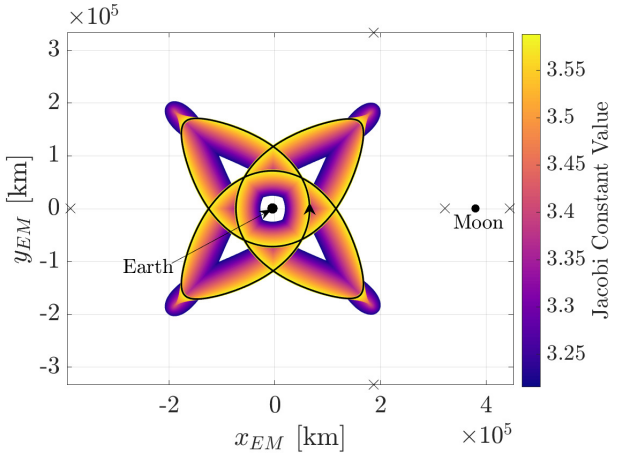

(a) 4 : 1 resonant orbit family

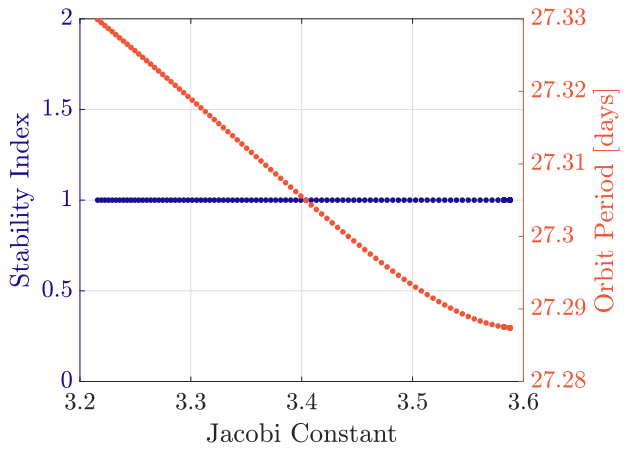

(b) 4 : 1 stability and period evolution

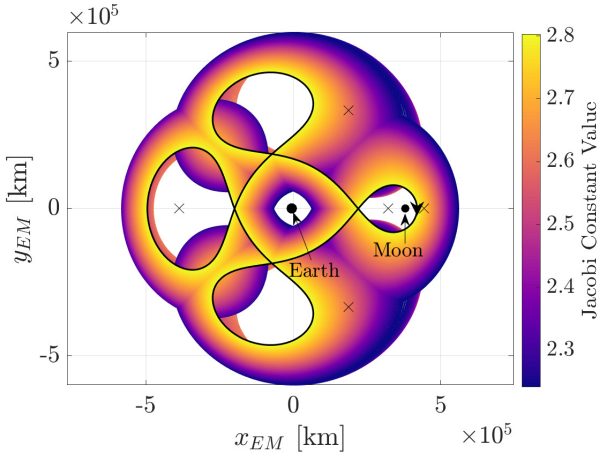

(c) 4 : 3 resonant orbit family

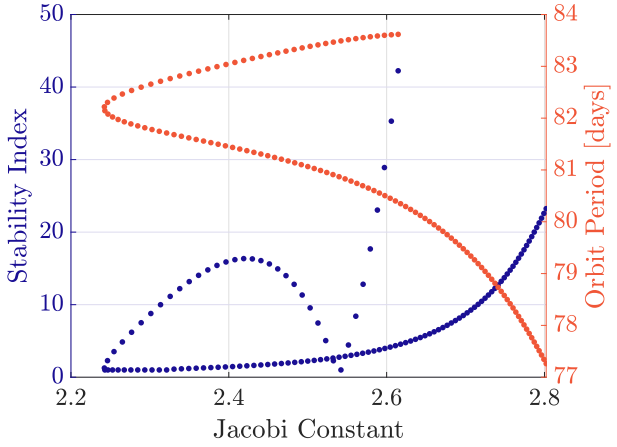

(d) 4 : 3 stability and period evolution

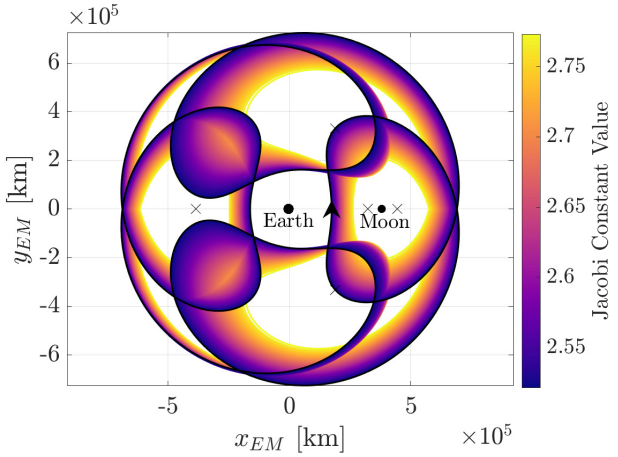

(e) 4 : 5 resonant orbit family

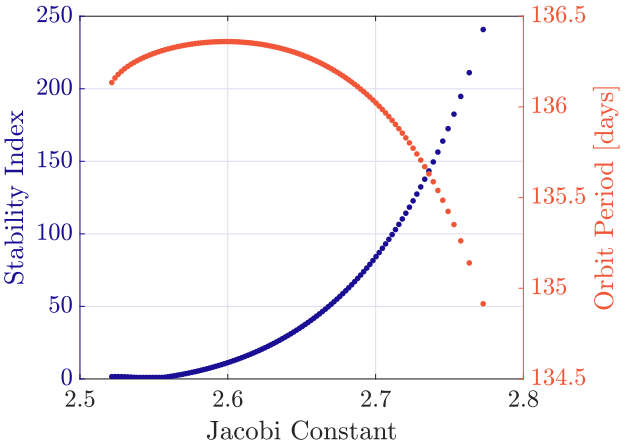

(f) 4 : 5 stability and period evolution

Figure 4.7. Families of planar resonant orbits corresponding to various $4:q$ resonant ratios obtained in the Earth-Moon CR3BP.

Table 4.1. Initial conditions for selected planar resonant orbits in the Earth-Moon CR3BP system.

Resonance Ratio	$\boldsymbol{x_0}$ $[nd]$	$\boldsymbol{\dot{y}_0}$ $[nd]$	$\boldsymbol{C}$	**Period** $[nd]$
1 : 1	0.153862	3.140080	2.093600	6.282755
1 : 2	0.181659	2.905124	1.817405	12.544220
1 : 3	4.056387	-3.944789	1.386438	18.848089
2 : 1	0.148266	3.115805	2.658738	6.282734
2 : 3	0.968292	1.121194	2.938193	16.504591
2 : 5	-2.687986	2.277306	2.784109	31.414921
3 : 1	0.892859	-0.765710	2.649782	6.282625
3 : 2	0.399518	1.465157	2.853480	12.564971
3 : 4	0.254937	2.307397	2.171259	25.131392
4 : 1	0.071268	4.519106	3.293543	6.282760
4 : 3	1.435953	-1.104885	2.259758	18.851590
4 : 5	0.506067	1.232588	2.599756	31.358859

resonant orbits are produced as well. Each subsequent orbit in the family is incremented by a fixed value in the $\hat{\boldsymbol{z}}$-direction, and the resulting initial state is iteratively corrected. Increments in the positive $\hat{\boldsymbol{z}}$-direction result in *northern* spatial resonant orbits, while stepping in the negative $\hat{\boldsymbol{z}}$-direction results in *southern* spatial resonant orbits. Spatial analogs for the planar resonant orbit families from the previous section are illustrated in Figures 4.8 – 4.10. To highlight the complex out-of-plane geometry that manifests in the rotating frame, projections on the $\hat{\boldsymbol{x}} - \hat{\boldsymbol{y}}$, $\hat{\boldsymbol{y}} - \hat{\boldsymbol{z}}$, and $\hat{\boldsymbol{x}} - \hat{\boldsymbol{z}}$ planes for a single orbit from each family appear in the figures in grey as well. Additionally, the evolution of the orbital period and stability

index for the given orbits are plotted as a function of the Jacobi constant value for each family. Section 4.5 summarizes the initial value for the x- and z-positions and the y-velocity, Jacobi constant, and the period for selected members from each family of spatial resonant orbits.

Table 4.2. Initial conditions for selected spatial resonant orbits in the Earth-Moon CR3BP system.

Resonance Ratio	$\boldsymbol{x_0}$ $[nd]$	$\boldsymbol{z_0}$ $[nd]$	$\boldsymbol{\dot{y}_0}$ $[nd]$	$\boldsymbol{C}$	**Period** $[nd]$
1 : 1	0.157512	-0.065407	2.975925	2.063267	6.282874
1 : 2	0.400017	-0.847935	0.830551	1.589312	12.542272
1 : 3	0.908786	3.080866	-0.531585	1.165613	18.839069
2 : 1	0.163711	-0.063925	2.820262	2.660795	6.275032
2 : 3	0.209035	0.915128	0.968818	1.223816	18.815016
2 : 5	-2.249466	1.312564	1.819059	2.519744	31.393848
3 : 1	-0.703637	0.430252	0.081939	2.928229	6.261122
3 : 2	0.310545	-0.215848	1.625235	2.578213	12.528079
3 : 4	0.456989	-0.828089	0.696201	1.824712	25.057990

4.6 Resonant Orbits with Sidereal-Synodic Overlap

For certain sidereal resonant orbit families in the CR3BP, it is possible to identify members that, in addition to being nearly sidereal resonant with the Moon, exhibit lunar synodic resonance as well. This characteristic arises due to the orbits being *nearly* sidereal resonant, a characteristic that allows the family of sidereal resonant orbits to span a wide range of orbital periods in the rotating frame. Thus, the orbits retain favorable geometries and stability properties inherent to their sidereal resonant structure, with the added advantage of

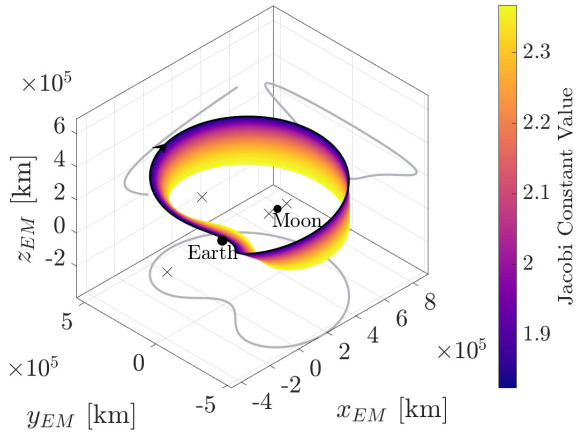

(a) 1 : 1 resonant orbit family

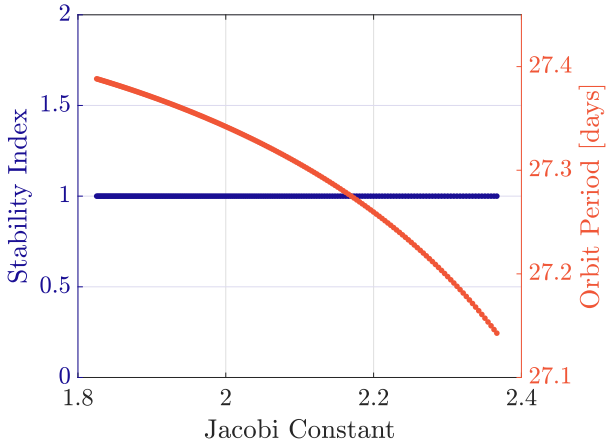

(b) 1 : 1 stability and period evolution

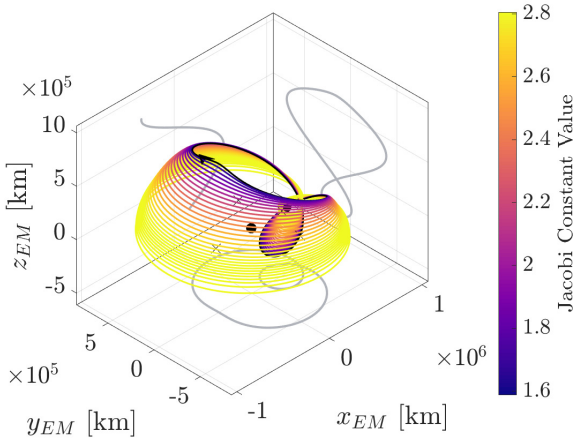

(c) 1 : 2 resonant orbit family

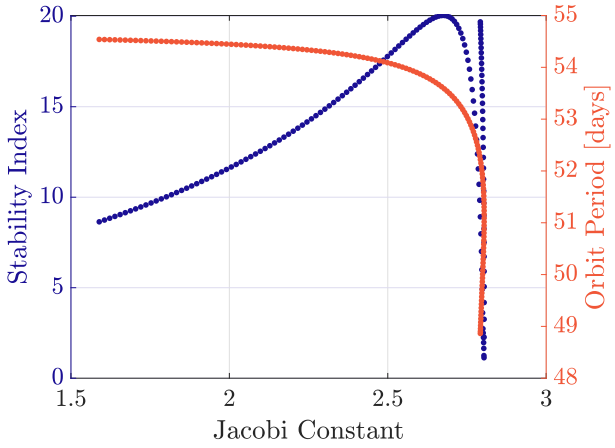

(d) 1 : 2 stability and period evolution

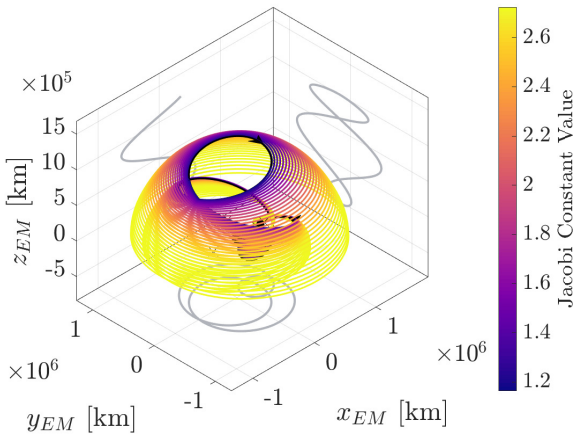

(e) 1 : 3 resonant orbit family

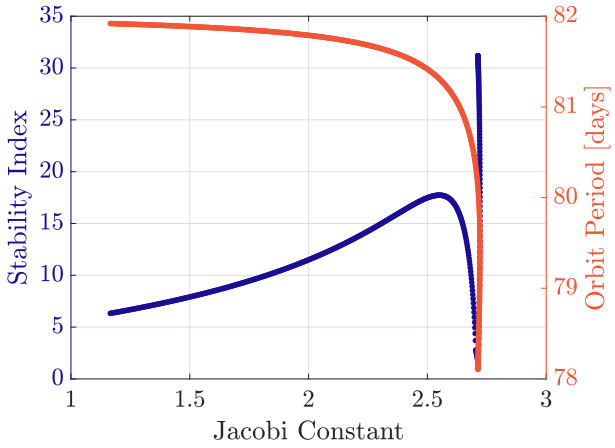

(f) 1 : 3 stability and period evolution

Figure 4.8. Families of spatial resonant orbits corresponding to various $1:q$ resonant ratios obtained in the Earth-Moon CR3BP.

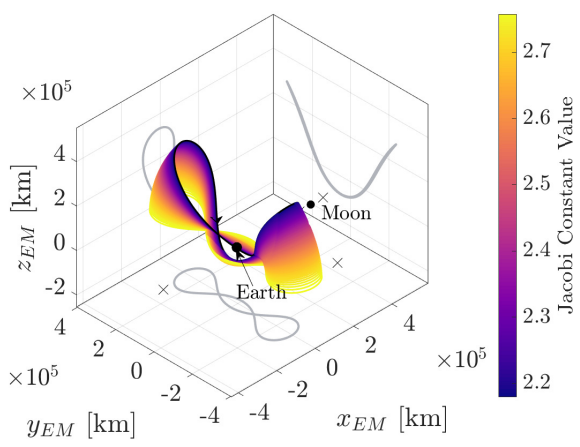

(a) 2 : 1 resonant orbit family

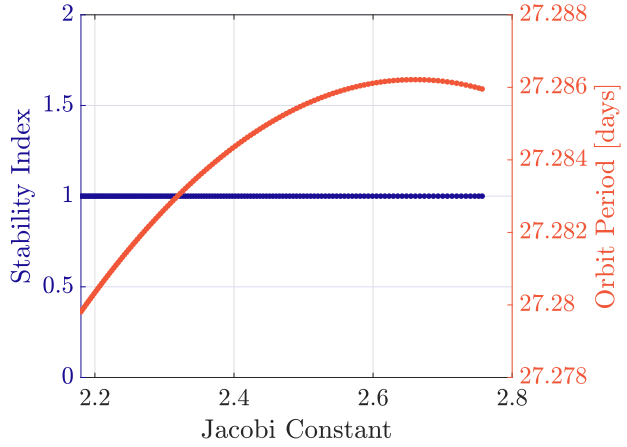

(b) 2 : 1 stability and period evolution

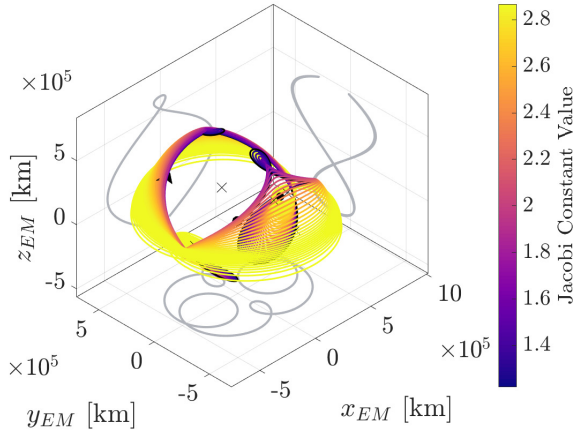

(c) 2 : 3 resonant orbit family

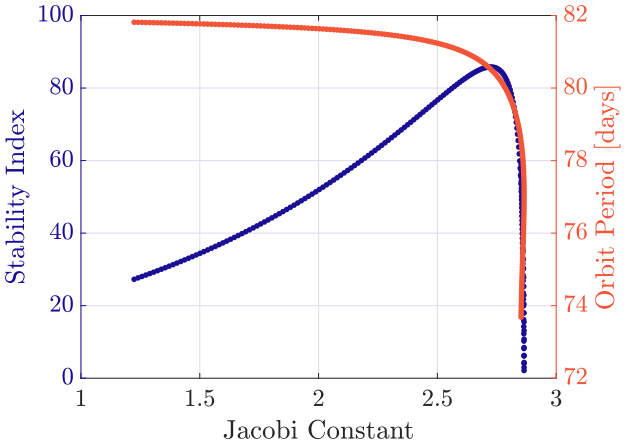

(d) 2 : 3 stability and period evolution

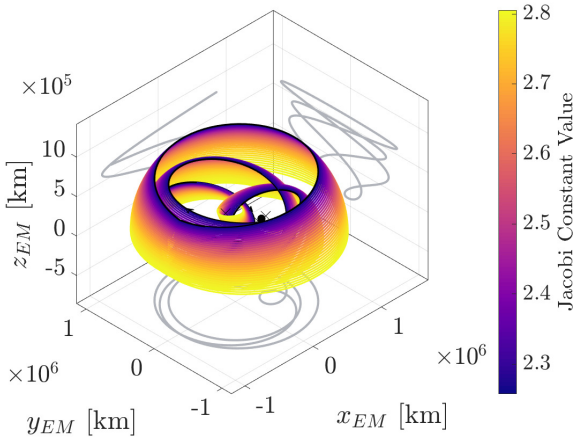

(e) 2 : 5 resonant orbit family

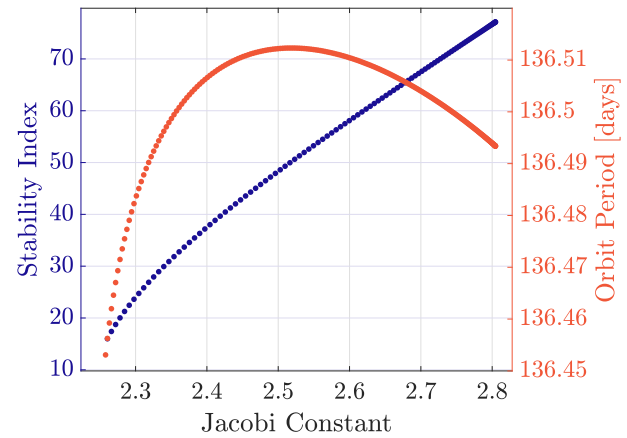

(f) 2 : 5 stability and period evolution

Figure 4.9. Families of spatial resonant orbits corresponding to various $2:q$ resonant ratios obtained in the Earth-Moon CR3BP.

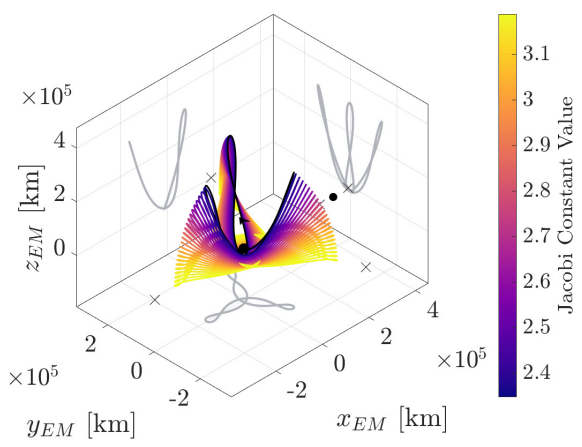

(a) 3 : 1 resonant orbit family

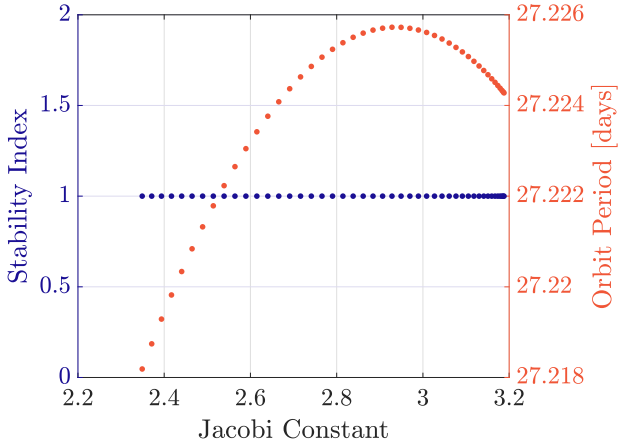

(b) 3 : 1 stability and period evolution

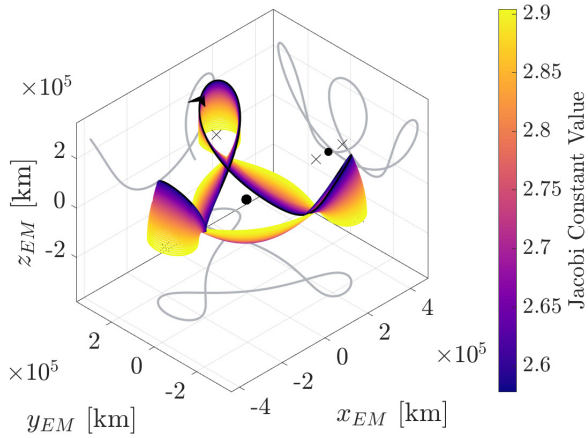

(c) 3 : 2 resonant orbit family

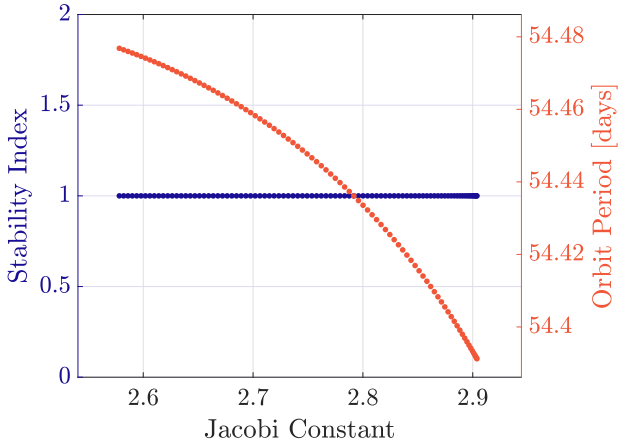

(d) 3 : 2 stability and period evolution

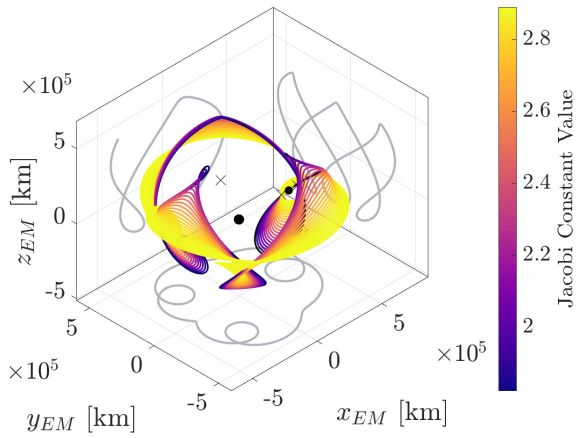

(e) 3 : 4 resonant orbit family

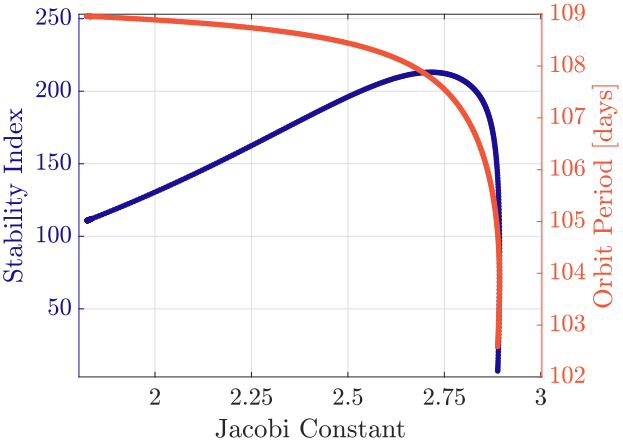

(f) 3 : 4 stability and period evolution

Figure 4.10. Families of spatial resonant orbits corresponding to various $3:q$ resonant ratios obtained in the Earth-Moon CR3BP.

repeatability with respect to the orientation of the Sun in the Earth-Moon rotating frame. This characteristic is particularly relevant for Space Situational Awareness (SSA) operations beyond the vicinity of the Earth, where illumination and visibility conditions are evaluated [29].

As an example, consider the orbits illustrated in Figure 4.11 that represent members from the $4:2$ and $5:3$ sidereal resonant orbit families. The two orbit families are produced from period-doubling bifurcations from the planar $2:1$ resonant orbit family. Because of the nature of the bifurcation, the periods of the resulting orbits in the rotating frame are longer and approximately twice the lunar sidereal period. Apparent from the geometry of the orbits in Figure 4.11(a), a spacecraft in this orbit encounters the Moon twice over two sidereal periods. There exists a repeating pathway from the Earth to the Moon, followed by a natural return towards the vicinity of the Earth. This return is followed by an excursion out towards L_3 and back towards the Earth and the GEO belt in the prograde direction. At the half-period mark, or after approximately one sidereal period, a second lunar encounter occurs, causing a shift in the osculating Right Ascension of the Ascending Node (RAAN) for the orbit. The spacecraft then departs on this shifted plane towards the Earth and L_3 and eventually returns to the Earth.

The evolution of the family of orbits and their characteristics is more complex in the example of the second orbit family that appears in Figure 4.11(c). In this case, the planar bifurcating orbit is characterized by a period that is longer than the lunar sidereal period. The resulting spatial orbit, thus, possesses a period that is longer than twice the sidereal period. This deviation from the predicted $4:2$ resonance grows larger as the orbit family is numerically continued farther beyond the Earth-Moon plane due to an increase in the orbital period. Additionally, the geometry of the orbits evolves to accommodate the increased period, with the appearance of an additional apoapse, i.e., *loop* in the rotating frame. As a result, these orbits are denoted the $5:3$ spatial resonant orbit family. In contrast to the $4:2$ spatial orbits, these orbits do not pass near the GEO belt. Nevertheless, the orbits, with options possessing large $\hat{\boldsymbol{z}}$ amplitudes, span the cislunar volume and are operationally stable.

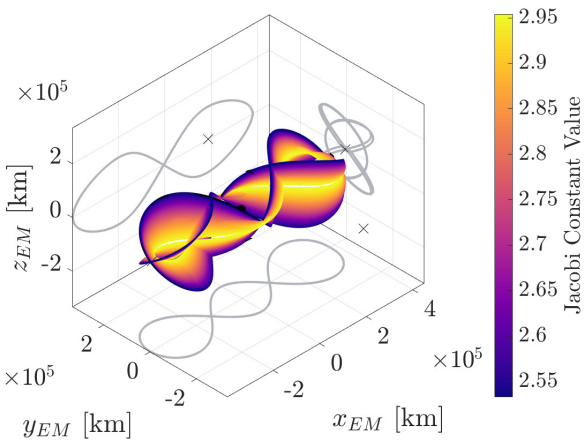

(a) 4 : 2 resonant orbit family

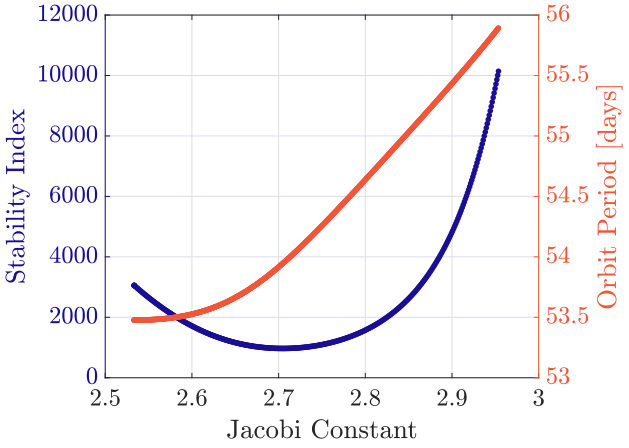

(b) 4 : 2 stability and period evolution

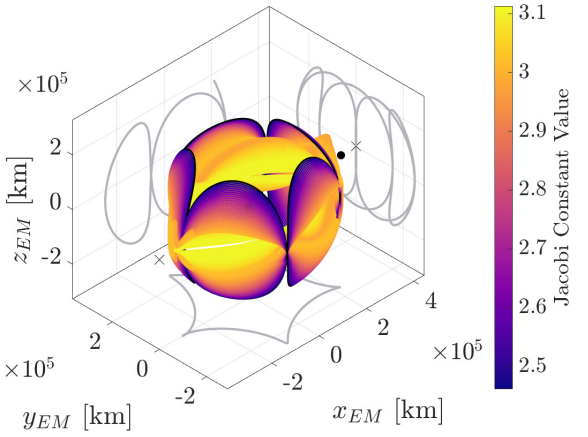

(c) 5 : 3 resonant orbit family

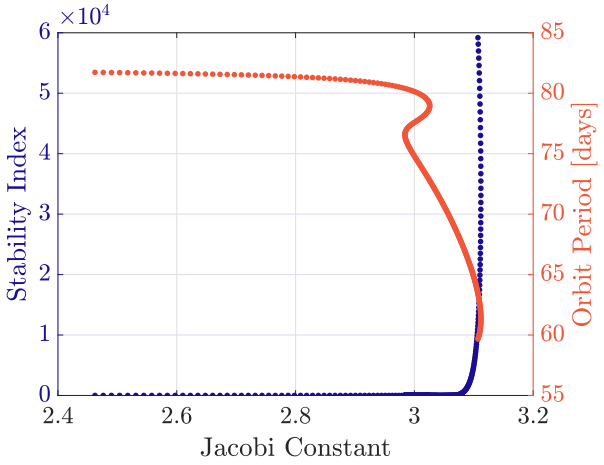

(d) 5 : 3 stability and period evolution

Figure 4.11. Families of spatial resonant orbits that bifurcate from the prograde 2 : 1 planar resonant orbit family.

Interestingly, the evolution of the orbital period as a function of the Jacobi constant for the 5 : 3 family appears as the red curve in Figure 4.11(d). Orbits with higher $\hat{\boldsymbol{z}}$-amplitudes, i.e., larger excursions beyond the Earth-Moon plane, exist at lower values of Jacobi constant (higher energies) and possess longer periods. By visualizing the ratio of the lunar synodic period, 29.53 *days*, with the period of each orbit along the family, orbits that are in synodic resonance are identified. Figure 4.12(a) illustrates this ratio of periods as a function of the Jacobi constant, where the black line identifies a member from the orbit family that is in 2 : 5 synodic resonance (or 1:$\frac{5}{2}$). This synodic resonance implies that, for every two revolutions of this orbit in the rotating frame, the Moon completes five synodic periods. The synodic resonant orbit is plotted as viewed in the Earth-Moon rotating frame in Figure 4.12(b) in blue; the orbit in black illustrates a lower-amplitude orbit in the family to demonstrate the evolution of the orbit geometry along the family. While the synodic resonant orbit does not approach as closely to the GEO belt (plotted in grey) as other interior resonant orbits, it does cover the Earth-Moon volume substantially with close lunar flybys.

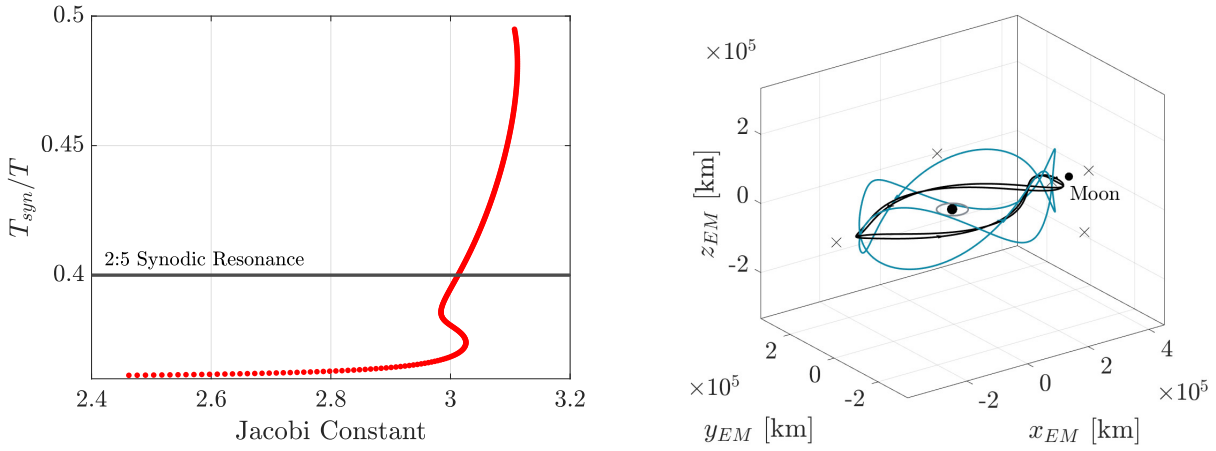

(a) Period across the family

(b) Bifurcating and synodic resonant members

Figure 4.12. Evolution of the orbital period for the sidereal 5:3 sidereal resonant family. The bifurcating (black) and synodic resonant (blue) orbits appear in the Earth-Moon rotating frame.

While the sidereal resonant orbit with a synodic overlap as identified in Figure 4.12 provides one option with utility for cislunar operations, other near-sidereal resonant orbits exist that are commensurate with the lunar synodic period as well. Especially from the planar

families of resonant orbits, due to the large ranges of orbital periods spanned by the family, more options for orbits that exhibit a sidereal-synodic overlap are identified. Figure 4.13 illustrates sample planar sidereal resonant orbits that possess synodic resonant members. The vertical axes in the left column of the plots in Figure 4.13 represent the ratio of the lunar synodic period, approximately 29.53 *days*, with the period of the orbits in the family as evaluated in the rotating frame. Integer ratios from these plots are identified, highlighting several options for orbits with the sidereal-synodic overlap. However, for practical purposes, it is useful to consider the orbits that exhibit a smaller resonance order, since those members tend to possess shorter periods in the rotating frame. Figures 4.13(b), 4.13(d) and 4.13(f) illustrate selected synodic resonant members from their sidereal resonant orbit families. As expected, the orbits display their characteristic sidereal resonant geometries, with the added advantage of synodic resonance with the Moon.

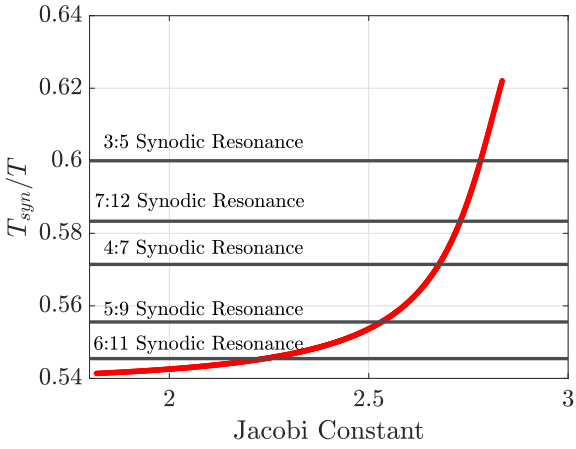

(a) 1 : 2 family

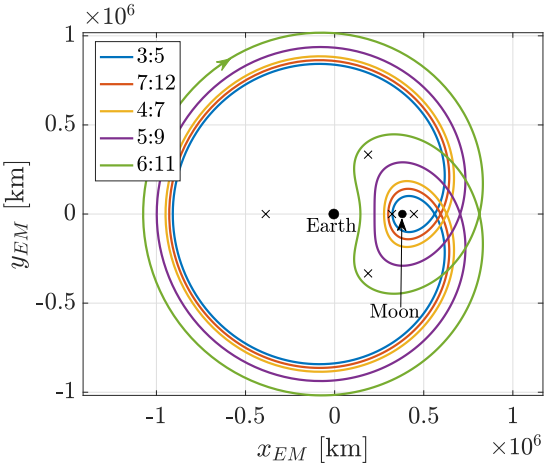

(b) Synodic resonant orbits

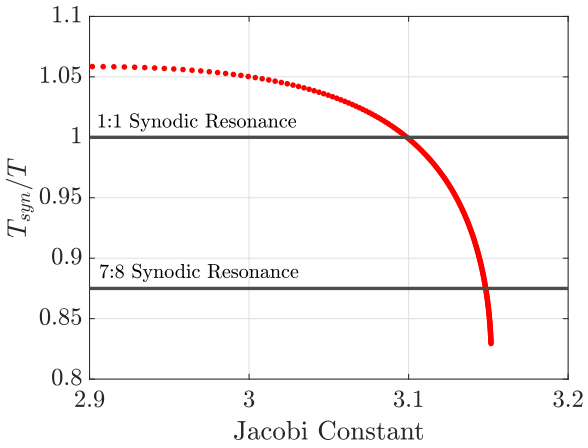

(c) 2 : 1 family

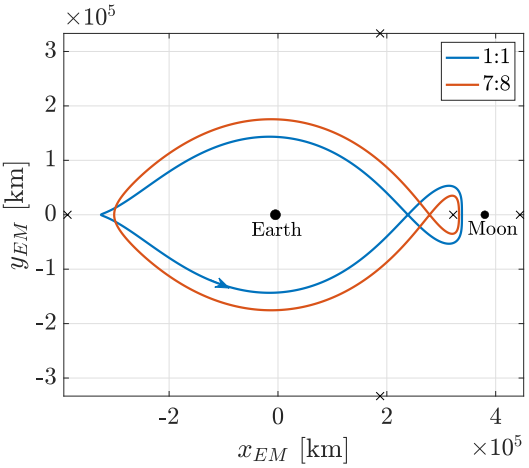

(d) Synodic resonant orbits

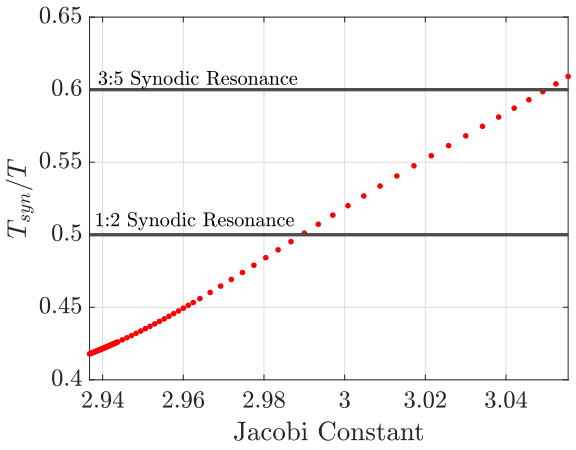

(e) 4 : 3 family

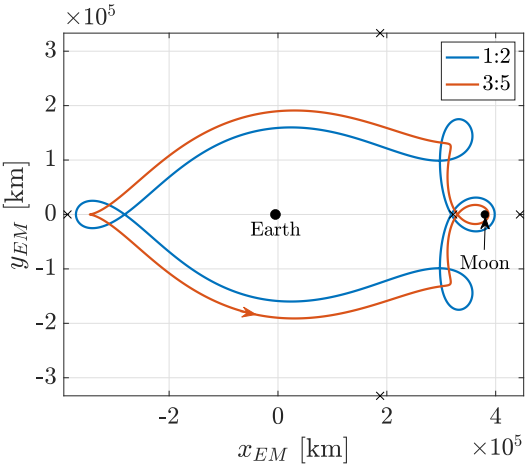

(f) Synodic resonant orbits

Figure 4.13. Members from various planar sidereal resonant orbit families with orbits that are commensurate with the lunar synodic period.

5. CONSTRUCTION OF RESONANT TRAJECTORIES FOR REPEATING EARTH-MOON ACCESS

There is increasing general interest in trajectories within the cislunar regime in support of wide ranging types of activities, including Space Domain Awareness (SDA) and Space Situational Awareness (SSA) operations. The expanse of cislunar space, extending beyond the geosynchronous (GEO) belt and towards the lunar orbit, necessitates trajectories that are able to span this vast volume while maintaining Earth access [64]. To design trajectories to sustain commercial activities, aid surveillance applications, and consistently monitor cislunar space, orbits with repeating geometries under natural dynamical motion offer clear advantages. Earth-Moon sidereal resonant orbits naturally remain phased with the lunar orbit while also traversing various different regions within cislunar space, and providing a recurring link between the lunar vicinity and the near-Earth region. The availability of natural dynamical structures in the vicinity of the resonant orbits allows additional options for expanding the scope of cislunar coverage. Sample orbits in a $2:1$ sidereal resonance are identified as appropriate options to support and maintain a long-term presence in cislunar space. Such orbits are constructed in the Earth-Moon CR3BP and validated in the HFEM to assess their utility for space applications. In light of operational considerations in cislunar space and, specifically, eclipsing due to the Earth and the Moon, techniques to identify and mitigate eclipses for sidereal resonant trajectories are introduced.

5.1 Earth-Moon 2:1 Sidereal Resonant Orbits

With their expansive geometries and availability at various energy levels, orbits characterized by different sidereal resonant ratios with the Moon provide a wide array of options for cislunar applications. Periodic orbits in a $2:1$ resonance with the lunar sidereal period are of particular interest for applications focused towards suppporting cislunar SSA, due to their shorter orbital periods and geometries that allow recurring and rapid access between the Earth and the Moon. These $2:1$ orbits may be retrograde or prograde relative to the Earth, possessing periods that are approximately equal to the lunar sidereal period in the

rotating frame. In Figure 5.1, members from the retrograde and prograde orbit families in 2 : 1 resonance are plotted as viewed in the Earth-Moon rotating and Earth-centered inertial frames, where each orbit is colored by its Jacobi constant value. In each plot, the orbit in black highlights the direction of motion along the orbit. Due to natural resonance with the lunar orbit, a spacecraft placed in an orbit from either family completes two revolutions about the Earth in approximately the time that the Moon requires to complete one Earth revolution. This fact is evident by visualizing the motion in the Earth-centered inertial frame, as demonstrated in Figures 5.1(c) and 5.1(d), where each *elliptical lobe* corresponds to a time of flight (TOF) of approximately half the lunar sidereal period. Between the two families, a wide range of Jacobi constant values and, thus, energy options are available.

Due to their retrograde nature, the retrograde orbits in Figure 5.1(a) are characterized by lower Jacobi constant values and relatively higher energies. Within the subset of these orbits, the members possessing higher values of Jacobi constant undergo natural apsidal precession against the lunar orbit with each subsequent lunar encounter. This characteristic, predictably, only appears for orbits with lower perigee radii and apogees close to the lunar orbit, i.e., the more "eccentric" orbits. Because of their characteristic low Jacobi constant (high energy) values, transfers to and from other dynamical structures and orbits of interest may necessitate significant propellant costs. However, these properties render these 2 : 1 orbits operationally stable and potentially useful for surveillance missions.

The prograde orbit family, as seen in Figure 5.1(b), exists in a higher Jacobi constant range of values and possesses lower energies. As apparent in the rotating frame view, as these orbits evolve, they deliver a considerable coverage of the Earth-Moon plane as well, most notably providing access from the vicinity of the Earth out towards the Moon in the prograde direction. Because of their resonant nature, this Earth-Moon access naturally repeats with every period of these orbits as well. Apsidal precession is also observed in the prograde orbit family, where orbits with lower perigee radii appear more eccentric and precess in the same direction as the motion of the Moon in its orbit. In the inertial frame views in Figures 5.1(c) and 5.1(d), the dashed curve represents the lunar orbit – the higher the Jacobi constant value, the further the orbit extends towards the orbit of the Moon with an increasing value of its maximum radius relative to the Earth.

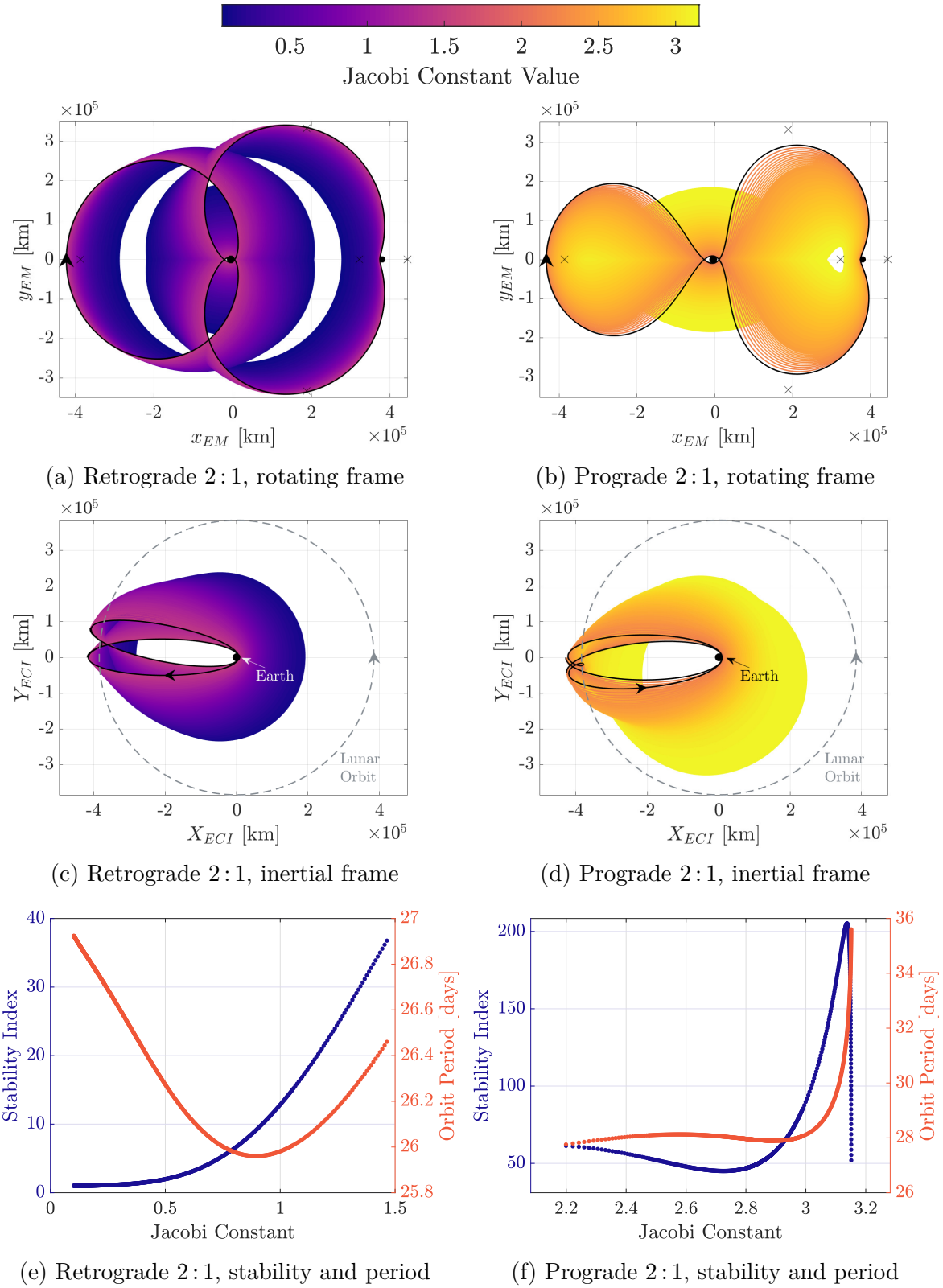

(a) Retrograde 2 : 1, rotating frame

(b) Prograde 2 : 1, rotating frame

(c) Retrograde 2 : 1, inertial frame

(d) Prograde 2 : 1, inertial frame

(e) Retrograde 2 : 1, stability and period

(f) Prograde 2 : 1, stability and period

Figure 5.1. Members from the Earth-Moon 2 : 1 retrograde and prograde resonant orbits constructed in the CR3BP.

For the subsets of the retrograde and prograde 2 : 1 resonant orbit families in Figure 5.1, the stability indices are evaluated and plotted in blue in Figures 5.1(e) and 5.1(f) as a function of the Jacobi constant value. For the retrograde family, the orbits become linearly unstable as the Jacobi constant increases. While the orbits are linearly unstable, the magnitude of the stability index is relatively small, indicating that the invariant manifolds associated with the orbit remain in the vicinity of the orbit for several revolutions before their eventual departure. For reference, the period of the orbits appears in red in Figure 5.1(e) as well. Overall, the periods are shorter than the lunar sidereal period; the retrograde apsidal precession in the inertial frame arises as a result, where the spacecraft appears to move against the lunar orbit to maintain the near-resonance.

A similar evolution of the stability indices and orbital periods for the prograde 2 : 1 family appears in Figure 5.1(f) in blue and red, respectively. The prograde orbits tend to be more unstable than their retrograde counterparts and, while the orbital period is approximately equal to the lunar sidereal period for a majority of the orbits, the orbits with higher Jacobi constant values possess significantly longer periods. The higher magnitude of the stability index suggests the existence of strong unstable and stable manifolds associated with these orbits that further extend the natural reach of spacecraft moving along these orbits.

5.1.1 Mapping the Cislunar Plane

With their unique geometries, several orbits from the family for both retrograde and prograde 2 : 1 resonant orbits present convenient opportunities for cislunar observation. However, of particular interest are orbits that guarantee natural ballistic access between the Earth and the Moon. As an example, from Figure 5.1(a), an orbit with a radius of perigee equal to the radius of the geosynchronous orbit (GEO) is identified. A spacecraft on this orbit repeatedly approaches and departs the GEO belt in the retrograde direction. In addition to providing access to GEO, the same orbit spans out to the vicinity of the Moon and the L_1 libration point on the Earth-outbound leg. Since the orbit is periodic, this GEO-Moon passage recurs with every revolution, approximately once every lunar sidereal period. As such, this particular orbit provides repeated direct links between the more familiar and

accessible GEO region, and the outer reaches of cislunar space in the neighborhood of the lunar orbit. Figure 5.2(a) illustrates a view of the orbit in the Earth-Moon rotating frame, and Section 5.1.1 summarizes the relevant orbital characteristics. The orbit possesses a low Jacobi constant value of 0.8964. This value corresponds to a relatively high orbital energy, not surprising given the size of the orbit. Additionally, although the resonance ratio is not a perfect integer, the orbit is closed and periodic as observed in the rotating frame.

Table 5.1. Characteristics of the selected 2 : 1 resonant orbits.

Orbit	**Jacobi Constant**	**Period** [days]	**Stability Index**
Retrograde 2 : 1	0.8964	25.96	8.59

Due to this favorable pathway connecting these high-interest cislunar subspaces, this particular orbit, with a perigee radius approximately equal to $42,164$ km, is selected for further analysis as a sample scenario. The time of flight between the GEO belt and the perilune radius of the orbit, and vice versa, is approximately 7.15 *days*. A spacecraft in this orbit is able to depart the Earth from the GEO region in the retrograde direction, approach the Moon to within $8,500$ km of the lunar surface, and return to the GEO belt, again in the retrograde direction, within a 14.3 *day* time frame. Again, it is noted that due to the periodicity of the orbit, this 14.3 *day* span for a GEO-Moon-GEO transit repeats approximately once a month.

When the orbit is propagated for about 20 revolutions (approximately 507 *days*) using the CR3BP equations of motion, the resulting trajectory completely maps out the Earth-Moon planar subspace of the cislunar region without deviations from its inherent geometry. This multi-revolution trajectory is plotted in Figure 5.2(c) as viewed in the Earth-centered inertial frame, with the arrow indicating the retrograde nature of this trajectory. An operational advantage of the orbit is that, due to the lunar sidereal resonance, the natural precession observed in the inertial frame persists with subsequent revolutions as well. Additionally, note that the inherent retrograde 2 : 1 orbit geometry is maintained over this 507 *day* period as viewed in the Earth-Moon rotating frame for 20 revolutions in Figure 5.2(a).

A prograde resonant counterpart is identified from Figure 5.1(b), one that possesses a perigee radius equal to the radius of GEO. The relevant characteristics for this orbit are listed in Section 5.1.1. The perilune altitude for this orbit is approximately $8,330\ km$. This orbit possesses a higher Jacobi constant value and period than its retrograde counterpart. With the longer period, the time of flight from GEO to the Moon, and vice versa, is approximately 7.82 *days*, which repeats with successive revolutions. Figure 5.2(d) illustrates multiple revolutions of the orbit as seen in the Earth-centered inertial frame. Because of the longer period of the orbit relative to its retrograde $2:1$ counterpart, and due to smaller precession after subsequent lunar encounters in the inertial frame, it requires a significantly longer interval for the orbit to completely map the Earth-Moon plane in the inertial frame. Specifically, it requires 34 revolutions (approximately 956 *days*) to map the Earth-Moon planar subspace. Despite the shifting apogee as apparent in the inertial frame, the orbit perigee maintains tangency with the GEO belt, that appears in grey for reference. This particular multi-revolution trajectory associated with the prograde $2:1$ resonant orbit, as seen in the Earth-Moon rotating frame, is plotted in Figure 5.2(b).

5.1.2 Lunar Free Returns

When considering pathways that traverse between the GEO belt and the vicinity of the Moon, it is also useful to investigate lunar free return trajectories. Within the context of the Earth-Moon domain, lunar free returns are trajectories that transfer from the Earth to the lunar vicinity and, without requiring any propulsive maneuvers, return to the vicinity of the Earth [65]. These trajectories were exploited in the Apollo era, guaranteeing safe crew return in case of emergencies or communications disruptions. For supporting mission operations in cislunar space, such trajectories are, thus, potential avenues for transfer options between the Earth and the Moon, without risking the loss of spacecraft. For transit specifically from the GEO belt, it is useful to assess the transfer times and energy levels of lunar free returns against those of the $2:1$ resonant orbits identified in Section 5.1.1.

Lunar free returns are typically constructed from an Earth-centered departure ellipse and a Moon-centered hyperbola, where the hyperbola shifts the velocity vector by a sufficient

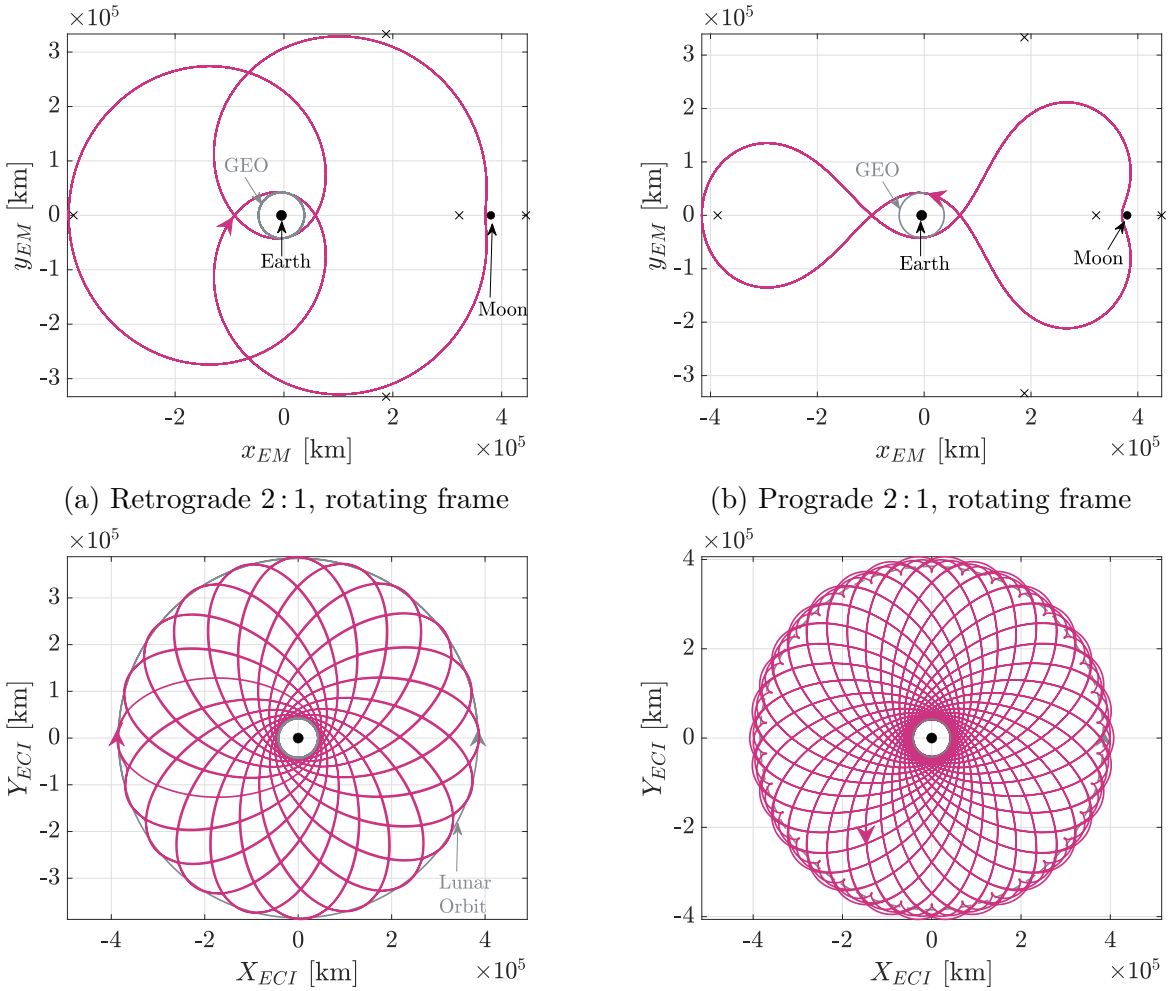

(a) Retrograde 2 : 1, rotating frame

(b) Prograde 2 : 1, rotating frame

(c) Retrograde 2 : 1, inertial frame

(d) Retrograde 2 : 1, inertial frame

Figure 5.2. Retrograde and prograde 2 : 1 sidereal resonant orbits with perigee radii equal to the geosynchronous orbit radius propagated for multiple revolutions in the CR3BP.

margin to guarantee an Earth return. Because of the close proximity to both the Earth and the Moon, the CR3BP serves as the appropriate dynamical model in the generation of such trajectories. Lunar free returns are characterized as being either cislunar, where the perilune lies between the Earth and the Moon, or circumlunar, with a perilune that occurs on the lunar far-side. These trajectories also exhibit varying characteristics depending upon whether their Earth-departure orbits are prograde or retrograde. Finally, while spatial free returns exist, only Earth-Moon planar trajectories are investigated here for a direct comparison against the 2 : 1 resonant orbits.

Free returns in the CR3BP were originally analyzed in-depth by Schwaniger [66], who numerically targeted free returns in the Earth-Moon system. In this investigation, the methodology detailed by Pavlak is adopted for the construction of planar free return trajectories in the Earth-Moon CR3BP [67]. Similar to the determination of sidereal resonant orbits, this approach relies on transitioning a two-body initial guess to the CR3BP using differential corrections techniques. The process initiates at the periapsis of the Earth-centered ellipse, termed the translunar injection (TLI) point. A summary of the process is as follows:

1. The initial Earth-centered TLI states are determined in the inertial frame.
2. The states are transformed to the Earth-Moon rotating frame, centered on their barycenter.
3. The trajectory is propagated to produce the final velocity at a crossing of the $\hat{\boldsymbol{x}}$-axis near the Moon.
4. Differential corrections are applied to render the $\hat{\boldsymbol{x}}$-component of the final velocity equal to zero, yielding a perpendicular crossing of the $\hat{\boldsymbol{x}}$-axis.

Since these free returns are symmetric, only the outbound leg of the trajectory (i.e., departing from the Earth) is targeted numerically. Additional constraints, namely Earth departure altitude, lunar arrival altitude, and Earth departure flight path angle are incorporated into a multiple shooting scheme to compute the desired free return trajectory [67]. Once a lunar free return trajectory is generated, natural parameter continuation in the perigee/perilune altitude produces *families* of free returns. For this investigation, continuation in perilune altitude is considered to analyze the evolution in the time of flight and Jacobi constant value along the family of trajectories that depart from the GEO belt.

To obtain a direct comparison against the $2:1$ sidereal resonant orbits, consider an Earth-departure altitude of $35,700\ km$, approximately equal to the altitude of the GEO belt. A fixed Earth-departure flight path angle of 0° is assumed. Then, perilune altitudes at lunar arrival are varied to construct a family of free return trajectories for the same departure location from the Earth. These families are either circumlunar (i.e., perilune occurs at the lunar far-side), or cislunar (perilune occurs at the lunar near-side), and depart along both

the retrograde and prograde directions. All four cases appear, plotted in the Earth-Moon rotating frame, in Figure 5.3. For clarity in their geometries, only the Earth-outbound legs for the free return trajectories appear. Additionally, while there exists a perpendicular crossing of the $\hat{\boldsymbol{x}}$-axis at perilune for all trajectories, the departure from Earth is *not* a perpendicular crossing. Thus, at the TLI point and at the end of the symmetric Earth-inbound leg (not shown), the trajectories do not close, i.e., they are not periodic orbits. In each family in Figure 5.3, the lunar arrival altitude varies between $1,500$ km and up to $20,000$ km. Each trajectory is colored by its Jacobi constant value.

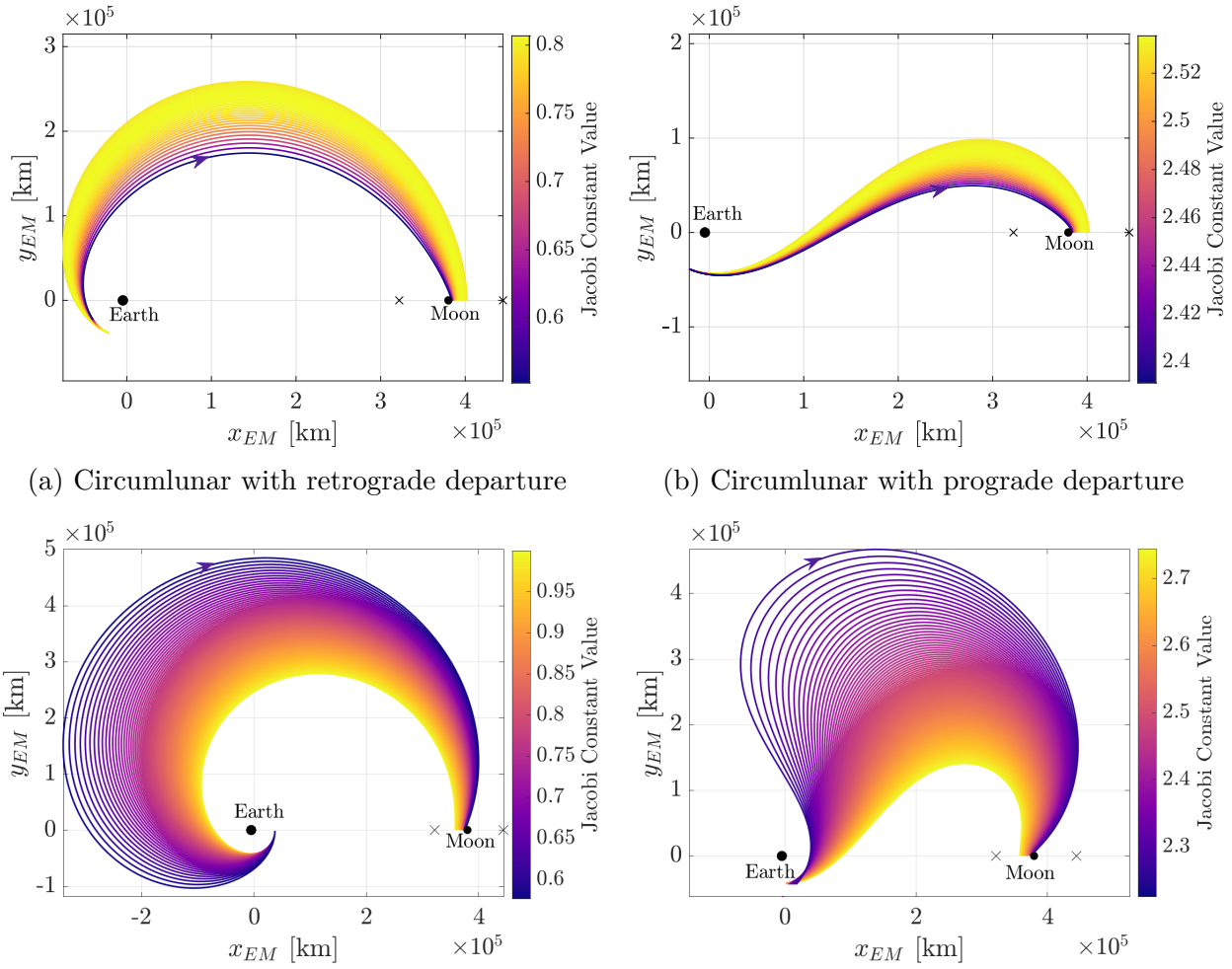

(a) Circumlunar with retrograde departure

(b) Circumlunar with prograde departure

(c) Cislunar with retrograde departure

(d) Cislunar with prograde departure

Figure 5.3. Families of lunar free return trajectories departing from a $35,700$ km altitude Earth orbit constructed in the Earth-Moon CR3BP.

The variation in the one-way time of flight and the associated Jacobi constant value for each of the four free return cases is plotted in Figure 5.4 as a function of the perilune altitude. In each plot, the solid curves represent prograde departures from the Earth departure orbit, while retrograde departures are reflected along the dashed curves. Figure 5.4(a) represents the characteristics of circumlunar free returns, where the one-way TOF increases with an increase in the perilune altitude. There is a significant Jacobi constant gap in the prograde-departure (solid) and retrograde-departure (dashed) curves, due to the high energy of the retrograde trajectories. The planar free returns that depart the Earth along the prograde direction arrive at their respective lunar orbits sooner than the trajectories departing the Earth in the retrograde direction. In general, the circumlunar free returns exhibit relative short times of flight, bounded between approximately 3.5 and 5.5 *days*.

Similarly, Figure 5.4(b) summarizes the characteristics of the cislunar free returns plotted in Figures 5.3(c) and 5.3(d). It is immediately apparent that for departures from the same Earth orbit, cislunar free returns take significantly longer to arrive at the same perilune altitude as their circumlunar counterparts. The TOF range spanned by these trajectories is between 6 and 15 *days*. Additionally, the times of flight decrease as a function of increasing perilune radius, also evident in Figure 5.3(d) and Figure 5.3(c), where the $\hat{\boldsymbol{y}}$-amplitude of the trajectories decreases as the arrival location moves further from the Moon.

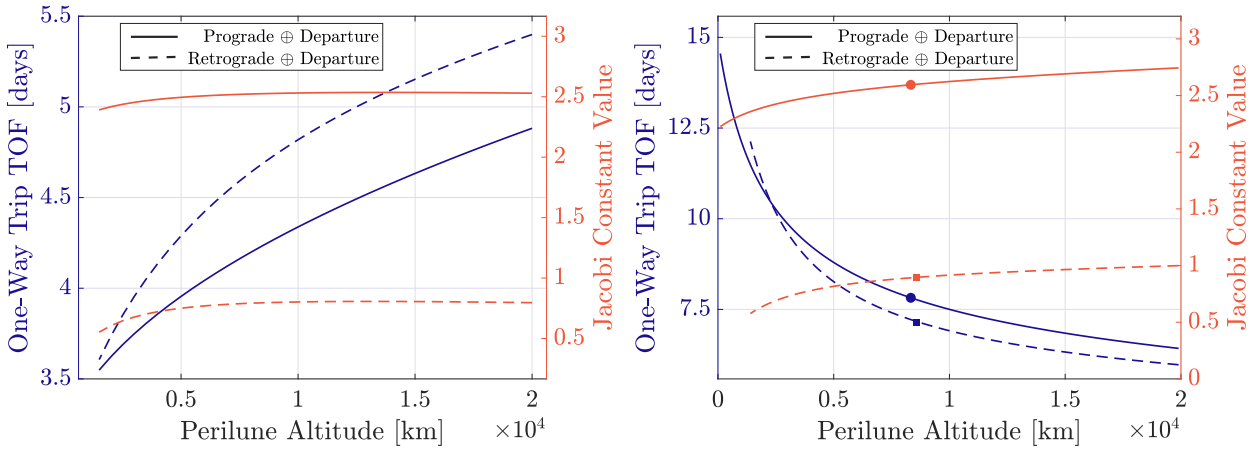

(a) Circumlunar free returns

(b) Cislunar free returns

Figure 5.4. Evolution of one-way time of flight and the Jacobi constant value for circumlunar and cislunar free returns as a function of the perilune radius.

While circumlunar free returns provide lunar far-side access, further analysis of the cislunar free returns yields direct comparisons against the 2 : 1 retrograde and prograde resonant orbits that are tangent to the GEO belt. For accessing higher perilune altitudes, the families of cislunar free returns provide options for faster transit from the GEO region to the vicinity of the Moon, as evident in Figure 5.4(b). For reference, the outbound times of flight of the retrograde and prograde 2 : 1 sidereal resonant orbits are indicated for their corresponding perilune altitudes by the square and circular markers, respectively, along the blue curves. The Jacobi constant values of the orbits are also indicated on the red curves in Figure 5.4(b).

Immediately, a relationship between these sidereal resonant orbits and the family of lunar free returns departing from the same Earth-altitude is identified. For periodicity, the free returns must cross the $\hat{\boldsymbol{x}}$-axis perpendicularly at perilune; additionally, the Earth-outbound time of flight must be approximately one-fourth of the lunar sidereal period. Certain combinations of Earth-departure altitudes and lunar arrival altitudes for cislunar free returns yield periodic orbits that exist in a 2 : 1 sidereal resonance with the Moon. In the example trajectories departing from GEO in Figures 5.3(c) and 5.3(d), the corresponding periodic lunar free returns are actually the 2 : 1 resonant orbits identified in Section 5.1.1. Due to the inherent constraints on the period of resonant orbits, not all lunar free returns are resonant periodic orbits. Specifically, circumlunar free returns are defined by shorter times of flight and, thus, cannot satisfy the natural resonance criterion. Cislunar free returns exhibit longer times of flight and, when propagated for longer times, demonstrate near-resonant periodic behavior. Thus, the lunar free returns that are closed periodic orbits in the rotating frame exist in a 2 : 1 sidereal resonance with the Moon. While non-periodic lunar free returns provide options for rapid transfers from the Earth to the lunar vicinity, periodic lunar free returns provide repeating options that sustain the transfer pathways for months.

5.1.3 Access to the Lunar Far-Side

From a more comprehensive support infrastructure in cislunar space, it may be necessary to access the lunar far-side. Specifically, observations from the vicinity of the Earth-Moon L_2 libration point and, consequently, the lunar far-side can enable SSA operations where

direct line-of-sight with the Earth is not always available. Since they do not circumvent the lunar orbit, the retrograde and prograde families of $2:1$ resonant orbits are suited for interior observations and providing pathways within the volume encompassed by the lunar orbit. As such, access to the near-side of the Moon only is directly available via these orbits, and opportunities for obtaining observations of the lunar far-side are lacking. However, while the $2:1$ prograde resonant orbits remain circumlunar themselves, the natural flow associated with these orbits allows access to the far side of the Moon via invariant manifolds. The linear instability of the prograde $2:1$ resonant orbits is, thus, exploited in designing trajectories that yield periodic excursions to the lunar far-side. Periodic orbit chains are constructed that extend the range of access to the lunar far-side.

The $2:1$ prograde resonant orbit with a perigee radius equal to the radius of GEO is selected to design trajectories that enable lunar far-side access. Noting the instability of the selected prograde resonant orbit, as mentioned in Section 5.1.1, its invariant manifolds are constructed to identify excursions from the underlying periodic orbit. Trajectories that lie on its stable manifold asymptotically approach the orbit over time, while trajectories on its unstable manifold depart the orbit when propagated in forward time. By leveraging Poincaré maps, trajectories on these manifolds that traverse beyond the Moon are identified.

To obtain the trajectories on its invariant manifolds, the orbit is discretized into 500 fixed points. From each fixed point, a manifold step-off value of $d = 40\ km$ is employed to step along the associated unstable and stable eigenvector directions. For this example, Poincaré maps are constructed by locating the hyperplane, Σ, at $y = 0$. The Jacobi constant value for the map is fixed and, in this case, equal to the Jacobi constant of the selected $2:1$ resonance at $C = 2.5946$. The manifold trajectories are propagated for 30 nd, that is approximately equal to 130 $days$ or 5 revolutions of the underlying orbit. While propagating for long times is not necessary, it encompasses any deviations from the periodic orbit that may yield useful excursions. The intersections with the hyperplane of the trajectories on the stable and unstable manifolds are recorded. Since the orbit and its manifold trajectories are planar, the full 4-dimensional state corresponding to each intersection with the hyperplane is available.

The x-$\dot{x}$ projection of the Poincaré map appears in Figure 5.5, where returns associated with trajectories on the stable manifold appear in blue, and returns of the unstable manifold trajectories appear in red. The location of the Moon is indicated by the solid black marker. Additionally, bounds on the returns of the manifold trajectories appear as black curves computed via the ZVCs at this Jacobi constant value.

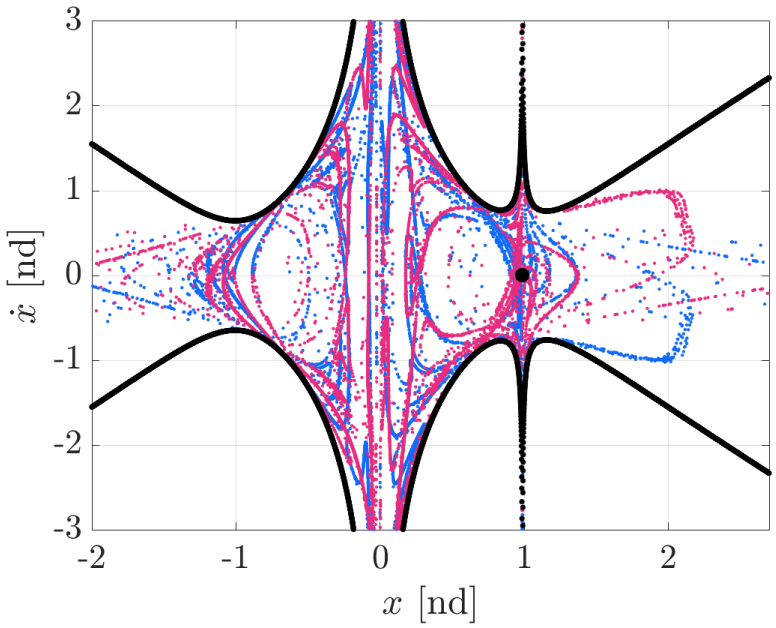

Figure 5.5. Poincaré map ($\Sigma : y = 0$) for the returns of the stable (blue) and unstable (red) manifold trajectories for the prograde $2:1$ resonant orbit.

Of particular interest are the locations on the map where the stable and unstable returns intersect, as these indicate the existence of a homoclinic connection to the orbit. A homoclinic connection is a maneuver-free transfer trajectory that connects the orbit to itself, allowing deviations from the orbit geometry while guaranteeing a return to the periodic orbit [50]. While the Poincaré map depicts several homoclinic connections, intersections that correspond to an $\hat{\boldsymbol{x}}$-value beyond the Moon are of interest, since the underlying trajectories are circumlunar. The trajectories would, thus, allow excursions to the lunar far-side from the original $2:1$ cislunar orbit. One such homoclinic connection is identified, corresponding to an $\hat{\boldsymbol{x}}$-value of approximately 1.378. Propagating the stable and unstable manifold trajectories

in forward and backward time, respectively, yields the trajectory in Figure 5.6 as viewed in the Earth-Moon rotating frame. The 2 : 1 resonant orbit appears in black, along with the radius of the GEO belt indicated by the grey circle. The intersection of the manifolds that is obtained from the Poincaré map in Figure 5.5 is represented by the black star. Clearly, the homoclinic connection preserves the geometry of the orbit, but with an acceptable deviation that allows circumlunar transit. Note that both forward/backward manifold trajectories possess the same energy value.

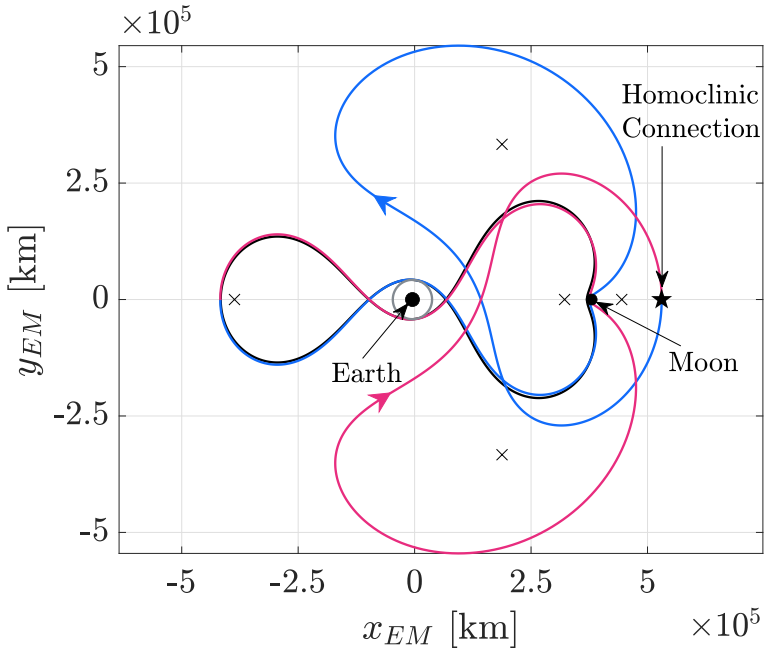

Figure 5.6. Homoclinic connection to the 2 : 1 resonant orbit.

Notably, the deviation in geometry for the underlying orbit, i.e., the 2 : 1 resonance that appears in black, originates from a Moon-centered orbit. Specifically, the structure of the manifold trajectories shadows the geometry of orbits belonging to the Moon-centered H_1 family of orbits [68]. The homoclinic connection identified in Figure 5.6 leverages the flow associated with the H_1 orbit at the same energy level as the 2 : 1 resonant orbit to achieve circumlunar access. Additionally, as observed in Figure 5.6, the selected stable and unstable manifold trajectories exhibit near-perpendicular crossings of the $\hat{\boldsymbol{x}}$-axis in the rotating frame. It is then possible to seed these manifold trajectories as initial guesses into a

perpendicular crossing targeter, producing a precisely periodic solution that shadows the flow associated with the homoclinic connection. This new periodic orbit appears in Figure 5.7 in the Earth-centered inertial and rotating frames and reflects the dynamical behavior of both the $2:1$ and the H_1 orbits at this energy level. This $2:1$-H_1 orbit *chain* possesses a period of approximately 87.93 *days* and reflects a geometry that provides excursions to the lunar far-side from the baseline prograde $2:1$ resonant orbit.

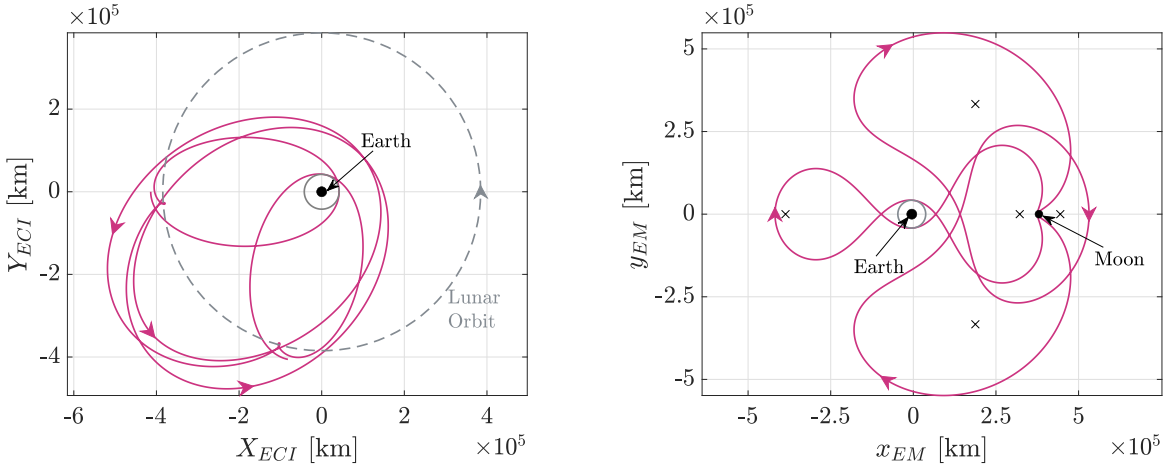

(a) Earth-centered inertial frame

(b) Earth-Moon rotating frame

Figure 5.7. Periodic orbit constructed via a homoclinic connection to the $2:1$ resonant orbit in the CR3BP.

As is true for all periodic orbits computed in the CR3BP, the existence of this new periodic orbit indicates the existence of a family of orbits with similar geometries. Figure 5.8(a) illustrates a subset of this orbit family as visualized in the Earth-Moon rotating frame, with the orbits colored by their respective Jacobi constant values. Evidently, the $\hat{\boldsymbol{y}}$-amplitude of the orbits reduces significantly as the Jacobi constant increases, indicating a decrease in the orbit period as well. The perigee radius increases, while the perilune radius decreases with an increase in the Jacobi constant value, with the smallest orbits "shrinking" closer to the lunar vicinity. The evolution of the orbital period and stability index as a function of the Jacobi constant appears in Figure 5.8(b). It is noted that the extent of the $2:1$-H_1 orbit family is restricted to the energy levels at which the underlying homoclinic connection exists [69].

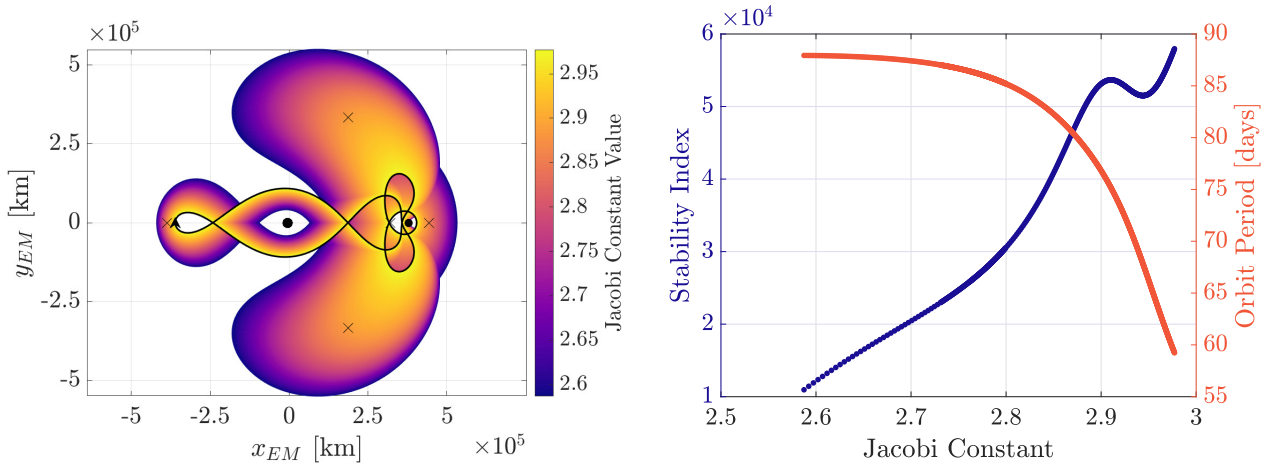

(a) Orbit family in the rotating frame

(b) Stability and period evolution

Figure 5.8. Family of the $2:1$-H_1 periodic orbits constructed in the Earth-Moon CR3BP.

5.2 Space-Based Observers in Retrograde Resonant Orbits

For the purposes of surveying cislunar space, trajectories for multiple space-based observers that together constitute a network of sensors is designed. Due to their unique geometries that span the Earth-Moon plane and their short periods, the $2:1$ retrograde and prograde families of resonant orbits identified in Figure 5.1 offer options to conduct observations in space. Specifically, the natural sidereal resonance allows the accessibility between the geosynchronous region and the lunar vicinity to persist for multiple revolutions. An accompanying advantage that arises due to this resonance is that the configuration relative to other spacecraft in similar orbits is sustained naturally with time as well. Thus, for a selected chief orbit, additional spacecraft located in nearby orbits from the same family naturally remain in the relative vicinity of other spacecraft in the network. Such a network of sensors is significant for surveying cislunar space and supporting Space Situational Awareness (SSA) needs. Each spacecraft in the system, together comprising a *constellation* of observers, is assumed to operate independently of the other spacecraft in the system. The resonance between the orbits and the Moon and, by design, other observers in the constellation, ensures that the relative phasing of the spacecraft in the constellation is naturally maintained, without necessitating active control for the baseline network [70], [71].

To demonstrate the design of a cislunar observer constellation, a spacecraft is placed in the $2:1$ retrograde orbit with perigee at GEO, and designated the chief. Recall that this particular orbit is defined with a Jacobi constant value of 0.8964 and a period of 25.96 *days*, as described in Section 5.1.1. As demonstrated in Section 5.1.1, the chief spacecraft situated in this orbit repeatedly and, without maneuvers, travels between the vicinity of the Earth and the Moon. Another observer, termed the deputy, is then placed in a second orbit from the family of $2:1$ retrograde orbits to facilitate observations and provide redundancy to sustain cislunar operations. The Jacobi constant value of this orbit is approximately 0.8721, and its period is 25.96 *days*. While the selection of the deputy orbit and the number of deputies is free, this example deputy orbit is determined such that the spacecraft remains over time within reasonable proximity of the chief vehicle. A long-term surveillance scenario is simulated by analyzing the chief and deputy trajectories over multiple revolutions. Specifically, 20 revolutions of both the spacecraft are propagated using the CR3BP equations of motion, that corresponds to approximately 507 *days*. The resulting trajectories are plotted in blue and pink for the chief and deputy, respectively, in the Earth-Moon rotating frame in Figure 5.9(b). In Figure 5.9(a), the Earth-centered inertial frame view of the trajectories is plotted as well, where the multiple revolutions of the orbits are more apparent. The natural $2:1$ sidereal resonance causes the orbits to continually precess in the retrograde direction, eventually overlapping themselves in the inertial frame as well.

The deputy orbit is defined such that its inertial precession is similar to that of the chief orbit, thereby guaranteeing that the relative configuration of the observers is generally maintained over time without requiring phasing maneuvers. Figure 5.10(a) and Figure 5.10(b) represent the distance between the spacecraft over one revolution (approximately 26 *days*) as well as the full 507-day period, respectively. This isochronous distance between the chief and the deputy over one period of the orbits, as plotted in Figure 5.10(a), remains bounded between 350 km and $8,500$ km, with their closest approach to each other occurring at perilune. Intuitively, the farthest separation between the spacecraft occurs when they are closest to the Earth.

The closest approach with the Moon occurs at an altitude of approximately $8,400$ km for the chief orbit, and at $8,700$ km for the deputy. These values, as illustrated in Figure 5.11,

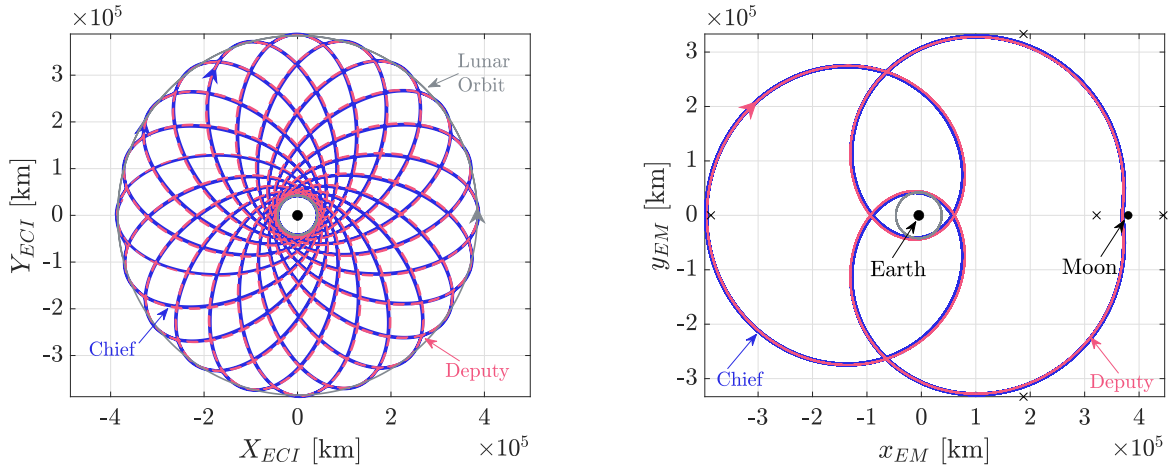

(a) Earth-centered inertial frame

(b) Earth-Moon rotating frame

Figure 5.9. Trajectories of the chief (blue) and deputy (pink) spacecraft constructed in the Earth-Moon CR3BP for 20 revolutions or approximately 507 *days*.

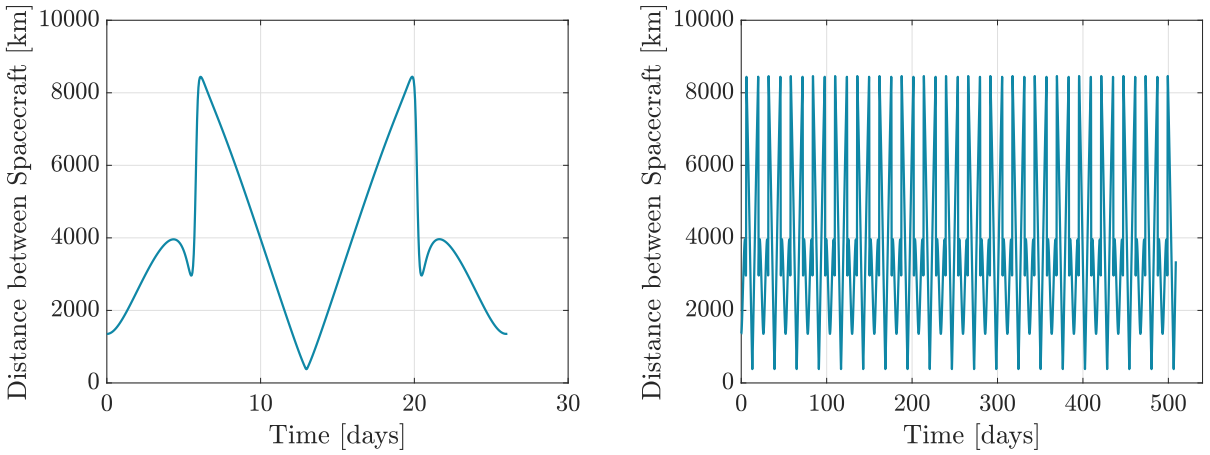

(a) Relative distance over one revolution

(b) Relative distance over 20 revolutions

Figure 5.10. Distance between the two spacecraft over one and 20 revolutions of the orbits in the CR3BP.

repeat for the full 20-revolution propagation and without deviation from the bounds seen over one period. Notably, the link between the vicinity of the Earth near GEO and the lunar vicinity is preserved for both the orbits over 20 revolutions, yielding opportunities for GEO-Moon-GEO transit once every month. It is also useful to assess the speed of the deputy relative to the chief and appears in Figure 5.12 as seen over one revolution and the 20

revolution case. For the majority of the propagation time, the speed of the deputy relative to the chief is below 100 m/s. Intuitively, the spikes that appear in Figure 5.12(a) align with the perigee locations of the spacecraft. Extending the analysis to the 20 revolution case, the relative speeds are consistently maintained without maneuvers.

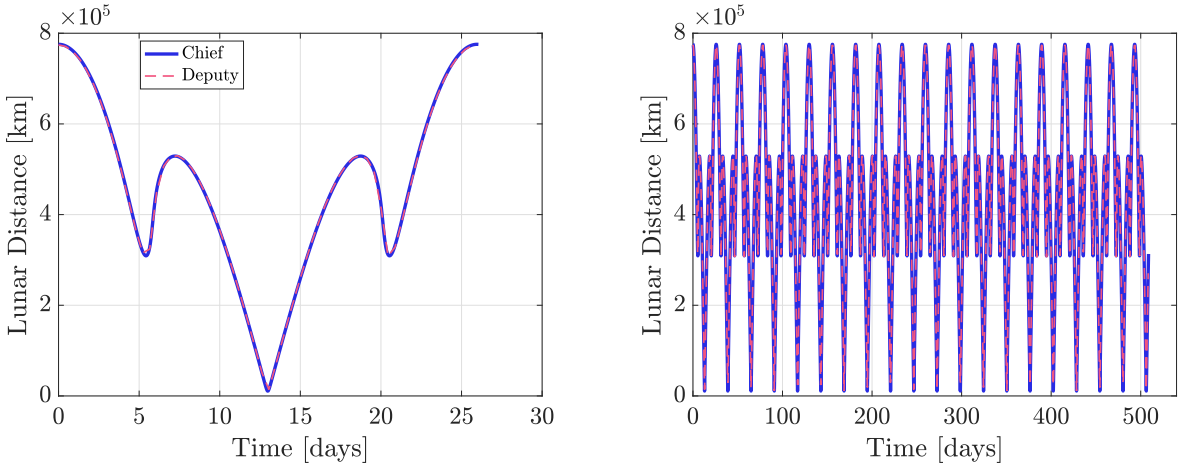

(a) Lunar distance over one revolution

(b) Lunar distance over 20 revolutions

Figure 5.11. Distance between the Moon and the chief (blue) and deputy (pink) over one and 20 revolutions of the orbits in the CR3BP.

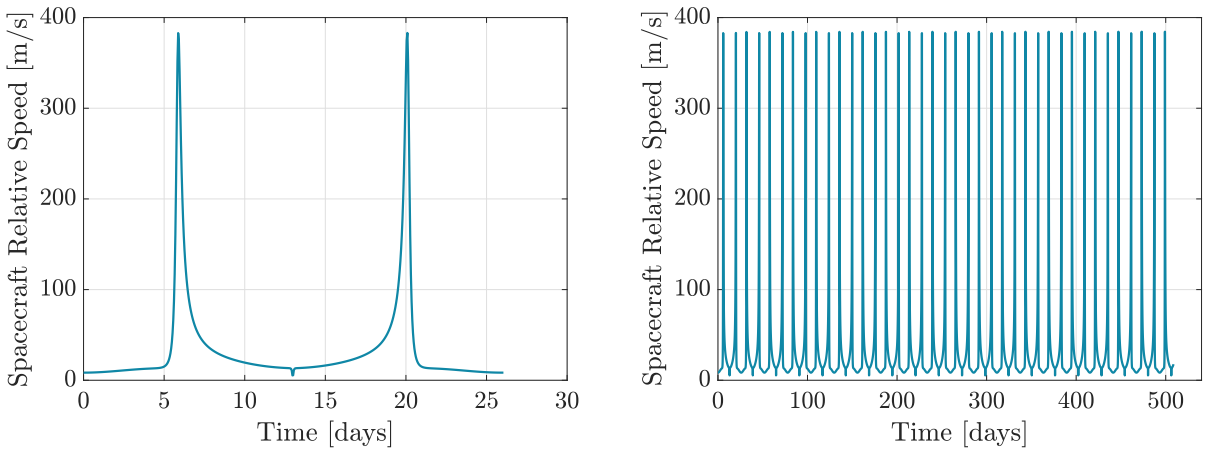

(a) Relative speed over one revolution

(b) Relative speed over 20 revolutions

Figure 5.12. Speed of the deputy spacecraft relative to the chief over one and 20 revolutions of the orbits in the CR3BP.

5.2.1 Validation in the HFEM

While the Earth-Moon CR3BP provides preliminary insight into the behavior of the trajectories, transitioning the trajectories into the HFEM delivers additional understanding into the dynamics of the underlying structures and their validity in the presence of perturbations. This fact is especially valid for long-term analysis, as in the case of the 507 *days*-long trajectories of the chief and the deputy spacecraft. The long-term behavior of two spacecraft in their respective orbits is modeled via the Earth-Moon-Sun-Jupiter HFEM, with the Earth selected as the central body.

To replicate the full mapping of the Earth-Moon plane seen in Figure 5.9(a), the CR3BP stack of 20 revolutions of the chief and deputy orbits is seeded into an ephemeris multiple shooting scheme. Considering the long duration targeted in this corrections scheme, the multiple shooting algorithm incorporates intermediate maneuvers along the trajectory to aid the convergence process such that the desired geometry is preserved [72]. As an example, four maneuvers of 100 m/s each are initially allowed over the course of the full stack for both sets of trajectories. The resulting converged ephemeris trajectory, with the intermediate maneuvers included, is then supplied as an initial guess to target the same trajectory with a reduced maximum allowable maneuver magnitude. Incrementally stepping down the maximum allowable maneuver magnitude, a completely ballistic ephemeris trajectory that is analogous to the ballistic CR3BP 20-revolution stack is constructed for both orbits.

The resulting ballistic ephemeris trajectories for both the chief and the deputy spacecraft appear in Figure 5.13. The Earth-centered inertial J2000 view of the trajectories appears in Figure 5.13(a), while the Earth-Moon rotating frame view is plotted in Figure 5.13(b). Note that while only the $\hat{\boldsymbol{x}}$-$\hat{\boldsymbol{y}}$ and $\hat{\boldsymbol{X}}$-$\hat{\boldsymbol{Y}}$ projections of the trajectories are plotted here, the trajectories exhibit spatial excursions in both frames. It is also apparent from both views in Figure 5.13 that, in configuration space, the ephemeris trajectories for both spacecraft retain their inherent CR3BP geometries, aided by the stacking corrections process. Additionally, recall that in the CR3BP, the 20-revolution trajectory maps the entirety of cislunar space (in the Earth-Moon plane) in approximately 507 *days*; in this ephemeris model, the same pattern appears over the course of 523 *days*. The ephemeris validation reveals additional

possible advantages of these retrograde resonances for space-based sensor applications. The clear recurring passageway between the GEO region and the lunar vicinity persists without deterministic maneuvers along the baseline paths. The perigee radii for both the chief and deputy spacecraft remain tangent to, or in the proximity of, the geosynchronous orbit radius.

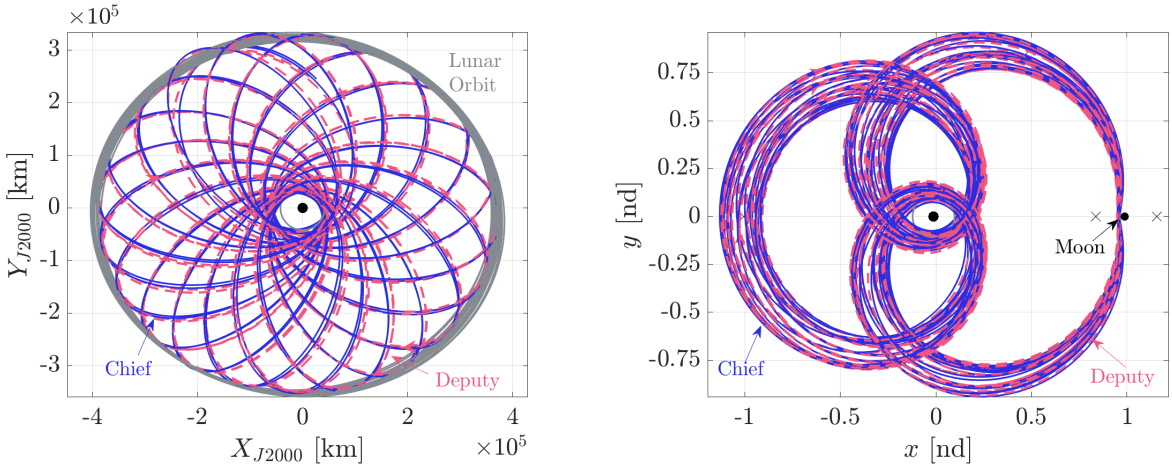

(a) ECI J2000 frame

(b) Earth-Moon rotating frame

Figure 5.13. Ephemeris trajectories for the chief (blue) and deputy (pink) spacecraft constructed in the Earth-Moon-Sun-Jupiter HFEM for 20 revolutions.

It is also useful to compare the distance between the chief and deputy spacecraft in the HFEM over the course of a single revolution, as well as the 20-revolution period, plotted in Figure 5.14. The bounds on the spacecraft distance are generally consistent with the values observed in the CR3BP. There are notable spikes in the relative distance between the two spacecraft, and these increased distances reflect a secular growth in the phase difference between the two spacecraft. While the trajectories remain close generally, phase control strategies may be implemented to target periapsis times and mitigate the increased phase difference [73]. The distance between the Moon and the two spacecraft over one revolution and 20 revolutions appears in Figure 5.15. In the CR3BP, the closest approach to the Moon occurs at the altitudes of $8,400\ km$ and $8,700\ km$ for the chief and the deputy, respectively; the same values drop to about $7,581\ km$ and $8,289\ km$ for the two spacecraft in the HFEM.

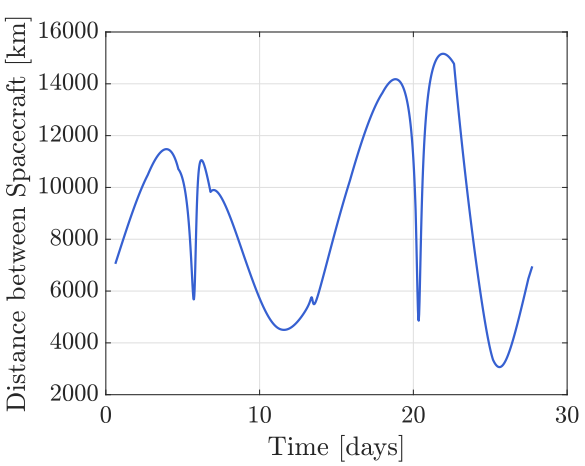

(a) Relative distance over one revolution

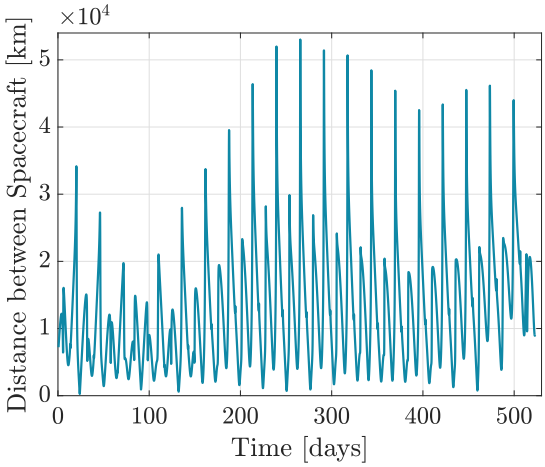

(b) Relative distance over 20 revolutions

Figure 5.14. Distance between the two spacecraft over one and 20 revolutions in the HFEM.

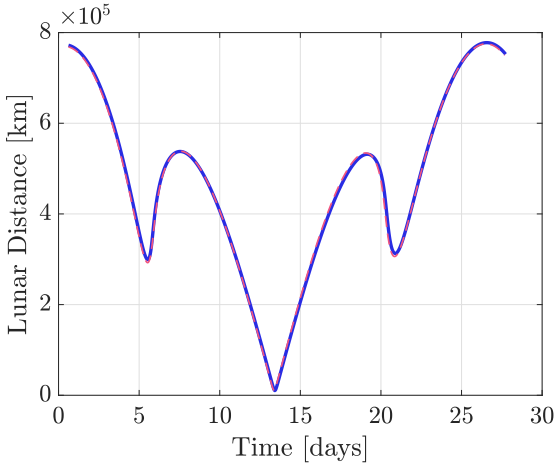

(a) Lunar distance over one revolution

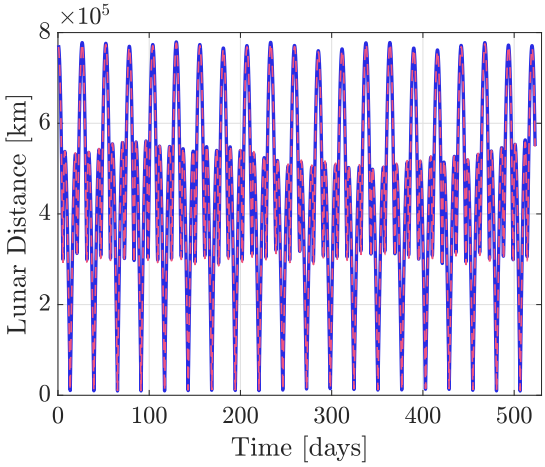

(b) Lunar distance over 20 revolutions

Figure 5.15. Distance between the Moon and the chief (blue) and the deputy (pink) over one and 20 revolutions in the HFEM.

5.3 Eclipse Avoidance Strategies

A major challenge for spacecraft operating in cislunar space is eclipsing due to the Earth and the Moon, since passing through their shadows may strain the power and thermal systems onboard spacecraft [74], [75]. Transit through the shadow of a celestial body has the potential to affect the delivery of spacecraft power by pushing the onboard hardware to

temperatures below acceptable operational limits [76]. As a result, spacecraft trajectories are typically subject to constraints on the eclipse duration that must be satisfied for nominal mission operations. In addition to these challenges, passage through shadow regions impacts illumination and visibility conditions, that is crucial to assess the utility of trajectories for cislunar operations [29]. Thus, as an important step, it is necessary to accurately identify and mitigate any eclipses that may hamper nominal spacecraft operations in cislunar space. Eclipse mitigation may involve simply a reduction in length of the longest eclipse duration, a reduction in the frequency of eclipses, or an avoidance of eclipses altogether [77], [78]. The process of identifying eclipsing events, along with methodologies to avoid eclipses are discussed.

5.3.1 Eclipse Identification

Due to its accuracy and potentially reasonably close passes of the Earth and Moon, the current investigation utilizes the conical eclipse model for the detection of eclipse events. The shadow regions behind the Earth and the Moon are modeled by the umbra and penumbra cones. Figure 5.16 represents the geometries of the penumbra (light grey) and umbra (dark grey) shadow cones in this model identified by their vertices V_1 and V_2, and cone half-angles γ and η, respectively [79], [80]. Passage through the umbra is characterized by a period of total eclipse, while the penumbra region causes partial eclipsing. The center of the Sun is denoted via S in the schematic, while the center of the occluding body, that is either the Earth or the Moon in this case, is denoted via O. The relevant quantities that determine the eclipse cone geometries are computed as,

$$d_p = \frac{\mathbb{r}_O \cdot r_{SO}}{\mathbb{r}_S + \mathbb{r}_O} \tag{5.1}$$

$$d_u = \frac{\mathbb{r}_O \cdot r_{SO}}{\mathbb{r}_S - \mathbb{r}_O} \tag{5.2}$$

where $\mathbb{r}_i$ represents the equatorial radius of the celestial bodies. The radius of the Sun, that is the primary source of light in the system, is represented by $\mathbb{r}_S$, while $\mathbb{r}_O$ represents the radius of the occluding body. For this investigation, either the Earth or the Moon may occlude

the spacecraft from being illuminated by the Sun and, thus, are the two occluding bodies considered. The cone half-angles that characterize the penumbra and umbra are calculated as,

$$\gamma = \arctan\left(\frac{\mathbb{r}_O}{d_p}\right) \tag{5.3}$$

$$\eta = \arctan\left(\frac{\mathbb{r}_O}{d_u}\right) \tag{5.4}$$

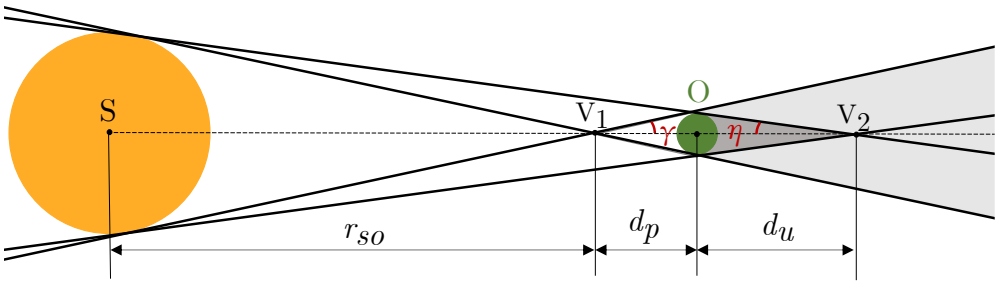

Figure 5.16. Representation of penumbra (light grey) and umbra (dark grey) cone geometries for eclipse identification.

It is convenient to visualize the trajectories of interest in the Sun-body rotating frame to gain intuition regarding the occurrence of eclipses. As such, orbits constructed in the CR3BP are transformed from the Earth-Moon rotating frame to the Sun-Earth and the Sun-Moon rotating frames as appropriate; trajectories produced in the Earth- or Moon-centered ephemeris models are transformed from their respective inertial frames to the same rotating frames as well. Since the penumbra and umbra cones are oriented along the horizontal axis in the Sun-body rotating frames, the conditions for locating passage through the shadow regions are defined directly within the context of those frames. For passage through the penumbra, both of the following two conditions are met,

$$r_{S-sc} > r_{SO} \tag{5.5}$$

$$r_{O-sc}\ \sin\zeta \leq \left(d_p + \frac{\boldsymbol{r}_{SO}\cdot\boldsymbol{r}_{O-sc}}{r_{SO}}\right)\ \tan\gamma \tag{5.6}$$

where $\boldsymbol{r}_{ij}$ represents the position vector between the various bodies, and r_{ij} represents the distance between the bodies. The angle ζ locates the spacecraft relative to the cone axes and is computed as,

$$\zeta = \arccos\left(\frac{\boldsymbol{r}_{SO} \cdot \boldsymbol{r}_{O-sc}}{||\boldsymbol{r}_{SO}||\ ||\boldsymbol{r}_{O-sc}||}\right) \tag{5.7}$$

While, by definition, the umbra is contained entirely within the penumbra, it is useful to compute the conditions for passage through the umbra cone as well. Similar to the penumbra case, the following two conditions dictate whether the spacecraft is located within the occluding body's umbra cone, i.e,

$$r_{S-sc} > r_{SO} \tag{5.8}$$

$$r_{O-sc}\ \sin\zeta \leq \left(d_u - \frac{\boldsymbol{r}_{SO} \cdot \boldsymbol{r}_{O-sc}}{r_{SO}}\right)\ \tan\eta \tag{5.9}$$

For each state along the trajectory of interest, passage through the penumbra and umbra cones is recorded. For any points that lie within the umbra and/or the penumbra regions, the total duration of each eclipse event is then evaluated as,

$$T_{ecl} = T_U + \frac{T_P}{2} \tag{5.10}$$

where T_U and T_P denote the time spent within the umbra and penumbra, respectively. This scaled value of the total time in shadow serves as a proxy for the effect of the eclipse time on the power and thermal requirements of the spacecraft [76].

The process of identifying eclipses due to occlusion from the Earth and the Moon is demonstrated using a spatial $3:1$ resonant orbit from the family computed and illustrated in Figures 4.10(a) and 4.10(b). A sample orbit from the family is selected and possesses a period of 27.22 *days*. To analyze the effects of eclipses, the CR3BP trajectory is transitioned to the Earth-Moon-Sun-Jupiter HFEM with the Earth as the central body. As an initial guess, the epoch at the beginning of the trajectory is selected as July 08 2025 00:00:00 UTC. This initial point occurs at perigee along the trajectory. The ephemeris trajectory is

propagated for multiple revolutions, specifically 408 *days* (15 revolutions), to deliver a sense of the possible occlusion periods over a longer horizon that a spacecraft in such a trajectory may encounter. The resulting ephemeris trajectory appears in Figure 5.17 as viewed in the Earth-Moon rotating, Earth-centered inertial, and the Moon-centered inertial frames.

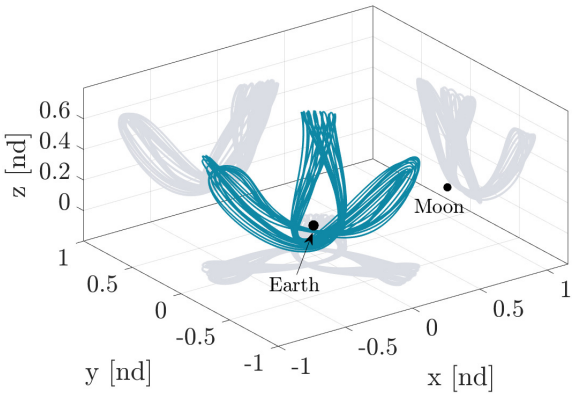

(a) Earth-Moon rotating frame

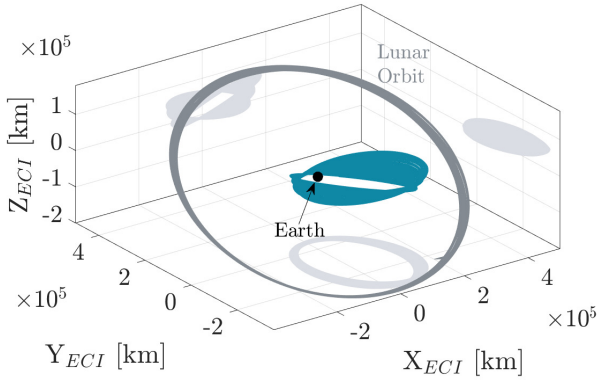

(b) Earth-centered inertial frame

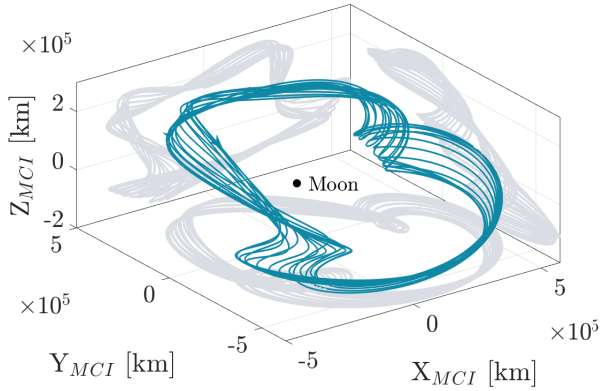

(c) Moon-centered inertial frame

Figure 5.17. Spatial 3 : 1 sidereal resonant orbit constructed in the HFEM for 408 *days*. The orbit of the Moon appears in grey in the Earth-centered inertial frame view.

The inertial ephemeris trajectory from Figure 5.17 is transformed to the Sun-Earth rotating frame, with the various views in this frame plotted in Figure 5.18. The penumbra (pink) and umbra (blue) cones cast by the Earth's shadow in this Sun-Earth rotating frame highlight the locations along the trajectory that remain under partial or total eclipse. Specif-

ically, the plot of the $\hat{\boldsymbol{y}}$-$\hat{\boldsymbol{z}}$ frame in Figure 5.18(d) provides a view looking down the shadow cone axes; any portion of the trajectory that passes through the cones in this view, and lies behind the Earth, undergoes Earth eclipse events. These locations of partial (penumbra passage) and total (umbra passage) eclipse are highlighted by the dark red and blue markers, respectively. As expected, the large spatial component of this trajectory relative to the Earth ecliptic results in minimal eclipsing events. Only three eclipse events occur, lasting 92.31 *min*, 67.55 *min*, and 50.97 *min* each. Over the course of 408 *days*, these eclipses are spaced 163.4 and 153.8 days apart. The same analysis is repeated in the Sun-Moon rotating frame to evaluate the impact of lunar eclipses over the same time period. In Figure 5.19, the different views of the trajectory in this frame are plotted with a zoomed-in view near the Moon. Given the equatorial radius of the Moon, the penumbra cone in this frame is significantly smaller than the Earth penumbra, and appears in red in Figures 5.19(a) and 5.19(b). The umbra cone, while plotted in blue, is smaller still and is completely encompassed by the penumbra cone in the plots. Passage through the lunar umbra will only occur for trajectories that possess short perilune radii. For the current trajectory of the 3 : 1 resonant orbit, the spacecraft remains outside of these narrow cones, with only one instance of a lunar eclipse that is highlighted in Figure 5.18(d), lasting just under 6 *min*. Naturally, unmodeled perturbations, as well as errors in modeling and/or navigation, can easily shift the path to increase the eclipse frequency and duration. However, for this particular resonant trajectory in general, eclipses due to the Earth's shadow dominate. While the potential for operational disruptions due to eclipses is dictated by the specific hardware onboard, these eclipse events and the geometries relative to the Sun-body axes guide the computation of reference solutions that are eclipse feasible. Depending upon the mission needs, as well as the spacecraft hardware limitations, different approaches are suitable for addressing eclipsing concerns.

5.3.2 Geometry-Informed Epoch Selection

The geometries exhibited by sidereal resonant orbits, along with their inherent stability, renders such orbits favorable for predicting and mitigating eclipses. Naturally, one of the driving factors for eclipses and their severity is the corresponding trajectory epoch, since such

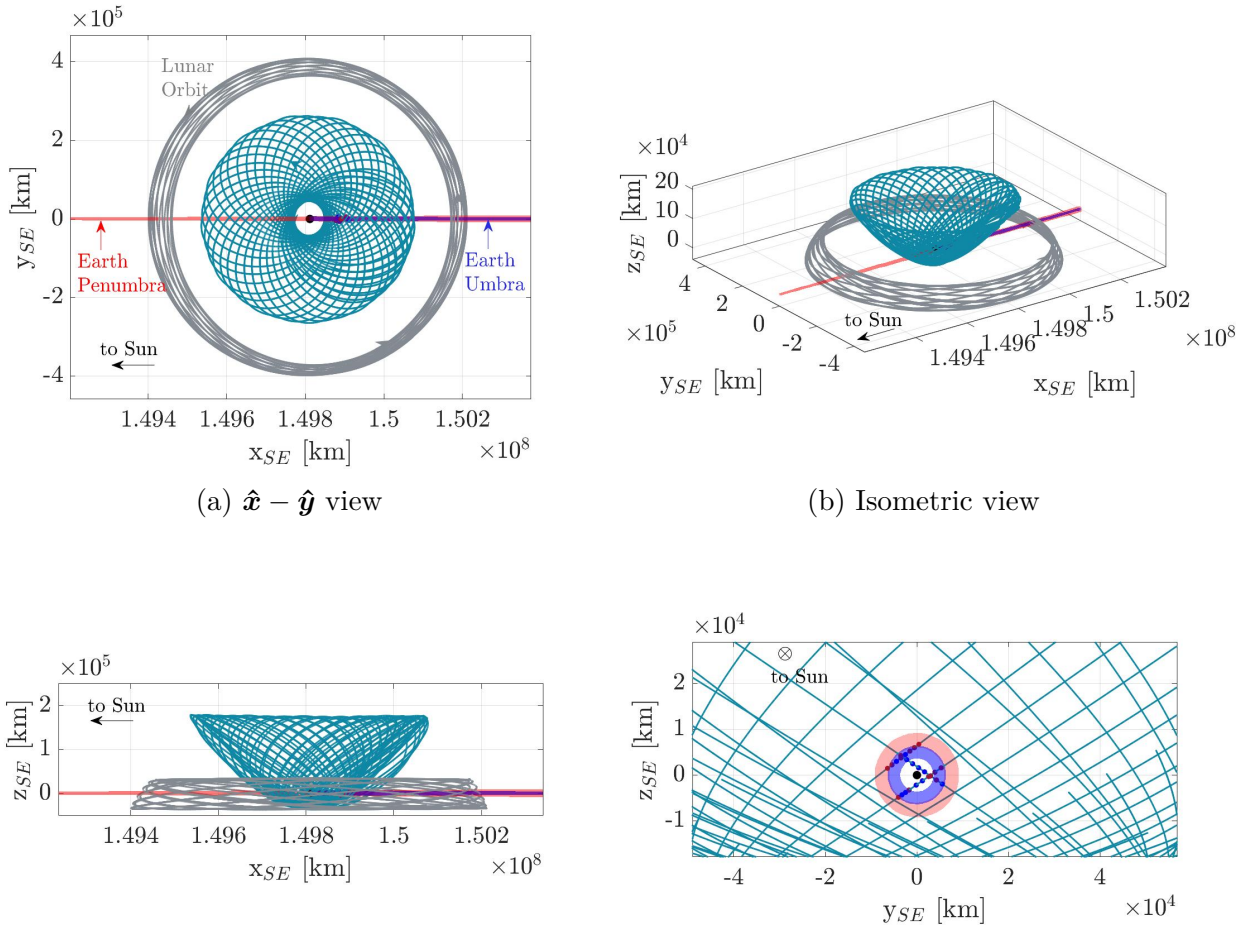

(a) $\hat{\boldsymbol{x}} - \hat{\boldsymbol{y}}$ view

(b) Isometric view

(c) $\hat{\boldsymbol{x}} - \hat{\boldsymbol{z}}$ view

(d) Zoomed-in $\hat{\boldsymbol{y}} - \hat{\boldsymbol{z}}$ view

Figure 5.18. Spatial 3 : 1 sidereal resonant trajectory in the ephemeris model as viewed in the Sun-Earth rotating frame with the penumbra (pink) and umbra (blue) regions indicated.

timing determines the orientation of the trajectory relative to the Sun-Earth and Sun-Moon axes. Within the context of this investigation, the trajectory epoch is defined as the initial time at a specific state along the ephemeris analog of the trajectory of interest. As such, when possible, variation in this initial time, or trajectory insertion epoch, is the simplest and most economical approach for producing eclipse-friendly solutions.

As an example, the spatial 3 : 1 resonant orbit transitioned to the ephemeris model in Figure 5.17 is considered. For the original trajectory epoch specified as July 08 2025, three instances of Earth eclipses are identified along the path over 408 *days*. The geometry for

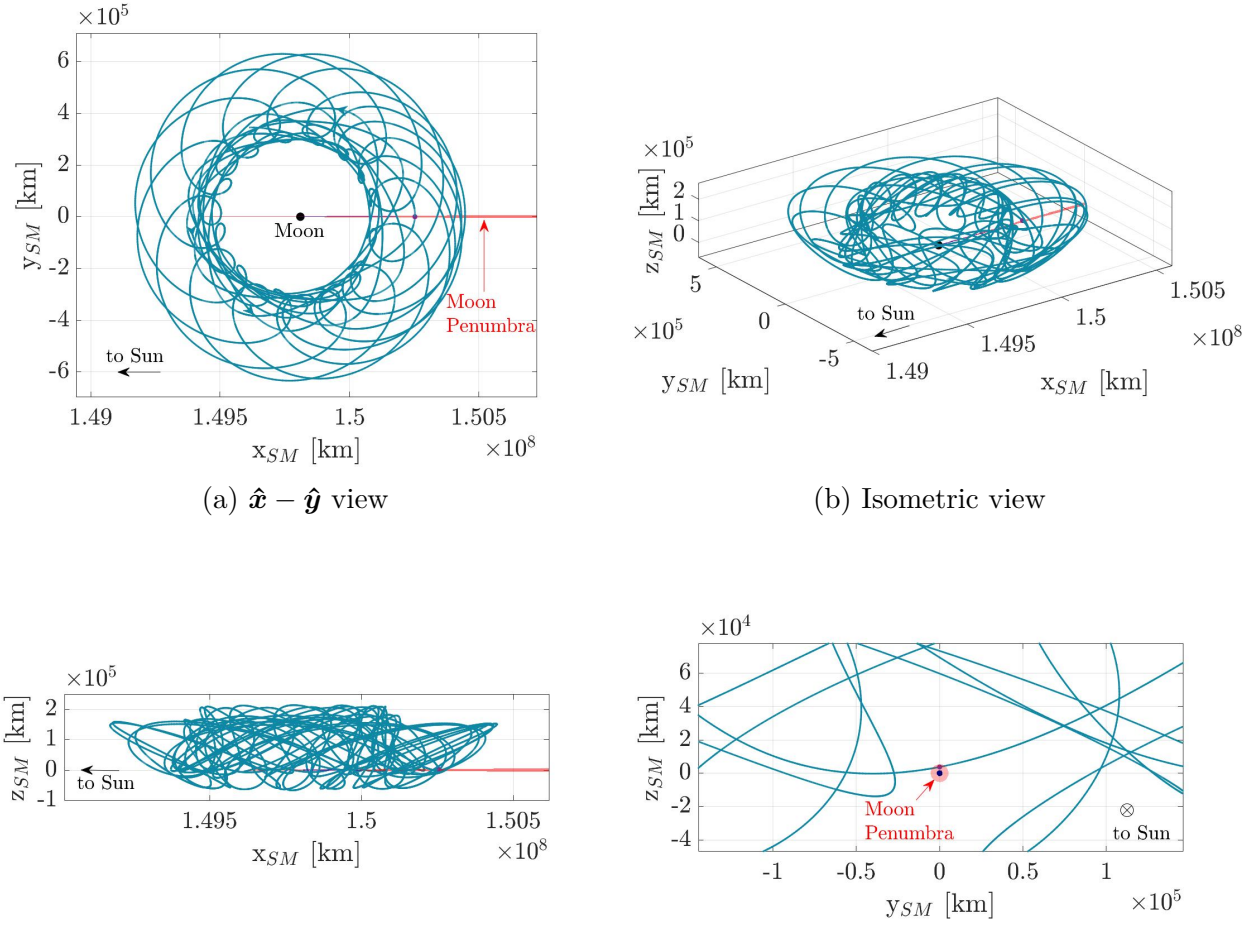

(a) $\hat{\boldsymbol{x}} - \hat{\boldsymbol{y}}$ view

(b) Isometric view

(c) $\hat{\boldsymbol{x}} - \hat{\boldsymbol{z}}$ view

(d) Zoomed-in $\hat{\boldsymbol{y}} - \hat{\boldsymbol{z}}$ view

Figure 5.19. Spatial 3 : 1 sidereal resonant trajectory in the ephemeris model as viewed in the Sun-Moon rotating frame with the penumbra (pink) region indicated.

this resonant trajectory is such that, for certain epochs, there exist ephemeris solutions that avoid eclipses entirely. For instance, if the trajectory insertion epoch date of May 09 2025 04:00:00 UTC is selected as an alternative, the resulting ephemeris trajectory passes outside the shadow regions of both the Earth and the Moon. In Figure 5.20, the Sun-Earth rotating frame view is plotted for this trajectory over the same 408-day propagation period. Looking down the Sun-Earth axis in Figure 5.20(d), it is apparent that the spacecraft passes outside of the penumbra (pink) and umbra (blue) cones, thus evading periods of partial or total eclipse that may hinder spacecraft operations. Additionally, for this epoch, the spacecraft

avoids all lunar eclipses as well, as illustrated in Figure 5.21. Although the adjustment of the trajectory insertion epoch yields an eclipse-free solution in this sample case, the geometries for other orbits of interest might not produce desirable solutions. In such cases, additional constraints are implemented to compute eclipse feasible solutions.

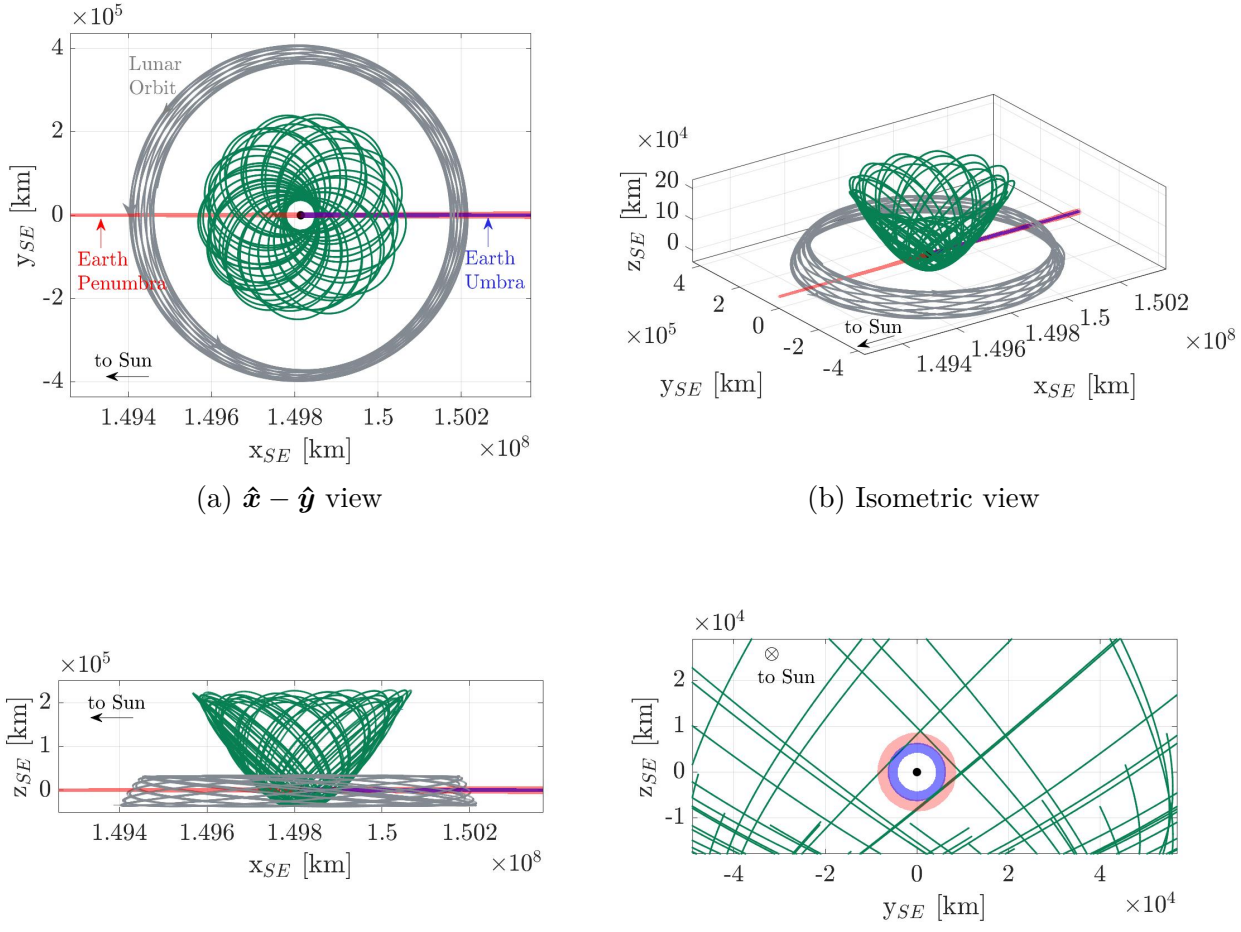

(a) $\hat{\boldsymbol{x}} - \hat{\boldsymbol{y}}$ view

(b) Isometric view

(c) $\hat{\boldsymbol{x}} - \hat{\boldsymbol{z}}$ view

(d) Zoomed-in $\hat{\boldsymbol{y}} - \hat{\boldsymbol{z}}$ view

Figure 5.20. Spatial 3 : 1 sidereal resonant trajectory in the ephemeris model as viewed in the Sun-Earth rotating frame for the updated trajectory insertion epoch. The trajectory does not pass through the penumbra and umbra cones cast by the Earth.

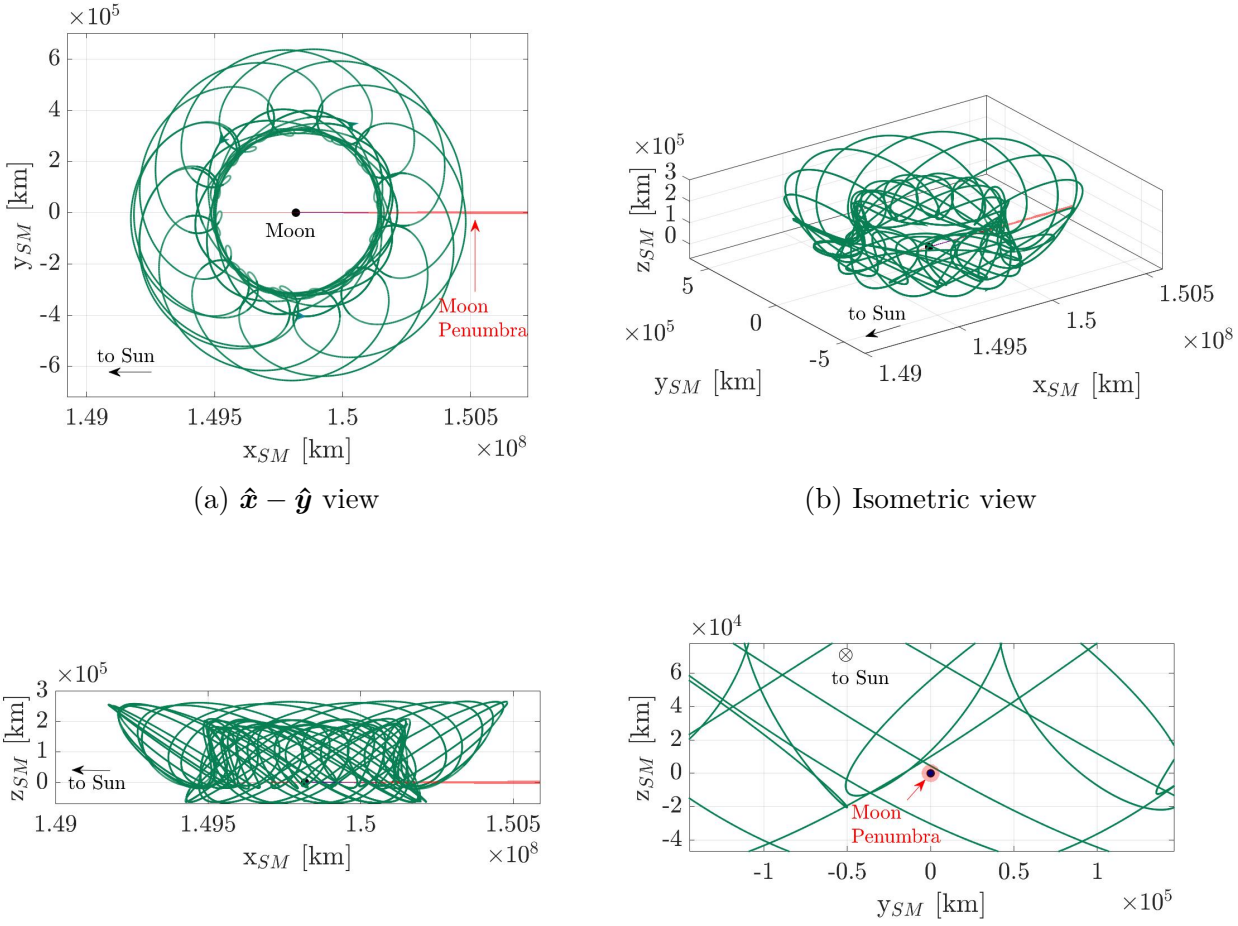

(a) $\hat{\boldsymbol{x}} - \hat{\boldsymbol{y}}$ view

(b) Isometric view

(c) $\hat{\boldsymbol{x}} - \hat{\boldsymbol{z}}$ view

(d) Zoomed-in $\hat{\boldsymbol{y}} - \hat{\boldsymbol{z}}$ view

Figure 5.21. Spatial 3 : 1 sidereal resonant trajectory in the ephemeris model as viewed in the Sun-Moon rotating frame for the updated trajectory insertion epoch. The trajectory does not pass through the penumbra cone cast by the Moon.

5.3.3 Penumbra Avoidance Path Constraint

For a trajectory insertion epoch that is not flexible, additional constraints in the trajectory design process are incorporated to compute eclipse-free solutions directly in the ephemeris model. Depending upon the geometry of the trajectory in the Sun-body rotating frame, the solution produced by incorporating the constraints may no longer be ballistic, or may include deviations from the baseline orbit geometry to avoid the shadow cones. One

formulation of a constraint to mitigate the severity of eclipses is a penumbra avoidance path constraint [79], [80], that is evaluated as,

$$F_{\text{path}_j} = \int_{\tau_j}^{\tau_j+T_j} H\left(r_{S-sc} - r_{SO}\right) \cdot \left(f_{\text{pen}} - |f_{\text{pen}}|\right)\, dt \tag{5.11}$$

where the path constraint, denoted F_{path_j}, is added to the constraint vector in the HFEM multiple shooting corrections algorithm. The variables τ_j and T_j denote the epoch and propagation time for the j^{th} arc segment in the multiple shooter. The term $H\left(r_{S-sc} - r_{SO}\right)$ is a Heaviside function that describes the condition for passage through penumbra, i.e., that the spacecraft is located behind the occluding body as viewed in the Sun-body rotating frame. Finally, the function f_{pen} in Equation (5.11) assesses the location of the spacecraft at each point along the arc to determine whether the point lies within the penumbra shadow cone. This function is computed as,

$$f_{\text{pen}} = r_{O-sc}\ \sin\zeta - \left(d_p + \frac{\boldsymbol{r}_{SO} \cdot \boldsymbol{r}_{O-sc}}{r_{SO}}\right)\ \tan\gamma \tag{5.12}$$

To yield an eclipse-free solution, in addition to constraints that ensure position, velocity, and epoch continuity along the trajectory segments, this path constraint is incorporated directly into the ephemeris multiple shooting scheme.

As an example, return to the multi-revolution spatial 3 : 1 trajectory in the ephemeris model computed in Figures 5.17 – 5.19. For the trajectory insertion epoch in this sample case, July 8 2025 00:00:00 UTC, several instances of eclipses due to both the Earth and the Moon are detected. Without modifying the trajectory insertion epoch, the trajectory is recomputed in the ephemeris model, now with the addition of the penumbra avoidance path constraint along with the usual ephemeris targeting continuity constraints. The path constraint is implemented for both the Earth and the Moon to remove predicted eclipse events, as well as to prevent any further downstream eclipse events. This re-converged trajectory appears in Figures 5.22 and 5.23, illustrating the various views of the trajectory as plotted in the Sun-Earth and Sun-Moon rotating frames. The Earth and the Moon penumbra cones appear in red in their respective rotating frames. In both cases, looking down the $\hat{\boldsymbol{y}}$-$\hat{\boldsymbol{z}}$ axes in

Figures 5.22(d) and 5.23(d) illustrates the clear gap in the trajectory as it passes around the penumbra cones, circumventing the shadow regions entirely. Thus, for the entirety of the 15 revolutions (408 *days*) of the trajectory, eclipses due to the Earth and the Moon are avoided for a previously unfavorable epoch. In this example, no maneuvers are necessary to achieve eclipse avoidance for the selected epoch. More importantly, the original characteristics of the trajectory are retained without any significant departure from the underlying resonant geometry.

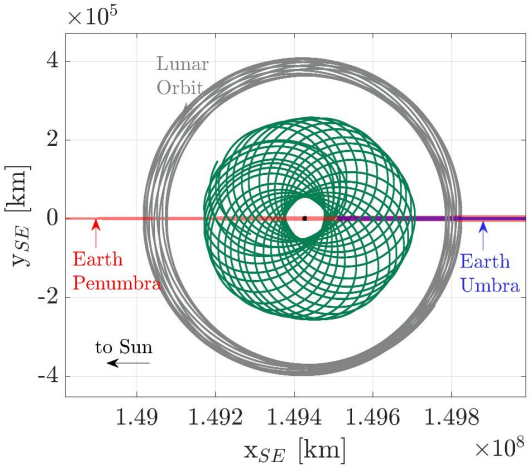

(a) $\hat{\boldsymbol{x}} - \hat{\boldsymbol{y}}$ view

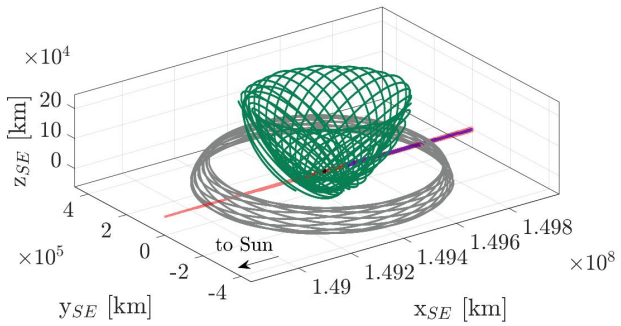

(b) Isometric view

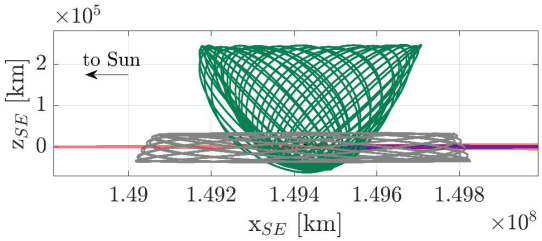

(c) $\hat{\boldsymbol{x}} - \hat{\boldsymbol{z}}$ view

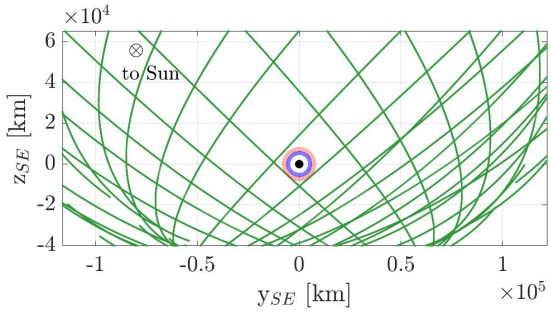

(d) Zoomed-in $\hat{\boldsymbol{y}} - \hat{\boldsymbol{z}}$ view

Figure 5.22. Sun-Earth rotating frame views of the spatial 3 : 1 resonant orbit constructed with the penumbra avoidance path constraint. The trajectory circumvents the penumbra and umbra cones cast by the Earth.

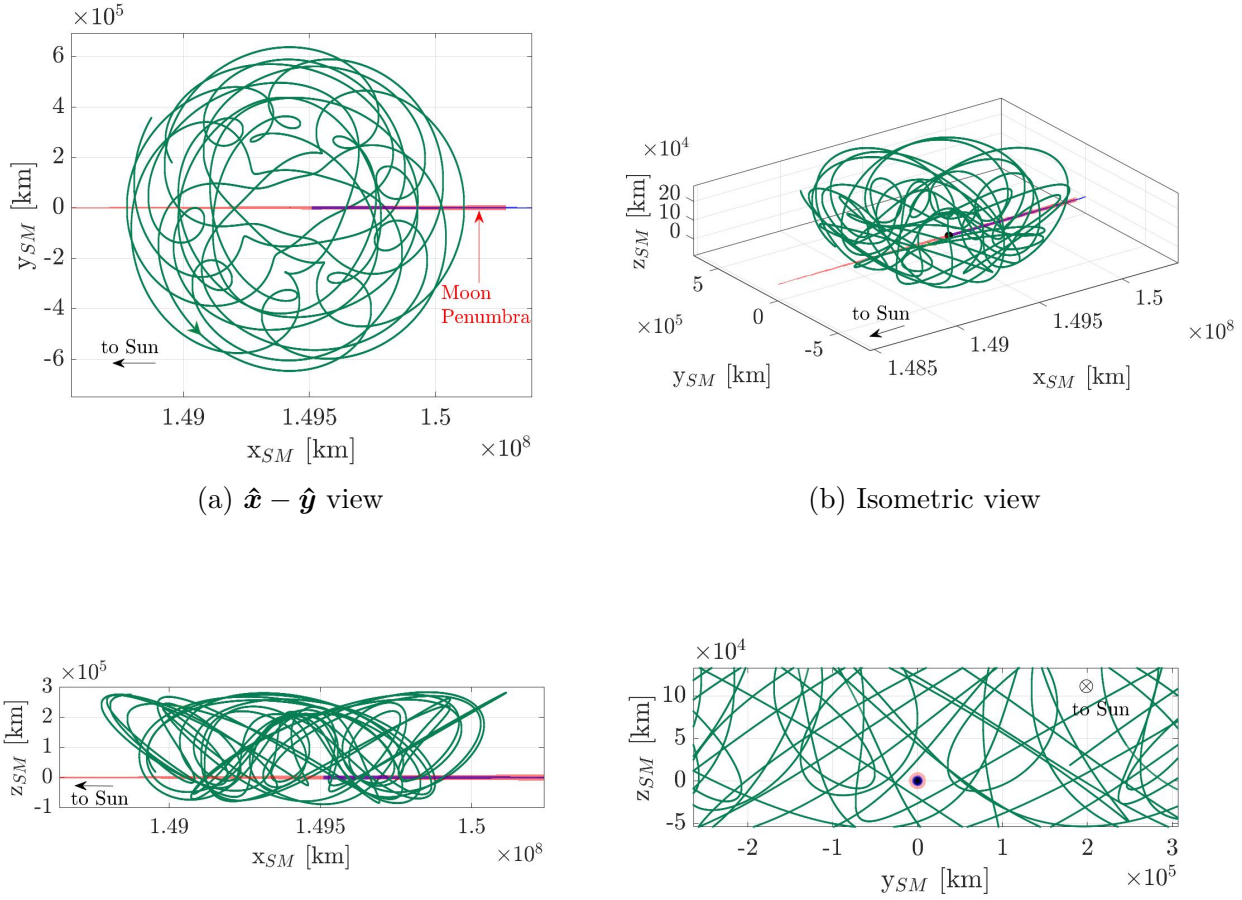

(a) $\hat{\boldsymbol{x}} - \hat{\boldsymbol{y}}$ view

(b) Isometric view

(c) $\hat{\boldsymbol{x}} - \hat{\boldsymbol{z}}$ view

(d) Zoomed-in $\hat{\boldsymbol{y}} - \hat{\boldsymbol{z}}$ view

Figure 5.23. Sun-Moon rotating frame views of the spatial $3:1$ resonant orbit constructed with the penumbra avoidance path constraint. The trajectory circumvents the penumbra cone cast by the Moon.

The effectiveness of the penumbra avoidance path constraint is apparent in examples where trajectories reflect eclipses that may hamper nominal operations. The implementation of the path constraint can also be adjusted such that the eclipse-free solution clears the Earth and Moon shadow cones with larger buffer zones. One strategy to accommodate errors in eclipse modeling and prediction is to inflate the radii of the occluding bodies, forcing the path constraint to clear the penumbra cones by a larger margin of error. Additionally, to ensure the accurate detection of eclipsing events, the propagation time step may be fixed and sufficiently reduced to detect passage through the penumbra cones.

6. CONSTELLATIONS FOR VISIBILITY AND CONNECTIVITY IN CISLUNAR SPACE

Owing to the vastness of cislunar space, it is useful to assess the proposed trajectories for their utility towards Space Situational Awareness (SSA) applications. Metrics that inform the qualitative nature of the trajectories for visibility and connectivity within cislunar space are introduced. Sample constellations are designed, leveraging both sidereal and synodic resonant behaviors, to assess the visibility and connectivity within this space supplied by the orbits of interest. While the selection of some combination of orbits in a cislunar constellation is mission specific, constellation design methodologies that incorporate multiple observers in orbits from the same periodic orbit families, as well as orbits of varying geometries and energy levels, are introduced.

6.1 Measuring Visibility within Cislunar Space

To establish a comprehensive SSA architecture in cislunar space, the need for space-based sensors has been recognized [27], [81]. With the availability of unique vantage points across the domain of cislunar space, space-based sensors may be utilized for the detection and tracking of objects in space, especially beyond GEO and in the vicinity of the Moon. Observations from space-based sensors are crucial for supporting autonomous navigation, communication, and sustaining operations beyond the Earth. For optical sensors in space, an inherent operational challenge is that the asset or target of interest in space may not be visible, or the viewing conditions may not be feasible for the onboard hardware. These conditions for evaluating the visibility of a target, as viewed by space-based optical observers, are discussed in the context of cislunar space.

6.1.1 Line-of-Sight (LOS)

A primary requirement for tracking and communicating with assets in space is line-of-sight. In the Earth-Moon CR3BP, line-of-sight between two spacecraft in their respective

orbits may not be possible when the target is occluded by either the Earth or the Moon. For line-of-sight to exist, the following constraint arises,

$$\arccos\left(\frac{\boldsymbol{r}_{O-P_i}\cdot\boldsymbol{r}_{O-T}}{||\boldsymbol{r}_{O-P_i}||\ ||\boldsymbol{r}_{O-T}||}\right) \leq \arctan\left(\frac{\mathbb{r}_{P_i}}{||\boldsymbol{r}_O-\boldsymbol{r}_{P_i}||}\right) \tag{6.1}$$

where $i = 1, 2$ correspond to the Earth and the Moon, respectively. The value $\mathbb{r}_{P_i}$ represents the radius of either body, and $\boldsymbol{r}_{P_i}$ represents the location of either body relative to their barycenter, $\mathcal{B}$, as defined in the Earth-Moon rotating frame. The subscripts O and T denote the observer and the target, respectively. When Equation (6.1) is satisfied for either or both of the primaries, there exists no line-of-sight between the the observer and target and, consequently, observation and communication are not possible.

6.1.2 Limiting Magnitude

In astronomy, the visual magnitude is a measure of the brightness of an object [29]. The visual magnitude of a space-based target as seen by an observer is critical in determining the brightness and, by extension, how "visible" a target is [82]. The magnitude of an object is computed as,

$$\mathbb{M}_T = \mathbb{M}_S - 2.5\log\left[\frac{2\ C_d\ \mathbb{r}_T^2}{3\ \pi^2\ r_{OT}^2}\left(\sin\psi + (\pi-\psi)\cos\psi\right)\right] \tag{6.2}$$

where C_d is the reflection parameter of the target, $\mathbb{r}_T$ is the radius of the target, i.e., an indicator of its size. The angle ψ is the Sun-target-observer angle and is termed the solar phase angle. The value $\mathbb{M}_S$ is the visual magnitude of the Sun and is constant at -26.74. The magnitude scale is reverse logarithmic, and a lower value of the magnitude is indicative of a brighter object. For reference, Figure 6.1 illustrates the orientation of the target relative to the Sun and the observer. The utility of any space-based observer may be assessed by quantifying how bright various targets will appear to the observer, and whether the obtained value is less than some limiting magnitude. While this limiting magnitude is inherently a function of the sensor aperture and properties of the detector, a representative value of $\mathbb{M}_{lim} = 20$ is employed in this investigation. Thus, when a target possesses a magnitude less

than $\mathbb{M}_{lim}$, it is assumed to be visible to the observer. In this investigation, all targets are characterized as Lambertian spheres with a $\mathbb{r}_T = 3.54\ m$ and a diffuse reflection coefficient equal to $C_d = 0.5$ [26]. Finally, since the Earth-Moon CR3BP is the primary dynamical model in this investigation, the magnitude of each target is directly computed in the Earth-Moon rotating frame, with the position of the Sun obtained via the SPICE Toolkit and transformed directly into this frame [83].

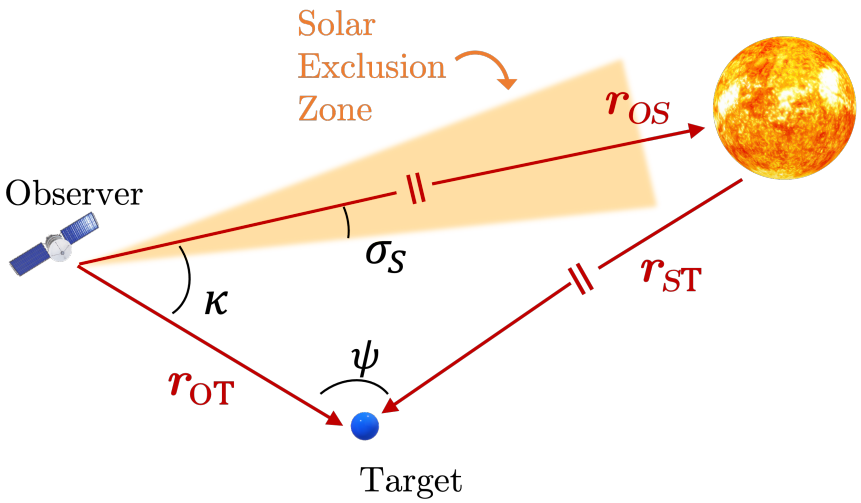

Figure 6.1. Schematic for the visual magnitude of a target as viewed by a space-based observer.

6.1.3 Exclusion Zones

For targets that lie close to the line-of-sight with the Sun, the Earth, or the Moon, the brightness of the celestial body causes the target to be backlit as viewed by the observer. As such, any onboard optical sensors may be unable to obtain or maintain custody of the target, if solely optical measurements are considered. To identify the severity of this effect, exclusion zones are defined for each body. These conical zones, such as the solar exclusion zone depicted in Figure 6.1, are centered on the observer and expand out towards the celestial body. The exclusion angle, denoted σ_i, is the cone half-angle that defines the exclusion zone cast by the body. The angle κ locates the target relative to the axis of the exclusion zone,

as defined in Figure 6.1. For a target to be visible in space, then, the following exclusion condition is defined,

$$\kappa(t) > \sigma_i \tag{6.3}$$

where σ_i represents the exclusion angle for each of the three bodies. The solar exclusion angle is represented as σ_S, σ_E represents the Earth exclusion angle, and σ_M defines the lunar exclusion zone. Table 6.1 summarizes the nominal values for the cone half-angles employed in this investigation to describe these exclusion zones. For a target to be visible to the observer at any time, Equation (6.3) must be satisfied for exclusion resulting from all three celestial bodies at that time.

For challenges with solar exclusion, the long range between the Sun and the observer (and target) is leveraged to inform a solar phase angle that minimizes exclusion. From Figure 6.1, it is apparent that,

$$\kappa + \psi \approx 180^\circ \tag{6.4}$$

When $\kappa \leq \sigma_S$, the target lies within the solar exclusion zone and is not visible to the observer. Thus, a relative phasing between the observer and target is desired such that $\psi \in [0, 180 - \sigma_S]$. By phasing the observer appropriately, the impact of solar exclusion on the visibility of a target is reduced.

Table 6.1. Constraints on target illumination.

Parameter	Symbol	Value
Limiting magnitude	$\mathbb{M}_{lim}$	20
Solar exclusion angle	σ_S	30°
Earth exclusion angle	σ_E	10°
Lunar exclusion angle	σ_M	10°

Modified Lunar Exclusion Zone

For targets in cislunar space and, in particular, those operating in the vicinity of the Moon, lunar exclusion imposes significant restrictions on visibility [27]. While the nominal value of the lunar exclusion zone defined in Table 6.1 aids preliminary analyses, one methodology of increasing the fidelity of modeling the lunar exclusion zone considers the brightness of the Moon itself. Depending upon the lunar phase as seen by the space-based observer, the Moon may appear full (i.e., brightest), or new (i.e., dimmest). Intuitively, this cycle is equivalent to the phases of the Moon as seen by the Earth every lunar synodic period. During a full Moon event, as viewed by the observer, the target will be completely backlit. As such, exclusion due to the Moon is maximized, and $\sigma_M(t) = \sigma_M = 10°$. Conversely, during a new Moon, the Moon is the dimmest as viewed by the observer, and $\sigma_M(t) = 0°$. Based on the lunar phase viewed by the observer at any time, then, the modified lunar exclusion zone is defined as a function of the lunar phase angle, denoted $\chi(t)$, and illustrated in Figure 6.2. The case of $\chi(t) = 0°$ occurs when Moon lies between the observer and the Sun and causes no exclusion; when $\chi(t) = 180°$, the Sun-observer-Moon orientation occurs and results in maximum lunar exclusion. Based on the value of $\chi(t)$ for every time step, the lunar exclusion zone angle is instantaneously determined as,

$$\sigma_M(t) = 10° \cdot \frac{\chi(t)}{180°} \tag{6.5}$$

where $\chi(t)$ is measured in [°], and the value 10° is the standard, constant lunar exclusion angle defined in Table 6.1. Equation (6.5), then, essentially scales the nominal value of the lunar exclusion angle based on the brightness of the Moon.

Lunar Exclusion Cone (LEC)

For a given solar phase, the illumination of the Moon may be such that Earth ground-based observations of a target located between the Earth and the Moon may not be possible due to lunar exclusion. As such, this conical volume centered at the Earth and facing out towards the Moon is identified as a high priority zone for maturing the current tracking and

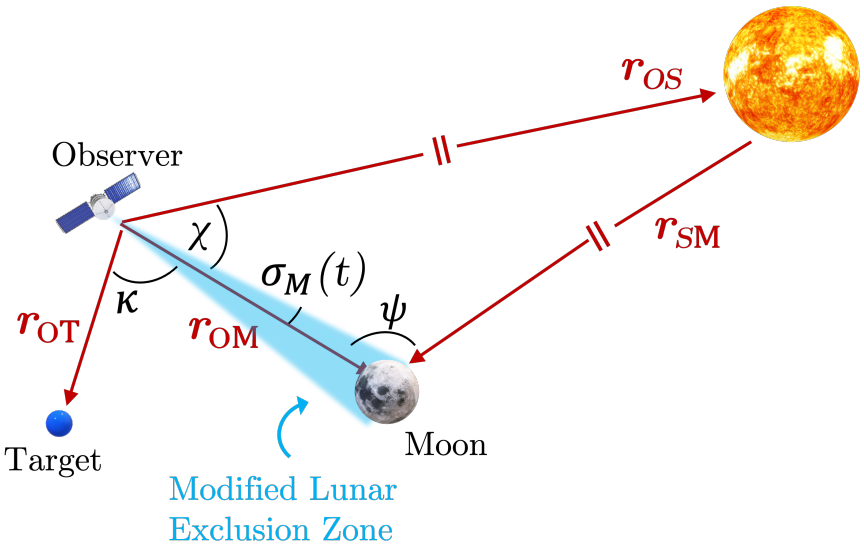

Figure 6.2. Schematic for the modified lunar exclusion zone defined as a function of the lunar phase viewed by the observer.

surveillance capabilities in cislunar space [84]. As a conservative estimate, a fixed cone with a 30° half-angle is employed to characterize this zone. Periodic orbits near the L_1 and L_2 libration points offer options that remain in the lunar vicinity and inside this 30° surveillance cone, also called the "cone of shame" [84]. In this investigation, this region is denoted the Lunar Exclusion Cone (LEC).

6.1.4 Selection of Targets

While it is not possible to uniquely examine the visibility for every point in cislunar space, a representation of the quality of an observer trajectory is assessed by determining the visibility of various targets. To assess the ability of an observer to track various locations within cislunar space, the following three options are considered:

- **Targets within the LEC**: Since the LEC is recognized as a high priority region, the volume defined by the 30° half-angle cone facing the Moon is considered. Targets are considered to be fixed positions that are randomly sampled from a uniform distribution of points in this cone. In the current work, the length of the LEC is assumed to equal

$500,000\ km$, extending just beyond the the L_2 libration point. Figure 6.3(a) illustrates an example distribution of targets located in the LEC.

- **Targets within the cislunar domain**: It is also possible to randomly sample various target locations across the entire volume of the cislunar domain. Since only the knowledge of the target positions is assumed, depending upon their velocity, targets may be able to rapidly access other locations of interest. Figure 6.3(b) illustrates a sample distribution of targets dispersed across the spherical volume of cislunar space. In the current work, the radius of this sphere is equal to $500,000\ km$ and encompasses all the libration points.

- **Targets operating in cislunar orbits**: The knowledge of existing periodic orbits in the Earth-Moon CR3BP also provides insight into the possible locations of targets. By considering targets operating in various periodic orbits, the knowledge of their velocity at a given energy level is also available. In this investigation, five representative targets are considered that operate independently near the L_1, L_2, L_4, and L_5 libration points. An additional target is assumed to operate in a spatial Distant Retrograde Orbit (DRO). These sample target orbits are represented in Figure 6.3(c) as viewed in the Earth-Moon rotating frame. The visibility of any number of the five possible target orbits is evaluated.

The first two approaches represent the *probable* locations of targets in cislunar space, whereas the third approach is guided by the *possible* locations of targets. For visibility, each target is instantaneously evaluated for following conditions as viewed by the observer:

1. There exists line-of-sight between the observer and target.
2. The visual magnitude of the target is less than the limiting magnitude.
3. The target lies outside the solar exclusion zone.
4. The target lies outside the Earth exclusion zone.
5. The target lies outside the modified lunar exclusion zone.

For any observer-target pair, these metrics allow a preliminary assessment of the visibility of the target as viewed by the observer.

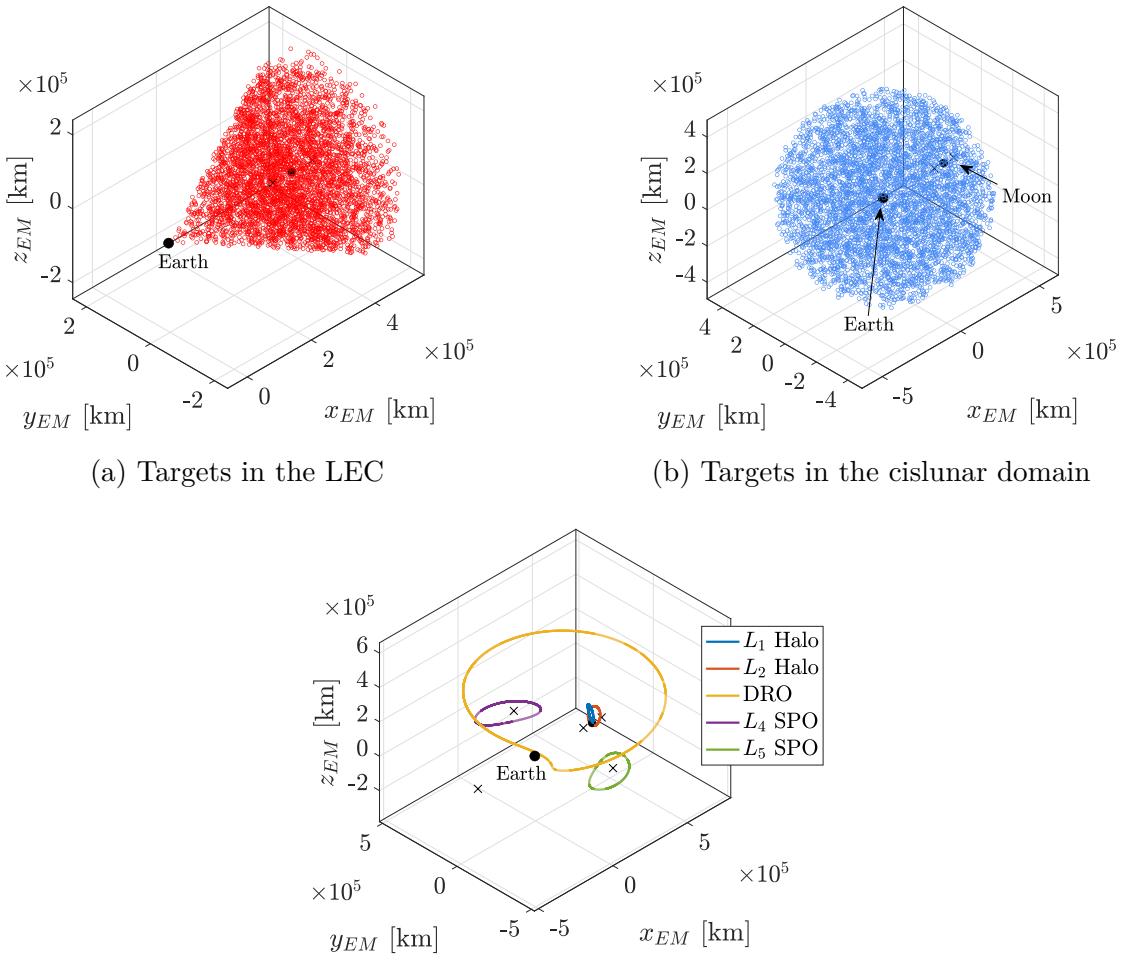

(a) Targets in the LEC

(b) Targets in the cislunar domain

(c) Targets in cislunar orbits

Figure 6.3. Sample targets identified within various regions in cislunar space.

6.2 Measuring Connectivity within Cislunar Space

For the purposes of quantifying the connectivity supplied by cislunar trajectories, the Earth-Moon plane is delineated into *zones*, as described in Figure 6.4. It is possible, then, to characterize the trajectories of spacecraft of interest as they traverse through these zones. For any orbit, the following two figures of merit quantify the connectivity supplied by a spacecraft in that orbit:

- **Time spent in each zone**: For each orbit, the time spent in each zone is computed over a single period of the orbit. Notably, Zone 1 in Figure 6.4 is approximately coincident with a planar projection of the LEC; as such, coverage within Zone 1 is recognized as high priority.

- **Revisit rate per zone**: For orbits that traverse through multiple zones (e.g., sidereal resonant orbits with expansive geometries), the time it takes for the orbit to revisit each zone is also computed. The frequency with which each orbit traverses through the zones may guide the selection of orbits that yield broad coverage and connectivity within the Earth-Moon plane.

Given the vastness of the cislunar domain, spacecraft operating in multiple different orbits are necessary to provide comprehensive coverage and connectivity. Together with orbits that possess sweeping geometries, orbits that provide localized access are assessed as constellations of spacecraft.

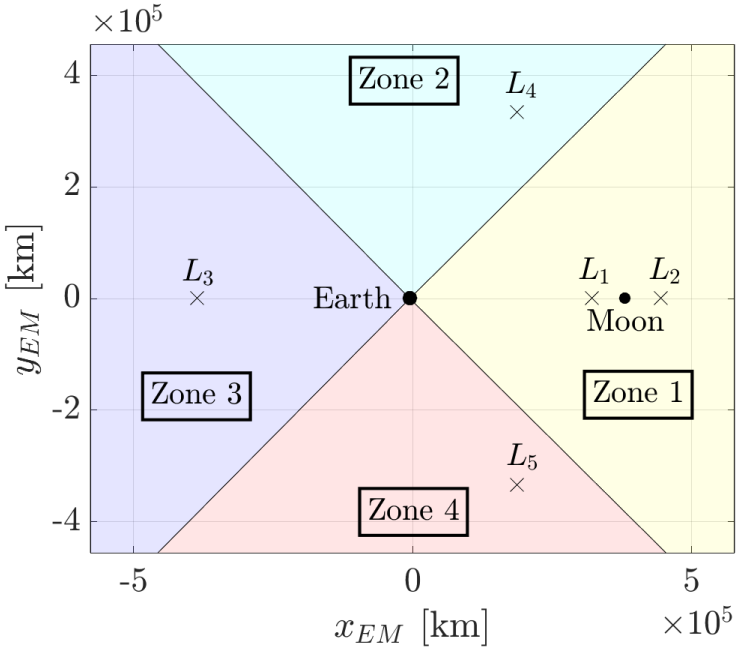

Figure 6.4. Schematic for the cislunar planar zones of interest.

6.3 Example: Visibility and Connectivity via the 1:1 Synodic Resonant Member of the 2:1 Sidereal Resonant Orbit Family

To demonstrate the assessment of visibility and connectivity metrics in cislunar space, an orbit from the family of prograde 2 : 1 resonant orbit family is selected. Specifically, the orbit identified in Figure 4.13(d) that exhibits a sidereal-synodic overlap is assessed, since visibility conditions are commensurate with the lunar synodic period. This orbit appears in Figure 6.5 as viewed in the Earth-Moon rotating frame, with the various zones indicated as well. The geometry of the orbit is such that it passes through all zones once per revolution in the rotating frame. To locate the Sun for assessing the visibility, the initial epoch is assumed to be January 01 2025. The initial direction of the Sun at this epoch appears in Figure 6.5.

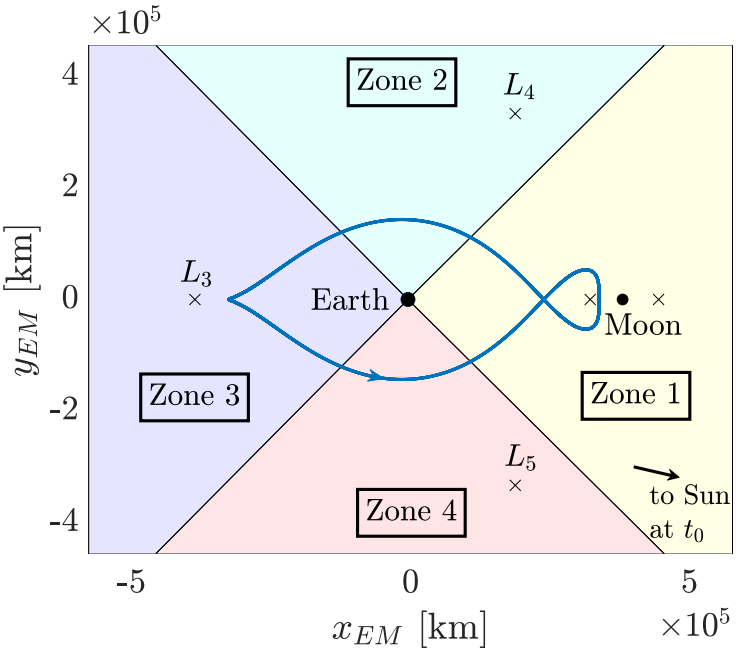

Figure 6.5. Orbit in 1 : 1 lunar synodic resonance from the 2 : 1 prograde sidereal resonant orbit family.

6.3.1 Connectivity in the Earth-Moon Plane

The connectivity supplied by this orbit for cislunar operations is described by the values indicated in Table 6.2. Recall that the orbit is 1 : 1 synodic resonant in the rotating frame;

as such, its dimensional period is precisely equal to 29.53 *days*. Over this period, the orbit remains in Zone 1 the longest, for approximately half the period. Noting the symmetry of the orbit relative to the Earth-Moon axis, the orbit remains within Zones 2 and 4 for approximately 1.86 *days* each. Finally, the remaining 10.78 *days* are spent in Zone 3 near the L_3 libration point. While the excursion to L_3 and Zone 3 may not be required for cislunar SSA needs, the close access to the lunar vicinity in Zone 1, along with the Earth approaches in Zones 2 and 4, renders this orbit favorable for cislunar coverage.

Table 6.2. Connectivity values for the $1:1$ synodic resonant orbit.

	Time Spent [days]	**Revisit Rate** [days/rev]
Zone 1	15.03	14.50
Zone 2	1.86	27.67
Zone 3	10.78	18.75
Zone 4	1.86	27.67

6.3.2 Visibility of Targets in the LEC

The efficacy of an observer operating in the $1:1$ synodic resonant member of the $2:1$ sidereal resonant family is assessed for targets located inside the Lunar Exclusion Cone (LEC). In this investigation, $5,000$ points are randomly distributed inside the LEC, as illustrated in Figure 6.3(a). The targets are stationary, and there is no assumed knowledge of their velocity. For various points along the observer in its orbit, the number of targets that are visible to the observer at each time is computed. The results over one synodic period appear in Figure 6.6, where the vertical axes represent the number of targets, out of 5000, that are visible to the observer at the sampled time step along the orbit. For reference, the observer is assumed to be located at apolune (near L_3) at initial time. Intuitively, as the observer approaches the vicinity of the Moon, after traversing through Zone 4, the number of visible targets increases. The phasing of the observer and the Moon is such that when the observer is at the half-period mark (near L_2), the Sun is located towards L_3; thus, solar exclusion effects

also reduce. The modified lunar exclusion zone leverages the instantaneous location of the Sun and, as apparent in Figure 6.6(d), when the observer is far away from the Moon, lunar exclusion does not occur. When the observer is close to the Moon, the Sun-Moon-observer phasing is such that lunar exclusion is minimized. Figure 6.6(e) illustrates the overall target visibility considering all the visibility conditions together. Overall, solar exclusion is the most limiting effect. Notably, since this orbit is in $1:1$ synodic resonance with the Moon, the visibility of targets obtained over the demonstrated case of one revolution will persist over subsequent revolutions as well.

6.3.3 Visibility of the Cislunar Domain

A similar analysis of targets in the cislunar domain, defined in Figure 6.3(b), yields a visibility assessment of the cislunar volume. As a representative example, $5,000$ points are sampled from this volume to represent stationary targets that are dispersed throughout cislunar space. The number of targets that are visible to the observer under various conditions appear in Figure 6.7. In general, the volume is well observed in the presence of solar, Earth, and lunar exclusion zones. The limiting magnitude is the predominant factor that restricts the visibility of the targets. However, the number of targets visible to the observer in Figure 6.7(a) is commensurate with the solar phase angle. Thus, multiple observers may be incorporated such that their phase is offset from the solar phase angle to improve the overall visibility.

6.3.4 Visibility of the Cislunar Target Orbits

The final strategy of assessing the visibility capabilities of an observer orbit is by evaluating the targets in the representative periodic orbits illustrated in Figure 6.3(c). The same initial conditions are assumed for the observer, with the spacecraft initially located at apolune and the Sun oriented at the epoch January 01 2025. The observer, and the targets in their orbit, are propagated for one synodic period and appear in Figure 6.8(a) as viewed in the Earth-Moon rotating frame. Figure 6.8(b) illustrates the visual magnitude of each target as viewed by the observer over the propagated synodic period, where the black line indicates

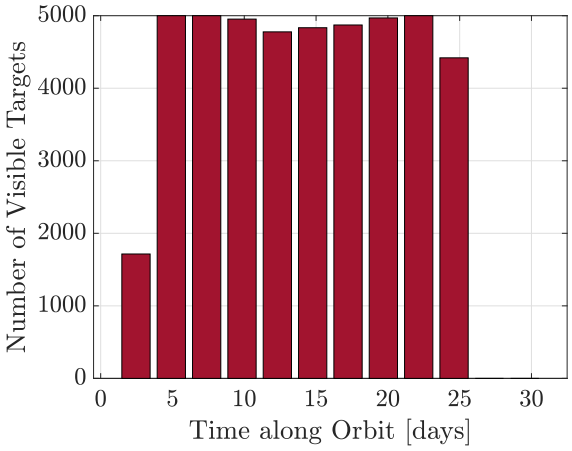

(a) Targets with visible magnitude

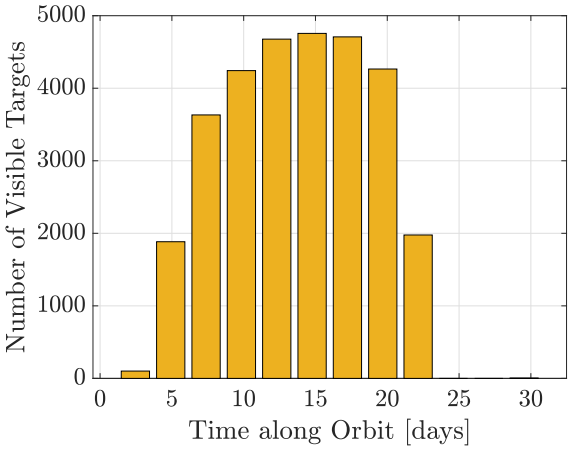

(b) Targets outside solar exclusion

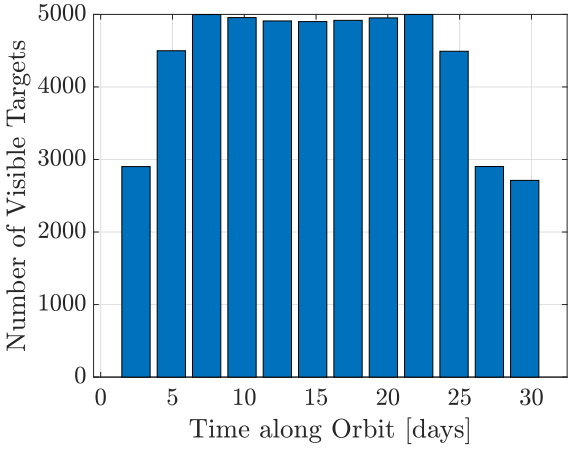

(c) Targets outside Earth exclusion

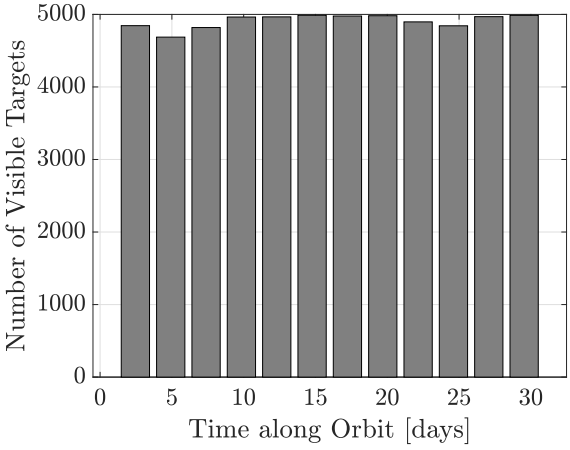

(d) Targets outside lunar exclusion

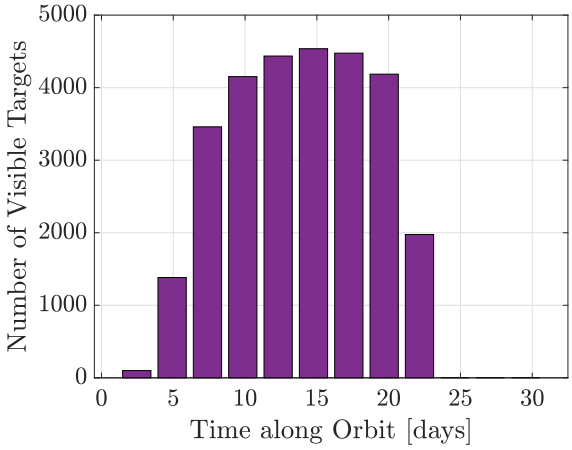

(e) Overall target visibility

Figure 6.6. Visibility of fixed-position targets in the LEC as viewed by the 1 : 1 synodic resonant observer.

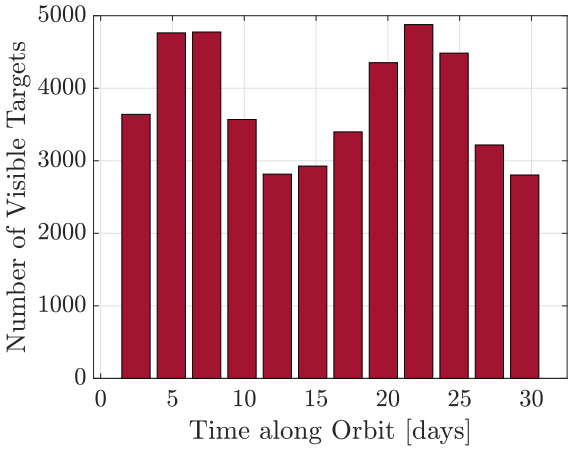

(a) Targets with visible magnitude

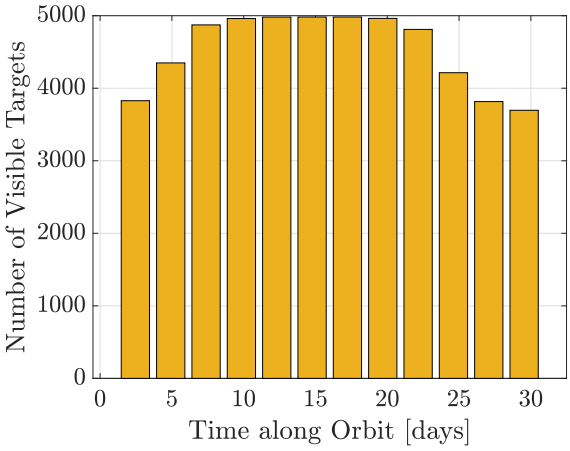

(b) Targets outside solar exclusion

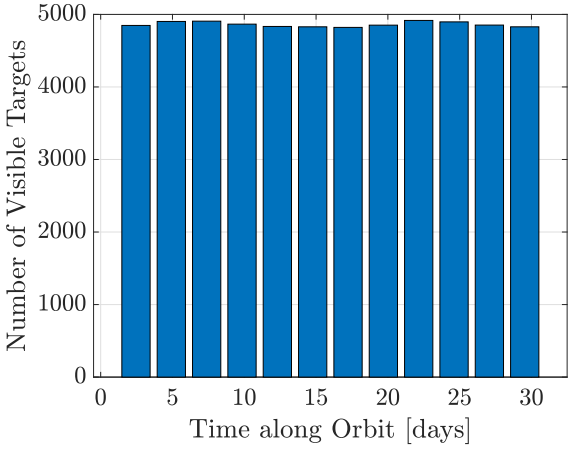

(c) Targets outside Earth exclusion

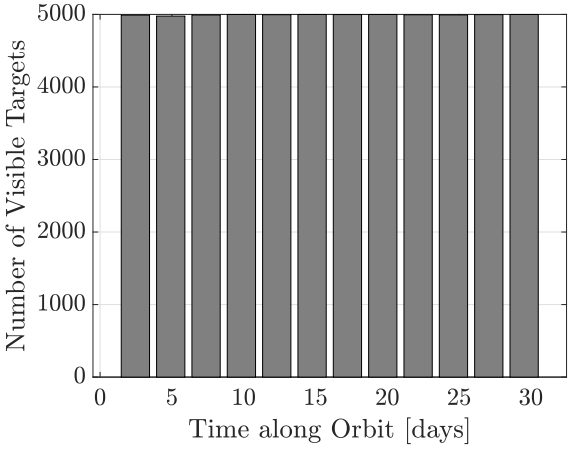

(d) Targets outside lunar exclusion

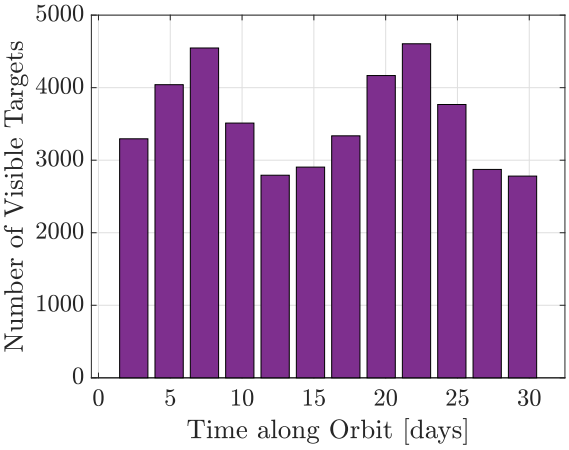

(e) Overall target visibility

Figure 6.7. Visibility of fixed-position targets in the cislunar domain as viewed by the 1 : 1 synodic resonant observer.

the limiting magnitude. Considering all the visibility conditions together, the number of days that each target is visible to the observer are summarized in Table 6.3. Evidently, solar exclusion is the predominant issue that inhibits visibility for all the planar targets. This result is intuitive since all the objects lie in the same plane as the solar exclusion zone. Despite the higher magnitude values for the libration point orbits seen in Figure 6.8(b), passage through the solar exclusion zone limits their visibility. For the target in the spatial DRO, however, the magnitude constraint is dominant.

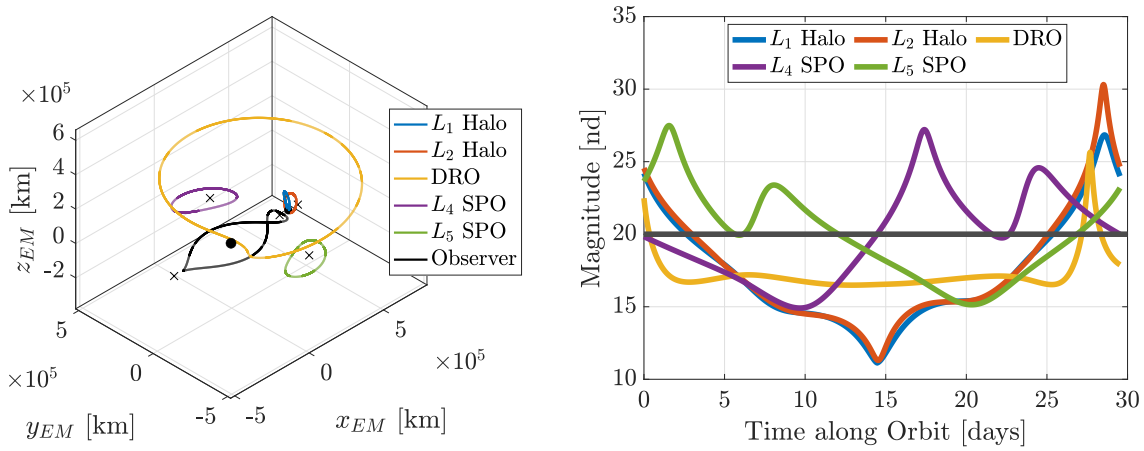

(a) Observer and target orbits

(b) Visual magnitude of targets

Figure 6.8. Visual magnitude of targets in various periodic orbits as viewed by the 1 : 1 synodic resonant observer.

Table 6.3. Visibility of targets in cislunar orbits for one period of the 1 : 1 synodic resonant orbit. The phasing of the observers and the targets assumes an initial epoch of January 01 2025.

Target Orbit	Number of Days Visible	Predominant Visibility Issue
L_1 Halo	16.4	Solar exclusion
L_2 Halo	14.9	Solar exclusion
DRO	27.9	Limiting magnitude
L_4 SPO	14.7	Solar exclusion
L_5 SPO	14.3	Solar exclusion

One option for mitigating the challenges imposed by a sensor's limiting magnitude is varying the relative phase of the observer, the target, and the Sun. Without any modifications to the target in its orbit, and with the initial location of the observer fixed at apolune, the epoch is allowed to vary. This change in epoch induces a variation in the solar phase angle, as illustrated in Figure 6.9. For this set of observer and target orbits, there exists an epoch, specifically January 30 2025, that results in the lowest visual magnitude over the course of the propagation. Additionally, for the minimum magnitude case that appears in Figure 6.9 in yellow, the locations of the highest magnitude of the target coincide with the passage of the target through the solar exclusion zone. This configuration, that occurs at the initial epoch of January 31 2025, yields the ideal visibility conditions for the target in the DRO as viewed from the observer. The updated visibility values for each target at this epoch appear in Table 6.4. Clearly, in addition to the improved visibility of the DRO, this observer phasing relative to the Sun increases the visibility of the remaining targets as well.

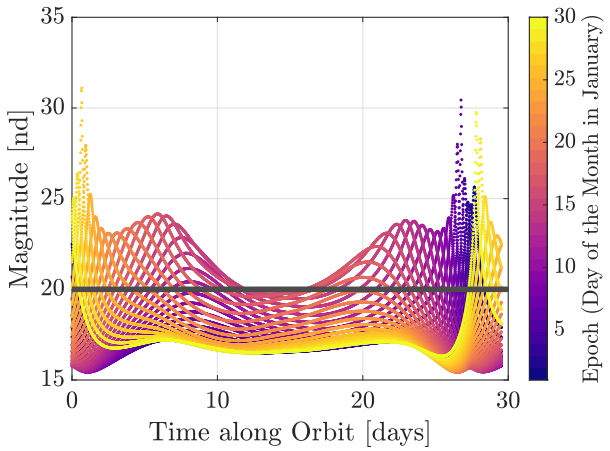

Figure 6.9. Variation in the visual magnitude of a target in a spatial DRO as a function of the initial epoch. The observer is located in a 1 : 1 synodic resonant orbit.

6.4 Designing for Connectivity Leveraging Sidereal Resonance

Combinations of space-based observers in various orbits together provide options for the constant surveillance of and connectivity within cislunar space, with monitoring capabilities

Table 6.4. Visibility of targets in cislunar orbits for one period of the 1 : 1 synodic resonant orbit. The phasing of the observers and the targets assumes an initial epoch of February 01 2025.

Target Orbit	Number of Days Visible
L_1 Halo	17.9
L_2 Halo	16.5
DRO	28.3
L_4 SPO	18.1
L_5 SPO	18.7

for specific regions of interest as well. Periodic orbits computed in the CR3BP are considered to demonstrate localized access for focused operations in cislunar space. For instance, in addition to observations toward the Earth, L_1 libration point orbits are applicable for monitoring the near-side of the Moon; L_2 libration point orbits, then, are useful for surveying the lunar far-side. Broader access of cislunar space, such as the volume of space near the Earth but beyond GEO, as well as the neighborhood of the L_3 libration point, is more broadly achievable by leveraging resonant orbits that traverse larger areas. Various sidereal resonant orbits are incorporated into the design of the observer orbits due to their expansive geometries. Additionally, libration point orbits with periods that are commensurate with resonant orbits and, as a result, also resonant with the lunar orbit period are identified. The resonance between the constellation orbits and the Moon and, by design, other observers in the constellation, ensures that the relative phasing of the spacecraft in the constellation is naturally maintained. As an example, the selection and analysis of orbits for a four-satellite constellation is detailed; one of the four is a Data Relay Satellite (DRS) that periodically approaches the Earth near the GEO belt, while the remaining three spacecraft are assumed to be observers in cislunar space.

6.4.1 Orbits for Data Relay Satellites

To conduct and maintain operations in support of cislunar SSA, it is necessary to facilitate periodic communications and data relay between the space-based observers and the Earth. However, the large volume of cislunar space that requires surveillance and, consequently, the long distances between observers in the lunar vicinity and the Earth, introduces challenges to sustain constant ground-based communications. These concerns are alleviated by potentially incorporating a Data Relay Satellite (DRS) into the constellation architecture. The wide variety of geometries available in CR3BP periodic orbits allows the selection of a DRS orbit such that it periodically interfaces with observers in specific cislunar regions of interest, such as the libration points, while also passing close to the Earth. Thus, when direct communications with the Earth are not possible, but information relay to the Earth is necessary, data from the observers may be communicated to the Earth by means of the DRS. Favorable characteristics of periodic orbits suitable for the DRS include short periods, repeated and close encounters with both the Earth and the Moon, and the orbital stability to sustain long-term operations as well. Additionally, the DRS must be phased such that it encounters the observers in their orbits periodically as well, ideally without the necessity of phasing maneuvers. Given these characteristics, sidereal resonant orbits offer viable options for hosting a cislunar DRS. One example of orbits that facilitate cislunar surveillance and data relay from the observer satellites to the Earth is the family of prograde orbits in $2:1$ sidereal resonance with the Moon illustrated in Figure 5.1(b). A DRS in such an orbit repeatedly encounters the neighborhood of the L_1 and L_2 libration points as well as the Moon, presenting opportunities for transferring data from observers in such orbits to the Earth. Thus, in addition to facilitating cislunar coverage for surveillance, the $2:1$ resonance family provides options for orbits that for periodic data relay between the Earth and the observer satellites that comprise the surveillance constellation.

6.4.2 Orbits for Space-Based Observers

While the selection of the DRS orbit supplies global coverage of cislunar space, a focus on the specific regions of interest within the entire volume of space is critical to facilitate

surveillance [64]. As such, periodic orbits that provide localized coverage near the lunar vicinity are necessary. However, as previously noted, spacecraft in orbits near the L_2 point do not establish a direct line-of-sight for communications with the Earth. Nevertheless, by incorporating the DRS into a surveillance constellation, these challenges are potentially mitigated. Various CR3BP periodic orbits are introduced and examined as potential hosts for observer satellites with on-board sensors that collect surveillance data. Even beyond sidereal resonant orbit families, a wide variety of CR3BP periodic orbit families are available that exhibit varying geometries, such as the subsets from the families of L_1 and L_2 Lyapunov orbits illustrated in Figures 3.5 and 3.6. These families provide options for periodic orbits that possess periods that are approximately equal to, or an integer ratio of, the period of $2:1$ sidereal resonant orbits. To interface with other vehicles in a constellation and maintain a relative phasing, specific orbits in a sidereal resonance with the lunar orbit are identified.

Resonant orbits characterized by other resonance ratios are also considered, given their footprint throughout cislunar space. Interior resonant orbits with shorter periods remain interior to the Earth-Moon system and typically pass close nearby to either the Earth or the Moon, or both. Such a feature is particularly useful for surveillance capabilities inside the LEC, i.e., the 30° cone from the Earth to the Moon, within which ground-based SSA capabilities are limited. Thus, space-based sensors in these resonant orbits facilitate the tracking of natural objects and assets in cislunar space. Some examples of interior resonant orbits that are suitable for Earth-Moon surveillance include, but are not limited to, members from the families of $3:1$ and $4:3$ sidereal resonances. In addition to offering cislunar coverage, these orbits also encounter prograde $2:1$ resonant orbits with every revolution, thus allowing inter-satellite communications and potential periodic data relay.

6.4.3 Sample Constellation Orbits

The selection of some combination of orbits for the design of a cislunar constellation is mission specific; however, an example of the selection process and analysis is discussed. The DRS is assumed to be operating in a $2:1$ resonant orbit selected from the orbit family in Figure 5.1(b). The remaining three satellites, i.e., the observers, are distributed across

cislunar space for a wide-ranging but also localized set of surveillance requirements. A 3 : 1 resonant orbit, and two 1 : 1 sidereal resonant members from the L_1 and L_2 Lyapunov orbit families are selected as the observer orbits. Table 6.5 lists the Jacobi constant values and the orbital periods for the selected orbits, all plotted in Figure 6.10 as viewed in the Earth-Moon rotating frame. The 2 : 1 DRS orbit is plotted in black, with the radius of a geosynchronous orbit indicated in blue. While this particular orbit is not precisely tangent to the GEO altitude, it passes the GEO belt fairly closely in the prograde direction. Notably, the 2 : 1 orbit periodically approaches the vicinity of the other observers, thus, allowing recurring opportunities for data relay away from the Earth. The selected 3 : 1 resonant orbit, plotted in purple, is defined with a higher Jacobi constant value than the other observers and, thus, exists at a lower energy level. Clearly, the perigee of this orbit is similar to the perigee radius for the prograde 2 : 1 resonant orbit. The observer in this 3 : 1 orbit completes three Earth revolutions in one month. The remaining two observers operate in approximate 1 : 1 sidereal resonant L_1 and L_2 Lyapunov orbits that are plotted in blue and green, respectively. While the low amplitude of the L_2 Lyapunov orbit inhibits line-of-sight communications with the Earth, the selected DRS orbit passes sufficiently close to the L_2 Lyapunov orbit to relay data back to the Earth from the lunar far-side.

Table 6.5. Characteristics of the selected sidereal resonant constellation orbits.

Spacecraft	**Orbit**	**Jacobi Constant** [-]	**Period** [days]	**Perilune Altitude** [km]
DRS	2 : 1 Resonant	2.7029	28.07	11,268.53
Observer 1	3 : 1 Resonant	3.1302	28.07	65,343.97
Observer 2	1 : 1 L_1 Lyapunov	2.9148	28.07	5,551.87
Observer 3	1 : 1 L_2 Lyapunov	2.9350	28.07	22,58.36

A number of criteria are employed to evaluate the applicability and feasibility of the selected observer orbits for surveillance applications. First, for observers to obtain valuable surveillance data, in particular in the regions that the Earth ground-based systems are unable to collect data, time within the Lunar Exclusion Cone (LEC) is evaluated. Next, to minimize the reliance on direct communications with the Earth, the ability of the observers in their

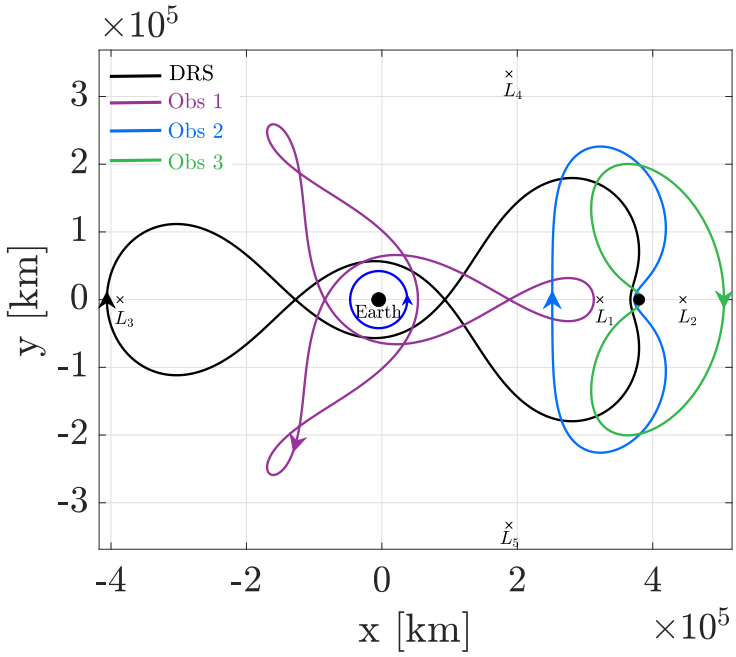

Figure 6.10. Selected orbits for a set of satellites in a constellation as viewed in the Earth-Moon rotating frame and computed in the Earth-Moon CR3BP.

orbits to interface with the DRS in its orbit is examined. This metric is assessed in terms of line-of-sight access between the two spacecraft as well as the relative distance between the spacecraft over time. For spacecraft that are within $120,000$ km of each other at a given time, it is assumed that inter-satellite communications allow the relay of data from the observer to the DRS to occur. Naturally, the spacecraft onboard hardware drives the inter-satellite communications capabilities; however, this distance is the assumed nominal value in the current work and may be modified as necessary. Based on this maximal range for communications, the relative phasing between the DRS and the observers is analyzed as well.

Observers in the Lunar Exclusion Cone

To gauge the ability of the spacecraft in the observer orbit to track objects within the specialized region of interest, i.e., the Lunar Exclusion Cone (LEC), the total time spent within the cone by each orbit is evaluated. For the constellation as a whole, the goal is

defined as at least one observer collecting data from inside the LEC at all times, since any objects in this region are not visible from the Earth. The 30° LEC is illustrated in Figure 6.11, with the locations along each orbit that fall within the cone indicated by the bold trajectory arcs. Over the course of 28.07 *days*, the DRS in the 2 : 1 resonant orbit remains inside the cone for 9.32 *days*, or about 33% of its orbital period. However, the observer orbits remain within the cone for 9.33, 17.32, and 25.84 *days* for the 3 : 1, L_1 Lyapunov, and L_2 Lyapunov orbits, respectively. These times correspond to approximately 33%, 61%, and 92% of the propagation times. Thus, over intervals when ground-based SSA from the Earth is lacking, the observers are able to track and survey objects and activity near the Moon. Also apparent in Figure 6.11 is that this particular 1 : 1 sidereal resonant L_2 Lyapunov orbit remains almost entirely inside the LEC, offering constant monitoring capabilities from the lunar far-side.

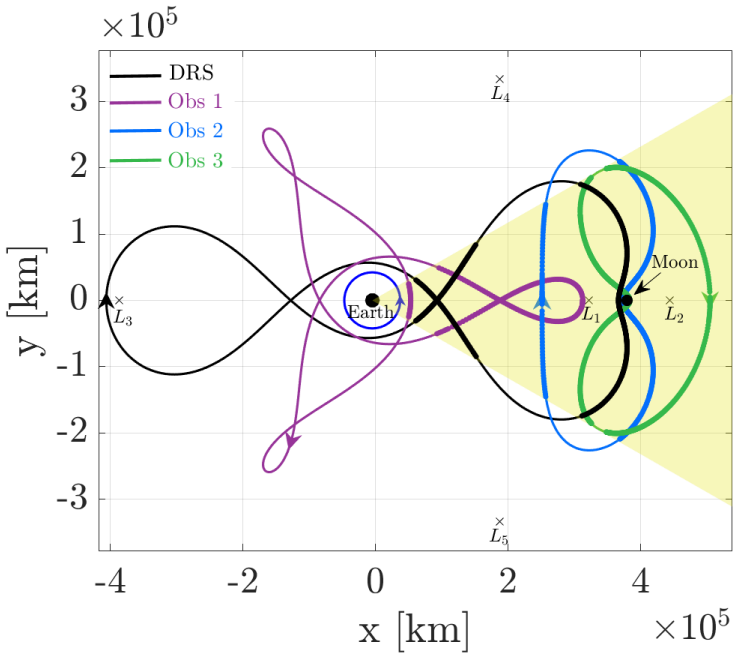

Figure 6.11. Constellation orbits located within the Lunar Exclusion Cone (LEC) illustrated in yellow.

Line-of-Sight with the DRS

Since the observers rely on the DRS for contact with the Earth when direct communications are unavailable, line-of-sight (LOS) with the DRS in its orbit must be maintained. Equation (6.1) is employed to evaluate the LOS constraint. For the orbits in this sample constellation, locations at which there exists no LOS between the DRS and each observer appear in Figure 6.12, as identified by the red markers in each plot. For the $3:1$ resonant orbit observer, the Earth prohibits line-of-sight with the relay satellite for a total of 0.32 $days$ or 7.6 hrs over the course of 28.07 $days$. For the observer in the L_1 Lyapunov orbit, the total time over which the constraint is violated is approximately 0.35 $days$ or 8.5 hrs, spread out over three separate intervals during approximately one sidereal month. For the L_2 Lyapunov orbit in Figure 6.12(c), the lack of a line-of-sight and, thus, lack of data relay opportunities, occurs for a longer total duration: 0.6 $days$ or 14.5 hrs over three intervals due to the Earth and two intervals due to the Moon. However and, in most part due to the geometry of the $2:1$ resonant orbit, the communications link for all the observers with respect to the DRS persists for the majority of the trajectory.

Distance Relative to the DRS

For data relay from the observer satellites to the DRS in the $2:1$ resonant orbit, the distance of each observer relative to the relay satellite is also examined. The total time that each observer is within communications range relative to the relay satellite (i.e., within $120,000\ km$) serves as a metric to evaluate the efficacy of the observer orbits. As an example, consider the isochronous distance for the second observer, i.e., the observer in the $1:1$ L_1 Lyapunov orbit, relative to the DRS in its $2:1$ resonant orbit. As a preliminary guess, the DRS is assumed to be located at apolune and the observer at perilune at initial time ($t = 0$). The initial conditions at those states for both orbits are propagated forwards in time using the CR3BP equations of motion for approximately one sidereal period. The isochronous relative distance and velocity between the two spacecraft is then evaluated. The data relay time is calculated, that is simply the total time that the observer is within the selected nominal range relative to the DRS.

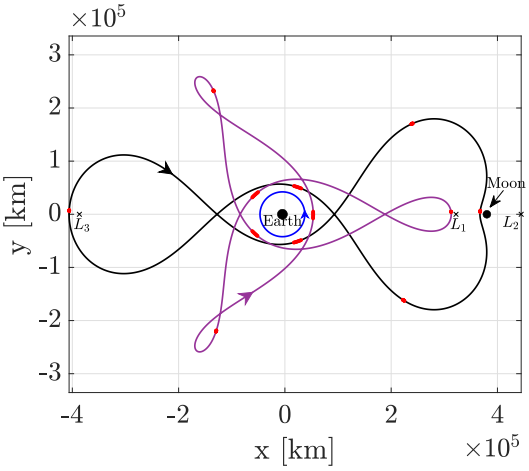

(a) 3 : 1 resonant observer

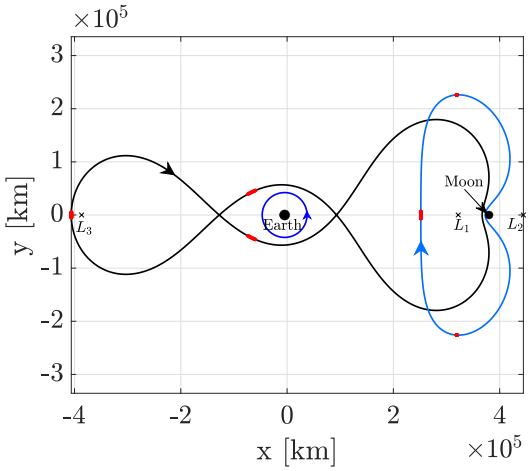

(b) L_1 Lyapunov observer

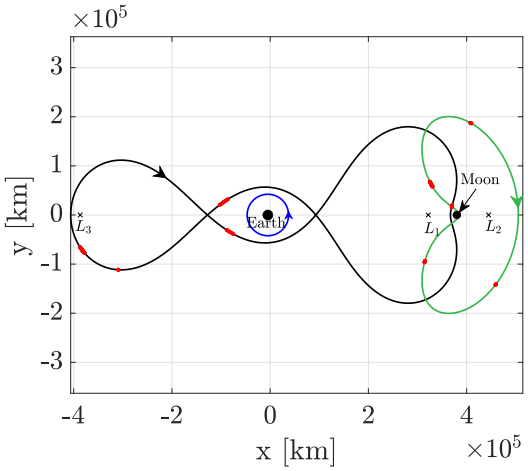

(c) L_2 Lyapunov observer

Figure 6.12. Line-of-sight between the DRS and various observers. Red markers indicate locations without line-of-sight between the DRS and each observer spacecraft.

The relative distance between the two spacecraft is determined over the propagation time, that is one month. In Figure 6.13(b), the resulting distance is plotted as a function of time; the black line indicates the range limit below which data relay is assumed to be possible between the spacecraft. Clearly, despite the proximity of the orbits in configuration space, the initial relative phasing causes the spacecraft to deviate in phase from each other downstream. As such, the observer is outside the allowable data relay range for the majority of the propagation time, i.e., for a total of 27.73 *days* of the 28.07 *day* propagation time. The instances within communication range are indicated by the bold arcs in each plot in

Figure 6.13. For reference, the relative velocity between the two spacecraft is assessed as well and appears in Figure 6.13(c). For the times when the observer is within range of the DRS, its velocity relative to the DRS is excessively high, approaching almost 1.75 km/s, and data transmission may be significantly inhibited. Thus, the preliminary guess for the relative phasing between the DRS and the observer (apolune and perilune, respectively) is not feasible, and other strategies to determine more suitable phasing options are sought.

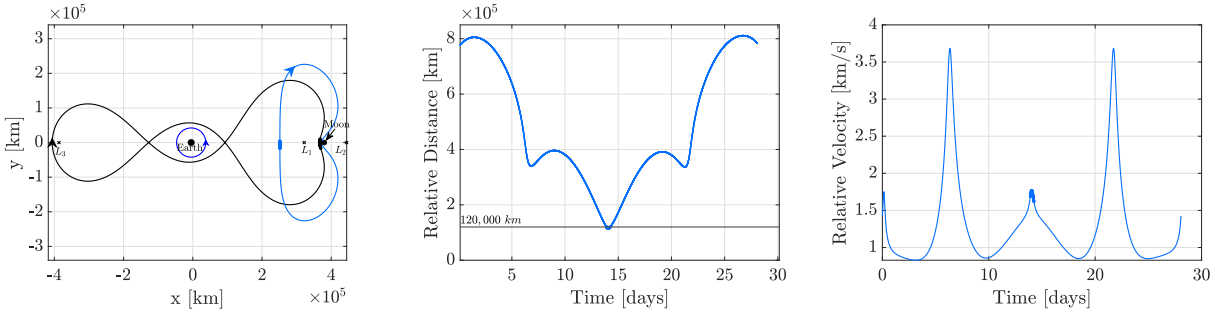

(a) Rotating frame (b) Relative distance (c) Relative velocity

Figure 6.13. DRS and an observer in the L_1 Lyapunov orbit propagated from apolune and perilune, respectively. The isochronous distance and the relative velocity between the two spacecraft is also plotted.

An angular representation for the locations along the DRS and the observer orbits is necessary to determine the ideal relative phasing between the two spacecraft. However, in contrast to Keplerian orbits, locations along CR3BP periodic orbits cannot be directly represented by angles, e.g., the true anomaly, mean anomaly, or eccentric anomaly, due to their complex geometries. This challenge is especially significant when working with resonant orbits due to their repeating geometries. For example, in the inertial frame, the $3:1$ resonant orbit traces out three "elliptical-type revolutions" about the Earth. An alternative cyclic metric that represents the passage of time along the orbit allows the relative phasing between orbits to be assessed. The trigonometric encoding methodology detailed by Lafarge et al. is adopted to discretize the orbit into angular locations [85]. This angle, termed the encoding angle, is evaluated as,

$$\xi_i = \frac{t_{po} \cdot 2\pi}{\mathbb{T}} \tag{6.6}$$

where $\mathbb{T}$ is the period of the orbit, and t_{po} is the time since a fixed reference state along the path ($t_{po} \in [0, \mathbb{T}]$). The selection of the fixed reference state along the orbit is arbitrary, and is assigned to be apolune in this investigation. Thus, $\xi_0 = 0$ corresponds to apolune, and $\xi_{\mathbb{T}/2} = \pi$ corresponds to the half-period location along the orbit. Specific locations along the orbits for the DRS and the observers are then discretized and represented by their respective encoding angles. For the DRS orbit and for the observer in the $1:1$ sidereal L_1 Lyapunov orbit, the locations along the orbits represented by their encoding angles appear in Figure 6.14.

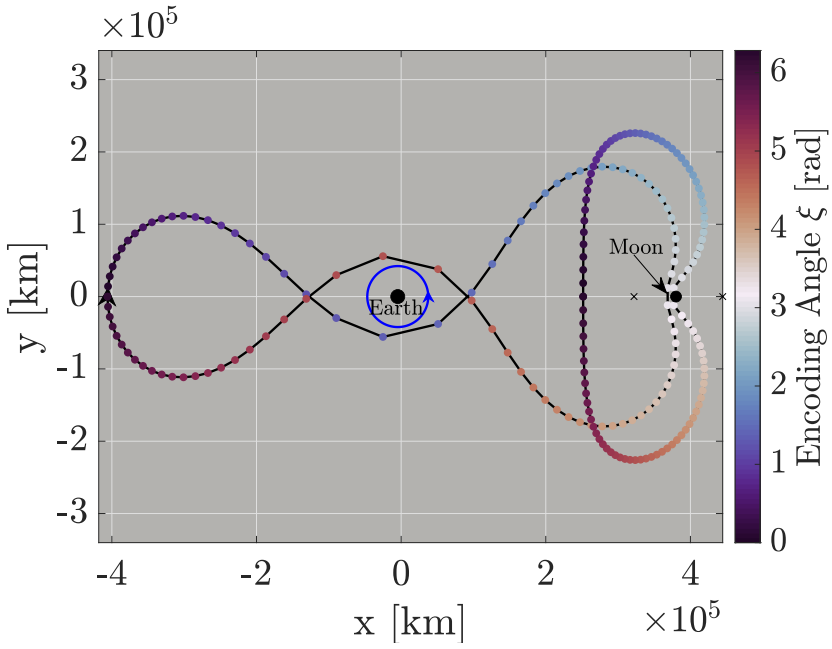

Figure 6.14. Trigonometric encoding for the DRS orbit and the 1:1 L_1 Lyapunov orbit

For each ξ_{DRS} and ξ_{obs} encoded angle along both orbits in Figure 6.14, the corresponding states are propagated for one sidereal period in the CR3BP. A contour plot identifying the time that both spacecraft are within relay range (relative distance $\leq 120,000\ km$) over the course of one month is generated for each encoding angle combination. The resulting map appears in Figure 6.15(a). Previously, the preliminary guess for the phasing between the $2:1$ resonant orbit for the DRS and the L_1 Lyapunov orbit for the observer is assumed as an initial phase represented by $\xi_{DRS} = 0\ [rad]$ and $\xi_{obs} = \pi\ [rad]$, that yields only 0.33 *days* of relay time over one month. This particular phasing guess lands in the purple

region in Figure 6.15(a), yielding the lowest possible relay time. However, by selecting phase combinations in the brighter regions of the map in Figure 6.15(a), configurations that naturally yield longer relay times are identified. Options that lie in the yellow regions may provide opportunities for up to 8 *days* of data relay over one sidereal period. The locations at which the spacecraft are within communications range are denoted by the bold arcs in Figure 6.15(c), and the red markers locate the initial locations of the DRS and the observer in their respective orbits. The CR3BP trajectories propagated over five months corresponding to both the DRS and the observer, appear in Figure 6.15(d) as plotted in an Earth-centered inertial view. As the DRS in its $2:1$ orbit, in black, precesses in the inertial frame to maintain its resonance with the Moon, the $1:1$ Lyapunov orbit follows over subsequent revolutions. Since the orbital periods are all in equal resonance with the Moon and, as a result, with each other, the feasible phasing over one month persists over time as well. Consequently, the relative distance between the L_1 observer and the DRS is consistent over five months, as apparent in Figure 6.15(b). The two spacecraft maintain their relative phase as determined from the contour plot, and the relay time as evaluated over one month persists through longer propagation times as well. For a five month propagation time, a total of 42.02 *days* of relay opportunities exist between the observer and the DRS. This value corresponds to approximately 30% of the propagation time, a significant difference from the preliminary guess that yields relay opportunities for only approximately 1.2% of the propagation time. The same process is repeated for the other observers in the constellation. Rather than guessing and checking, angle encoding and contour plots are leveraged to determine the phase difference between the DRS and each observer such that the time within a specified communications range is maximized. Additionally, while the total relay time is the primary metric in this investigation, this methodology is adaptable for the determination of the relative phase to accommodate other desired criteria as well for various other applications.

The methodology is easily adapted for the other observers in the constellation as well. For the observer in the $3:1$ resonant orbit, the contour plot to determine the ideal relative phasing appears in Figure 6.16. The ideal phase that maximizes relay time corresponds to $\Delta\xi = \pi$ $[rad]$, yielding 3.5 *days* of relay opportunities per revolution, and is propagated for five sidereal periods. The locations at which data relay windows occur are indicated

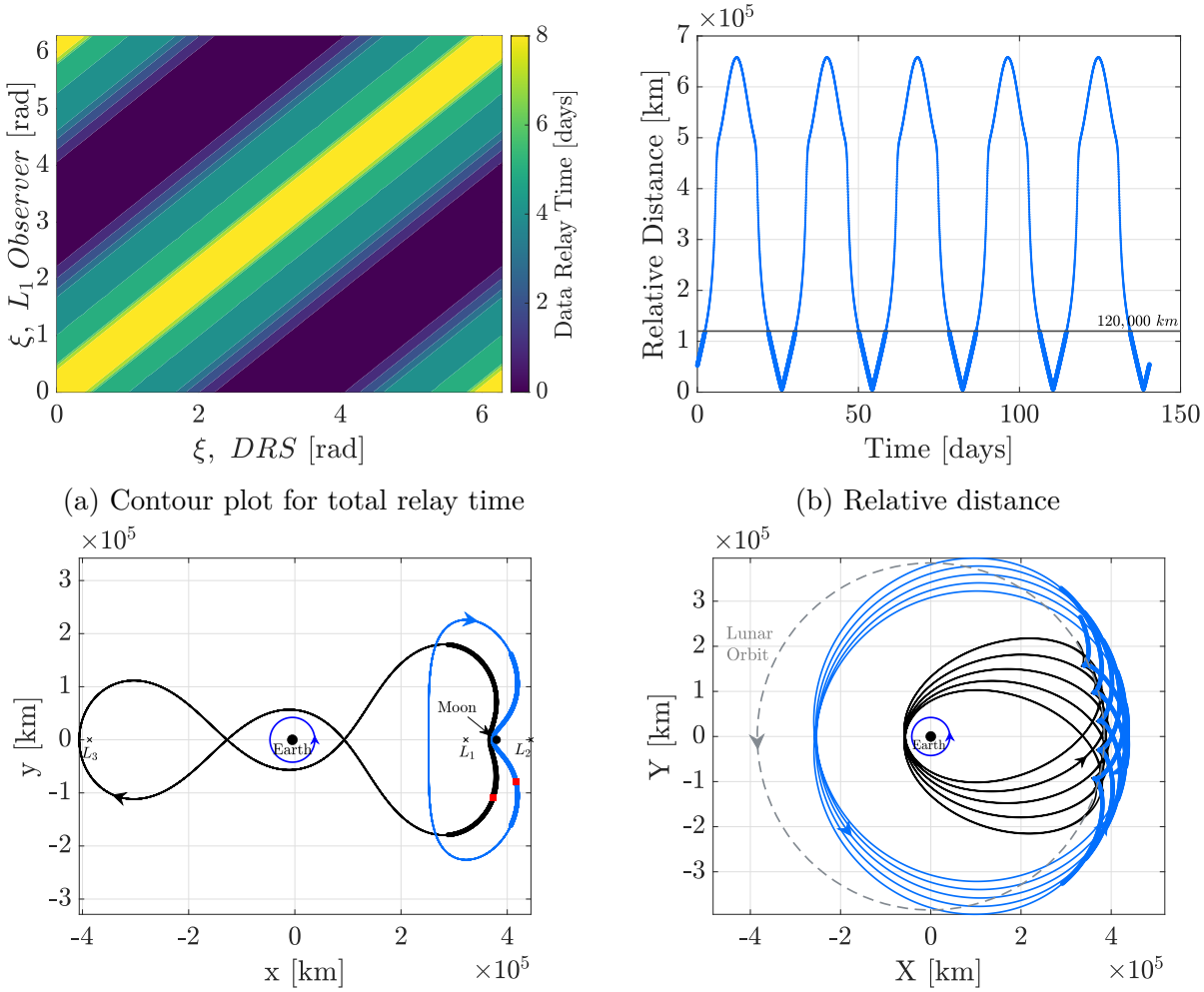

(a) Contour plot for total relay time

(b) Relative distance

(c) Relay locations, rotating frame

(d) Relay locations, inertial frame

Figure 6.15. Contour plot for relative phasing and data relay times for the observer in the $1:1$ L_1 Lyapunov orbit (blue) and the DRS (black).

in Figure 6.16(c) as viewed in the rotating frame, with the red markers locating the initial position of each spacecraft. Another notable feature for this particular resonant orbit, in addition to its proximity to the lunar vicinity, is repeatable passes to the vicinity of the GEO belt, as plotted in blue in Figure 6.16(c) and in the inertial frame in Figure 6.16(d). Thus, while the total time for data relay to the relay satellite in the $2:1$ resonant orbit may be limited, as identified by the contour plot, the observer spacecraft in this orbit is able to communicate directly with the Earth as well. Over five months, because of their periods, the

phasing with the DRS is maintained without a requirement for maneuvers. Such is apparent in Figure 6.16(b), where the relay opportunities repeat every month.

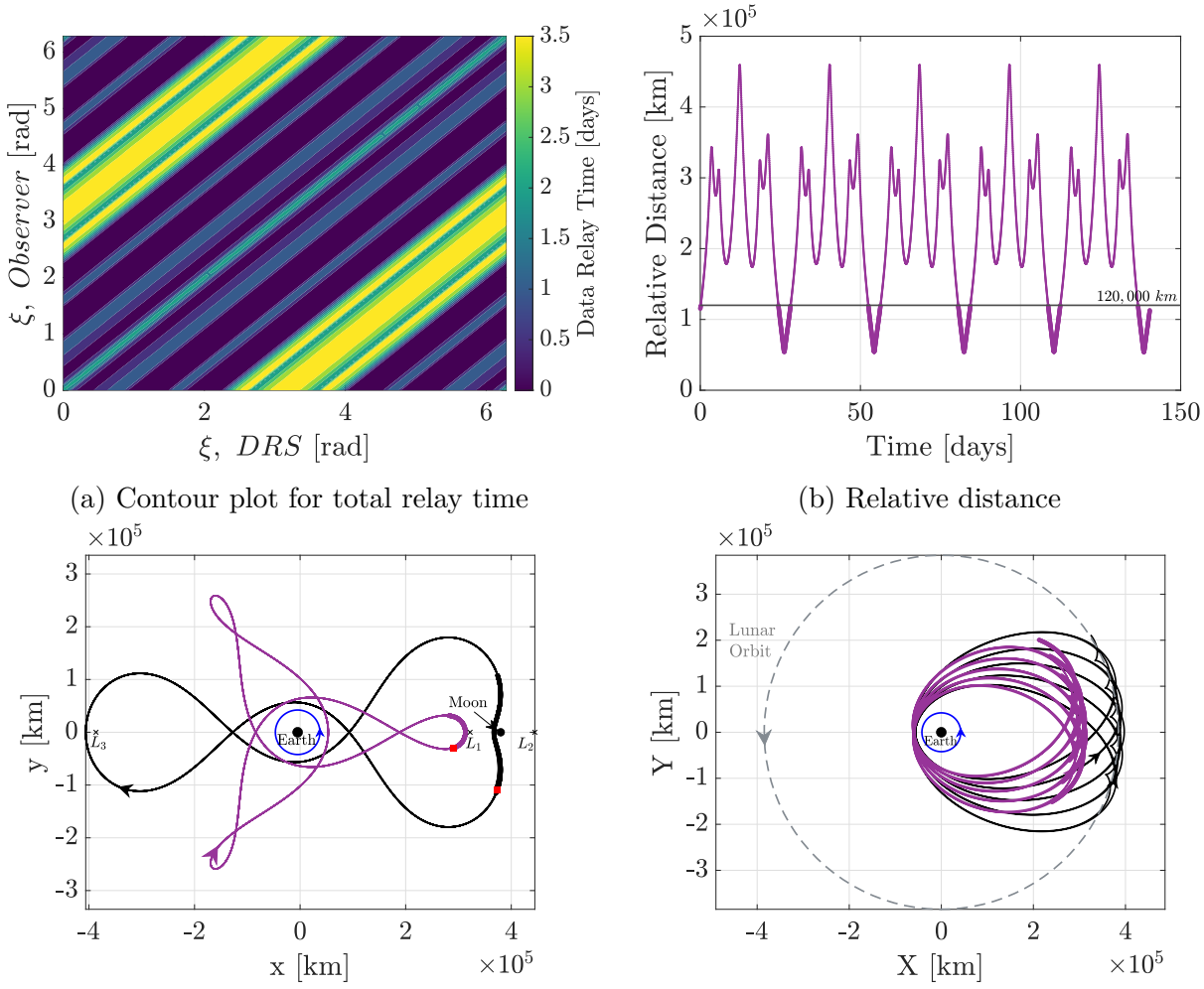

(a) Contour plot for total relay time

(b) Relative distance

(c) Relay locations, rotating frame

(d) Relay locations, inertial frame

Figure 6.16. Contour plot for relative phasing and data relay times for the observer in the 3 : 1 resonant orbit (purple) and the DRS (black).

Finally, a similar analysis for the 1 : 1 L_2 Lyapunov orbit reveals the ideal phasing for data relay to the DRS orbit as well, as demonstrated in Figure 6.17. The ideal phasing predicted by the contour plot in Figure 6.17, resulting in over 4.5 *days* of relay time, is non-intuitive for this particular orbit. The locations at which the observer is within range of the DRS, indicated by the bold markers in Figure 6.17(c) and Figure 6.17(d), occur as the DRS is departing the lunar vicinity and en route to the vicinity of the Earth. Thus, the observer

is able to transfer surveillance data from the lunar far-side to the DRS for further relay to the Earth. For this orbit as well, the relative phasing for the two spacecraft persists over subsequent revolutions, and the observer is within $120,000\ km$ of the DRS for 24.3 *days* over five months, as apparent in Figure 6.17(b). In addition to the relay opportunities when the observers are within the nominal communications range of the DRS, each observer maintains line-of-sight with the DRS for over 95% of the propagation time. Also, besides the observer in the L_2 Lyapunov orbit, the orbits themselves possess geometries such that direct communications with the Earth are possible as well.

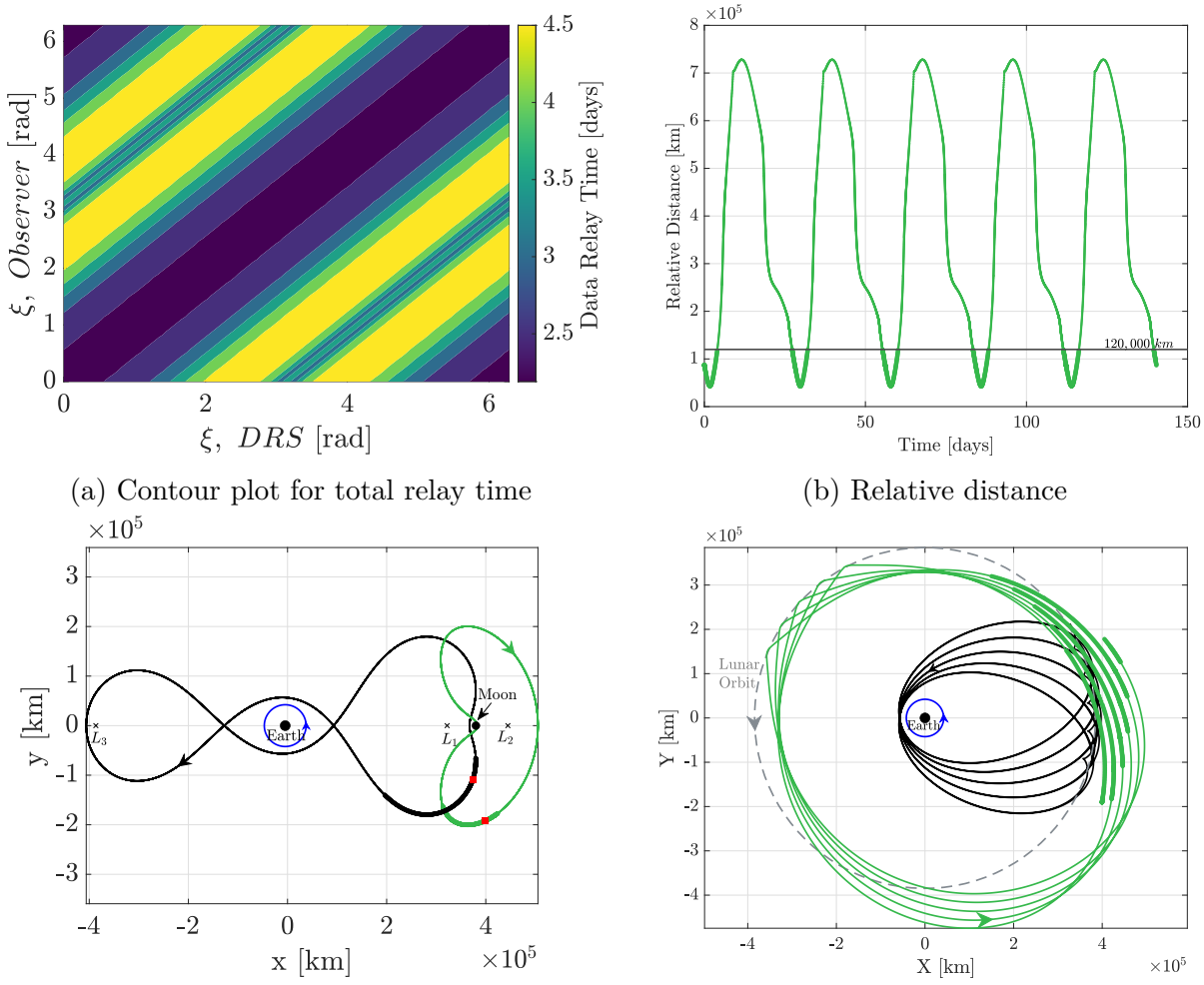

(a) Contour plot for total relay time

(b) Relative distance

(c) Relay locations, rotating frame

(d) Relay locations, inertial frame

Figure 6.17. Contour plot for relative phasing and data relay times for the observer in the $1:1$ L_2 Lyapunov orbit (green) and the DRS (black).

Velocity Relative to the DRS

While the line-of-sight and range considerations for data relay are critical, it is also useful to compare the velocities of the observers relative to the DRS. The relative velocity metric is especially significant for the locations at which the constellation spacecraft are within the nominal communications range of $120,000\ km$. For this analysis, the ideal relative phase determined for each observer is employed. The DRS and the observers are propagated for five months each; since the orbits are periodic, the behaviors over this time horizon reflect the general behavior that appears over longer times as well. The relative velocities for each observer are evaluated, with the locations at which each observer is within the nominal communications range of the DRS indicated via the bold arcs. For the observer in the L_1 Lyapunov orbit, the relative velocity during data relay lies between 170 m/s and 530 m/s, as evident in the plot in Figure 6.18(b). For the observer in the $3:1$ resonant orbit, Figure 6.18(a) illustrates the velocity with respect to the DRS in the $2:1$ resonant orbit. At the relay locations, this velocity is bounded between 480 m/s and 750 m/s, that coincides with apogee on the resonant orbit. Finally, for the L_2 Lyapunov observer, the relay velocity is between 375 m/s and 680 m/s, as apparent in Figure 6.18(c).

Connectivity and Coverage

For each spacecraft in the constellation, the connectivity in cislunar space is measured using the metrics introduced in Section 6.2. The time spent by the DRS and each observer in each zone is computed, along with the time it takes for the spacecraft to revisit that zone. Observers 2 and 3, located in L_1 and L_2 Lyapunov orbits respectively, operate only in Zone 1, as is apparent in Figure 6.19. However, for the DRS and the observer in the $3:1$ resonant orbit, it is useful to compute the time spent and the revisit rate for each cislunar zone of interest. Table 6.6 summarizes the values for the two spacecraft for each parameter and zone. The complex geometry of the $3:1$ orbit, i.e., observer 1, allows access to all the zones in the cislunar plane frequently, with the spacecraft predominantly operating in Zones 1, 2, and 4. The DRS, on the other hand, stays inside Zones 1 and 3 for the majority of time, but

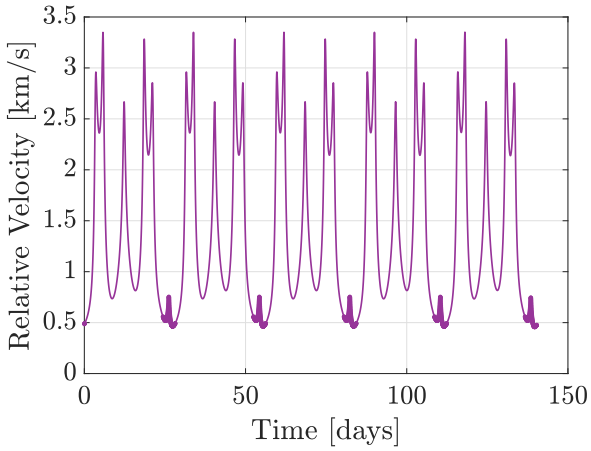

(a) 3 : 1 observer

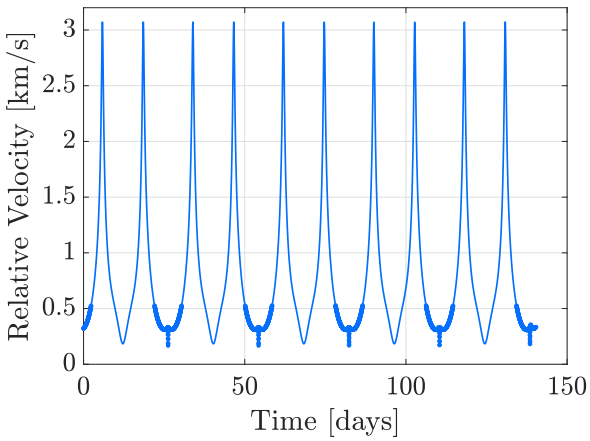

(b) L_1 Lyapunov observer

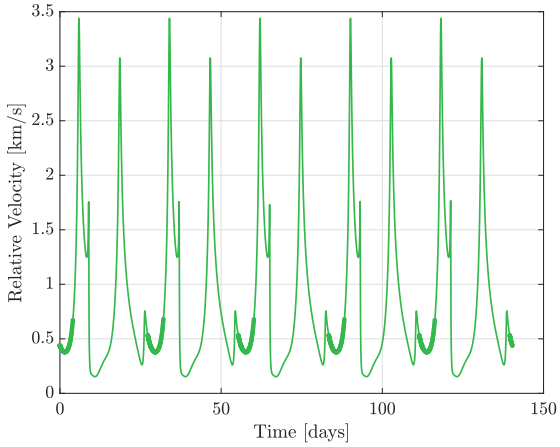

(c) L_2 Lyapunov observer

Figure 6.18. Velocity of each observer relative to the DRS computed in the Earth-Moon CR3BP.

access to the Earth is achieved through Zones 2 and 4 for approximately 8 hrs each once every sidereal period.

HFEM Validation

The constellation orbits are transitioned into the Earth-Moon-Sun-Jupiter HFEM model for further validation. The geometry-preserving transition process employed in the case of the retrograde observers in Section 5.2 is implemented to produce multi-revolution HFEM

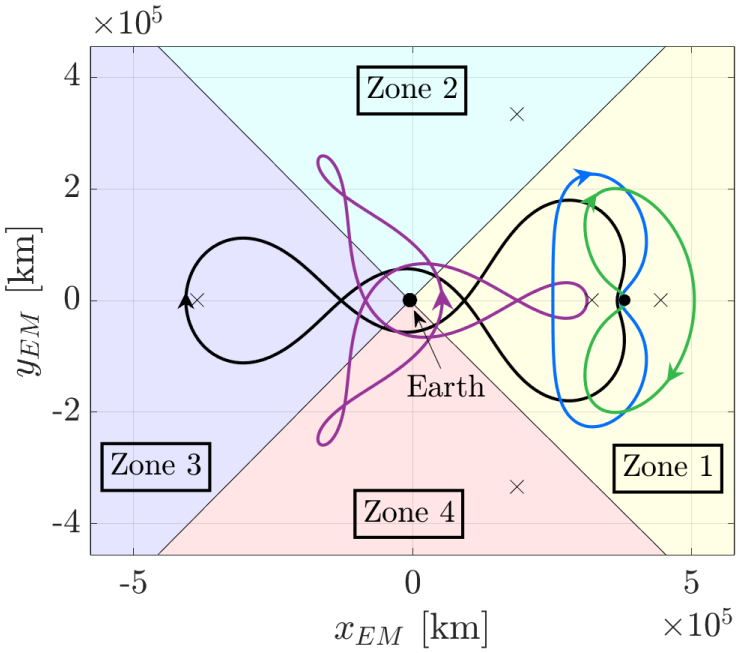

Figure 6.19. Constellation orbits and the cislunar zones of interest.

Table 6.6. Connectivity values for spacecraft in the sidereal constellation over one orbital period.

	DRS		Observer 1	
Zone	**Time Spent** [days]	**Revisit Rate** [days/rev]	**Time Spent** [days]	**Revisit Rate** [days/rev]
1	15.11	12.96	9.88	9.10
2	0.34	27.73	8.18	9.94
3	12.26	15.80	1.81	13.13
4	0.34	27.73	8.18	9.94

baselines for the four spacecraft in the constellation. The model epoch is selected as February 24 2025, 00:00:00 UTC.

The corrected ephemeris trajectories appear in Figure 6.20 for the 3 : 1 resonant orbit observer in purple, and the 2 : 1 resonant trajectory for the DRS in black. The trajectories are plotted in the J2000 Earth-centered inertial frame in Figure 6.20(b), also demonstrating the recurring Earth-Moon access via both orbits. Due to the stacking transition process, the trajectories generally retain their CR3BP geometries. Phasing between the orbits is

also maintained to the same levels as observed in the CR3BP model. The trajectories are propagated for a total of 184 *days*; over this interval, the observer is within $120,000$ km of the DRS for approximately 22 *days*. The periodic interface between the observer and DRS is apparent in Figure 6.20(c). The relative velocities over the same time period are plotted in Figure 6.20(d), with the bold arcs highlighting the relay opportunities. For the observer in the L_1 Lyapunov orbit, a similar transition process yields the observer trajectory in Figures 6.21(a) and 6.21(b) in the rotating and inertial frames, respectively. The observer passes within nominal communications range for 49.6 *days* of the 184-day time period. Consistent with previous examples, the relative phasing between the two spacecraft is maintained due to the appropriately phased initial guess generated in the CR3BP model. The geometries are generally bounded as well, but may be refined to yield "tighter" trajectories if desired. Finally, Figure 6.22 represents the results of transitioning the L_2 Lyapunov orbit into the ephemeris model. The observer interfaces with the DRS once a month and at relative velocities < 1 km/s. As such, the observer is able to sustain lunar far-side surveillance with the opportunity to communicate and transmit relevant data to the DRS as necessary. Notably, the ballistic phasing and surveillance characteristics translate from the CR3BP into the HFEM. The selection of orbits that are in equal sidereal resonances with the Moon, as well as each other, assists in maintaining the relative configuration of the constellation spacecraft in both the models.

6.5 Designing for Visibility Leveraging Sidereal-Synodic Overlap

Sidereal resonant orbits are a primary focus of this investigation. However, it is also possible to leverage orbits that exhibit a sidereal-synodic overlap to marry the advantages of the sidereal geometry with the predictability of synodic resonances. This predictability is especially sought for visibility and illumination analysis, since orbits in synodic resonance exhibit repeating orientations relative to the Sun. Specifically, the $2:5$ synodic resonant orbit from the family of $5:3$ spatial resonant orbits identified in Figure 4.12(b) is selected. Although there exist options for synodic resonant orbits with shorter periods, this orbit traverses the cislunar volume spatially, providing additional vantage points for observations

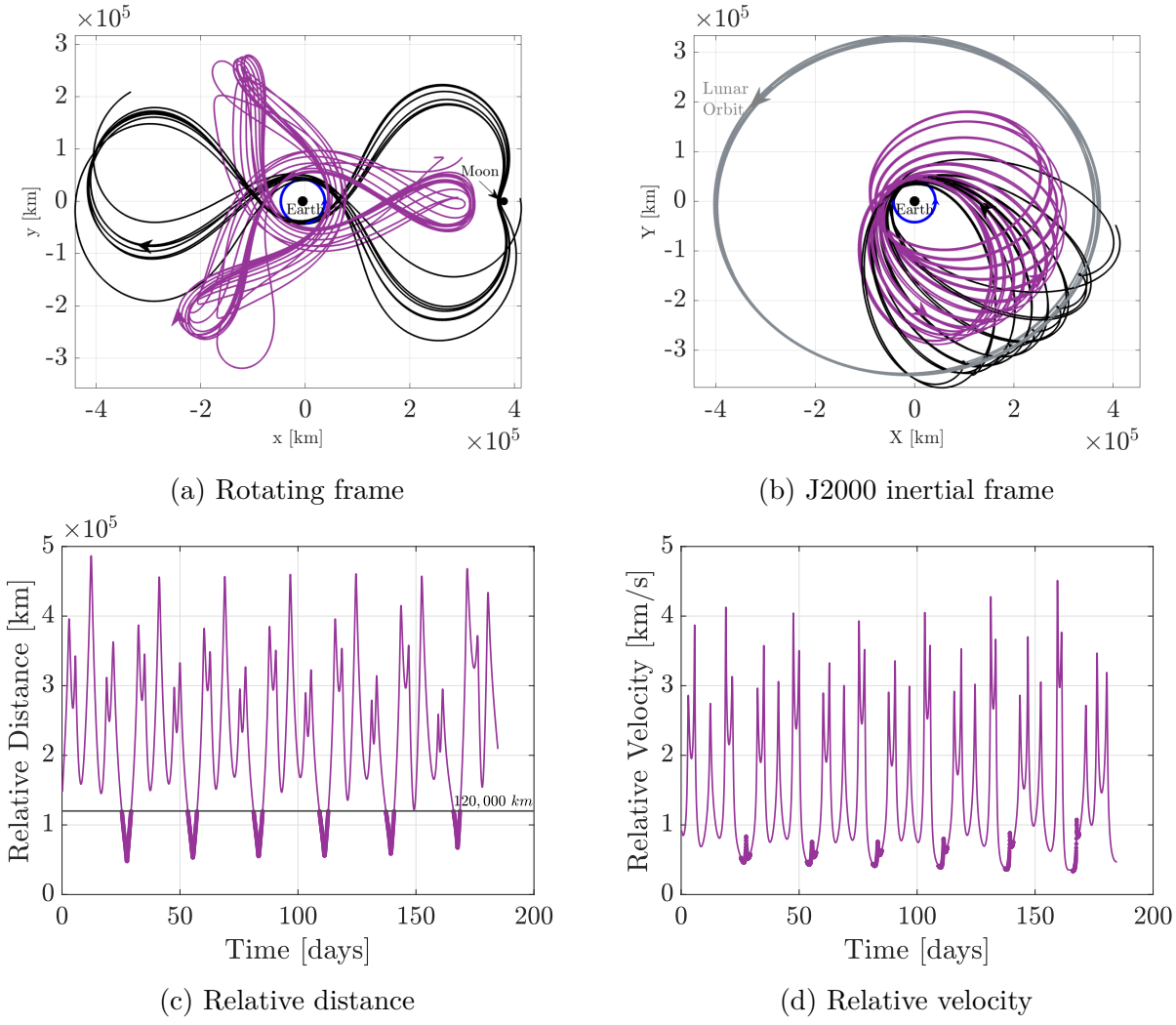

(a) Rotating frame

(b) J2000 inertial frame

(c) Relative distance

(d) Relative velocity

Figure 6.20. 3:1 resonant observer (purple) and the 2:1 resonant DRS (black) in the Earth-Moon-Sun-Jupiter HFEM.

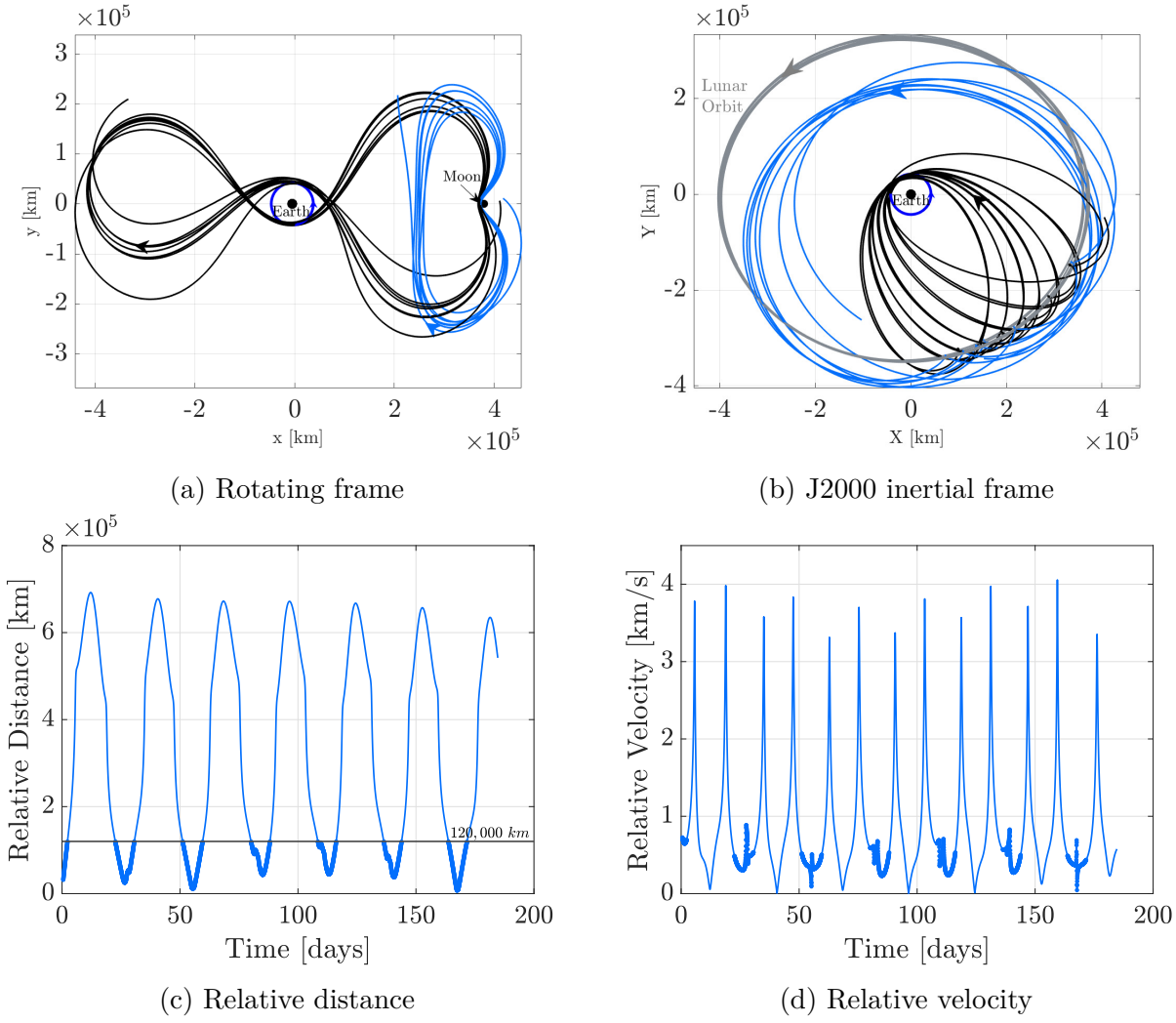

(a) Rotating frame

(b) J2000 inertial frame

(c) Relative distance

(d) Relative velocity

Figure 6.21. 1:1 resonant L_1 Lyapunov observer (blue) and the 2:1 resonant DRS (black) in the Earth-Moon-Sun-Jupiter HFEM.

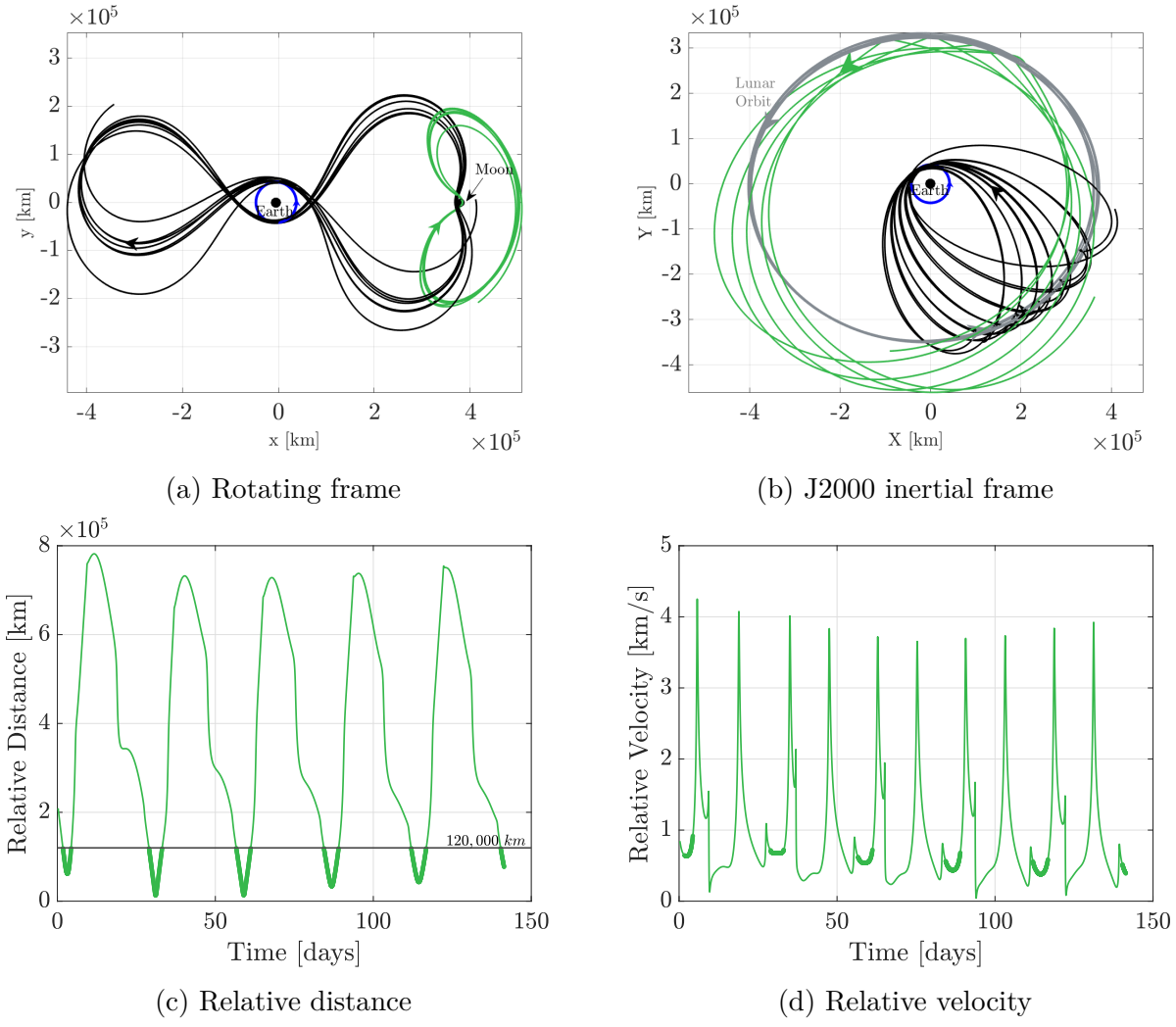

(a) Rotating frame

(b) J2000 inertial frame

(c) Relative distance

(d) Relative velocity

Figure 6.22. $1:1$ resonant L_2 Lyapunov observer (green) and the 2:1 resonant DRS (black) in the Earth-Moon-Sun-Jupiter HFEM.

and visibility beyond the Earth-Moon plane. The spatial geometry of the orbit is also favorable for achieving line-of-sight with assets on the lunar far-side.

Table 6.7. Characteristics of the selected resonant orbit with sidereal-synodic overlap.

Parameter	Value
Jacobi Constant	3.0127
Period [days]	73.81
Maximum Spatial Excursion [km]	91,040
Perilune Altitude [km]	69,000

A sample constellation of multiple space-based observers operating in the 2 : 5 synodic resonant orbit is designed. Comprehensive surveillance could, in such a scenario, be achieved by phasing the sensors such that they pass through different regions of cislunar space at the same time. From an operations standpoint, this architecture offers redundancy in cislunar coverage, since a volume that is swept by one observer is revisited by the other observers in the network. Additionally, depending upon the selection of the primary orbit, concerns regarding communications with the Earth may be alleviated. In contrast to a spacecraft located behind the Moon, all observers in the network have the opportunity to directly interface with Earth-based ground stations.

As an example, four space-based observers are located in this orbit. For resonant orbits, a natural choice for the initial phasing of the observers is the locations of apses or, in the Earth-Moon rotating frame, along the loops around the orbit. Two observers are placed at two of the four periapses along the orbit that appear around either side of the Earth. The remaining two are located at two of the four apoapses, one near L_3 and the other at the orbit perilune. Figure 6.23 illustrates the four observers at their initial locations along the orbit as viewed in the Earth-centered inertial and Earth-Moon rotating frames. Note that in the Earth-centered inertial frame, two of the observers (blue and red) are overlaid due to the coincidence of periapses at that point. In The visibility of cislunar targets in the representative orbits introduced in Figure 6.3(c) is assessed for each observer. In Figure 6.24,

each subplot illustrates the visual magnitude of all the targets as seen by each observer in the constellation. Notably, at every instant in time, all the targets are visible to at least one observer. The high spatial component of the observer orbits in this constellation, along with the synodic phasing, allow for favorable viewing conditions.

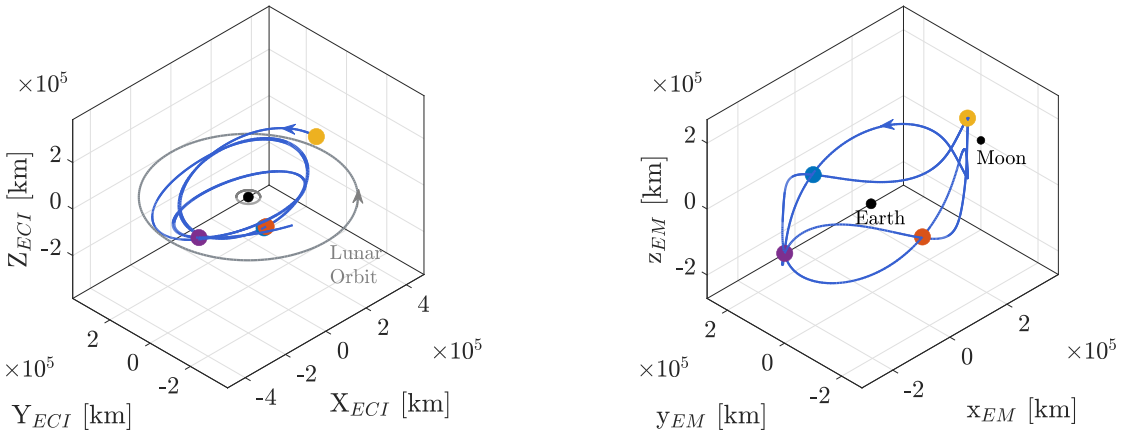

(a) Earth-centered inertial frame

(b) Earth-Moon rotating frame

Figure 6.23. Initial locations of four observers phased along the 2:5 synodic resonant orbit in the CR3BP as seen in the Earth-centered inertial and Earth-Moon rotating frame.

The advantages of selecting a synodic resonant orbit are apparent when eclipsing events are considered. Using the geometry of the observer trajectories in the Sun-Earth and Sun-Moon rotating frames, the trajectory insertion epoch for each observer in the constellation is determined such that no eclipsing events occur. This insertion epoch is selected as Jan 12 2025 00:00:00 UTC for each observer, propagated simultaneously from each initial location. The Sun-Earth and Sun-Moon rotating frame views for each observer trajectory, propagated for two orbit period (approximately 147.62 *days*) are plotted in Figures 6.25 and 6.26, where the colors identifying each observer are consistent with those in Figure 6.23. The Earth and Moon penumbra cones appear in red and blue respectively. The resulting trajectories avoid both Earth and Moon eclipses naturally, as is evident in the $\hat{\boldsymbol{y}}$-$\hat{\boldsymbol{z}}$ projections in Figures 6.25(d) and 6.26(d). Due to the underlying synodic resonant of the orbits, this favorable orientation for the entire network of observers repeats every synodic period as well, allowing significant flexibility in the trajectory selection process without any increase in the overall computational

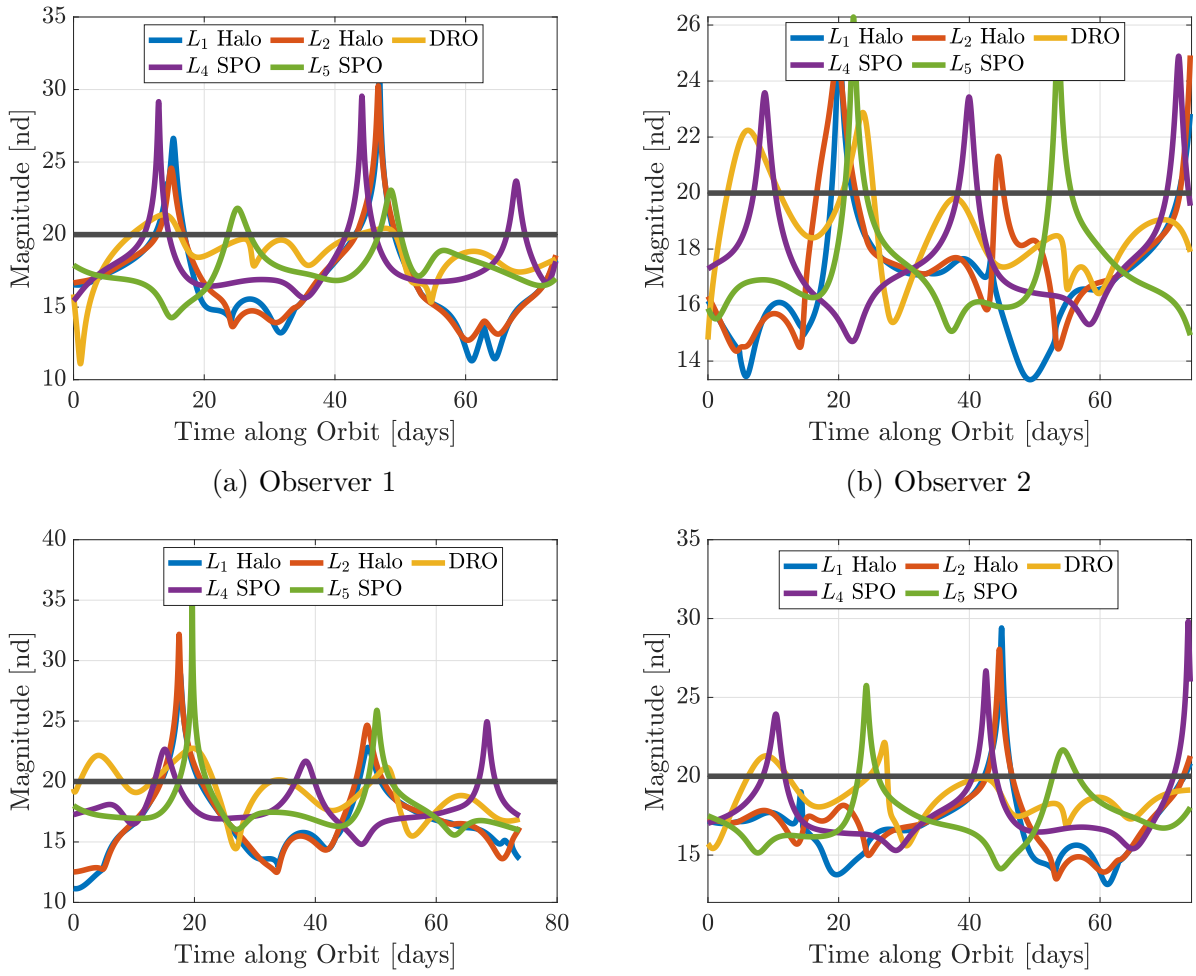

(a) Observer 1

(b) Observer 2

(c) Observer 3

(d) Observer 4

Figure 6.24. Visual magnitude of the various targets as viewed by each observer in the constellation.

cost. Another advantage of this particular orbit, along with the observer spacing, is that the observer lines-of-sight are maintained with the other spacecraft in the network, as an option for inter-satellite communications as necessary.

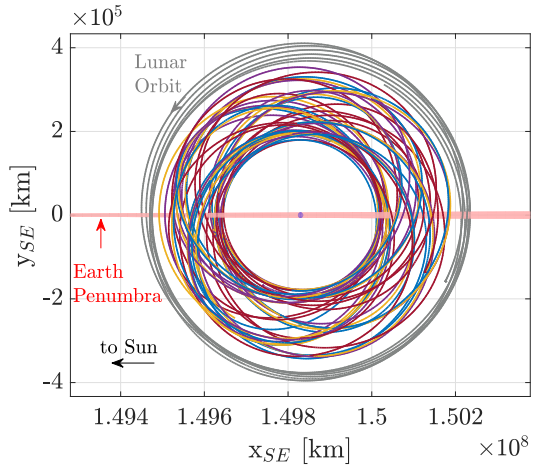

(a) $\hat{\boldsymbol{x}} - \hat{\boldsymbol{y}}$ view

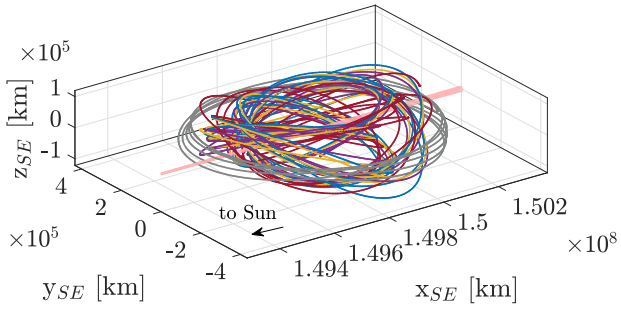

(b) Isometric view

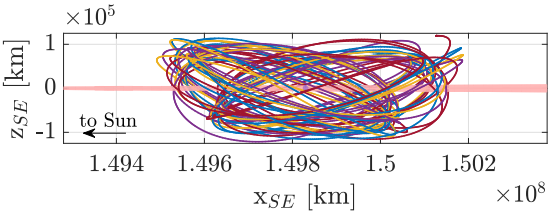

(c) $\hat{\boldsymbol{x}} - \hat{\boldsymbol{z}}$ view

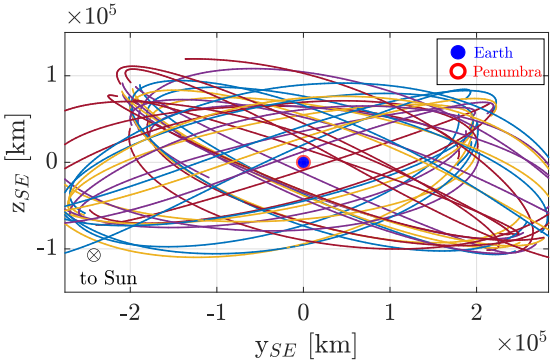

(d) Zoomed-in $\hat{\boldsymbol{y}} - \hat{\boldsymbol{z}}$ view

Figure 6.25. Sun-Earth rotating frame views of the 2 : 5 synodic resonant orbit. Careful selection of the trajectory epoch ensures that none of the observers pass through the Earth's penumbra.

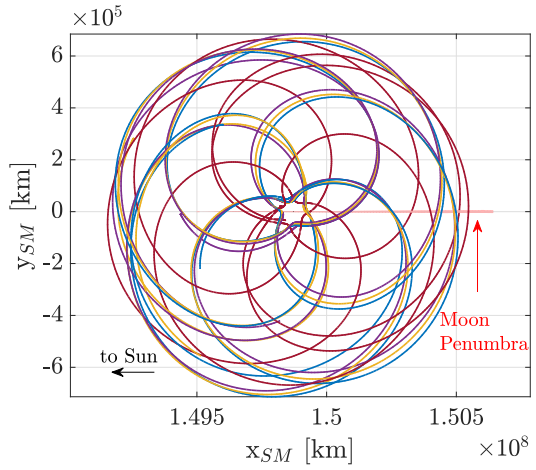

(a) $\hat{\boldsymbol{x}} - \hat{\boldsymbol{y}}$ view

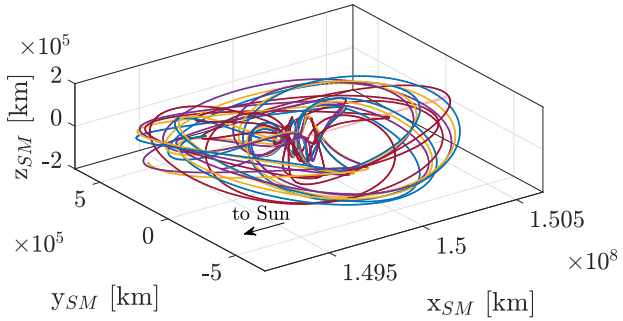

(b) Isometric view

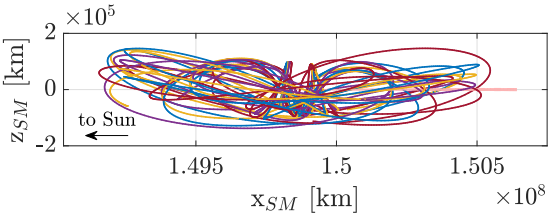

(c) $\hat{\boldsymbol{x}} - \hat{\boldsymbol{z}}$ view

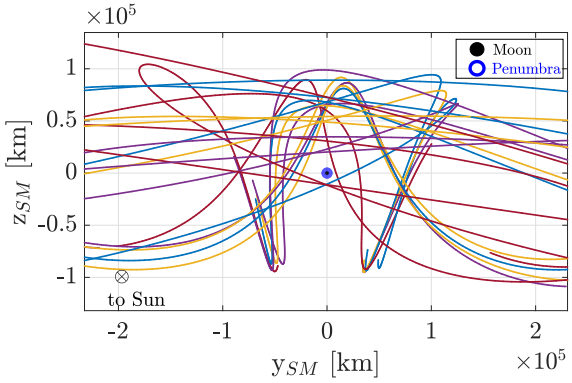

(d) Zoomed-in $\hat{\boldsymbol{y}} - \hat{\boldsymbol{z}}$ view

Figure 6.26. Sun-Moon rotating frame views of the 2 : 5 synodic resonant orbit. For the selected epoch, the observers circumvent the lunar penumbra.

7. CONCLUDING REMARKS

In the coming decades, numerous spacecraft are expected to populate cislunar space, reaching beyond the geosynchronous orbit region and out to the lunar vicinity. The complex cislunar dynamical environment necessitates the use of new and unique multi-body trajectories for sustaining long-term operations. In this investigation, resonant orbits are incorporated into the trajectory design process to explore the range of cislunar trajectories as options for Space Situational Awareness (SSA). The properties of the proposed orbits facilitate their long-term viability, that is validated in higher-fidelity dynamical models. Techniques for the construction of constellations that support cislunar SSA are presented. Metrics for visibility and connectivity in space are introduced to assess the utility of the proposed trajectories for cislunar applications.

7.1 Construction of Resonant Orbits

One of the primary objectives of the current work is the construction and analysis of resonant orbits and their associated properties for incorporation into future mission scenarios. Although the original foundation for resonant orbits is the two-body dynamical model, resonant orbits in the three- and $\mathcal{N}$-body dynamical models are obtained. Specifically, the dynamics of resonant orbits in the Circular Restricted Three-Body Problem (CR3BP) are detailed in the Earth-Moon system, with relevant trajectories validated in the Higher-Fidelity Ephemeris Model (HFEM) as well. The tools and techniques necessary to explore periodic orbits in the CR3BP are developed, and their functionality, specifically within the context of resonant orbits, is demonstrated via examples.

Both planar and spatial families of orbits in sidereal resonance are identified in the Earth-Moon CR3BP. Depending upon the resonance ratio, the orbits in these families offer a variety of solutions that span wide ranges of energy (Jacobi constant) levels. The evolution of the linear stability of the orbits is assessed, providing insight into the versatility of these orbits for cislunar applications. While sidereal resonant orbits exhibit expansive geometries that span the orbital plane of the Moon and beyond, the benefits of synodic resonant behavior are recognized. Orbits from sidereal resonant families that are commensurate with the lunar

synodic period in the rotating frame are identified for applications pertaining to illumination and visibility constraints in cislunar space.

7.2 Cislunar Access via Sidereal Resonant Orbits

Earth-Moon sidereal resonant orbits constructed in the CR3BP offer options for trajectories that span the volume of cislunar space. The orbits explored in this investigation possess unique geometries that traverse the vicinity of both the Earth and the Moon, providing recurring pathways between the two bodies. In addition to this favorable connectivity, the orbits maintain their resonance with the lunar orbit over time and demonstrate behavior feasible for long-term mission applications in the complex cislunar regime.

Orbit families in $2:1$ resonance with the lunar sidereal period offer favorable options to support cislunar operations as well. Retrograde and prograde orbits are identified that provide high- and low-energy options connecting the geosynchronous orbit region to the vicinity of the Moon. The retrograde family provides options for operationally stable orbits that continually survey cislunar space. Conversely, the linearly unstable prograde $2:1$ resonant orbits provide options for excursions to the lunar far-side. By leveraging dynamical systems theory and Poincaré mapping techniques, novel periodic orbits are uncovered that extend trajectories past the lunar orbit as well.

7.3 Resonant Trajectories for Sustaining Cislunar Space Situational Awareness

To address the specific needs for cislunar SSA, trajectories for space-based observers are constructed in the Earth-Moon CR3BP and validated in Earth-Moon-Sun-Jupiter HFEM. From these observer orbits, the visibility of various targets is assessed. The criteria considered for visibility include line-of-sight between the observer and the target, visual magnitude of the target with the true Sun position at each instant in time, and solar, Earth, and lunar exclusion conditions. The fidelity of lunar exclusion zone modeling is improved by introducing the modified lunar exclusion zone that incorporates the lunar phase as seen by the observer. Fixed-position target points in the vicinity of the Moon are assessed, as well as targets dispersed in the spherical cislunar volume as a whole. Additionally, to account

for possible target locations within cislunar space, representative periodic orbits from the CR3BP are identified to assess their visibility from various observers. Metrics for quantifying connectivity in cislunar space are introduced; for resonant orbits with complex and unique geometries, these metrics provide insight into their coverage of the cislunar plane.

Sample constellations that incorporate both sidereal and sidereal-synodic resonant orbits are designed for the surveillance of the cislunar domain. As an example, orbits in sidereal resonance with the Moon and with each other comprise one such constellation, allowing periodic interface between the spacecraft in the network. Challenges in phasing resulting from the varying resonance ratios are addressed via phasing maps that preserve the natural configuration of the constellation over time in both the CR3BP and the ephemeris models.

Another example constellation demonstrates the selection of spatial sidereal-synodic resonant orbits, with the observers in the constellation phased along the same periodic orbit. The synodic resonance is leveraged to identify epochs that naturally yield eclipse-free solutions for all the observers in the network. Additionally, the visibility of targets in various cislunar orbits is assessed for the observers in the constellation. The choice of the spatial periodic orbits, along with the relative phasing of the spacecraft, allows each target to be visible to at least one observer at all instants in time. Together, the two sample constellations demonstrate the versatility of resonant orbits for trajectory design in support of cislunar SSA operations.

7.4 Recommendations for Future Work

The techniques presented in this investigation lay the groundwork for the further incorporation of resonant orbits into trajectory design for cislunar applications. Some avenues for future work are suggested:

- **Solar exclusion zone avoidance**

  Solar exclusion is one of the predominant issues that inhibits target tracking as viewed from the space-based sensors considered in the current work. Sidereal-synodic resonant orbits provide flexible options for phasing relative to the Sun to mitigate these challenges; however, incorporating an exclusion zone avoidance path constraint may

allow the computation of observer trajectories that consistently observe the desired target(s). One implementation of such a constraint may build upon the penumbra avoidance path constraint detailed in this investigation.

- **Resonance transitions for phase modification**

  For the orbits considered in the current work, the challenges with visibility and connectivity are inherently tied to the period of the underlying resonant orbit. By temporarily varying the period of the underlying orbit, i.e., by transitioning to a different resonant orbit, these issues may be alleviated. Trajectories may, then, be constructed with transitions between multiple different resonance ratios that maintain cislunar accessibility with minimal propellant expenditure.

- **Resonant orbit station-keeping strategies**

  Long-term reference trajectories that adequately retain the baseline orbit geometry require orbit maintenance and station-keeping strategies. The implementation of existing as well as novel station-keeping techniques specific to resonant orbits is warranted.

REFERENCES

[1] R. Kraft, *Analysis Confirms Successful Artemis I Moon Mission, Reviews Continue*, https://www.nasa.gov/feature/analysis-confirms-successful-artemis-i-moon-mission-reviews-continue, last accessed at 2023-08-31, Mar. 2023. (visited on 08/31/2023).

[2] ISRO, *Chandrayaan-3*, https://www.isro.gov.in/Chandrayaan3-Details.html, last accessed at 2023-08-31, Aug. 2023. (visited on 08/31/2023).

[3] *The results of the Moon Landing by the Smart Lander for Investigating Moon (SLIM)*, https://global.jaxa.jp/press/2024/01/20240120-1_e.html, last accessed at 2024-04-01, Japan Aerospace Exploration Agency, Jan. 2024. (visited on 04/01/2024).

[4] NASA, *Gateway space station*, https://www.nasa.gov/reference/gateway-about/, last accessed at 2024-04-01, Jun. 2023. (visited on 04/01/2024).

[5] Advanced Space, *Oracle: Space Situational Awareness Missions Beyond GEO*, https://advancedspace.com/missions/oracle/, last accessed at 2024-04-01, 2023. (visited on 04/01/2024).

[6] B. Dunbar, *Commercial Lunar Payload Services Overview*, https://www.nasa.gov/commercial-lunar-payload-services-overview, last accessed at 2023-08-28, May 2023. (visited on 08/28/2023).

[7] R. Hoover, *NASA VIPER Robotic Moon Rover Team Raises Its Mighty Mast*, https://www.nasa.gov/news-release/nasa-selects-astrobotic-to-fly-water-hunting-rover-to-the-moon/, last accessed at 2024-04-01, Apr. 2024. (visited on 04/01/2024).

[8] *Space Doctrine Publication 3-100, Space Domain Awareness*, Space Training and Readiness Command (STARCOM), Nov. 2023.

[9] United States Space Force, *Space Capstone Publication: Spacepower Doctrine for Space Forces*, Jun. 2020.

[10] J. A. Sims, "Jupiter Icy Moons Orbiter Mission Design Overview," in *16th AAS/AIAA Space Flight Mechanics Conference*, Tampa, Florida, 2006.

[11] C. D. Murray and S. F. Dermott, *Solar System Dynamics*. Cambridge University Press, 2000. DOI: 10.1017/cbo9781139174817.

[12] I. Newton, *Philosophiae naturalis principia mathematica*. Jussu Societatis Regiae ac Typis Josephi Streater, 1687. DOI: 10.5479/sil.52126.39088015628399.

[13] V. Szebehely, *Theory of Orbits: The Restricted Problem of Three Bodies*. Academic Press Inc., 1967, ISBN: 978-0-12-395732-0.

[14] J. Wisdom, "The Resonance Overlap Criterion and the Onset of Stochastic Behavior in the Restricted Three-Body Problem," *Astronomical Journal*, vol. 85, no. 8, pp. 1122–1133, Aug. 1980. DOI: 10.1086/112778.

[15] D. A. Minton and R. Malhotra, "Secular Resonance Sweeping of the Main Asteroid Belt During Planet Migration," *The Astrophysical Journal*, vol. 732, no. 1, 2011. DOI: 10.1088/0004-637X/732/1/53.

[16] K. M. Deck, M. Payne, and M. J. Holman, "First-Order Resonance Overlap and the Stability of Close Two-Planet Systems," *The Astrophysical Journal*, vol. 774, no. 2, 2013. DOI: 10.1088/0004-637X/774/2/129.

[17] R. L. Anderson, "Low Thrust Trajectory Design for Resonant Flybys and Captures Using Invariant Manifolds," Ph.D. Dissertation, University of Colorado, Boulder, Colorado, 2005.

[18] E. Belbruno and B. G. Marsden, "Resonance Hopping in Comets," *Astronomical Journal*, 1997, ISSN: 0004-6256. DOI: 10.1086/118359.

[19] W. S. Koon, M. W. Lo, J. E. Marsden, and S. D. Ross, "Heteroclinic Connections between Periodic Orbits and Resonance Transitions in Celestial Mechanics," *Chaos: An Interdisciplinary Journal of Nonlinear Science*, vol. 10, no. 2, pp. 427–469, 2000, ISSN: 1054-1500. DOI: 10.1063/1.166509.

[20] K. C. Howell, B. G. Marchand, and M. W. Lo, "Temporary Satellite Capture of Short-Period Jupiter Family Comets from the Perspective of Dynamical Systems," *Journal of the Astronautical Sciences*, 2001, ISSN: 00219142.

[21] M. Vaquero, "Poincaré Sections and Resonant Orbits in the Restricted Three-Body Problem," M.S. Thesis, Purdue University, West Lafayette, Indiana, 2010.

[22] M. Vaquero, "Spacecraft Transfer Trajectory Design Exploiting Resonant Orbits in Multi-Body Environments," Ph.D. Dissertation, Purdue University, West Lafayette, Indiana, 2013.

[23] S. Vutukuri, "Spacecraft Trajectory Design Techniques Using Resonant Orbits," M.S. Thesis, Purdue University, West Lafayette, Indiana, 2018.

[24] D. Canales, M. Gupta, B. Park, and K. C. Howell, "A Transfer Trajectory Framework for the Exploration of Phobos and Deimos Leveraging Resonant Orbits," *Acta Astronautica*, vol. 194, pp. 263–276, 2022, ISSN: 0094-5765. DOI: https://doi.org/10.1016/j.actaastro.2022.02.001.

[25] J. K. Vendl and M. J. Holzinger, "Cislunar Periodic Orbit Analysis for Persistent Space Object Detection Capability," *Journal of Spacecraft and Rockets*, 2021, ISSN: 15336794. DOI: 10.2514/1.A34909.

[26] C. Frueh, K. Howell, K. J. DeMars, and S. Bhadauria, "Cislunar Space Situational Awareness," in *31st AAS/AIAA Space Flight Mechanics Meeting*, Charlotte, North Carolina (Virtual), Feb. 2021.

[27] M. Thompson, N. Ré, C. Meek, and B. Cheetham, "Cislunar Orbit Determination and Tracking via Simulated Space-Based Measurements," in *Advanced Maui Optical and Space Surveillance Technologies Conference*, Sep. 2021.

[28] A. W. J. Dahlke and R. Bettinger, "Preliminary Comparative Assessment of L2 and L3 Surveillance using Select Cislunar Periodic Orbits," in *AAS/AIAA Astrodynamics Specialist Conference*, Aug. 2022.

[29] S. Bhadauria, C. Frueh, and K. C. Howell, "Cislunar Space Domain Awareness Using Bi-Circular Four Body Geometry," in *AAS/AIAA Astrodynamics Specialist Conference*, Charlotte, North Carolina, Aug. 2022.

[30] E. E. Fowler and D. A. Paley, "Observability Metrics for Space-Based Cislunar Domain Awareness," *Journal of the Astronautical Sciences*, vol. 70, no. 2, p. 10, Apr. 2023. DOI: 10.1007/s40295-023-00368-w.

[31] K. A. LeGrand, A. V. Khilnani, and J. L. Iannamorelli, "Bayesian Angles-Only Cislunar Space Object Tracking," in *33rd AAS/AIAA Space Flight Mechanics Meeting*, Austin, Texas, Jan. 2023.

[32] J. Iannamorelli and K. LeGrand, "Adaptive Filtering for Multi-Sensor Maneuvering Cislunar Space Object Tracking," in *Advanced Maui Optical and Space Surveillance (AMOS) Technologies Conference*, Sep. 2023.

[33] M. Gupta, "Finding Order in Chaos: Resonant Orbits and Poincaré Sections," M.S. Thesis, Purdue University, West Lafayette, Indiana, 2020.

[34] R. S. Park, W. M. Folkner, J. G. Williams, and D. H. Boggs, "The JPL Planetary and Lunar Ephemerides DE440 and DE441," *The Astronomical Journal*, 2021, ISSN: 0004-6256. DOI: 10.3847/1538-3881/abd414.

[35] A. D. Cox, "A Dynamical Systems Perspective for Preliminary Low-Thrust Trajectory Design in Multi-Body Regimes," Ph.D. Dissertation, Purdue University, West Lafayette, Indiana, 2020.

[36] B. D. Tapley, B. E. Schutz, and G. H. Born. Academic Press, 2004. DOI: https://doi.org/10.1016/B978-0-12-683630-1.X5019-X.

[37] H. Schaub and J. L. Junkins, *Analytical Mechanics Of Space Systems*. American Institute of Aeronautics and Astronautics, 2003. DOI: 10.2514/4.861550.

[38] R. W. Brockett, *Finite Dimensional Linear Systems*. Philadelphia, PA: John Wiley and Sons, 1970, ISBN: 978-0-471-10585-5.

[39] C. T. Kelley, *Iterative Methods for Optimization*. Philadelphia, PA: Society for Industrial and Applied Mathematics, 1999. DOI: 10.1137/1.9781611970920.

[40] C. M. Spreen, "Automated Patch Point Placement Capability for Hybrid Trajectory Targeting," Ph.D. Dissertation, Purdue University, West Lafayette, Indiana, 2017.

[41] A. E. Roy and M. W. Ovenden, "On the Occurrence of Commensurable Mean Motions in the Solar System: The Mirror Theorem," *Monthly Notices of the Royal Astronomical Society*, 1955, ISSN: 0035-8711. DOI: 10.1093/mnras/115.3.296.

[42] H. Poincaré, *Les Méthodes Nouvelles de la Mécanique Céleste*. Gauthier-Villars, 1893.

[43] H. Keller, "Numerical Solutions of Bifurcations and Nonlinear Eigenvalue Problems," *Applications of Bifurcation Theory*, pp. 359–383, 1977.

[44] V. A. Yakubovich and V. M. Starzhinskii, *Linear Differential Equations with Periodic Coefficients*. New York: Wiley, 1975.

[45] N. Bosanac, "Leveraging Natural Dynamical Structures to Explore Multi-Body Systems," Ph.D. Dissertation, Purdue University, West Lafayette, Indiana, 2016.

[46] D. J. Grebow, "Generating Periodic Orbits in the Circular Restricted Three-Body Problem with Applications to Lunar South Pole Coverage," M.S. Thesis, Purdue University, West Lafayette, Indiana, 2006.

[47] E. Zimovan, "Characteristics and Design Strategies for Near Rectilinear Halo Orbits within the Earth-Moon System," M.S. Thesis, Purdue University, West Lafayette, Indiana, 2017.

[48] E. T. Campbell, "Bifurcations from Families of Periodic Solutions in the Circular Restricted Problem with Application to Trajectory Design," Ph.D. Dissertation, Purdue University, West Lafayette, Indiana, 1999.

[49] A. H. Nayfeh and B. Balachandran, *Applied Nonlinear Dynamics: Analytical, Computational, and Experimental Methods*. John Wiley & Sons, 1995, ch. 3, pp. 147–230. DOI: https://doi.org/10.1002/9783527617548.ch3.

[50] T. S. Parker and L. O. Chua, *Practical Numerical Algorithms for Chaotic Systems*. New York: Springer-Verlag, 1989. DOI: https://doi.org/10.1007/978-1-4612-3486-9.

[51] B. T. Barden and K. C. Howell, "Fundamental Motions Near Collinear Libration Points and Their Transitions," *The Journal of the Astronautical Sciences*, vol. 46, no. 4, pp. 361–378, 1998, ISSN: 2195-0571. DOI: https://doi.org/10.1007/BF03546387.

[52] M. W. Lo, B. G. Williams, W. E. Bollman, *et al.*, "Genesis Mission Design," *The Journal of the Astronautical Sciences*, vol. 49, no. 1, pp. 169–184, 2001, ISSN: 2195-0571. DOI: https://doi.org/10.1007/BF03546342.

[53] R. Malhotra, "Orbital Resonances and Chaos in the Solar System," *Solar System Formation and Evolution: ASP Conference Series*, vol. 149, p. 37, 1998.

[54] S. J. Peale, "Orbital Resonance in the Solar System," *Annual Recivews Inc.*, vol. 14, pp. 215–246, Jan. 1976. DOI: 10.1146/annurev.aa.14.090176.001243.

[55] S. J. Peale, P. Cassen, and R. T. Reynolds, "Melting of Io by Tidal Dissipation," *Science*, vol. 203, no. 4383, pp. 892–894, 1979. DOI: 10.1126/science.203.4383.892.

[56] E. J. Rivera, G. Laughlin, R. P. Butler, S. S. Vogt, N. Haghighipour, and S. Meschiari, "The Lick-Carnegie Exoplanet Survey: a Uranus-Mass Fourth Planet for GJ 876 in an Extrasolar Laplace Configuration," *The Astrophysical Journal*, vol. 719, no. 1, pp. 890–899, Aug. 2010. DOI: 10.1088/0004-637X/719/1/890.

[57] M. Lecar and F. A. Franklin, "On the Original Distribution of the Asteriods. I.," *Icarus*, vol. 20, no. 4, pp. 422–436, 1973. DOI: https://doi.org/10.1016/0019-1035(73)90015-8.

[58] A. Lemaître, "High-Order Resonances in the Restricted Three-Body Problem," *Celestial Mechanics*, vol. 32, pp. 109–126, 1983.

[59] P. Goldreich and S. Tremaine, "The Formation of the Cassini Division in Saturn's Rings," *Icarus*, vol. 34, no. 2, pp. 240–253, May 1978.

[60] R. R. Bate, D. D. Mueller, and J. E. White, *Fundamentals of Astrodynamics* (Dover Books on Aeronautical Engineering Series). Dover Publications, 1971.

[61] N. I. Sadaka, "There and Back Again: Generating Repeating Transfers Using Resonant Structures," M.S. Thesis, Purdue University, West Lafayette, Indiana, 2023.

[62] F. R. Moulton, *An Introduction to Celestial Mechanics*. New York: The Macmillan Company, 1914.

[63] M. Vaquero and K. C. Howell, "Design of Transfer Trajectories between Resonant Orbits in the Earth-Moon Restricted Problem," *Acta Astronautica*, 2014, ISSN: 00945765. DOI: 10.1016/j.actaastro.2013.05.006.

[64] *Memorandum of Understanding between the National Aeronautics and Space Administration and the United States Space Force*, https://www.nasa.gov/wp-content/uploads/2015/01/nasa_ussf_mou_21_sep_20.pdf?emrc=a97009, last accessed at 2024-03-26, Sep. 2020. (visited on 03/26/2024).

[65] M. Jesick and C. Ocampo, "Automated Generation of Symmetric Lunar Free-Return Trajectories," *Journal of Guidance, Control, and Dynamics*, vol. 34, no. 1, pp. 98–106, 2011. DOI: https://doi.org/10.2514/1.50550.

[66] A. J. Schwaniger, "NASA Technical Note: Trajectories in the Earth-Moon Space with Symmetrical Free Return Properties," *Lunar Flight Study Series*, 1963.

[67] T. A. Pavlak, "Mission Design Applications in the Earth-Moon System: Transfer Trajectories and Stationkeeping," M.S. Thesis, Purdue University, West Lafayette, Indiana, 2010.

[68] M. Gupta and K. C. Howell, "Cislunar Eclipse Mitigation Strategies for Resonant Periodic Orbits," in *AAS/AIAA Astrodynamics Specialist Conference*, Big Sky, Montana, Aug. 2022.

[69] M. Gupta, K. C. Howell, and C. Frueh, "Long-Term Cislunar Surveillance via Multi-Body Resonant Trajectories," in *AAS/AIAA Astrodynamics Specialist Conference*, Charlotte, North Carolina, Aug. 2022.

[70] D. Ivanov and M. Ovchinnikov, *6 - Constellations and formation flying*. Cambridge: Elsevier Science, 2020, pp. 135–146. DOI: https://doi.org/10.1016/B978-0-12-817884-3.00006-0.

[71] S. Bandyopadhyay, R. Foust, G. P. Subramanian, S.-J. Chung, and F. Y. Hadaegh, "Review of Formation Flying and Constellation Missions Using Nanosatellites," *Journal of Spacecraft and Rockets*, vol. 53, no. 3, pp. 567–578, 2016. DOI: 10.2514/1.A33291.

[72] J. P. Almanza-Soto, "Zero-Momentum Point Analysis and Ephemeris Transition for Interior Earth to Libration Point Orbit Transfers," M.S. Thesis, Purdue University, West Lafayette, Indiana, 2023.

[73] D. C. Davis, E. M. Zimovan-Spreen, S. T. Scheuerle, and K. C. Howell, "Debris Avoidance and Phase Change Maneuvers in Near Rectilinear Halo Orbits," in *44th Annual AAS Guidance, Navigation, and Control Conference*, Breckenridge, Colorado, Feb. 2022.

[74] D. E. Lee, *Gateway Destination Orbit Model : A Continuous 15 Year NRHO Reference Trajectory*, NASA Johnson Space Center White Paper, Aug. 2019.

[75] J. Williams, D. Lee, R. Whitley, K. Bokelmann, D. Davis, and C. Berry, "Targeting Cislunar Near Rectilinear Halo Orbits for Human Space Exploration," in *27th AAS/AIAA Space Flight Mechanics Meeting*, San Antonio, Texas, Feb. 2017.

[76] T. Williams, S. Shulman, N. Ottenstein, *et al.*, "Operational Techniques for Dealing with Long Eclipses during the MMS Extended Mission," in *IEEE Aerospace Conference Proceedings*, 2020, ISBN: 9781728127347. DOI: 10.1109/AERO47225.2020.9172276.

[77] T. A. Pavlak, P. W. Stumpf, Y. Hahn, R. S. Bhat, and J. R. Johannesen, "Design and Implementation of the Juno Eclipse Avoidance Maneuver," in *AAS/AIAA Astrodynamics Specialist Conference*, Charlotte, North Carolina, Aug. 2022.

[78] M. S. Smith, Y. Takahashi, B. Rush, and D. Koh, "Orbit Determination Performance of the Jupiter Eclipse Avoidance Maneuver by the Juno Spacecraft," in *AAS/AIAA Astrodynamics Specialist Conference*, Charlotte, North Carolina, Aug. 2022.

[79] E. M. Zimovan-Spreen, K. C. Howell, and D. C. Davis, "Dynamical Structures Nearby NRHOs with Applications to Transfer Design in Cislunar Space," *The Journal of the Astronautical Sciences*, vol. 69, pp. 718–744, 2022, ISSN: 2195-0571. DOI: {https://doi.org/10.1007/s40295-022-00320-4}.

[80] J. Ojeda Romero and K. C. Howell, "Transfers from Geosynchronous Transfer Orbits to Sun-Earth Libration Point Trajectories," *The Journal of the Astronautical Sciences*, vol. 69, pp. 251–283, 2022, ISSN: 2195-0571. DOI: {https://doi.org/10.1007/s40295-022-00308-0}.

[81] M. Holzinger, C. Chow, and P. Garretson, *A Primer on Cislunar Space*, Jun. 2021.

[82] D. A. Vallado, P. J. Cefola, R. Kiziah, and M. Ackermann, "Removing the Solar Exclusion with High Altitude Satellites," in *AIAA/AAS Astrodynamics Specialist Conference*, 2016. DOI: 10.2514/6.2016-5433.

[83] *SPICE Data (SPICE Kernels)*, https://naif.jpl.nasa.gov/naif/data.html, last accessed at 2022-07-15, The Navigation and Ancillary Information Facility, Jul. 2022. (visited on 07/15/2022).

[84] J. J. Roth and E. J. Felt, "Overcoming Technical Challenges from Low Earth Orbit to Cislunar," Maui, Hawaii (Virtual): Presented at the 2020 AMOS Conference, Sep. 2020.

[85] N. B. Lafarge, K. C. Howell, and D. C. Folta, "An Autonomous Stationkeeping Strategy for Multi-Body Orbits Leveraging Reinforcement Learning," in *AIAA SciTech Forum*, San Diego, California, Jan. 2022.

[86] C. Frueh, K. Howell, K. J. DeMars, S. Bhadauria, and M. Gupta, "Cislunar Space Traffic Management: Surveillance through Earth-Moon Resonance Orbits," in *8th European Conference on Space Debris*, Virtual, Apr. 2021.

[87] J. L. Worthy III, M. Holzinger, and K. Fujimoto, "Optical sensor constraints on space object detection and admissible regions," *Advances in the Astronautical Sciences*, vol. 150, pp. 93–112, 2014.

[88] N. Kinzly, B. Polzine, C. Short, and J. Woodburn, "Simulating a Dynamics-Informed Cislunar RPO Mission Incorporating Orbit Determination," in *AAS/AIAA Astrodynamics Specialist Conference*, Charlotte, North Carolina, Aug. 2022.

[89] D. Somavarapu, D. Guzzetti, and S. Hesar, "Feasibility Studies for an Autonomous Cislunar Position, Navigation and Timing Constellation," in *AAS/AIAA Astrodynamics Specialist Conference*, Charlotte, North Carolina, Aug. 2022.

[90] K. Hill and G. H. Born, "Autonomous Interplanetary Orbit Determination Using Satellite-to-Satellite Tracking," *Journal of Guidance, Control, and Dynamics*, vol. 30, no. 3, pp. 679–686, 2007. DOI: 10.2514/1.24574.

[91] L. Zhang, "Development and Prospect of Chinese Lunar Relay Communication Satellite," *Space: Science & Technology*, vol. 2021, 2021. DOI: 10.34133/2021/3471608.

[92] "Proximity-1 Space Link Protocol – Rationale, Architecture, and Scenarios," Tech. Rep., Dec. 2013.

[93] R. Kozman and A. Curiel, "Commercial Data Relay Services in the Cis-Lunar Environment with SSTL's Lunar Pathfinder," in *Small Satellite Conference*, Logan, Utah, Aug. 2023.

A. VISIBILITY AND RANGE METRIC REFERENCE VALUES

In the current work, nominal values for visibility and connectivity metrics, including the limiting magnitude and various exclusion angles, as well as the range for communications are assumed for preliminary analysis. The values employed in this investigation are representative examples; the trajectory design and analysis framework is adaptable to incorporate other values as necessary. In the following subsections, the nominal values assumed in the current work are summarized, along with the ranges of existing values in literature.

A.1 Limiting Magnitude

The reference limiting magnitude values employed by various authors are detailed in Table A.1. In the current work, a nominal limiting magnitude value of $\mathbb{M}_{\text{lim}} = 20$ is utilized to obtain a broad evaluation of the observer performance. For further analysis and, to accommodate for various optical sensor apertures, lower values of the limiting magnitude may be utilized.

Table A.1. Reference values for limiting visual magnitude.

Author	Limiting Magnitude
Thompson et al. [27]	$13 - 16$
Frueh et al. [26], [86]	20
Bhadauria et al. [29]	20
Vallado et al. [82]	$16.5 - 17.5$
Worthy et al. [87]	$12 - 15$
Vendl et al. [25]	$17 - 20$

A.2 Exclusion Angles

The current work characterizes the solar, Earth, and lunar exclusion zones as conical volumes within which targets are not visible to space-based optical observers. Table A.2

summarizes the exclusion angles employed by various authors in modeling these exclusion zones. In this investigation, the nominal values that describe these exclusion zones are $\sigma_S = 30°$, $\sigma_E = 10°$, $\sigma_M = 10°$ for the Sun, Earth, and the Moon, respectively. To further increase the fidelity of lunar exclusion modeling, a modified lunar exclusion model is introduced that scales this nominal lunar exclusion zone as a function of the lunar phase as viewed by the observer. Depending upon the spacecraft onboard hardware and sensor characteristics, the exclusion angles may be varied to assess the visibility of targets from space-based observers.

Table A.2. Reference values for exclusion metrics.

Author	**Solar Exclusion** [deg]	**Earth Exclusion** [deg]	**Lunar Exclusion** [deg]
Thompson et al. [27]	30	10	10
Bhadauria et al. [29]	50	35	30
Vallado et al. [82]	30	-	10
Fowler et al. [30]	30	-	-
Kinzly et al. [88]	10	10	10
Somavarapu et al. [89]	15	-	-

A.3 Range Metric for Satellite Communications

The current work employs a range metric to identify opportunities for communications between satellites in a constellation. This nominal range value, that serves as a means to design the constellation orbits for periodic interfacing, is selected as $120,000\ km$. While inter-spacecraft communications are inherently tied to the onboard hardware and signal properties, this value is selected for the preliminary design of trajectories for the vastness of cislunar space. Reference architectures for inter-spacecraft communication include the LIAISON system investigated by Hill et al., demonstrating orbit determination via satellite crosslink for ranges up to $86,000\ km$ [90]. More recently, the China National Space Administration's

(CNSA) Queqiao relay satellite, operating in an L_2 halo orbit to provide a communications link for the Chang'e-4 lander on the lunar far-side, has demonstrated communications ranging up to $79,000\ km$ between the spacecraft [91]. Finally, the Lunar Pathfinder satellite, that seeks to provide communications services around the Moon, is expected to be equipped with hardware that can accommodate ranges up to $100,000\ km$ [92], [93]. Thus, while the nominal value employed in this investigation permits preliminary analysis, for further refinement of the constellation architecture and to account for spacecraft specifications, shorter ranges may be considered.

VITA

Maaninee Gupta hails from New Delhi, India, and moved to the United States in 2014 to pursue her Bachelor of Science in Aeronautical and Astronautical Engineering at Purdue University. After the completion of her undergraduate studies in 2018, she joined the Multi-Body Dynamics Research Group led by Prof. Kathleen Howell to pursue a masters in Aeronautics and Astronautics. To enable her graduate studies at Purdue, Maaninee was awarded the Charles C. Chappelle Fellowship in 2018. Her masters research focused on resonant orbits for trajectory design in various planet-moon systems leveraging Poincaré maps and orbit chaining. After graduating with her masters in the spring of 2020, she continued on under Prof. Howell's guidance to pursue a PhD in Aeronautics and Astronautics at Purdue. Her research continued the exploration of resonant orbits for trajectory design in the cislunar domain. In 2022, Maaninee received the Zonta International Amelia Earhart Fellowship, awarded annually to women pursuing doctoral degrees in the aerospace industry.